# A 3D Culture Model to Investigate Cellular Responses to Mechanical Loading in Spinal Cord Injury

Jenny Thompson Smith

Submitted in accordance with the requirements for the degree of Doctor of Philosophy

The University of Leeds

School of Mechanical Engineering

September 2016

The candidate confirms that the work submitted is his/her own and that appropriate credit has been given where reference has been made to the work of others.

# Acknowledgements

I would like to thank my supervisors, Professor Joanne Tipper, Professor Richard Hall and Doctor James Phillips for all of their help and support throughout the project. Thank you for giving me the freedom to experience different laboratories and collaborations; without these collaborations I would not have been able to generate the results that I did. Joanne, you have been very patient and supportive throughout the entirety of my project, I am very grateful for the time you put in, especially when I was so last minute, to read abstracts, presentations, and thesis chapters! I have thoroughly enjoyed the last five years working with you all.

Thank you to everyone at James' Open University and University College London labs, thanks for always being on the end of the phone to help me troubleshoot the many things that weren't quite working as expected! Special thanks go to Caitriona and Ruth, you were a massive help in the lab and always made sure I had a great time in London!

I would like to thank Nik Kapur, for giving me access to the rheometer which ended up contributing such a large chunk of my research; I know I said I only needed to run a few experiments for a couple of months, thanks for letting me spend over a year and a half popping in and out to just 'run one more test!'.

Thank you to Ronaldo and Yazi, for the use of their facilities, and especially the impactor, without your training and equipment, the final part of this study might not have happened!

I would like to thank iMBE, the Eileen Ingham lab, and everyone I shared an office with; I will miss you all, thanks for all your help! To my friends, who have also supported me through the late nights and stress, thank you for always being there for me. The CDT program provided me with so many wonderful friends; some of whom

became my lovely housemates Emily, Chris and Steve; I couldn't have got through without you guys! Helen - we struggled along through the tough times in the lab, thanks for keeping me on track! Everyone in the office – Imran always had some delicious food waiting for us, and Ash, thanks for getting my second computer monitor up and running – image analysis would have been a horrible task without it!

Thank you to my Mum, Dad, Anna, Grandad and Great Auntie Janet; your love and support over the years is what got me to the stage where I could apply for a PhD, and your continued support, late night phone calls, motivation and love is what has got me to the point of completion! I love you all, thank you! James, I wouldn't have been able to complete this final year without you; you have taken the brunt of my stress and tiredness, yet you have only ever been supportive, loving and caring. I owe you at least one cooked meal a day for the next year, and about $10^6$ cups of tea! You have looked after me so well, and I will be forever grateful.

I would like to dedicate my PhD to my wonderful Grandad who sadly passed away this year; you were always so supportive of me and especially my academic progress and I wish I could have told you that I'd finally finished.

# Abstract

Spinal cord injury (SCI) can cause paralysis, loss of sensation, and respiratory dependency, which has a significant impact on the quality of life of patients, their life expectancy and is also a significant economic burden due to the high costs associated with primary care and loss of income. One of the difficulties in establishing a treatment method is the heterogeneity of SCI; there are many different types and severities of traumatic primary injury, across different age groups of patients and different locations within the spinal cord, whilst at a cellular level, there are multiple, interacting secondary injury cascades that amplify the primary damage inflicted during the traumatic insult. Many techniques have been developed to mimic particular injuries found in human SCI, however *in vivo* animal models can be extremely costly and time consuming. The modest translation of therapeutic treatments from animal models to successful clinical trials suggests that there is a need for simplified models of SCI, in which the complex secondary cascade can be broken down into specific cellular interactions under controlled injury parameters.

It was hypothesised that *in vivo* injuries could be simulated using a 3D *in vitro* model of SCI within a tethered, self-aligned, type-I collagen gel. An *in vitro* model such as this could advance the understanding of cellular responses to injury and help inform animal studies which may facilitate the design of therapeutics.

Initially, different matrices were investigated in order to determine their suitability for use as matrix components for a 3D *in vitro* model of SCI. The matrices were characterised in terms of their mechanical properties, and the cellular responses of astrocytes following culture within the matrices. A fully hydrated matrix was selected which had a lower elastic modulus in comparison to spinal cord tissue, and which maintained astrocytes in a non-reactive state, as determined by the expression of markers for reactive astrogliosis. Contusion models of SCI are thought to generate the most relevant animal models of SCI, therefore their suitability as an injury mechanism within a 3D cellular model was investigated. A pilot study using the

Hatteras contusion device, demonstrated that there was potential for *in vivo* type contusion devices to be utilised with an *in vitro* 3D collagen gel SCI model. The remainder of the study utilised the Infinite Horizons (IH) *in vivo* impactor, which is a force controlled contusion device. The experimental parameters utilised with the IH impactor within an *in vivo* setting were investigated as to their suitability for collagen gel impactions. Following a detailed investigation, the *in vivo* parameters of an impact force of 200 kdyn and a dwell time of 0 ms, using a 2.5 mm diameter impaction tip were adopted; however the calibration start height of the impaction tip was altered to avoid full penetration of the impactor tip through the gel. The limitations of the contusion device affected the consistency of the impaction and resulted in a lack force output data. These limitations need to be resolved in order to directly compare *in vivo* and *in vitro* SCI using the IH impactor. The impaction of 3D aligned, collagen gels, seeded with primary rat astrocytes, using the IH impactor generated a 3D cavity bordered by reactive astrocytes, which was reminiscent of the glial scar and cystic cavity which forms at the lesion site *in vivo*. An increasing gradient of the astrocyte reactivity marker, glial fibrillary acidic protein, was expressed by cells closest to the impact zone. Astrocytes within the first 100 µm of the impact zone were highly ramified with cellular filaments aligned with the edge of the impact zone. An increase in the expression of astrocyte reactivity markers was observed over a ten-day period following impaction.

In summary, a 3D model of SCI was developed that was highly adaptable, and suitable for further advancement to increase the complexity and experimental outputs that were presented in this study. More detailed analysis of the cellular responses, over longer time courses, and perhaps with the additional complexity of multiple cell types would complement investigations within *in vivo* models. 3D *in vitro* tethered collagen gel models such as this could provide valuable insights into the cellular mechanisms which may progress the translation of treatments into the clinic.

# Table of Contents

# List of Figures

# List of Tables

# List of Abbreviations

| | |
|---|---|
| **2D** | Two Dimensional |
| **3D** | Three Dimensional |
| **AFM** | Atomic Force Microscopy |
| **APW** | Average Polymer Molecular Weight |
| **ATP** | Adenosine 5'-Triphosphate |
| **BBB** | Blood Brain Barrier |
| **BDA** | Biotinylated Dextran Amines |
| **BDNF** | Brain Derived Neurotrophic Factor |
| **BSA** | Bovine Serum Albumin |
| **C6** | C6 ATCC® CCL-107™ Glial Cell Line |
| **CAM** | Calcein AM |
| **CCL2** | Chemokine Ligand 2 |
| **CCL3** | Chemokine Ligand 3 |
| **CNS** | Central Nervous System |
| **$CO_2$** | Carbon Dioxide |
| **CSF** | Cerebrospinal Fluid |
| **CSPG** | Chondroitin Sulphate Proteoglycan |
| **CXCL10** | Chemokine Ligand Motif 10 |
| **CXCL2/3** | Chemokine Ligand Motif 2/3 |
| **$dH_2O$** | Distilled Water |
| **DMA** | Dynamic Mechanical Analysis |
| **DMEM** | Dulbecco's Modified Eagles Medium |
| **DNA** | Deoxyribonucleic Acid |
| **DNS** | Data Not Shown |
| **DRG** | Dorsal Root Ganglia |
| **EBSS** | Earles Balanced Salt Solution |
| **ECM** | Extracellular Matrix |
| **EDTA** | Ethylenediaminetetraacetic acid |
| **EH** | Ethidium Homodimer-1 |
| **ELISA** | Enzyme-Linked Immunoabsorbant Assay |
| **ESCID** | Electromechanical SCI Device |
| **F** | Force |
| **FCS** | Foetal Calf Serum |
| **FDA** | Federal Drug Association |
| **FH** | Fully Hydrated |
| **FIJI** | Fiji Is Just ImageJ |
| **FS** | Fully Stabilised |
| **G*** | Complex Modulus |
| **G'** | Shear Storage Modulus |
| **G''** | Shear Loss Modulus |
| **GFAP** | Glial Fibrillary Acidic Protein |
| **GFP** | Green Fluorescent Protein |
| **HCL** | Hydrochloric Acid |
| **Hoechst** | Hoechst 33258 |
| **IH** | Infinite Horizons |
| **IL-1** | Interleukin-1 |
| **IL-10** | Interleukin-10 |
| **kPa** | Kilopascal |
| **L** | Litre |
| **LISA** | Louisville Injury System Apparatus |

| | |
|---|---|
| **LVER** | Linear Viscoelastic Region |
| **M1** | Neurotoxic Microglia |
| **M2** | Neuroprotective Microglia |
| **MEM** | Minimal Essential Medium |
| **$MgSO_s$** | Magnesium Sulphate |
| **Ml** | Millilitre |
| **MP** | Methylprednisolone |
| **MPa** | Megapascals |
| **MRI** | Magnetic Resonance Imaging |
| **N** | Newton |
| **NaOH** | Sodium Hydroxide |
| **NT-3** | Neurotrophin-3 |
| **NGF** | Nerve Growth Factor |
| **NS** | Non-Significant |
| **NSCISC** | National Spinal Cord Injury Statistical Centre |
| **NYU** | New York University |
| **Pa** | Pascal |
| **PBS** | Phosphate Buffered Saline |
| **PDL** | Poly-D-Lysine |
| **PEEK** | Polyether Ether Ketone |
| **PFA** | Paraformaldehyde |
| **PI** | Propidium iodide |
| **PLA** | Poly-lactic Acid |
| **PNS** | Peripheral Nervous System |
| **PS** | Partially Stabilised |
| **QMU** | Queen Mary University |
| **r** | Radius |
| **RAFT** | Real Architecture For 3D Tissue |
| **rIL-6** | Rat Interleukin 6 |
| **ROI** | Region Of Interest |
| **SBTI** | Soybean Trypsin Inhibitor |
| **SCI** | Spinal Cord Injury |
| **SEM** | Standard Error Of The Mean |
| **Streptavidin-HP** | Streptavidin-Horseradish Peroxidase |
| **TBI** | Traumatic Brain Injury |
| **TGF-β1** | Transforming Growth Factor-β1 |
| **TNF-∝** | Tumour Necrosis Factor-Alpha |
| **v/v** | Volume/Volume |
| **w/v** | Weight/Volume |

# Chapter 1

# Introduction

## 1.1 General Introduction

Spinal cord injury (SCI) can occur at any age, causing life-long physical, emotional, and social problems such as paralysis, loss of sensation, and respiratory dependency (Sheerin, 2005a).

The (American) National Spinal Cord Injury Statistical Centre (NSCISC) defines spinal cord injury as "the occurrence of an acute traumatic lesion of neural elements in the spinal canal, resulting in temporary or permanent sensory and/or motor deficit". This definition of SCI excludes intervertebral disc disease, vertebral injuries in the absence of SCI, nerve root avulsions and injuries to nerve roots and peripheral nerves outside the spinal canal, cancer, spinal cord vascular disease, and other non-traumatic spinal cord diseases (NSCISC, 2011).

The incidence of SCI in developed countries is estimated to be 11.5 to 53.4 people per one million of the population (Burney, 1993; Bydon et al., 2014; DeVivo and Vogel, 2004; Sekhon and Fehlings, 2001). The incidence of SCI varies due to social and environmental factors such as gun crime and health and safety practices (Bydon et al., 2014). Following hospital discharge, less than 1 % of US patients experience complete neurologic recovery (NSCISC, 2011). In the UK and Ireland there are approximately 50,000 people recorded as living with the effects of SCI. If the present rate of recovery following current treatment methods continues, this number can be expected to increase annually (Macaya and Spector, 2012; Spinal Research, 2011).

The associated economic burden of SCI is approximately UK £1 billion per year (Spinal Research, 2011). The level of injury influences the treatments required and therefore the cost; for example patients may require respiratory assistance,

gastrointestinal treatments, wheelchair access and physiotherapy for the remainder of their lives.

The most common causes of SCI in the UK are traumatic incidents occurring over a very short period of time such as impacts or deceleration, for example; falls (41.7 %); road traffic accidents (36.8 %); sporting injuries (11.6 %) and violence (6.9 %) (Spinal Research, 2011). SCI studies in the USA have found young adults are generally affected most frequently and overall 80.8 % of injuries were in males. SCI tends to affect the younger demographic; most commonly affected are those between 10 and 40 years of age (Bydon et al., 2014).

The biological and biomechanical factors that might interfere with the regeneration of spinal cord tissue are not fully understood. This means that treatments are not specific to the patient, injury type, or preferred mechanism of regeneration.

The following literature review will discuss spinal anatomy, cell types and biomechanical implications of SCI. The current treatments and models available for research into SCI will also be discussed, highlighting their limitations and therefore identifying where future research could be targeted. Considering the currently available models, it is proposed that a three-dimensional *in vitro* culture method could be used to study specific events associated with SCI, which may provide additional research tools in order to gain a more thorough understanding of the pathophysiology of SCI.

## 1.2 Gross Spinal Anatomy

It is important to understand the anatomy of the vertebral column before discussing the spinal cord anatomy in depth, as they have a functional relationship and often bony fragments of vertebrae are involved in the initial SCI event (Snell, 2009).

### 1.2.1 Anatomy of the Vertebral Column

The vertebral column has four principle functions; to protect the spinal cord, provide stability to the torso, provide motion, and aid motion of the extremities (Harms and Tabasso, 1998). The vertebral column is a bony pillar that has a complex anatomy; a combination of bony structures, ligaments and muscles form the spinal canal within which the spinal cord can be found (Snell, 2009).

In humans, the vertebral column consists of thirty-three vertebrae and is divided into five main regions. The number of vertebrae in each region can vary between patients, although the overall number typically remains the same (Drake et al., 2009). There are usually seven separate vertebrae in the cervical (neck) region, twelve thoracic vertebrae (to which the ribs attach) and five lumbar vertebrae in the lower back. The vertebrae in the cervical, thoracic and lumbar regions are known as the articulating vertebrae, the remaining nine vertebrae are fused in adults. The sacrum usually contains five vertebrae and the coccyx is comprised of four vertebrae (Jenkins, 2008). The articulating vertebrae are often referred to by their corresponding segment letter, followed by a numerical reference to their position, with the highest numbers proceeding away from the skull, down the spine. For example, the fifth cervical vertebra is known as C5, and the twelfth thoracic vertebra is known as T12.

During growth into a normal healthy adult, the spine becomes naturally curved into an ‘S’ shape in the sagittal plane; two reverse curves form in the cervical and lumbar regions in order to balance the weight of the body on the spinal column more efficiently, providing a flexible structure which has adequate stiffness and stability (Jenkins, 2008). A schematic representing the different regions of the vertebral column, vertebral labelling and the curvature of the spine is represented in Figure 1.1.

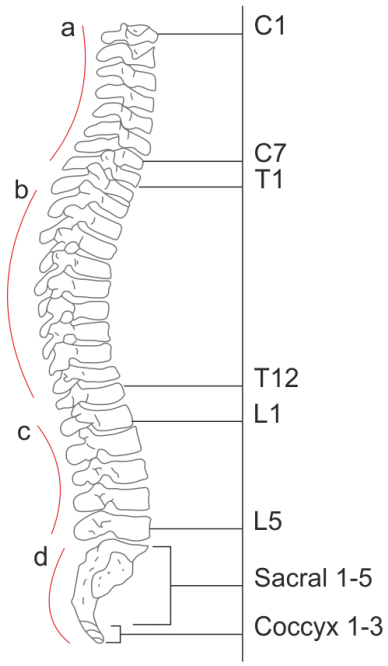


**Figure 1.1: The Vertebral Column.** A lateral view of the vertebral column which highlights the vertebral labelling system and spinal curvature. The cervical vertebrae are labelled C1-C7, the thoracic vertebrae are labelled T1-T12, and the lumbar vertebrae are labelled L1-L5. The five sacral vertebrae are fused, and four vertebrae make up the coccyx region. The spine is naturally curved, highlighted by the red lines in the schematic; **a** cervical curvature, **b** thoracic curvature, **c** lumbar curvature, and **d** pelvic curvature. Adapted from Jenkins (2008).

### 1.2.2 The Vertebrae

A typical vertebra is made up of several parts fused together to form a single bone. The vertebral body portion is the almost cylindrical base of the vertebra. The superior and inferior surfaces of the vertebral bodies are covered in a thin layer of cartilage; these surfaces are known as endplates (Jenkins, 2008).

On the posterior surfaces of the vertebral body there are pedicles. The pedicles project from the vertebral bodies forming a bony interface between the vertebral body and posterior elements. The pedicles form two projections which extend posteriorly to connect to the laminae, forming the vertebral arch. The vertebral foramen forms

between the body and the vertebral arches. The alignment of the vertebral foramen in the vertebral column forms the vertebral canal in which the spinal cord is situated. The transverse processes allow for the attachment of muscles, ligaments and tendons, and for the thoracic vertebrae they form a smooth articular surface for articulation with the ribs. The spinous processes provide another muscle attachment site. The superior and inferior articular processes have smooth facets and are the articular surfaces between the adjacent vertebrae. The cervical, thoracic and lumbar vertebrae vary in size and shape throughout the spinal column; they are specialised for their particular functions at their vertebral position. The vertebral bodies transmit most of the compressive load throughout the spinal column, whilst the main function of the posterior processes is to provide attachment points for the muscles, ligaments and tendons (Jenkins, 2008). The schematic in Figure 1.2 highlights the main features of a typical lumbar vertebra.

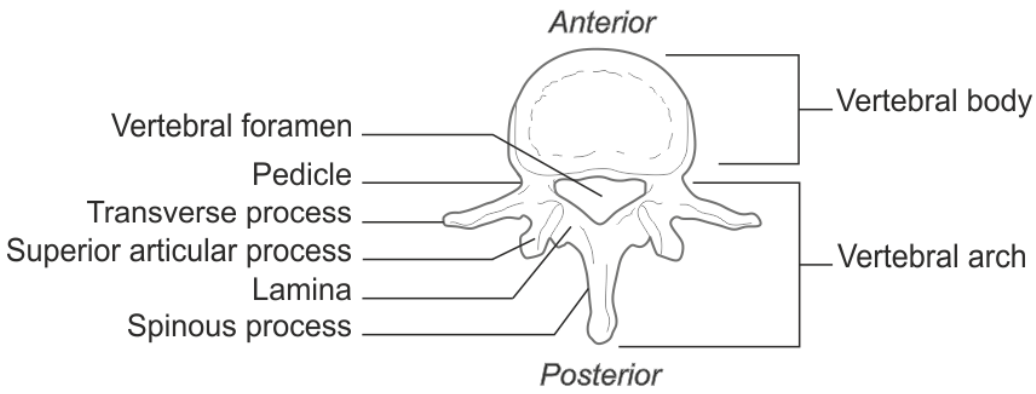


**Figure 1.2: A Typical Lumbar Vertebra.** **S**uperior view of a typical lumbar vertebra, with key features labelled. Adapted from Jenkins (2008).

## 1.3 The Central Nervous System

The nervous system is divided into the central nervous system (CNS) and the peripheral nervous system (PNS). The spinal cord and brain form the central nervous system (CNS), together with the auditory, olfactory, and optic systems. The CNS is mechanically and physiologically continuous with the PNS (Middleditch and Oliver, 2005). The PNS is made up of the peripheral nerves and ganglia that lie outside the brain and spinal cord.

The CNS is a two-layered system; the first layer consists of the sensory neuronal cells and the second layer consists of the motor neuronal cells. The reflex arc is the simplest form of neuronal pathway. A single sensory neuron brings information from receptors to the spinal cord and links, through an interneurone, with the motor neuron that carries impulses out to the effector cells, such as a muscle or gland (Sheerin, 2004). The conduction and interpretation of nerve signals between the CNS and PNS results in sensory, autonomic and motor control which allows the body to move, respire, and respond to external and internal stimuli (Squire et al., 2013).

The mechanical, electrical and physiological components of the CNS are interdependent on each other (Shacklock et al., 1994). The interdependence of the CNS components and the physiological connection between the CNS and PNS means that changes in either of these systems can result in repercussions throughout the body, such as paralysis and loss of sensation (Middleditch and Oliver, 2005).

### 1.3.1 Meninges

The term meninges relates to the three layers of membranous tissue surrounding the spinal cord; the dura mater, arachnoid mater and the pia mater.

The epidural space, sometimes referred to as the extradural space, is the space between the vertebral canal and the dura mater. Throughout the epidural space there are several different tissues: the spinal arteries and nerve roots pass through as they leave through the intervertebral foramina; semi-liquid fat; connective tissue, known as areola tissue; lymphatic vessels; and the intraspinal veins, known as the internal vertebral venous plexus (Middleditch & Oliver 2005).

The outermost covering of the meninges is the dura mater, which is a tube of connective tissue that is continuous with the cerebral dura mater of the brain. The dura mater is attached to bone tissue at the base of the skull and the posterior surface of the second and third cervical vertebral bodies. Tubular sheaths of the dura mater surround the roots of the spinal nerves as they leave the dural sac, becoming the

protective outer covering of the nerves (Drake et al. 2009; Middleditch & Oliver 2005).

The arachnoid mater is the next layer of tissue; it is situated against, but not attached to the dura mater. The arachnoid mater is much thinner than the dura mater. Although the arachnoid mater is relatively avascular, it provides support for blood vessels and aids the transfer of cerebrospinal fluid (CSF) into the blood stream for regeneration. Either side of the arachnoid mater are the fluid filled subdural and subarachnoid spaces. The subdural space contains serous fluid. The subarachnoid space contains cerebrospinal fluid (CSF) which supports the meninges through the delivery of nutrients and removal of waste from the CNS (Jenkins, 2008; Middleditch and Oliver, 2005). The presence of the CSF serves to disperse forces which act on the meninges (Persson et al., 2009).

The third and innermost meningeal layer is the pia mater. The pia mater is firmly adhered to the spinal cord surface; it is a vascular membrane, containing blood vessels to supply the spinal cord. The spinal cord and pia mater are suspended in the cerebrospinal fluid by the arachnoid mater trabeculae and the denticulate ligaments, which prevent excessive movements of the spinal cord in the vertebral canal (Oxland et al., 2011).

### 1.3.2 Macrostructure of the Spinal Cord

The spinal cord is protected by the spinal column. The cord runs through the vertebral canal where intervertebral discs, vertebral bodies and ligaments form the anterior canal wall. The lateral canal walls are formed by the vertebral arches and ligaments. Two pairs of spinal nerves, known as rami, branch off from the spinal cord at each vertebral level, usually exiting at the intervertebral foramina, to become the peripheral nerves that connect to muscle, skin and other structures (Drake et al., 2009).

The spinal cord is slightly flattened anteroposteriorly, such that it is almost cylindrical in shape. The spinal cord does not run the full length of the vertebral column; the

cord extends from the brain (through a hole in the base of the skull, known as the foramen magnum) to the approximate level of the first lumbar vertebra. Below this region the CNS tissue presents as lumbar and sacral nerve roots, known collectively as the cauda equina, which occupy the remainder of the lower spinal canal (Middleditch and Oliver, 2005).

The relationship of the spinal cord to the various structures described above is shown in the schematic in Figure 1.3.

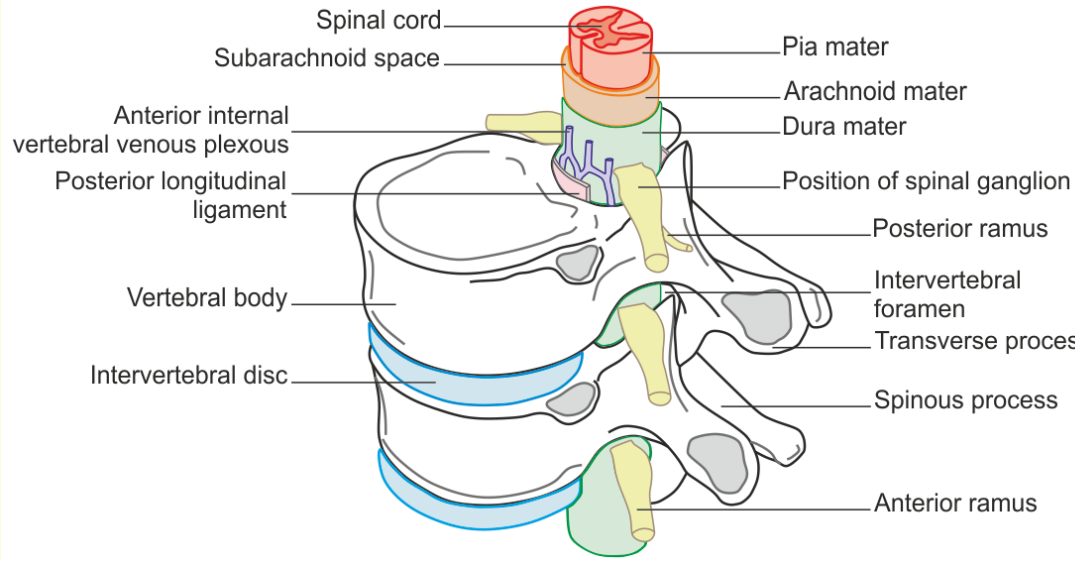


**Figure 1.3: The Spinal Cord within the Vertebral Column.** Segment of the spine with important anatomical features labelled. Adapted from Drake (2009).

### 1.3.3 Microstructure of the Spinal Cord

The spinal cord is divided into grey and white matter. Throughout the length of the spinal cord, the central core of grey matter is formed of two crescent shapes, which together form an 'H' shape when viewed in transverse section. The grey matter is surrounded by the white matter at its circumference. Both grey and white matter consists of nerve fibres, neuroglia and blood vessels (Waibl, 1973).

The white matter is so called because of its white appearance, due to the high content of the lipid, myelin, which surrounds nerve axons. Myelin surrounds almost all long

nerve fibres, acting as electrical insulation, which allows the nerve signals to pass quickly from cell to cell (Squire et al., 2013). White matter contains relatively few cell bodies, unlike grey matter which contains numerous cell bodies and relatively few myelinated axons (Purves et al., 2008).

The white matter is organized into bundles (known as funiculi or tracts), of myelinated and unmyelinated axons. Each tract conveys ascending or descending electrical signals between the CNS and the PNS. Damage to axons can disrupt nerve signals, leading to motor (paralysis) and/or sensory deficits, and/or neuropathic pain (Duval et al., 2015).

The grey matter is so called because of its pinkish-grey colour which is due to the content of capillary blood vessels and neuronal cell bodies. The grey matter can be divided into the posterior, lateral and anterior horns, and a centromedial region surrounding the central canal. The anterior and posterior horns (or columns) of grey matter, have different functions; the anterior cells give rise to fibres which extend to skeletal muscles, they also associate with motor fibres controlling the activity of smooth muscles and glands. The posterior horns receive sensory impulses from the spinal nerves, sending them upwards to the brain (Jenkins, 2008). The central canal runs throughout the length of the cord; it is filled with cerebrospinal fluid (Snell, 2009). A schematic of the grey and white matter is shown in Figure 1.4.

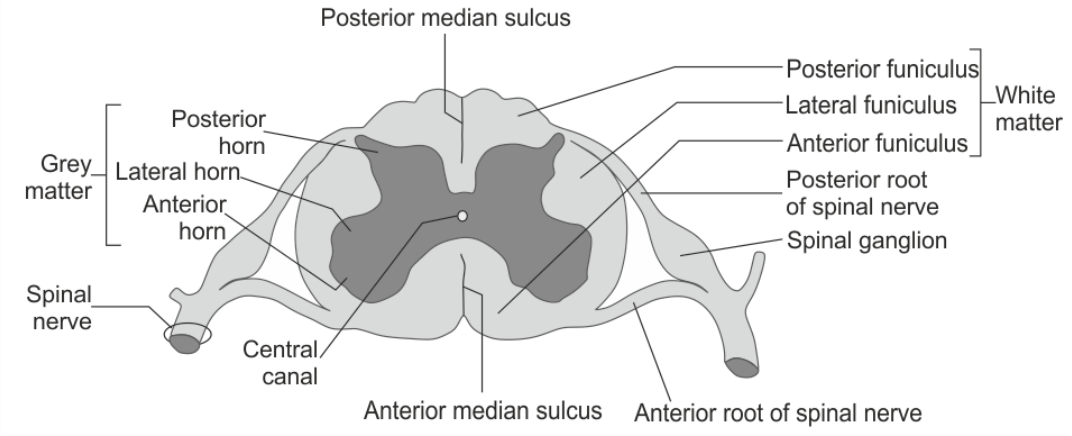


**Figure 1.4: Transverse Spinal Cord Segment with Anatomical Features Labelled.** The grey matter (central 'H' shape) is surrounded by white matter. Posterior and anterior roots leading to spinal nerves are shown. Adapted from Jenkins (2008).

## 1.4 Cells of the Spinal Cord

There are two main groups of cells in the CNS; neuronal and neuroglial cells. Neurons can be defined as the structural and functional units of the nervous system; they generate and conduct electrical changes in the form of nerve impulses. Neuronal physiology is supported and maintained by the neuroglial cells. The neuroglia grouping is in turn separated into two cellular groups; the microglial cells and the macroglia, the latter including astrocyte, oligodendrocyte, and ependymal cells (Schmidt and Leach, 2003; Sofroniew and Vinters, 2010; Squire et al., 2013). Functions of the neuroglial cells include myelination, secretion of trophic factors, and maintenance of the extracellular environment (Squire et al., 2013). In the healthy spinal cord the glial cells are highly organized into a continuous, longitudinal and transverse arrangement (Suzuki and Raisman, 1992).

### 1.4.1 Neurons

The neuron is a highly specialised cell type, found throughout the CNS. Neurons can be categorised in terms of their location, connectivity, neurochemical transmitter interaction, size, and shape (Squire et al., 2013).

A typical neuron can be described morphologically in terms of three main regions. Firstly, the cell body, which contains the nucleus and major cytoplasmic organelles. Secondly, the dendrites, which vary in size and number depending on the type, location or environment of the neuron. Dendrites are processes which extend from the cell body; they provide a large surface area for receiving signals. Thirdly, a neuron consists of an axon, which is a single extension from the cell body, usually extending further than the dendrites; axons vary considerably in length depending on their function and position in the body. An axon may be as short as one hundred micrometres or as long as one metre (in the case of the axon that innervates a muscle in the foot) (Barr and Kiernan, 2004). The axon is surrounded by an electrically insulating myelin sheath, which facilitates rapid conduction of impulses. The axon is responsible for transmitting nerve impulses. A neurite refers to any projection from the cell body of a neuron; this projection can be either an axon or a dendrite. Neurons communicate chemically and electrically through specialized contact zones called synapses (Squire et al., 2013).

Spinal neurons serve two main functions: they relay cutaneous sensory information to higher centres in the brain and they integrate proprioceptive input and motor output. These two functional systems are also segregated anatomically. The neurons and circuits that process cutaneous sensory input are concentrated in the dorsal spinal cord, whereas circuits involved in proprioception and motor control are largely confined to the ventral spinal cord (Brown, 1981; Jessell, 2000). An example of a typical neuron, found in the spinal cord, is shown in Figure 1.5.

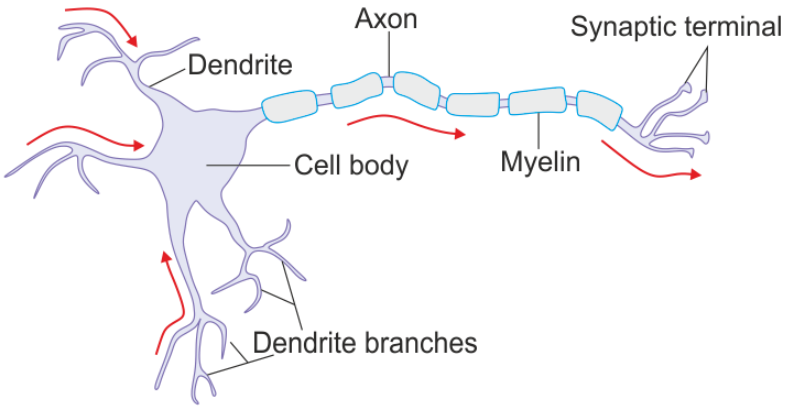


**Figure 1.5: A Typical Neuron.** The red arrows indicate the direction of the received or transmitted nerve impulse, which travels either towards, or away from the cell body. Adapted from (Quasar, 2009).

### 1.4.2 Astrocytes

Astrocytes are so called because of their stellate morphology, which was first described in 1863 (Lenhossék, 1893). It is estimated that astrocytes make up 25 % of the total cell volume in the CNS (Peters et al., 1976).

There are two main subtypes of morphologically distinct astrocytes; fibrous and protoplasmic. Protoplasmic astrocytes are predominant in grey matter; the cells are complex and have numerous fine processes. A protoplasmic astrocyte will typically have between five to ten main branches, each with thousands of fine branching processes extending from them (Barres, 2008). The fine astrocyte processes radiate in all directions and contain a specific form of cytoskeletal intermediate filament, glial fibrillary acidic protein (GFAP). Fibrous astrocytes are predominant in white matter, they are less complex, with fewer branching processes, which contain more GFAP than protoplasmic astrocytes (Kimelberg and Norenberg, 1989; Oberheim et al., 2012). A single astrocyte extends thousands of processes, though these are not visible through GFAP staining alone; GFAP is not present in astrocyte cell cytoplasm, therefore staining of this protein only highlights the main branches of the cytoskeleton (Sofroniew, 2009).

Both fibrous and protoplasmic astrocytes make contact with blood vessels via perivascular feet, which provide a source of energy metabolites for the cells and contribute to the CNS metabolism (Ransom et al., 2003). Astrocytes are able to transport glucose and other metabolites from vascular connections at their perivascular feet to neurons via their processes which attach to nerve axons and synapses (Peters et al., 1976; Sofroniew, 2009).

Astrocytes form an important dynamic partnership with other cells of the CNS, in particular with neurons and their synapses (Ransom and Ransom, 2012). Their processes form gap junctions with the distal processes of neighbouring cells, allowing cell-cell interactions. Astrocytes maintain the homeostasis of the neuronal synapse by removing neurotransmitters and ions, such as glutamate, from the synaptic cleft. Astrocytes maintain the glutamate stores of neurons, by providing the essential precursor amino acid, glutamine (Barres, 2008; Hamilton and Attwell, 2010; Kimelberg and Norenberg, 1989; Nógrádi and Vrbová, 2013). The rapid removal of neurotransmitters and ions is important for the maintenance of synaptic activity (Squire et al., 2013).

### 1.4.3 Oligodendrocytes

Oligodendrocytes produce myelin within the CNS, an electrically insulating lipid enriched material (Jakovcevski et al., 2009). One oligodendrocyte is able to myelinate several adjacent axons because it has several myelinating processes, which are each able to myelinate one axon (McLaurin and Yong, 1995). Oligodendrocytes wrap spiral layers of cell membrane around the axon, the membranes fuse to form the myelin sheath. Schwann cells are responsible for forming the myelin sheath in the PNS (Nógrádi and Vrbová, 2013).

In addition to providing insulation and trophic support to neurons, oligodendrocytes control axon diameter and the spacing and clustering of ion channels at nodes and paranodes, which are the spiralled lamellae of gradually terminating myelin (Barres, 2008).

Myelination is important because it speeds up the transmission of nerve impulses. Nodes of Ranvier are sections of unmyelinated axon, formed at the junction between two paranodes. The nerve impulse electrically jumps from node to node speeding up the rate at which the cell can transmit an action potential (FitzGerald and Folan-Curran, 2001; Snell, 2009). Normal neuronal activity and axonal transport is reliant on healthy myelination (Edgar et al., 2004; Kassmann and Nave, 2008).

### 1.4.4 Microglia

The CNS has a unique set of resident immune cells known as microglia, of which there are several subtypes (Cullheim and Thams, 2007; Jordan and Thomas, 1988; McTigue and Tripathi, 2008). Microglia make up approximately 10 % of the healthy CNS neuroglial cell population (Hanisch and Kettenmann, 2007). Un-activated microglia are highly branched cells covering a 30–50 μm wide area with no overlap of branches between neighbouring microglia (Kongsui et al., 2014; Nimmerjahn et al., 2005).

Microglia are involved in many of the processes that are essential for the development of the CNS in developing foetuses, such as the clearing of extracellular debris and apoptotic cells. In the developed CNS, microglia remain in a un-activated state; they are highly mobile cells that are involved in immune surveillance, antigen presentation, phagocytosis and neuroprotection (Kreutzberg, 1996; McTigue and Tripathi, 2008). Microglia are involved in tissue remodelling processes such as synaptic plasticity both during development of synapses and after injury (Cullheim and Thams, 2007).

Although microglia have phagocytic ability, they do not appear to have the strong professional phagocytic ability exhibited by activated macrophages (Barres, 2008; Streit et al., 1999). Under pathological circumstances microglial cells become activated, increase in size and number and are usually supplemented by blood-born macrophages (Nógrádi and Vrbová, 2013).

The cellular interactions of the cells of the CNS are complex; some of the key cellular interactions are highlighted in Figure 1.6.

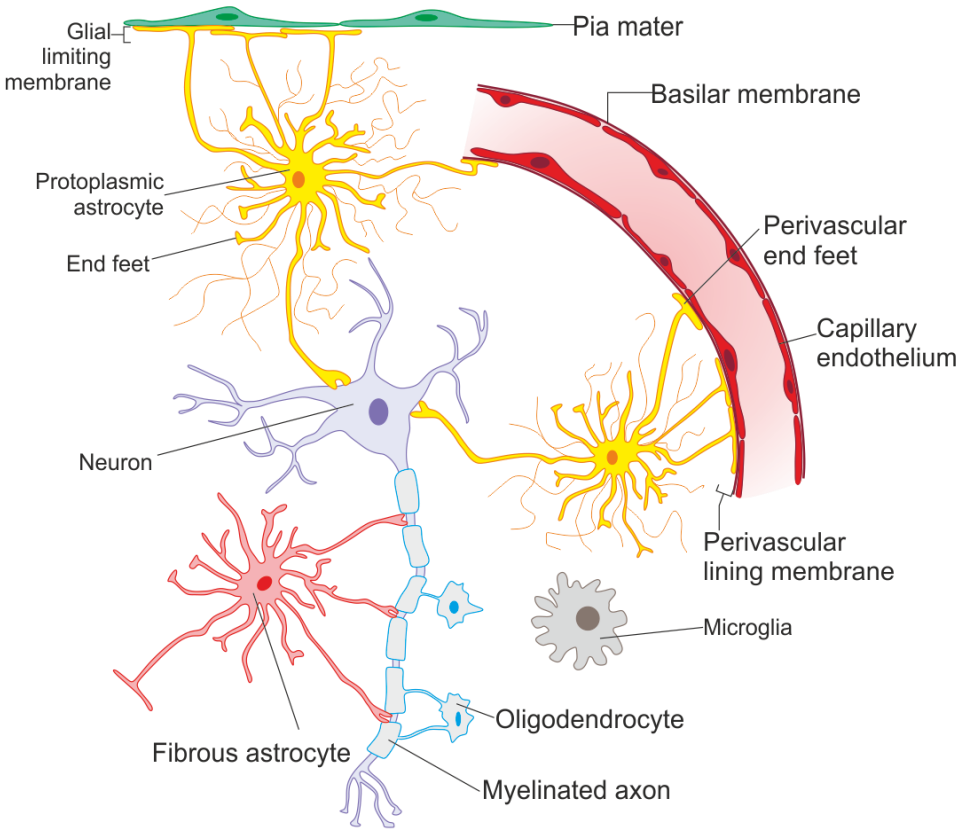


**Figure 1.6: Cellular Interactions in the Spinal Cord.** Schematic to highlight the common interactions of the cells of the spinal cord. Membranes, such as the glial limiting membrane and the perivascular lining membrane, are made up of the end feet of astrocyte processes. Adapted from (Anatomycorner, 2015).

## 1.5 The Biomechanical Properties of the Spinal Cord

Biomechanics is the study of forces and physical responses in static and dynamic biological systems. A system, such as the spinal cord, is likely to react in a specific way when a force, or load, is applied to it. Systems have a threshold, also known as tolerance, which is the point at which loading will cause tissue damage. The threshold is dependent on the type and duration of the load.

The basic terms used to describe applied loads are force and stress and the resulting responses are deformations and strains. These terms and other important biomechanical definitions are described in more detail in Table 1.1.

**Table 1.1: Biomechanical Terminology and Definitions**

| TERM | DEFINITION |
|---|---|
| Force (F) Units: Newton (N) | The force of one body on another will cause acceleration of the second body, unless an equal and opposite force acts upon the second body which counteracts the effect of the first body. A force may cause deformation or motion. |
| Deformation | The change in shape of a body subjected to a force. |
| Stress Units: Pascal (Pa) | The distribution of force relative to the area on which it acts. **Axial stresses (σ)** act perpendicular to the surface, while **shear stresses (τ)** act tangential to the surface. The amount of stress generated by a force is dependent on the size of the area over which the force is applied. |
| Strain | The relationship between the deformed and un-deformed body state. Strain is caused by stress. |
| Extensional strain (ε) | Linear load: change in length, divided by original length. If the result is positive strain, it may be further defined as **tension**. If the result is negative strain, it may be further defined as **compression**. |
| Shear strain (γ) | The extent of deformation after application of shear stress. For example, the change in length, divided by original length. Shear strain is a unit-less parameter. |
| Elasticity | The property of a material to deform to a defined extent in response to a force and then return to its original state when the force is removed. |
| Viscosity (η) | The measure of resistance of a fluid to a shear stress. |
| Yield stress ($\sigma_y$) | The maximum stress applicable to a system before deformation occurs. |
| Young's modulus (E) | A constant describing a material's resistance to deformation in extension or compression up to the point of yield stress. |
| Tangent Modulus | The slope of the stress-strain curve at any specified stress or strain. The tangent modulus is useful in describing the behaviour of materials that have been stressed beyond the elastic region. The tangent modulus quantifies the "softening" of material that generally |

| | |
|---|---|
| | occurs when it begins to yield. |
| Viscoelasticity | The time-dependent property of a material to show sensitivity to rate of loading or deformation; viscoelastic materials exhibit both viscous and elastic characteristics when undergoing deformation. |

Adapted from
(Benzel et al., 2012; Franze et al., 2013; Harrison et al., 1999a; LaPlaca et al., 2007)

The mechanical material properties of a sample are usually measured by applying a mechanical stress and measuring the resulting strain; the deformation of the sample. For simple elastic materials, the ratio of stress to strain determines a modulus, which defines the stiffness of the material. Most biological materials, such as cells and tissues, are viscoelastic. A viscoelastic material will respond to a mechanical stress or strain in a way that is partly elastic and partly viscous and depends on the timescale over which the stress is applied (Franze et al., 2013; Shetye et al., 2014).

As described previously, the structure of the spinal cord is complex. The parallel axial fibres of the white matter, and the less organised grey matter, containing randomly oriented neuronal and glial cell bodies, vascular tissues and the interwoven connective tissue, of the spinal cord, influence the mechanical behaviour of the tissue. The CNS has heterogeneous mechanical properties, resulting in different structural and functional tolerances of the CNS tissues, depending on the region tested (Bilston and Thibault, 1996; LaPlaca et al., 2007).

There is a lack of data on mechanical properties of the human CNS, probably due to the particular difficulties in terms of preparation and measurement of the properties of samples (Christ et al., 2010). For example, Oakland and colleagues found that there was a 33 % increase in the tangent modulus of the spinal cord following a 24 hour time difference between mechanical testing and dissection of the tissue (Oakland et al., 2006). For this reason, human samples are studied relatively rarely, because the excision of tissue within such a short time period is often not logistically possible (Cheng et al., 2008; Shetye et al., 2014).

Reports of mechanical properties of the CNS determined experimentally are confounded by a wide range of variables leading to variability in the reported figures (Clarke and Bilston, 2008). For example, in their review of the literature, Franze et al. (2013) discovered stiffness values for brain tissue of between 40 Pa and 20 kPa, therefore care must be taken to consider the strain rates and timescales of methodologies before making direct comparisons in the literature (Franze et al., 2013).

Experimental variables may include a range of strain rates, tissue species, sex of species, age of species, testing region of the cord, presence of the meninges, environmental testing conditions, cadaveric or non-cadaveric, and properties gathered computationally or with imaging techniques (Cheng et al., 2009; Christ et al., 2010; Clarke et al., 2009; Garo et al., 2007; Gefen and Margulies, 2004; Lee et al., 2013; Miller et al., 2000; Shetye et al., 2014; Soubeyrand et al., 2013). This is represented by the data presented in Table 1.2, which summarises the results from various investigations and details the various protocols used to obtain the results, following a review by Cheng et al., in 2008. The reported moduli of spinal cord tissue ranges from 0.0119 - 1.19 MPa, depending on experimental protocol (Cheng et al., 2008).

**Table 1.2: Protocols and Reported Moduli from the Mechanical Testing of Spinal Cord Tissue**

| Reference | *Specimen Preparation* | | | | | | Test type | *Testing Protocol* | | | Reported modulus |
|---|---|---|---|---|---|---|---|---|---|---|---|
| | **Specimen details** | **Region** | **Environment** | **Harvest-test time** | **Size** | ***N*** | | **Preconditioning** | **Max strain** | **Strain rate** | |
| (Tunturi, 1978) | Dog | Not specified | *in vivo* | N/A | 120 mm | 1 | Stress-strain response to tension | None | 19 % (failure) | Quasi-static (5g increments) 0.002 $s^{-1}$ | 0.0119 - 0.0168 MPa |
| (Hung et al., 1981a) | Cat | T8 - L1 | *in vivo* | N/A | 25 mm | 4 | | None | 8-12 % | 0.0008 $s^{-1}$ | 0.4 MPa |
| (Hung et al., 1981b) | Cat | L1 - L2 | *in vivo* | N/A | 7 mm | 3 in 2 groups | | None | 1 %, 16 % | 0.002 $s^{-1}$ | 0.295 MPa, 0.252 MPa |
| (Hung and Chang, 1981) | Puppy (3-4 kg) | L1 - L2 | *in vivo* | N/A | 8 mm | 3 | | None | 1.7 % | 0.003 $s^{-1}$ | 0.265 MPa |
| (Bilston and Thibault, 1996) | Human (30-84 yrs) | Cervical and thoracic | *in vitro* | <24 hrs | 30 - 45 mm | 3 | | None | c. 10% | 0.048 $s^{-1}$, 0.120 $s^{-1}$ 0.225 $s^{-1}$ | 1.02 MPa, 1.17 MPa, 1.37 MPa |
| (Fiford and Bilston, 2005) | Rat (c. 230g) | C1 - L4 | *in vitro* | Immediate | Not specified | c. 17 in 3 groups | | 10 cycles | 5 % | 0.002 $s^{-1}$, 0.02 $s^{-1}$, 0.2 $s^{-1}$ | 1.14 - 1.98 MPa |
| (Oakland et al., 2006) | Cow | Unknown | *in vitro* | 3 hrs | 130 - 180 mm | 1* | | 15 cycles | c. 8.5 % | 0.24 $s^{-1}$ | 1.19 MPa |
| (Ichihara et al., 2001) | Cow (2 yrs) | C3 white matter | *in vitro* | Immediate | 17 mm | 6 | | None | 40 % (failure) | 0.05 $s^{-1}$ | 0.166 MPa |
| (Ichihara et al., 2001) | Cow (2 yrs) | C3 grey matter | *in vitro* | Immediate | 17 cm | 6 | | None | 55% (failure) | 0.05 $s^{-1}$ | 0.025 MPa |

*Note, *N* refers to the specimens for which raw data was provided, not total specimens of study. Table adapted from (Cheng et al., 2008)

The pia pater has been shown to provide the cord with tensile strength in the axial direction; comparisons between spinal cords subjected to axial tension, tested with and without the pia mater, showed a significant statistical difference between the elastic moduli; the average elastic modulus tested with pia mater was 1.40 MPa, compared to an average elastic modulus of 0.089 MPa without the pia pater (Mazuchowski and Thibault, 2003).

On a cellular level, using scanning force microscopy, the Young's Modulus of neurons (from the hippocampus and retinal region of the brain) was shown to have a frequency dependent value of approximately 1 kPa in comparison to a Young's Modulus of approximately 400 Pa in astrocyte cells (Lu et al., 2006). Bernick et al. (2011) also found neuronal cells to be stiffer than glia, which may explain why white matter tends to be reported as stiffer than grey matter (Bernick, 2011; Christ et al., 2010; Franze et al., 2013; Georges et al., 2006).

### 1.5.1 Physiological Loads

The dura mater is connected to the bone tissue at the skull and the second and third vertebral bodies. The connection of the dura mater results in forces that are associated with movement of the vertebral canal, being transmitted to the meninges (Troup, 1986). The spinal cord and the surrounding meninges are able to move up and down within the vertebral canal (Oxland et al., 2011). The spinal ligaments tether the spinal cord; the balanced transverse forces of the two dentate ligaments provide stability and protection, maintaining the central position of the spinal cord within the spinal canal and limiting the movement (White and Panjabi, 1990).

Mechanical loading of the spinal column is part of normal function; without it atrophy of the bone and muscles would occur, leading to pathology. Normal function of the spine and spinal cord includes the input of biomechanical strain, compression and shear forces (Oxland et al., 2011). The spinal column supports vertical loads of three times body weight during walking; approximately 2100 N. During lifting, the column can support up to 5000 N (Izzo et al., 2013; Wilke et al., 1999). The spine has six

degrees of freedom, including a normal range of motion whereby it can undergo flexion (bending), extension (stretching) and rotation. However, injury may occur if a load exceeding the spinal cord mechanical tolerance is applied. The spinal column serves to protect the soft spinal cord which is situated within the spinal canal; the canal is formed by the alignment of the bony vertebral bodies of the spinal column. However, this anatomical arrangement, does not allow the spinal canal to deform without deforming the internal structures, such as the spinal cord. The level of deformation can be physiological, or injury inducing (Harrison et al., 1999b).

Flexion and extension lead to the largest changes to the spinal canal and therefore the spinal cord. During normal flexion of the spinal column, structures anterior to the bending axis will shorten and be exposed primarily to compressive forces, whereas tissues posterior to the bending axis will lengthen and be mainly exposed to tensile forces (Harrison et al., 1999a). Due to the biomechanics of the spinal column, different regions of the cord are seen to deform to different degrees during physiological flexion and extension movements. Within the cervical region the spinal cord has been shown to deform 1.8 to 2.8 cm (Rossitti, 1993). A study of the cord in the thoracic region of the spine showed a smaller amount of cord deformation of 0.9 to 1.3 cm. It is thought that this was due to the relatively small mobility of the spinal column in this region, due to the stiffening effects of the rib cage (Ruch, 1997). Within the lumbar region of the spine, cord deformation was reported between 1.0 to 2.8 cm (Penning and Wilmink, 1981).

The spinal cord behaves according to the Poisson's effect, which states that a decrease in cross-sectional area will cause an increase in length, such that the total volume remains constant. Similarly, an increase in cross-sectional area will result in a decrease in length (Harrison et al., 1999b). The rate of loading during physiological movement is relatively low; therefore the changes in length described above, are unlikely to cause neurological injury, because the viscoelastic properties of the spinal cord allow it to respond to deformation over physiological loading times (LaPlaca et al., 2007). Physiological loading of the spinal cord include rates between 0.002 to 0.2 $s^{-1}$ (Fiford and Bilston, 2005), and 0.04 to 0.24 $s^{-1}$ (Bilston and Thibault, 1996). These rates are thought to be clinically representative of physiological strains (Bueno

and Shah, 2008). Strain rates have been reported at very low strain rates of 0.0003 to 0.012 $s^{-1}$, which are thought to be much lower than those estimated to occur during both normal motion and injury (Clarke and Bilston, 2008; Oakland et al., 2006). Very slow stretching of the spinal cord (0.006 – 0.008 $s^{-1}$) at magnitudes of 25, 50, and 100% has been shown to cause very little damage to the cord in comparison to fast strain rates (355 – 519 $s^{-1}$), even when doing so doubled the original length of the cord, this is likely to be due to the viscoelastic properties of the spinal cord (Shi and Whitebone, 2006).

### 1.5.2 Loads Implicated in Spinal Cord Injury

Injury occurs to the spinal cord when the applied load is greater than the mechanical tolerances of the cells and tissue can allow. The rate of loading and the amount of deformation or load are important factors and are thought to affect the outcome of the injury (Oxland et al., 2011).

The mechanical impact of injury can cause the displacement of bone fragments, intervertebral discs, and ligaments, resulting in compression and contusion of the spinal cord tissue. Compression of the cord at the site of impact lengthens the surrounding tissue in the longitudinal direction. Similarly, an injury as a result of over-extension will also result in compression away from the site of injury (Shi and Pryor, 2002). Injury is most commonly caused by fracture and dislocation of the spinal column, resulting in a focal injury; 80 % of injuries are fracture-dislocations and burst fractures, which are high energy spinal fractures (Pickett et al., 2006; Sekhon and Fehlings, 2001). A burst fracture will typically cause the posterior aspect of the vertebral body to break away as the body bursts, propelling the bone into the spinal cord. Fracture-dislocations cause compression and shear of the spinal cord as adjacent vertebral segments are translated (Clarke and Bilston, 2008; Oxland et al., 2010). Small objects (in particular, those less than two inches in diameter), such as bony fragments that are propelled towards the cord during a burst fracture, result in high stress concentrations. This is associated with a greater risk for local, severe damage and tissue penetration (LaPlaca et al., 2007). The impact velocity of a bone

fragment from a burst fracture is estimated to travel at 4.5 m/s (Khuyagbaatar et al., 2014; Wilcox et al., 2002).

Loading can be static (rare clinically), or most commonly for SCI, dynamic; whereby the loading occurs very rapidly, often under fifty milliseconds (Chang et al., 1988; LaPlaca et al., 2007; Shetye et al., 2014). Loads that are applied quickly are more likely to cause higher levels of damage in non-linear viscoelastic materials because the tissue is not able to react to the force (LaPlaca et al, 2007).

The curved anatomy of the spine affects the way that biomechanical forces act on the spine; as such there are three points along the vertebral column that are particularly susceptible to injury; the junctions of C7 and T1, T12 and L1, and vertebra T7 (Sheerin, 2005a). The vertebrae in the thoracic spine are distant from the anterior-posterior balance axis of the body because of the natural curvature of the spine. This results in the thoracic vertebrae being subjected to eccentric loads. Eccentric axial loads create lever arms and bending moments in a ventral or lateral direction which concentrate stresses on the anterior part of the bodies favouring the occurrence of wedge compression fractures (Izzo et al., 2013). The difference in flexibility between the cervical and thoracic spine, also serves to focus the downward force on the cervical-thoracic junction. The junction between C7 and T1 is the most common injury site for this reason (Prendergast and Sullivan, 2000; Sheerin, 2005a). Similarly, the junction between T12 and L1, is also a rigid-flexible junction therefore this is the second most common site of spinal injury (Chiles and Cooper, 1996). The T7 vertebra represents an injury susceptible position because it is at the apex of the thoracic curve; axial compressive forces can cause a 'buckling' effect in this region (Sheerin, 2005a).

The size of the subarachnoid and intervertebral spaces affects the outcome of trauma; the cervical region is the most susceptible to contusion injuries due to the small subdural space (Stokes & Jakeman, 2002). This may be due to the protective nature of the cerebrospinal fluid (CSF) which was found to protect the spinal cord during impact by reducing its deformation (Persson et al, 2009). However, the CSF has also been shown to cause damage to the spinal cord because of the increased CSF pressure

which can be generated during an injury causing compression of the cord which decreases the blood flow, causing ischaemia (Fedorow et al., 2010; Soubeyrand et al., 2013).

The physical characteristics of the spinal column and cord anatomy modify the energy transfer created during an impact; the energy transfer can be thought of as a wave or pressure pulse which travels through the spinal column contributing to surface and tissue deformation. The pressure wave is thought to exceed speeds of 4 - 5 $m/s^{-1}$ in flexion/extension contusion injuries (Stokes and Jakeman, 2002).

## 1.6 Spinal Cord Injury

Injury to the spinal cord can lead to different levels of motor and sensory loss. Depending on the vertebral level of injury, different parts of the body will be affected. Death can occur almost instantly if the cord is completely severed around the cervical vertebrae C1 or C2, as respiration may stop due to paralysis of the intercostal muscles and diaphragm (Snell, 2009). SCI can cause paralysis below the level of injury and can be extremely debilitating; patients may need life-long wheelchair access, respiratory and gastrointestinal interventions. In some cases, patients are unable to regulate their body temperature or blood pressure below the level of injury. In most cases the quality of life for the patient is reduced (Fehlings and Baptiste, 2005; Spinal Research, 2011).

Different names are given to the types of paralysis; tetraplegia involves the total or partial loss of use of all four limbs and the torso, paraplegia relates to the total or partial loss of use of the lower limbs, and possibly the torso. Spinal cord injuries are generally classed as complete or incomplete; the majority of clinical cases are incomplete injuries (Engesser-Cesar et al., 2007). These are defined according to the degree of function in segments that are innervated below the injury site; a patient with incomplete SCI may be unable to control and move their limbs but might get tingling sensations, for example. Additionally, even if a patient has a clinically assessed complete injury with no function below the affected lesion, at the time of injury, there

is nearly always viable tissue through the lesion which may have the potential for regeneration (Macaya and Spector, 2012; Marsh et al., 2011).

SCI is a two-phase process involving primary and secondary injury mechanisms. The functional outcome for the patient is determined by the location of injury, type of load, force and duration of impact, and the mechanism of treatment. Although the primary injury causes tissue damage, it is the secondary injury which both increases this damage, and prevents the regeneration of tissue.

### 1.6.1 Primary Injury: Mechanical Insult

The primary injury involves the physical force of the initial incident, whereby local deformation and a transfer of energy cause mechanical injury. Compression, over-extension and tearing of the spinal cord may occur due to burst fractures, missiles, dislocation and the rupture of intervertebral discs.

The primary mechanism of SCI can cause compromised skin, bony fractures, tissue tearing, cellular rupture (non-specific cell death) and axon disruption, blood vessel rupture (causing micro-haemorrhages) and reorientation of the tissue. The spinal cord swells to occupy the entire diameter of the spinal canal at the injury level within minutes of injury; this can lead to secondary ischaemia if the swelling exceeds venous blood pressure (LaPlaca et al., 2007).

### 1.6.2 Secondary Injury: The Pathophysiological Response

The secondary injury involves several biological responses (initiated by the primary injury) in which cell damage and cell death occurs; collectively known as the secondary biological cascade or pathophysiological response. Investigation into cellular processes of the secondary injury may provide targets for clinical intervention and future treatments for SCI (de Castro et al., 2004; Faulkner et al., 2004).

The primary and secondary injury mechanisms have been described as having several stages; immediate, acute, sub-acute, and chronic stages, which are described in more detail in Figure 1.7 (Macaya and Spector, 2012).

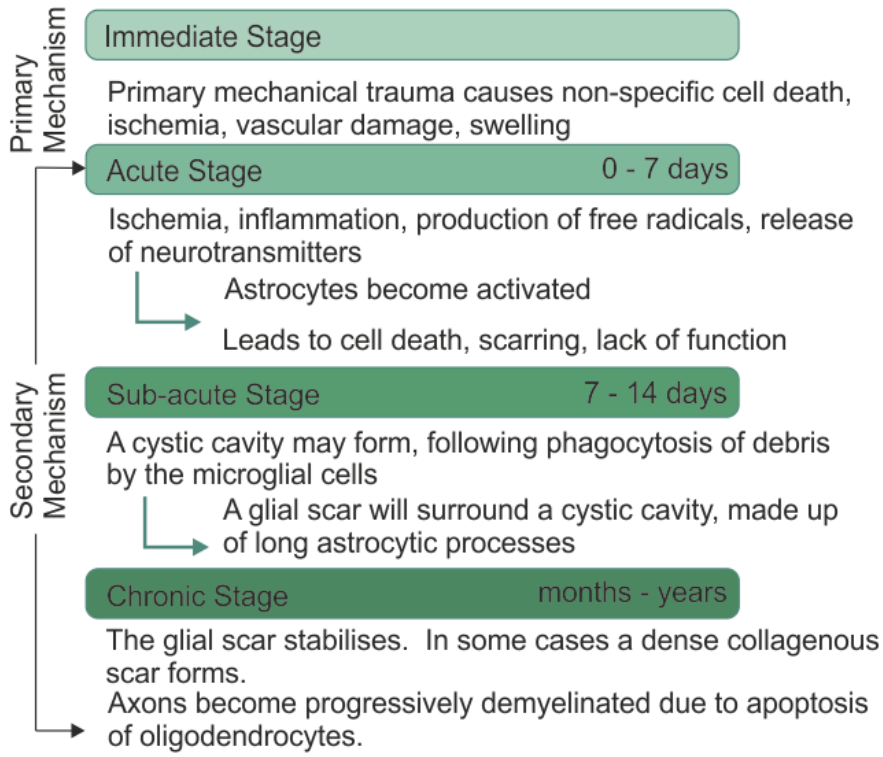


**Figure 1.7: The Stages of the Pathological Response in SCI.** Each stage of the response has biological consequences. The pathophysiological response is a major factor in the prevention of natural spinal cord regeneration and repair. Adapted from Macaya and Spector (2012).

It is postulated that the secondary injury mechanism is an attempt by the cells of the CNS to counteract the mechanical and biochemical disturbances, caused by the primary injury. However, the secondary cellular response often leads to chronic activation, which blocks functional recovery (Streit et al., 1999).

Many biological responses occur as part of the pathophysiological response, examples include: vascular changes such as neurogenic shock, haemorrhage, ischaemia (LaPlaca et al., 2007); neurotransmitter accumulation (Barr and Kiernan, 2004; Barres, 2008; McDonald and Sadowsky, 2002; Sofroniew, 2009), free radical

production (Jurewicz et al., 2005), inflammation and cellular apoptosis (Cullen et al., 2007), demyelination of axons (Bradl and Lassmann, 2010), and ionic derangement, such as the increase in intracellular calcium levels, extracellular potassium and increased permeability to sodium ions (Brown and Ransom, 2007; Cullen et al., 2007; McTigue and Tripathi, 2008).

It has been shown that the secondary responses cause physical and physiological changes to the spinal cord matrix and cellular components, ultimately leading to the formation of a glial scar which acts as a barrier to the regeneration of neuronal tissue (Fawcett and Asher, 1999; Fitch and Silver, 2008; Graeber and Streit, 2010; McKeon et al., 1991; Pekny and Nilsson, 2005; Schwab and Bartholdi, 1996; Sofroniew, 2009; Tator and Fehlings, 1991). The secondary response changes the behaviour of astrocytes, microglia and oligodendrocytes, from their physiological state (Emmetsberger and Tsirka, 2012). Astrocytes and microglia are the major cell populations that form the reactive response to injury (Streit et al., 1999).

*The Immunological Response:*

Microglia are the immunocompetent cells of the CNS. There are two main phenotypes of microglial cells; neurotoxic (M1) and neuroprotective (M2). After injury the cells present in both forms, however eventually the M1 phenotype predominates at 28 days post-injury (Guerrero et al., 2012; Kigerl et al., 2009). Microglia react within minutes of injury; experimentally, they have been shown to direct their cellular processes towards the site of a focal lesion (such as a micro-stab wound) at a rate of 1.25 μm per minute (Davalos et al., 2005). The cells migrate to the site of injury, directed by the products of the primary injury mechanism, such as the presence of extracellular adenosine 5'-triphosphate (ATP), forming a dense border that seems to be a mechanism for reducing the spread of damage (Hines et al., 2009). Microglia proliferate following injury; the time taken for activated microglia numbers to fall to 50 % of maximum recorded after SCI in rats was estimated to be 55 days, indicating a chronic inflammatory response after injury (Prüss et al., 2011).

Microglial activation is thought to be affected by the mechanism of neuronal cell death; in the developing CNS, where neuronal death is usually a controlled

mechanism, known as apoptosis, the activation of microglia is less intense in comparison to neuronal cell death stimulated by CNS injury. Uncontrolled cell death is associated with primary injury (Milligan, 1991). M1 cells that migrate to the injury site cause further damage due to the release of pro-inflammatory cytokines (such as chemokine ligand 2 (CCL2), CCL3, chemokine (C-X-C motif) ligand 2/3 (CXCL2/3) and CXCL10 (a T cell chemoattractant), tumor necrosis factor-alpha (TNF-∝), reactive oxygen species and proteases (Rice et al., 2007). These chemokines recruit peripheral polymorphonuclear leukocytes and monocytes to the lesion and nearby tissue. M1 cells promote neurotoxicity, generating free radicals and promoting apoptosis with detrimental effects, in particular to the oligodendrocyte cells. Apoptosis of oligodendrocytes causes demyelination of axons (Bradl and Lassmann, 2010; Emmetsberger and Tsirka, 2012). Probert and colleagues demonstrated that decreasing the release of TNF-∝ following an injury, reduced the levels of demyelination in mouse injury models (Probert et al., 2000).

Conversely, the M2 microglial phenotype can release nerve growth factor (NGF), neurotrophin-3 (NT-3), interleukin-1 (IL-1), IL-10 (an anti-inflammatory cytokine) and brain derived neurotrophic factor (BDNF), which are thought to influence axon regeneration. In addition, the phagocytic properties of microglia and macrophages promotes regeneration of tissue through the removal of tissue debris and myelin that is necessary for the effective re-myelination of axons and neurite out-growth (Emmetsberger and Tsirka, 2012; Friede and Brück, 1993).

The role of microglia in the reduction of the glial scar is unclear. The timing of the inflammatory response following SCI, in addition to other factors such as magnitude, location and duration of injury, influences whether the microglial response has a positive or negative impact on the SCI (Kwon et al., 2004; Rice et al., 2007). Treatments directed towards increasing the ratio of M2:M1 microglia could promote spinal cord repair, whilst limiting secondary injury (Kigerl et al., 2009).

*Astrogliosis and the Glial Scar:*

Following SCI a glial scar, generated by the mechanisms of the secondary response, forms at the injury site. The glial scar is considered a physiological and physical barrier to neuronal regeneration (Kimelberg and Norenberg, 1989). The process of glial scar formation is multifaceted; it is an extremely important area to understand, as there is the potential for therapeutic targets to be developed, which may aid the regeneration of damaged neuronal tissue following injury (Silver and Miller, 2004). Astrocytes are able to react to CNS injury in a process which is characterised by changes to the morphological and molecular expression of the cells to become reactive astrocytes, in a process known as reactive astrogliosis. Although this is known to be a healing process, reactive astrogliosis can lead to the formation of a glial scar (Kimelberg and Norenberg, 1989; Nógrádi and Vrbová, 2013).

The glial scar contains reactive, hypertrophic astrocytes, which up-regulate intermediate cell filaments such as vimentin and GFAP, they also deposit extracellular matrix proteins called chondroitin sulphate proteoglycans (CSPGs) which are known to inhibit axon regeneration (Lee et al., 2010; McKillop et al., 2013; Silver and Miller, 2004; Yiu and He, 2006). The reactive astrocyte processes link together by gap junctions to form a type of basement membrane at the interface between the astrocytes and the meningeal layers (Heck et al., 2003; Shearer and Fawcett, 2001; Stichel et al., 1999). A schematic of a glial scar and cyst formation in relation to the spinal cord is shown in Figure 1.8.

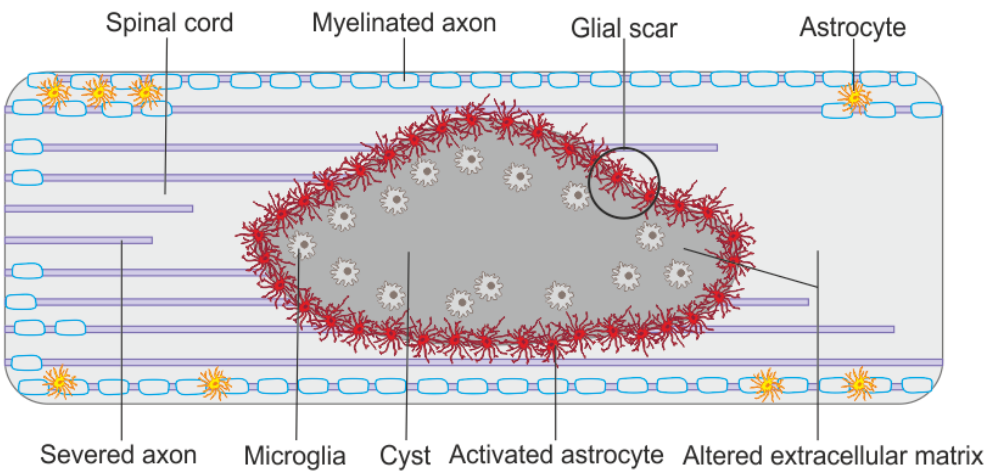


**Figure 1.8: The Glial Scar.** The glial scar serves as a physical and physiological barrier to regeneration of the injured spinal cord. The dense fibrous network of activated astrocytes, sustained release of inhibitors of axon growth, and demyelination of axons are aspects of the secondary injury mechanism. Microglia and macrophages invade the cyst which forms at the epicentre of the injury site. Spared myelinated axons may be found distal to the injury site. Adapted from Macaya and Spector (2012).

The severity of the mechanical insult has been shown to have an effect on the level of astrocyte response; astrogliosis is a spectrum of changes, regulated by both intra- and inter-cellular signalling molecules that can alter cell reactivity, causing direct and indirect changes to the surrounding extracellular matrix, neural and neuroglial cells (Sofroniew, 2009). It is possible for astrogliosis to occur following a mild-moderate trigger and subsequently be resolved so that the tissue returns to its original appearance (Sofroniew and Vinters, 2010). However, at extreme levels of tissue damage and inflammation, such as those involved in SCI, astrogliosis causes irreversible scar formation, whereby the tissue has abnormally high numbers of astrocytes with processes which overlap each other, sustained release of regeneration inhibitors such as CSPGs, and remodelling of the extracellular matrix (Sofroniew, 2009).

Studies have shown that reactive astrogliosis may also have a protective effect following SCI, though there are several influencing factors; for example injury type, location and duration. Using gene knock out models, generation of SCI without

astrocyte cells present, negatively influenced blood-brain barrier (BBB) repair and increased oligodendrocyte and neuronal death (Faulkner et al., 2004). In addition, it has been shown that the blockade of inflammatory cells due to glial scar formation may protect other areas of tissue from an overwhelming inflammatory response, and that astrocytes may actually preserve motor functions following mild-moderate SCI (Faulkner et al., 2004; Silver and Miller, 2004). Astrocytes and matrix components of the glial scar have been shown to create a scaffold for vascularisation, whilst also stimulating and recruiting fibroblasts and endothelial cells to form new capillaries; this is thought to aid neuronal survival (Rolls et al., 2009).

Sofroniew (2009) stated that the total inhibition of reactive astrogliosis would have a negative impact on CNS recovery and should not be considered a therapeutic option (Sofroniew, 2009). Following their review of the literature, Rolls et al. were also of the view that although the glial scar plays an important role in CNS damage, it has beneficial effects in different phases of the recovery process (Rolls et al., 2009). It seems that the benefit of a glial scar is the prevention of mass damage by protecting healthy tissue from the damaged lesion, though this might sacrifice long term functional regeneration for the patient (Silver and Miller, 2004).

## 1.7 Treatment of SCI

The initial treatment for most patients involves preserving the remaining spinal cord function, restoring spinal alignment, and achieving a pain-free fracture site. There are usually two stages to treatment: the persistent mechanical compression of the cord is relieved if appropriate and the acute inflammatory response is targeted with steroids (Macaya and Spector, 2012; Rolls et al., 2009; Sheerin, 2005b).

In fractures that are stable, surgery is usually avoided. Clinical stability is the ability of the spine to limit patterns of displacement under physiologic loads, such that damage or irritation to the spinal cord and nerve roots and incapacitating deformity or pain caused by structural changes is prevented (White and Panjabi, 1990). Decompression surgery is often undertaken for unstable fractures. Decompression surgery involves the removal of material (such as bone fragments) which impinge on

the spinal cord; it is an immediate means of relieving pressure and prevents further injury from the fragments due to instability, this is important for the outcome of regeneration (Jones et al, 2012; Mattei, 2012).

High-dose steroid administration is administered to reduce acute inflammation and decrease swelling to further reduce compression of the spinal cord (Macaya & Spector, 2012). The only FDA approved pharmacologic treatment for SCI in the acute phase is methylprednisolone (MP) (Mattei, 2012). However, the use of steroids is controversial as it has been shown that the neurological benefits are only short term (Gardner & Kluger, 2004; Hurlbert, 2000; Tator, 2006). In addition, to date no clinical trials have demonstrated a benefit of steroid administration to children in relation to SCI; and therefore steroids are not considered in the treatment of children. In adults, MP is commonly provided in the '8 hour window' following injury (Lim & Tow, 2007). However, a study by Short et al. (2000) concluded that MP use did not improve neurological recovery and recommended that it should not be used, particularly due to its links with myopathy (Short et al., 2000). A recent review by Ropper et al. stated that the authors did "not advocate its use given the significant increase in complications and lack of clearly defined benefits" (Ropper et al., 2015).

The initial injury mechanism has been shown to have an effect on the neurological outcome (Marar, 1974); a study by Choo et al. (2008) investigated the effect that three different primary injury mechanisms (contusion, dislocation and distraction) had on the neuropathology observed. The cervical regions of living rats were injured between the C4 and C5 vertebrae and the corresponding secondary mechanisms of pathology were observed after three hours. Sections of the injured cord were immunohistochemically stained for various indicators of the secondary response such as membrane permeability, microglial activation and astrocyte reactivity. The study found the greatest overall pathology in dislocation injuries relative to contusion and distraction; distraction was found to have the least extensive pathology. All injury mechanisms initiated a secondary response after three hours, although there were differences which could indicate that future treatment strategies could be altered or targeted specifically to the pattern of expression that occurs, for example the microglial phenotype was predominantly reactive in the contusion and dislocation

models, however few microglia presented in the reactive phenotype following distraction (Choo et al, 2008).

## 1.8 Models of SCI

As previously described, there is a clinical need for the development of new treatments for SCI; the ability to target the molecular and cellular mechanisms of injury might lead to better functional outcomes for patients. Models of injury are designed to simplify the cellular response to specific aspects or outcomes of SCI, such that treatments can be designed to specifically target cellular responses in order to promote regeneration.

### 1.8.1 *In vivo* Models of SCI

Very little of the current understanding of the SCI secondary pathophysiological response has been discovered from human studies; most is from animal models of a variety of species, ages and injury mechanisms (Kwon et al., 2004).

It is not feasible to study the secondary pathophysiological response following SCI in a human model; the removal of tissue for histological or molecular inspection would be highly damaging for the patient and not representative of the time scale or extent of injury. Although cadavers have been used to study the biomechanical impacts of injury, spinal cord tissue degrades rapidly post-mortem resulting in the tissue being logistically difficult to use (Carter et al., 2000; Kroeker et al., 2009; Oxland et al., 2011; Shetye et al., 2014). Cadaver tissue use for the study of the cellular response is also affected by tissue degradation, and despite use in tissue slice models, the use is controversial. Cadaver tissue tends to come from an older demographic than the clinical average for SCI; age has been observed to have an effect on the tissue properties of the spinal cord (Clarke and Bilston, 2008).

Animal models are commonly used throughout scientific research; they have many advantages and there is a need for them within SCI research (Teo et al., 2012). In particular, animal models are essential for testing novel therapeutic strategies aimed at

regenerating the spinal cord following SCI injury, in a reliable and reproducible manner. Additionally, animal models are thought to be the best way to determine how blood flow in the tissue affects the mechanical properties of CNS tissue (Bilston and Thibault, 1996). Experimentation using animal models allows manipulation of parameters not available for human tissue, such as varying the velocity of known impacts, types of treatments and time of sacrifice, whilst preserving much of the tissue complexity (LaPlaca et al., 2007). However, there are also limitations, as described on a species-specific basis in Table 1.3.

**Table 1.3: Advantages and Disadvantages of Animal Models of SCI**

| Species | Advantages of Species | Disadvantages of Species |
|---|---|---|
| **Lamprey** | • Simple model with few compounding factors (Luna et al., 2013).<br>• Restores spinal function easily – used as a model for how regeneration could be promoted in models without this capacity (Rodicio and Barreiro-Iglesias, 2012).<br>• Can be handled cheaply.<br>• Ethical regulation not as strict as other animal models. | • Neurological plasticity allows functional recovery following SCI – limited to studies of regeneration (Rodicio and Barreiro-Iglesias, 2012)<br>• Not neurologically similar to humans in terms of regenerative capacity (Rodicio and Barreiro-Iglesias, 2012).<br>• Does not contain as many spinal elements such as arteries and veins. Has less complicated set of meninges. (Luna et al., 2013). |
| **Mouse** | • Can be genetically manipulated – additionally, compared to other mammals, more is known about the genetic material of the murine model (Davies et al., 2006; McKillop et al., 2013; Steuer and Guertin, 2009).<br>• Low husbandry requirements (Zurita et al., 2012).<br>• Can be handled at low cost in large quantities. | • Has greater neurological plasticity than humans – may spontaneously regenerate from surviving axons.<br>• Very small size: hard to operate on and use surgical devices, also difficult to recreate clinically relevant injuries (Shetye et al., 2014; Talac et al., 2004).<br>• Postoperative care a challenge with complete injuries (Zurita et al., 2012).<br>• Neurologically not as complex as humans (Oberheim et al., 2009).<br>• Treatments developed are harder to translate to clinic (Jones et al., 2012).<br>• Can be restricted to female mice due to catheterization complications (Onifer et al., 2007).<br>• The time course of human SCI is typically extended with respect to rodents; loss of myelin in the degenerating axon tract takes months in rodents compared to approximately two-three years in humans (Macaya and Spector, 2012).<br>• There is a lower incidence of chronic demyelination in humans compared to rodents (Macaya and Spector, 2012). |
| **Rat** | • Can be genetically manipulated (Davies et al., 2006; McKillop et al., 2013).<br>• Most commonly used – lots of research | • Has greater neurological plasticity than humans – may spontaneously regenerate from remaining axons.<br>• Small size: hard to recreate clinically relevant injuries (Jones et al., 2012). |

| | | |
|---|---|---|
| | comparisons (Stokes and Jakeman, 2002; Tetzlaff et al., 2011).<br>• Low husbandry requirements (Zurita et al., 2012).<br>• Can be handled at low cost in large quantities (Onifer et al., 2007; Teo et al., 2012), for example one study utilised 43 rats (Choo et al., 2009). | • Spinal cord dimensions are considerably smaller than humans (Jones et al., 2012).<br>• Postoperative care a challenge with complete injuries (Zurita et al., 2012).<br>• Human astrocytes are larger (2.6 times bigger in diameter), and structurally more diverse and complex than rodents (10 times more GFAP is expressed in human astrocyte processes) (Oberheim et al., 2009).<br>• Treatments developed are harder to translate to clinic; success of a treatment in a rat model is rarely seen in humans (Teo et al., 2012; Zurita et al., 2012).<br>• Can be restricted to female rats due to catheterization complications (Onifer et al., 2007).<br>• Ethical considerations means no long term (chronic injury) cervical SCI can be studied (Choo et al., 2007).<br>• The relative size of the cerebrospinal fluid (CSF) filled space is not proportional to humans (Jones et al., 2012). The CSF has been shown to have a biomechanical impact on SCI (Kroeker et al., 2009; Persson et al., 2009).<br>• The time course of human SCI is typically extended with respect to rodents; loss of myelin takes months in rodents compared to two-three years in humans (Macaya and Spector, 2012).<br>• There is a lower incidence of chronic demyelination in humans compared to rodents (Macaya and Spector, 2012). |
| **Cat** | • Shown to be a suitable scale-up to a larger animal model from rats (Boyce et al., 2007).<br>• Domesticated, therefore relatively easy to train (Frigon, 2013).<br>• Relatively large size allows biomechanical analysis following injury (Frigon, 2013). | • Relatively large husbandry requirements.<br>• Relatively high initial cost and maintenance costs.<br>• Not commonly used – little comparisons (Talac et al., 2004)<br>• Spinal cord dimensions are considerably smaller than humans (Jones et al., 2012). |

| | | |
|---|---|---|
| **Dog** | • Domesticated, therefore relatively easy to train (Frigon, 2013).<br>• Relatively large size allows biomechanical analysis following injury (Frigon, 2013).<br>• Models have been developed that do not require laminectomy (Fukuda et al., 2005).<br>• Possible to use clinical dog cases from veterinary studies (Frigon, 2013). | • Relatively large husbandry requirements.<br>• Relatively high initial cost and maintenance costs.<br>• Spinal cord dimensions are considerably smaller than humans (Jones et al., 2012).<br>• Not commonly used – few comparisons (Talac et al., 2004). |
| **Miniature Pig** | • Already used as an organ transplantation source (Teo et al., 2012).<br>• Dimensions of spinal cord and CSF similar to that of humans (Jones et al., 2012).<br>• Relatively large size allows biomechanical analysis following injury (Shetye et al., 2014; Zurita et al., 2012). | • Requires expensive husbandry.<br>• Surgery complex and expensive, for example, requires more anesthesia than smaller models.<br>• Expensive rehabilitation.<br>• High maintenance costs.<br>• Advised to not work with more than three to four animals at a time for rehabilitation purposes (Zurita et al., 2012).<br>• Restricted to females due to catheterization complications (Zurita et al., 2012). |
| **Non-Human Primate (NHP)** | • Anatomically and pathophysiology closest to human (Iwanami et al., 2005; Teo et al., 2012).<br>• Has neuronal complexity compared to rodents (Teo et al, 2012).<br>• Therapeutics are easier to translate from animal to clinic (Teo et al., 2012).<br>• Behavioral studies post injury are more clinically relevant (Teo et al., 2012). | • Ability to use upper arms makes rehabilitation difficult (Zurita et al., 2012).<br>• Many studies use small NHPs (marmoset and macaque) where spinal cord dimensions are smaller than humans (Darian-Smith and Brown, 2000; Jones et al., 2012; Suresh Babu et al., 2012).<br>• For ethical reasons, study of the chronic stages of SCI are rarely permitted; normally study the acute stage only in NHP (Tetzlaff et al., 2011; Zurita et al., 2012).<br>• Surgery expensive; requires more anesthesia than smaller animal models.<br>• Difficult to get regulatory approval (Zurita et al., 2012).<br>• Very expensive husbandry (Talac et al., 2004).<br>• Very expensive rehabilitation (Teo et al., 2012).<br>• Human CNS tissue is softer in comparison to the rhesus monkey (Cheng et al., 2008). |

As is clear from Table 1.3, there is often a trade-off between an animal model that more closely resembles human anatomy and neurological complexity, and the related expense, stringent ethical considerations and type of injury that can be modelled. Conversely, sometimes a less complex model, such as the lamprey, is useful as there are fewer confounding factors; the lamprey is often used as a model of regeneration to investigate the differences between an animal that has regenerative abilities, compared to other models which have relatively minor regenerative capabilities, such as non-human primates and humans (Doyle et al., 2001; Talac et al., 2004).

The most commonly used and widely accepted animal model is the rat; this is partially due to the relatively low cost of higher animal quantities, and ease of genetic manipulation and handling (Stokes and Jakeman, 2002; Tetzlaff et al., 2011). Despite the list of limitations described in Table 1.3, many agree that the biochemical, morphological and functional changes that occur in the rat model following SCI are similar to humans (Fleming et al., 2006; McTigue et al., 2000; Metz et al., 2000; Norenberg et al., 2004; Onifer et al., 2007).

Different features are required of an animal model, depending on the outcome the researcher desires from an experiment; for example the available injury mechanisms are not achievable in all models (Shetye et al., 2014).

#### 1.8.1.1 Injury Simulation in *in vivo* Animal Models

The surgery required for the creation of a SCI in an animal model is complex, expensive and varied. Large sample sizes are often required to account for the inter-animal variability associated with animal surgery in order to ensure statistical validity (Talac et al., 2004). Many techniques have been developed to mimic particular injuries observed in human SCI; though most techniques require a laminectomy (the removal of a portion of vertebra and/or ligaments and muscles), which causes additional damage to the local area, spinal instability, which may lead to dislocations, and pathology which would either not have been present or would be exacerbated by this procedure. Although there have been reports of SCI in canine models whereby a laminectomy was not used, there were still disturbances to the

spinal area which would not be present in a clinical scenario, such as the insertion of needles, removal of ligaments (which would create instability, though less than vertebral removal), and the insertion of balloons to compress the cord (Fukuda et al., 2005; Sheng et al., 2004). The injuries replicated in animal models are briefly described in Table 1.4.

**Table 1.4: Mechanical Simulation of Injury in Animal Models**

| Injury Type: | Mechanism Simulation: |
|---|---|
| **Contusion** | • Computer feedback-controlled devices or weight drop rigs<br>• Blunt injury model<br>• Application of a sudden impact force in approx. 4 - 16 milliseconds<br>• Parameters such as impact velocity, compression rate, dynamic force and tissue displacement can be monitored<br>• Leads to tissue damage & haemorrhage<br>• Tissue is rarely fully transected (clinical application)<br>• Best suited for inflammation studies<br>• Comparative to human injury<br>(David and Kroner, 2011; Kwon et al., 2002; Onifer et al., 2007; Zurita et al., 2012) |
| **Compression** | • Sustained compressive force application<br>• Examples:<br>- Clip compression, using an aneurysm clip<br>- Calibrated forceps<br>- Inflatable balloon catheters<br>• Tissue is rarely fully transected (clinical application)<br>• Duration of compression can be studied<br>• Simulates compression and ischaemia damage<br>• Simulates dislocation and bone impingement (as in burst fracture)<br>• Comparative to human injury<br>(David and Kroner, 2011; Kwon et al., 2002; Onifer et al., 2007; Zurita et al., 2012) |
| **Hemisection** | • One half of the dorsal or lateral portion of the cord is sliced (usually with micro-scissors or a scalpel blade)<br>• Produces lower inflammatory response compared to contusion<br>• Useful for comparisons between injured and uninjured tracts<br>• Used for axon regeneration studies<br>• Difficult to reproduce<br>• Comparatively rare injury type in clinical setting<br>(David and Kroner, 2011; Kang et al., 2012; Kwon et al., 2002; Onifer et al., 2007; Stokes and Jakeman, 2002) |

Procedures in animal models can be extremely costly and time consuming, particularly on larger animal models (Jones et al., 2012). The time and cost implications increase further when the development of SCI from an acute injury to a chronic injury is studied. Although in some animal model studies the animal models are sacrificed in the hours following injury, there is huge value in studying the progression of an injury through to the chronic phase, particularly for the study of treatments of SCI, whereby axonal regeneration occurs after a longer period of time. However, long follow-ups are expensive and ethical considerations prevent the long-term study of cervical SCI in rats and primates (Choo et al., 2007; Zurita et al., 2012).

### 1.8.2 *Ex vivo* Models of SCI

*Ex vivo* testing of the spinal cord has limitations due to removal of the tissue from a complex *in vivo* environment. An *ex vivo* spinal cord is unlikely to be surrounded by CSF, be perfused, or maintain support from the spinal nerve roots and denticulate ligaments. In addition, some or all of the meningeal layers are often removed. These features have been previously shown to have an effect on the mechanical behaviour of the tissue (Mazuchowski and Thibault, 2003; Oakland et al., 2006; Persson et al., 2011; Shetye et al., 2014). As mentioned previously, CNS tissue degrades rapidly post-mortem which must be taken into account for both mechanical testing and cellular experimentation (Carter et al., 2000; Kroeker et al., 2009; Oxland et al., 2011; Shetye et al., 2014). However, due to the restrictions of live animal testing, the removal of CNS tissue for biomechanical testing and tissue slice modelling can be experimentally useful.

#### 1.8.2.1 Organotypic Slice Models of SCI

Organotypic slice models of SCI are *ex vivo* slices of spinal cord tissue, cultured whole, without the dissociation of individual cells. Organotypic slice models are advantageous as they maintain the *in vivo* three-dimensional (3D) structure of the tissue, spatial orientations of heterogeneous cell types, tissue architecture and neuronal connections at a synaptic level. For this reason, they are useful for the study of extracellular matrix molecules, cell-cell interactions including neuronal networks,

and in investigating treatment efficacy (Cavaliere et al., 2010; Morrison et al., 1998; Ravikumar et al., 2012).

Slices must be maintained in culture for relatively long periods of time to allow them to recover from the initial damage caused by slice preparation, before they can then be used as an injury model (Morrison et al., 1998). Although, organotypic slice models have also been used immediately after slice preparation as an injury model in themselves (Rice et al., 2007; Sundström and Mo, 2002). The time allowed for organotypic slice models to 'recover' from preparation varies in the literature; some studies state over 21 days (Balentine et al., 1988), whist others state culture for no less than five days (Krassioukov et al., 2002), seven days (Cho et al., 2009), or fourteen days (Parsley et al., 1998). The 'recovery' time period maximises the confidence in the quantification of cell death and the results obtained from induced injury and treatment experiments (Krassioukov et al., 2002). However, the excitotoxic effects of cell death due to the initial mechanical insult is likely to continue to have an influence on the organotypic slice environment after this period; it is likely that at least some cells remain stimulated in an injury-induced state (Kumaria and Tolias, 2008).

It is necessary for the tissue slices to be very thin (250 - 400 μm) to allow nutrient diffusion and avoid hypoxia and necrosis; this can make the slices difficult to handle and they can be easily distorted (Cavaliere et al., 2010; Daviaud et al., 2013; Morrison et al., 1998; Parsley et al., 1998). Trauma to the cells must be considered, in particular whilst producing thin slices; Parsley and colleagues noted that slices as thin as 80 μm caused increased cell death throughout the slice, in comparison to slices of 150 μm and 300 μm (Parsley et al., 1998).

Organotypic slice models have been used effectively to study synaptic plasticity and neuronal activity using culture on micro arrays and patch clamping techniques. These studies make particular use of the preserved cytoarchitecture and the dorsal-ventral orientation of the spinal segment from which they are derived (Avossa et al., 2003; Cifra et al., 2012; Czarnecki et al., 2012; Galante et al., 2001; Heidemann et al., 2014; Jäderstad et al., 2010; Kearns et al., 2006; Rosato-Siri et al., 2002; Tønnesen et al., 2011; Tscherter et al., 2001).

Weightman and colleagues designed a model of SCI using organotypic slice cultures of mouse spinal cord. In this model, a 439 μm lesion was created using a double-bladed scalpel to transect organotypic slices that had been cultured for between one to six days prior to injury simulation. The study did not mention a slice 'recovery' period. The slices were fixed up to ten days post-lesioning. Using various assays such as immunocytochemical staining for reactive molecules and Live/Dead assays, these authors demonstrated that pathological features of SCI *in vivo* could be mimicked in slice lesions such as astrogliosis, microglial infiltration of lesions and the limited random outgrowth of nerve fibres from the lesion margins of slices derived from older animals in comparison to younger animals. The study also investigated the cellular response of their organotypic slice model following the incorporation of poly-lactic acid (PLA) scaffolds or laminin-coated scaffolds into the lesion site (Weightman et al., 2014).

Organotypic slice models can provide a useful intermediate model between animal models and simple cell culture studies. However, in order to use organotypic slice models in an injury simulation setting, the model becomes less clinically relevant in terms of the direction that force can be applied, for example impacts to the periphery of the spinal cord. Additionally, the functional outcome of a therapeutic strategy cannot be evaluated like it can in an *in vivo* model, and in general, slice cultures can be only maintained for a few weeks, which means that long-term assessments are not possible (Daviaud et al., 2013). Therefore, the thin sectioning and slice orientation reduces the relevance of these models as a method of biomechanically recreating SCI to study the associated pathophysiological response.

### 1.8.3 *In vitro* Models of SCI

It is experimentally valuable to simplify the clinical presentation of SCI into a reproducible injury model that can be used within a controlled experimental setting. Simplifications allow the assessment of various outcomes at the cellular, tissue, and organism level in response to defined parameters that can be precisely controlled and manipulated (Daviaud et al., 2013; LaPlaca et al., 2007). The two-dimensional (2D)

and three-dimensional (3D) culture of CNS cells for use in *in vitro* models of SCI offers a relatively simple, highly controlled experimental method, whereby the intra- and extra-cellular environments can be manipulated, without the complexity of an animal model.

Cells are able to sense their physical surroundings such as the normal tissue matrix, synthetic substrate, or adjacent cells, through a process known as mechanotransduction. Therefore, it is important to understand cellular responses to their microenvironment.

*Cellular response to their microenvironment:*

Mechanotransduction has been defined as "the cellular processes that translate mechanical stimuli into biochemical signals, thus enabling cells to adapt to their physical surroundings" (Jaalouk and Lammerding, 2009).

Fluids will flow in response to a force, whereas solids have the ability to resist forces. Most soft tissues of the body, such as the CNS, skin and muscle, have a relatively elastic microenvironment (Discher et al., 2005). Cells are able to adjust their cellular and extracellular structure through the translation of mechanical forces and deformations into biochemical signals which can cause changes to the intracellular ion concentration or activation of signalling pathways. Specific structures, such as cytoskeletal myosin and actin filaments, within cells are specifically designed to translate mechanical inputs into biochemical signals. Mechanotransduction can involve the conformational changes of proteins as a result of applied forces, which can result in altered affinities to cellular adhesion molecules such as integrins and cadherins (Jaalouk and Lammerding, 2009; Yeung et al., 2005).

Generally, almost all cells respond to mechanical stimulation with adaptive changes in cell function mediated through multiple, overlapping signalling pathways. Adaptive changes can be short-term responses such as increases or decreases in intracellular tension, adhesion, spreading or migration, or have longer-term effects on the cell, such as protein synthesis and secretion, structural reorganization, proliferation and viability (Jaalouk and Lammerding, 2009). A schematic representation of the key

features and interactions relating to mechanotransduction in a typical cell are shown in Figure 1.9.

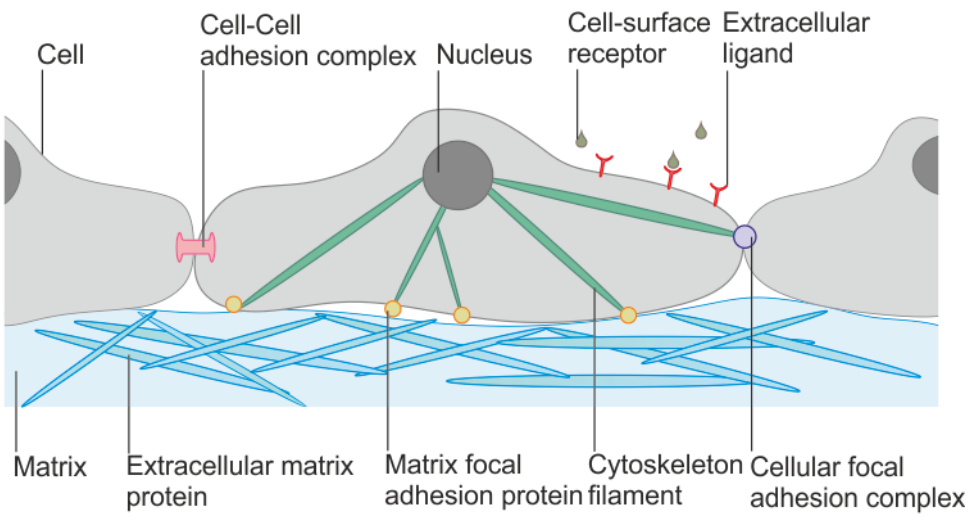


**Figure 1.9: Cellular Mechanotransduction.** Cells are able to sense and respond to the resistance of their microenvironment by adjusting their adhesions, cytoskeleton, and overall state (Discher et al., 2005). Cell–cell and extracellular matrix focal adhesions allow cells to probe their environments. Extracellular matrix proteins can become unfolded in response to applied forces, initiating mechanotransduction via the loss or gain of available adhesion sites. Similarly, conformational changes in cytoskeletal elements such as filaments can change binding affinities to specific molecules and activating signalling pathways. Adapted from (Jaalouk and Lammerding, 2009).

The elastic moduli of the microenvironment which surrounds mammalian cells can range from 10 Pa to 10 kPa, depending on cell type. Cells are commonly attached to other cells and or the extracellular matrix of their distinct microenvironment (Bao and Suresh, 2003; Wakatsuki et al., 2000).

Investigations into the effect of matrices of differing stiffness on stem cell lineage specification has shown that matrices of a soft stiffness (0.1 - 1 kPa) mimicking the CNS are neurogenic, whilst stiffer matrices (8 - 17 kPa) designed to mimic muscle are myogenic, and matrices designed to mimic collagenous bone (>100 kPa) are osteogenic (Engler et al., 2006). Cells have been reported to adhere differently

depending on the stiffness of their surroundings; within soft, lightly cross-linked gels with elastic moduli of less than 1 kPa, cells presented with dynamic adhesion complexes (Discher et al., 2005). Adhered fibroblasts have been shown to preferentially migrate from a soft to a hard surface (Lo et al., 2000). However, cells cultured within stiff, highly cross-linked gels with elastic moduli of between 30 to 100 KPa, presented with stable focal adhesions (Discher et al., 2005).

Cellular morphology is affected by the matrix elasticity; motor neurons derived from embryonic mouse spinal cord will extend neurites with extensive branches on soft (2300 dyne/cm$^2$) but not hard matrices (5500 dyne/cm$^2$) (Flanagan et al., 2002). Fibroblasts and smooth muscle cells develop a broader and flatter morphology on stiff matrices (3 kPa) in comparison to soft (2 Pa) (Lo et al., 2000; Yeung et al., 2005). The relationship between cells and their microenvironment depends, in part, on the different cell specific expression and engagement of adhesion molecules such as integrins and cadherins (Discher et al., 2005).

Georges and colleagues presented data which showed culture of rat neuron and astrocyte cell types on the surface of gels of differing stiffness had an effect on the reactivity and proliferation of the cells, both in homogeneous and heterogeneous culture. The astrocytes adopted a reactive phenotype on the stiffer gels (9 kPa), whereas they were more rounded and less reactive on soft gels (200 Pa). In contrast, neurons extended long neurites on both the soft and stiff gels. The soft gel was said to be similar in stiffness to the rat CNS, whereas the stiff gel was said to be stiffer than CNS tissue, though not stiffer than tissue culture plastic. Following co-culture of the cells, the astrocytes were low in number compared to neurons on soft gels (~20 % of total cell number), whereas on stiff gels the astrocytes were over 55 % of the total cell population (Georges et al., 2006).

#### 1.8.3.1 Two-Dimensional Cell Culture Models

Examples of 2D culture involve the culture of cells in a monolayer, on the surface of tissue culture plastic, membranes or gels.

Early 2D studies of SCI used relatively crude methodology to simulate injury in monolayer culture; a study by Yu et al. (1993), cultured primary rat astrocytes on culture dishes to confluency, then scratched a grid-like pattern across the cells. Although this simple method and unrealistic injury mechanism has little clinical relevance, activation of astrocytes was observed through the up-regulation of GFAP (Yu et al., 1993). More recently, models have been developed to investigate the effect of applied transient uniaxial stretch on the propagation of calcium transients in cultured neurons. This study showed that the application of mechanical force (>50 % strain) stimulated an increase in neuronal calcium levels (Lusardi et al., 2004). Deformable membranes have been used to transfer biaxial stretch to the attached cells (Cargill and Thibault, 1996; Ellis et al., 1995; Geddes et al., 2003; Morrison et al., 1998). *In vitro* models such as these, allow for isolation of specific biomechanical parameters (mode, rate and magnitude of deformation), in order to assess the effect of defined inputs on cellular responses (LaPlaca et al., 2007).

2D cell culture models have benefits such as reduced cost, and simplification of parameter control in comparison to other models. However, the relevance of 2D models to the highly complex *in vivo* 3D environment of the mature glial scar is limited.

#### 1.8.3.2 Three-Dimensional Cell Culture Models

The physiological environment of a cell involves cellular interactions and responses to mechanical stimuli, adjacent cells and extracellular matrices within a 3D microenvironment; these factors can influence cellular proliferation, morphology, migration and differentiation (Kofron et al., 2009; LaPlaca et al., 2005; Li et al., 2007; Sundararaghavan et al., 2009). In contrast, cells grown in 2D are often cultured on a solid-liquid interface between the matrix substrate and the culture media, a situation which is unlikely to occur *in vivo* (Bard and Hay, 1975; Greenburg and Hay, 1982; Yeung et al., 2005). In addition to the elasticity of the matrix, many cell types are seen to function differently when cultured in 2D compared to 3D conditions. Feng and colleagues compared fibroblast culture on 2D and within 3D matrices with exactly the same chemical composition, concentration/ligand density and degree of crosslinking. The results revealed that dimensionality affected cellular morphology;

cells were larger and more elongated in 3D, the cells also showed greater motility in 3D compared to 2D culture (Feng et al., 2013). The spatial arrangement of extracellular matrix adhesion sites on the ventral surface of the cell in 2D cultures compared to the entire surface of the cell in 3D cultures could explain some of these differences (Beningo et al., 2004).

A 3D cell culture involves culturing cells within a matrix, for example within a gel, where the cells are able to adopt a 3D morphology and receive biomechanical and biochemical cues in a 3D microenvironment. The 3D environment is important to consider whilst modelling SCI; the glial scar is part of a complex 3D environment which is difficult to replicate in 2D culture. 3D culture allows a greater degree of complexity to be studied than in 2D through the production of more representative conditions, allowing more translatable results to the physiological scenario, whilst still allowing control of variables, reduced cost, reduced ethical issues, ease of use and reproducibility in comparison to animal models (Kumaria and Tolias, 2008).

Neurite growth has been shown to be limited in 2D culture in comparison to culture in a 3D environment (Kofron et al., 2009; Li et al., 2007). Kofron and colleagues showed that despite neuron culture within a grid of inhibitory factors (CSPGs), neurites were able to grow in alternative directions, away from inhibitory factors, and continue to proliferate. Comparatively, neurons grown in 2D were restricted by the inhibitory factors and were limited in their proliferation in comparison to the neurons cultured in 3D (Kofron et al., 2009). This study highlighted the limitations of 2D study for exposing the entire cell surface to chemical cues. Additionally, it has been suggested that the cytokines and molecules released by cells may become diluted due to the high ratio of extracellular to intracellular volume in 2D cultures and the sink-like properties of the culture medium (LaPlaca et al., 2005).

East et al (2012) created a 3D culture model of the interface between astrocyte cells and neuronal cells, which provided valuable insights into the problems encountered at graft-cord interfaces. Interaction between cell types at a collagen gel interface caused astrocyte reactivity and the inhibition of neurite growth – neurites did not cross the interface (East et al., 2012). Use of 3D modelling is particularly advantageous when

assessing the reactivity of astrocytes, because the 3D culture environment minimises the base-line levels of astrocyte reactivity, in comparison to 2D culture (Georges et al., 2006).

Culture of astrocytes and neurons within a 3D gel matrix has been used to investigate the effect of shear strain by mimicking temporal strain patterns found in traumatic brain injury (TBI) using an electro-mechanical cell shearing device which generated shear strains up to 0.50 at strain rates of up to 30 $s^{-1}$ (Cullen and LaPlaca, 2006; LaPlaca et al., 2005).

An astrogliosis model was created using 3D collagen gels by East and colleagues (2009), whereby astrocyte cells were cultured in a type-I collagen gel matrix in which astrogliosis could be controlled and monitored. The astrocytes cultured within the 3D collagen gel matrix resembled astrocytes in their physiological environment, providing a 'ground state' model whereby triggers of astrogliosis could be studied. Additionally, the cells were shown to be less reactive in comparison to 2D monolayer culture. Astrogliosis was triggered following treatment of the 3D cultures with transforming growth factor-β1 (TGF-β1) which increased the amount of astrogliosis in the cultures over a 15-day period in comparison to their 'ground state' (East et al., 2009). TGF-β1 and - β2 are thought to be triggers of astrogliosis *in vivo* due to the increase in expression immediately after brain and spinal cord injury and the reduction in glial scarring following injection with TGF-β antagonists (Lagord et al., 2002; Silver and Miller, 2004).

The healthy adult CNS contains relatively few extracellular matrix (ECM) proteins in comparison to other tissues (Sobel, 1998). The ECM proteins are composed mainly of glycosaminoglycans, proteoglycans and other proteins such as laminin, which tend to be less structurally-linked compared to collagen, fibronectin and elastin which are found in non-CNS ECM (Volpato et al., 2013). However, the glial scar has been shown to include type -I, -III, -V, and -IV collagen, thought to be deposited by astrocytes and fibroblasts (Crapo et al., 2012; Heck et al., 2003; Hsiao et al., 2015; Joosten et al., 2000; Klapka and Müller, 2009; Okada et al., 2007; Sandner et al., 2012). Additionally, type-I collagen is a useful matrix substrate because it has been

used in various tissue engineering applications (East et al., 2010; Elias and Spector, 2012; Hadjipanayi et al., 2009; Haw et al., 2014; Liu et al., 2012; O'Connor et al., 2001), therefore there is a wide range of literature to draw comparisons with. The simplicity of the scaffold enables investigations into the cellular modification of the matrix. The gels enable versatile monitoring and non-destructive imaging such as real-time confocal microscopy, which makes the models suitable for investigations over a time-course of up to 15-days (East et al., 2009). However, due to the high liquid content of collagen gels, they have been reported to be mechanically unstable (Braziulis et al., 2012) and suffer from matrix contraction, volume loss and degradation over time when seeded with cells, particularly at high seeding densities (Braziulis et al., 2012; Engelhardt et al., 2010; Levis et al., 2012).

Techniques used to improve the material properties of collagen gels have included chemical crosslinking (Hovakimyan et al., 2012), increased collagen concentration (Abreu et al., 2010) and matrix stabilisation (Braziulis et al., 2012; Brown et al., 2005; East et al., 2010; Engelhardt et al., 2010; Georgiou et al., 2013; Levis et al., 2012; Micol et al., 2011). Stabilisation involves the application of an absorbent material to the surface of the gel matrix, sometimes in combination with a weight. The liquid component of the gel is absorbed, concentrating the collagen matrix (including any cells seeded into the matrix), into a sheet of collagen gel. The gel undergoes plastic compression which means it is permanently changed in structure, and even the addition of liquid to the stabilised gel does not rehydrate or reverse the compression of the gel (Brown et al., 2005).

Due to the concentration of collagen fibres, stabilised gels are thought to be mechanically stable in comparison to non-stabilised (fully hydrated) gels, which improves the handling of the gels (Braziulis et al., 2012; Brown et al., 2005). Additional advantages of gel matrix stabilisation include rapid and simple production which is reproducible, and produces easily manipulated, cell-seeded, membrane-like constructs that have been used for a variety of applications, such as surgery and implantation (human corneal endothelial cells into *ex vivo* porcine eye globes) (Levis et al., 2012), and as a graft treatment for skin defects (primary human keratinocyte and fibroblast cells into *in vivo* rat model) (Braziulis et al., 2012).

Relevant examples of nervous system studies utilising stabilised gels are those of East (2010) and Georgiou (2013). Both studies used stabilisation of gel matrices as a mechanism of transforming cell-seeded collagen gel matrices into mechanically robust implantable devices. The gels in these studies were tethered self-aligning models which simulated the matrix architecture and cellular orientation of the aligned tracts within the naturally occurring nervous system. The studies utilised the self-alignment of the gels to provide guidance cues for regenerating axons, directing neurite outgrowth along the aligned astrocyte processes (East et al., 2010) and directing neurite growth along aligned Schwann cells (Georgiou et al., 2013). Tethered self-aligned models that have not been stabilised have been shown to be too weak for implantation clinically (Phillips et al., 2005), therefore stabilisation after self-alignment enabled the advantages of the cellular and matrix organisation to be surgically implanted (Georgiou et al., 2013).

The effect of aligned astrocytes and aligned matrix components on the regeneration of neurites has been investigated using *in vitro* models (Davies et al., 2006; East and Phillips, 2008; East et al., 2010; Hsiao et al., 2015; Kofron et al., 2009; Vahidi et al., 2008; Weightman et al., 2014). Tethered gels generate tension in the longitudinal axis of the matrix as the gel contracts due to astrocyte remodelling of the matrix as the cells form stable integrin-mediated attachments with the fibrils of the collagen gel (Phillips et al., 2005). The cells self-align along the longitudinal axis in order to reduce the tensile forces that they experience, resulting in the alignment of both cell and collagen filaments within the gel matrix (Phillips, 2014). The model produced by East et al. (2010) was seeded with primary astrocytes, dorsal root ganglia (DRG) and neural fibroblasts. These authors found that when neurons were seeded on and within astrocyte gels, neurite length was greatest in the areas of astrocyte alignment (East et al., 2010).

The ability to culture CNS cells within a gel matrix in order to generate a 3D model of SCI offers an intermediate degree of complexity in comparison to 2D models. Depending on the orientation of cells within the matrix, there is the ability to apply bulk forces to the model resulting in heterogeneous strain fields at the cellular level.

This type of modelling is more relevant to the application of forces during SCI *in vivo*, whilst allowing the researcher flexibility to simplify the model in relation to the physiological environment and mechanical parameters (Cullen and LaPlaca, 2006; LaPlaca et al., 2005, 2007).

## 1.9 Aims and Objectives

### 1.9.1 Hypothesis

It is hypothesised that *in vivo* injuries can be simulated within a 3D *in vitro* tethered, self-aligned, type-I collagen gel model of spinal cord injury (SCI).

### 1.9.2 Aims

The aim of this study is to develop a 3D tethered, self-aligned, type-I collagen gel, with similar mechanical properties to spinal cord tissue, and investigate a mechanism of simulating injury, for use as a 3D *in vitro* model of *in vivo* SCI.

### 1.9.3 Objectives

- Determine the optimal matrix material for use as a 3D model of SCI, through investigations into the mechanical properties of different stabilised collagen gel matrix environments and the effect of matrix environment on primary astrocyte phenotype in terms of cell viability and expression of reactive astrogliosis markers.

- To determine the suitability of *in vivo* contusion devices for use with an *in vitro* 3D tethered collagen gel model through investigations into the effect of gel impaction on astrocyte phenotype adopting the parameters utilised *in vivo* in order to define an impaction protocol for use with 3D tethered collagen gels.

# Chapter 2

# Materials and Methods

## 2.1 General Materials

### 2.1.1 Equipment

The equipment used and equipment suppliers are listed in Appendix I within Table I.I.

### 2.1.2 Chemicals

The chemicals/reagents used and chemical suppliers are listed in Appendix I within Table I.II

### 2.1.3 Consumables

The consumables and plastic ware used and suppliers are listed in Appendix I within Table I.III.

### 2.1.4 Cell Lines and Primary Cells

#### 2.1.4.1 Cell Lines

In order to reduce the use of primary cells, the rat C6 ATCC® CCL-107™ glial cell line (C6) which is used as an astrocyte-like cell line (Quincozes-Santos et al., 2013), was utilised for the pilot studies and preliminary work, where possible. The C6 glial cell line (of rat brain origin) was donated by Doctor James Phillips, University College London, London, UK. Cell lines were received as frozen cultures and were expanded, subcultured and cryopreserved in liquid nitrogen, unless otherwise stated.

#### 2.1.4.2 Primary Cells

Primary astrocyte and microglia cells were isolated from Wistar rats, supplied by Central Biomedical Sciences, University of Leeds (Leeds, UK).

### 2.1.5 Antibodies

A list of the primary and secondary antibodies used throughout the study and suppliers information is presented in Table 2.1 and Table 2.2, respectively.

**Table 2.1: Primary Antibodies used Throughout the Study**

| Antigen | Type | Isotype | Dilution | Supplier |
|---|---|---|---|---|
| Glial Fibrillary Acidic Protein | Rabbit Anti-mouse | Polyclonal | 1:300 | Dako UK Ltd |

**Table 2.2: Secondary Antibodies used Throughout the Study**

| Antigen | Type | Fluorescent Conjugate | Dilution | Supplier |
|---|---|---|---|---|
| Rabbit IgG | Goat Anti-Rabbit | DyLight 594 | 1:300 | Vector Labs, UK |
| Rabbit IgG | Goat Anti-Rabbit | DyLight 488 | 1:300 | Vector Labs, UK |

## 2.2 General Methods

The general methods used throughout the study are described below.

### 2.2.1 Washing and Sterilisation of Equipment

#### 2.2.1.1 Washing and Disinfection of Equipment

Dissection instruments were washed and scrubbed with a toothbrush under hot tap water, then soaked in 1 % (v/v) Trigene for approximately 30 minutes. The instruments were then sprayed with 70 % (v/v) ethanol and left to dry, before being wrapped in foil and sterilised (190$^{o}$C for 4 hours) by dry heat.

Glassware was washed thoroughly with tap water and placed in 1 % (v/v) Trigene for approximately 24 hours. It was then rinsed with tap water before being dried and sterilised if required.

The class II safety cabinet was cleaned thoroughly before and after each use; all inside surfaces were sprayed with 1 % Virkon (w/v), followed by 70 % (v/v) ethanol. All items, including gloved hands, were sprayed with 70 % (v/v) ethanol, before entering the cabinet.

#### 2.2.1.2 Dry Heat sterilisation

Items to be sterilised were placed in a metal tin, the items were placed into a hot air oven at a temperature of 190$^{o}$C for 4 hours. Items were allowed to cool before they were removed from the oven.

#### 2.2.1.3 Moist Heat Sterilisation

An autoclave was used to sterilise items unsuitable for dry heat sterilisation. Items were placed into suitable containers and lids were secured then labelled with autoclave tape. Items were autoclaved at 15 psi, 121$^{o}$C, for 20 minutes. Items were allowed to cool before they were removed from the autoclave.

#### 2.2.1.4 Filter Sterilisation

A 0.22 μm filter was used to sterilise solutions where appropriate. Solutions were placed into a 10 ml syringe, the filter was attached, and the solution was dispensed into a suitable sterile container. Filter sterilisation procedures were performed within a class II safety cabinet.

### 2.2.2 Measurement of pH

Before use, the pH meter was calibrated by placement into purchased calibration solutions of pH 4, 7 & 10, at room temperature. The pH of solutions was measured at room temperature.

### 2.2.3 Microscopy

#### 2.2.3.1 Bright Field

An optical Olympus CK-40-SLP microscope was used to view cells during cell culture related activities, such as cell counting; the microscope was set up for standard Köhler illumination.

#### 2.2.3.2 Confocal

A Zeiss LSM700 inverted confocal microscope was used to image immunostained slides and gels. The laser settings used were Laser Diode 405: 405 nm (Hoechst; blue), Argon: 488 nm (GFAP; green), HeNe1: 543 nm (GFAP; red).

### 2.2.4 General Reagents and Solutions

The general reagents and solutions used throughout this study are listed below. Chapter specific reagents and solutions are described in detail in the relevant methods sections of Chapters 3 and 4.

#### 2.2.4.1 Astrocyte Cell Culture Medium

Cell culture media for primary astrocyte cell culture was prepared by combining DMEM cell culture media with 4.5 g/L glucose, 4 mM UltraGlutamine, 10% (v/v) foetal calf serum (FCS) and Penicillin-Streptomycin at 100 U/mL and 100 µg/ml, respectively. The supplements, FCS and Penicillin-Streptomycin, were stored at -20$^{o}$C and defrosted for five minutes in a water bath at 37$^{o}$C when required. Supplemented DMEM was stored at 4$^{o}$C for up to one month, prior to use it was incubated in a water bath at 37$^{o}$C for 30 minutes.

#### 2.2.4.2 C6 Cell Culture Medium

Cell culture media for culture of the C6 cell line was prepared by combining Ham's F-12 cell culture media with 2 mM L-glutamine, 10% (v/v) foetal calf serum (FCS) and Penicillin-Streptomycin at 100 U/mL and 100 µg/ml, respectively. The supplements, FCS and Penicillin-Streptomycin, were stored at -20$^{o}$C and defrosted for

five minutes in a water bath at 37$^{o}$C when required. Supplemented Ham's F-12 was stored at 4$^{o}$C for up to one month, prior to use it was incubated in a water bath at 37$^{o}$C for 30 minutes.

#### 2.2.4.3 Ethanol

A 70 % (v/v) ethanol solution was prepared by diluting 7 L of ethanol with 3 L of distilled water.

#### 2.2.4.4 Hoechst 33258

A 2 µg/ml solution of Hoechst 33258 (Hoechst) was prepared by adding 1000 µg of Hoechst powder to 500 µl of sterile water. The solution was triturated to ensure thorough mixing. The Hoechst solution was stored in 100 µl aliquots, at -20$^{o}$C for up to one year and defrosted at room temperature when required.

#### 2.2.4.5 Hydrochloric Acid (1 M)

A 1 M solution of hydrochloric acid (HCl) was prepared by slowly adding 821 µl of HCl solution to 2500 µl deionised water. The final volume of the solution was then adjusted to 10 ml with deionized water.

#### 2.2.4.6 Live/Dead Solution

Live/Dead solution was prepared by defrosting the ethidium homodimer-1 (EH) and calcein AM (CAM) kit components at room temperature (components were stored at -20$^{o}$C). A volume of 3 µl EH and 1 µl CAM were added to 3996 µl cell culture medium (media appropriate to cell type). The Live/Dead solution was protected from light and used immediately.

#### 2.2.4.7 Methanol

A 70 % (v/v) methanol solution was prepared by adding 7 ml of methanol, to 3 ml of distilled water. The 70 % (v/v) methanol solution was stored at room temperature for one month.

#### 2.2.4.8 Paraformaldehyde

A 4 % (w/v) paraformaldehyde (PFA) solution was prepared by heating 800 ml of phosphate buffered saline (see Section 2.2.4.9), in a glass beaker, to 60$^{o}$C. When the solution reached the required temperature, 40 g of paraformaldehyde powder was added. The solution was cleared by drop-wise addition of 1 N NaOH. The 4 % (w/v) PFA solution was allowed to cool, before adjustment of the pH to 6.9 by drop-wise addition of 1 M HCl. The 4 % (w/v) PFA solution was stored in 10 ml aliquots, at -20$^{o}$C for up to six months. Prior to use, the solution was defrosted at room temperature.

#### 2.2.4.9 Phosphate Buffered Saline

Phosphate buffered saline (PBS) was prepared by dissolving 1 PBS tablet per 100 ml of distilled water, in a clean, autoclave-resistant bottle. The solution was stirred until the tablets had fully dissolved. The solution was stored at room temperature for up to one month. The solution was autoclaved (Section 2.2.1.3) where a sterile PBS solution was required.

#### 2.2.4.10 Poly-d-lysine

A 1 μg/ml poly-d-lysine (PDL) solution was prepared by dissolving 50 μg of PDL powder in 50 ml distilled water. The solution was filter sterilised before aliquoting of 10 ml aliquots into sterile universals. The 1 μg/ml PDL solution was stored at -20$^{o}$C for up to two years and defrosted at 37$^{o}$C when required.

#### 2.2.4.11 Sodium Hydroxide (1 N)

A 1 N sodium hydroxide (NaOH) solution was prepared by adding 4 g of NaOH pellets to 100 ml distilled water, the solution was stirred until all the pellets had dissolved. The solution was stored at room temperature for up to one year.

#### 2.2.4.12 Triton$^{TM}$ X-100

A 0.1 % (v/v) solution of Triton$^{TM}$ X-100 was prepared by adding 1 ml of Triton$^{TM}$ X-100 solution to 999 ml sterile water, in a clean bottle. The solution was stirred until mixed thoroughly. The solution was stored at room temperature for up to one year.

#### 2.2.4.13 Virkon

A 1 % (w/v) solution of Virkon was prepared by adding 50 g Virkon powder to 5 L distilled water.

### 2.2.5 Isolation of Primary Cells

Primary astrocytes were isolated from postnatal day-2 or day-3 Wistar rat pups using the following protocols.

#### 2.2.5.1 Preparation of Solutions for Primary Cell Isolation

The following solutions were prepared in advance and stored under the appropriate conditions, as described.

***DNase (2000 U/ml)***

A stock solution of DNase was prepared by dissolving 10,000 U of DNase powder in 5 ml distilled sterile water. The DNase solution was stored in 1 ml aliquots, at -20$^{o}$C, for up to one year, prior to use it was defrosted at room temperature.

***Magnesium Sulphate ($MgSO_4$) (150 mM)***

A stock solution of $MgSO_4$ was prepared by dissolving 181 mg of $MgSO_4$ in 10 ml distilled water. The $MgSO_4$ solution was filter sterilised and stored at 4$^{o}$C for up to one month.

***Soybean Trypsin Inhibitor (SBTI) (2 mg/ml)***

A stock solution of SBTI was prepared by dissolving 20 mg of powdered SBTI in 10 ml distilled sterile water. The SBTI solution was stored in 1 ml aliquots, at -20$^{o}$C, until the expiration date shown on the manufacturers packaging, prior to use it was defrosted at room temperature.

***Trypsin (5 mg/ml)***

A stock solution of trypsin was prepared by dissolving 50 mg of powdered trypsin in 10 ml distilled sterile water. The trypsin solution was stored in 1 ml aliquots, at -20$^{o}$C, for up to one year, prior to use it was defrosted at room temperature.

The following solutions were made up at the beginning of every cell extraction:

***Disaggregation Medium***

Glucose powder, 252 mg, bovine serum albumin (BSA) powder, 300 mg, and 1 ml of the 150 mM $MgSO_4$ stock, were added to 99 ml of Earles Balanced Salt Solution (EBSS), without stirring. The disaggregation medium was stirred to mix after the powders had dissolved.

***Trypsin in disaggregation medium (250 µg/ml)***

A solution of trypsin in disaggregation medium was prepared to give a final concentration of trypsin of 250 µg/ml, by adding 1 ml of the trypsin stock (5 mg/ml) to 19 ml of disaggregation medium. The trypsin in disaggregation medium was triturated thoroughly to mix.

***Concentrated soybean trypsin inhibitor (SBTI) (133 µg/ml)***

A solution of concentrated inhibitor was prepared by adding 1 ml of the SBTI stock solution (2 mg/ml), 1 ml of the DNase stock solution (2000 U/ml), and 150 µl of the $MgSO_4$ stock solution (150 mM), to 13 ml of disaggregation medium. The final concentration of reagents within the concentrated SBTI solution was as follows: SBTI, 133 µg/ml; DNase, 133 U/ml; $MgSO_4$, 1.5 mM. The concentrated SBTI solution was triturated thoroughly to mix.

***Dilute soybean trypsin inhibitor (SBTI) (21.28 µg/ml)***

A solution of dilute SBTI inhibitor was prepared by adding 3.2 ml of the concentrated SBTI solution (133 µg/ml) to 16.8 ml of disaggregation medium, to produce a final concentration of 21.28 µg/ml. The dilute SBTI solution was triturated thoroughly to mix.

***Bovine Serum albumin (BSA) (40 mg/ml)***

A 40 mg/ml solution of BSA was prepared by adding 400 mg of BSA powder to 10 ml disaggregation medium, the BSA powder was allowed to dissolve without stirring. The solution was triturated thoroughly to mix once the BSA powder had fully dissolved.

#### 2.2.5.2 Preparation of Tissue Culture Flasks

Following preparation of the aforementioned solutions, 75 $cm^3$ flasks were coated with 4 ml PDL, and allowed to incubate for at least one hour at 37$^oC$ in 5 % (v/v) $CO_2$ in air. After incubation, the PDL was removed and discarded, before the flasks were rinsed twice with 4 ml sterile PBS, and once with 4 ml supplemented DMEM. The flasks were left to dry with the caps on, inside the incubator at 37$^oC$ in 5 % (v/v) $CO_2$ in air until required.

#### 2.2.5.3 Dissection of Cortex Tissue

Rat pups were sacrificed at postnatal day-2 or day-3 by cervical distraction, followed by decapitation, according to the UK Animals (Scientific Procedures) Act 1986, under the Home Office Project License: PPL 70/8085.

All procedures were performed inside a class II safety cabinet.

The disaggregation medium was filter sterilised and 10 ml was pipetted into tissue culture dishes (one dish appropriate for up to three cortices). Each head was placed onto a piece of tissue and sprayed liberally with 70% (v/v) ethanol. The snout was held between three fingers, with the snout pointing towards the palm of the hand, in order to easily locate the region in the back of the head, where the brain stem joined the brain, as represented schematically in Figure 2.1.

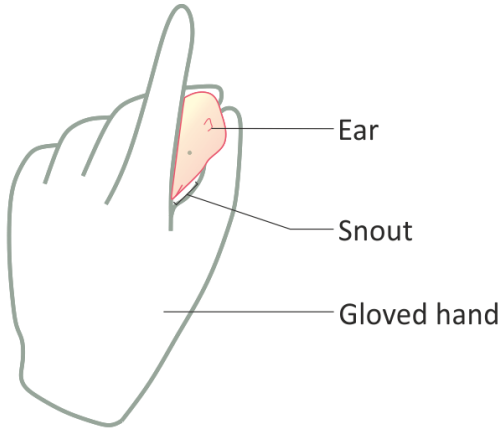


**Figure 2.1: Positioning of Head for Dissection.** Throughout the dissection, rat heads were held between the thumb, index and middle finger, with the snout pointing towards the palm of the hand. The hand was positioned with the palm facing the researcher, to allow access to correct region of the brain.

The dissection of the cortex was performed, as described in Figure 2.2.

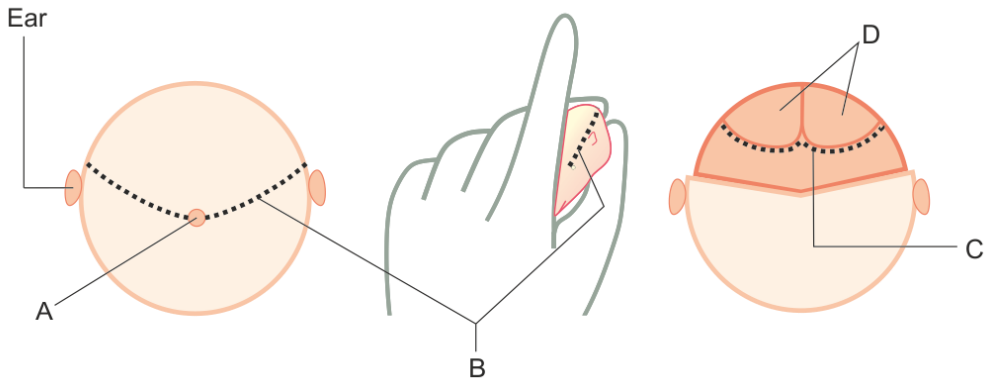


**Figure 2.2: Dissection of Rat Cortex.** Curved scissors were inserted into the hole (A) and the edge of the skull was cut from the rear to the front (B) on both sides of the head. The cut passed above the ears and towards the eyes, whilst moving only the outer blade of the scissors, in order to protect the brain. The brain was exposed, and a spatula was inserted (C) to loosen the cortex (D).

Following dissection, the cortex was placed onto a sterile tissue culture dish lid, the meninges and any visible blood vessels were removed and discarded using fine tweezers. The cortex was placed into the tissue culture dish containing filter sterilised disaggregation media, and the process was repeated with any remaining pup heads, allowing three cortices per tissue culture dish. Equipment was rinsed in 70% (v/v) ethanol between each dissection.

#### 2.2.5.4 Isolation of Astrocytes and Microglia from Cortex Tissue

Following filter sterilisation, 7 ml of the trypsin in disaggregation medium, was added to a sterile tissue culture dish. Using a pipette, the disaggregation medium was carefully removed from the tissue culture dish containing the cortex tissue. The cortices were placed onto the flat lid of a sterile tissue culture dish. A scalpel was used to chop the cortices in a grid-like pattern. The chopped cortices were added to the tissue culture dish containing the trypsin in disaggregation medium and incubated on a rocker at 50 rpm for 15 minutes at 37$^{o}$C in 5% (v/v) $CO_2$ in air.

The dilute SBTI (21.28 μg/ml) was filter sterilised and 7 ml was added to the tissue culture dish containing the incubated cortices. The contents of the dish were transferred into sterile 50 ml falcon tubes, and centrifuged at 400 g for five seconds, at room temperature. The supernatant was discarded, and the pellet resuspended in 10 drops of filter sterilised concentrated SBTI (133 μg/ml). The tissue was mechanically dissociated, using a wide bore pipette tip. The tissue was allowed to settle in the concentrated inhibitor (133 μg/ml), before carefully pipetting the cell suspension, into a sterile 15 ml falcon tube. The cell suspension layer was identified as the clear, liquid layer suspended above the tissue debris. The remaining tissue was resuspended in a further 10 drops of concentrated inhibitor (133 μg/ml), mechanically dissociated and left to settle once more, before pooling the cell suspensions. One 15 ml falcon tube was suitable for the collection of cell suspension from up to three cortices.

The BSA solution (40 mg/ml) was filter sterilised, and used to underlay the cell suspension in the falcon tubes, using a 5 ml pipette. Approximately the same volume of BSA solution as cell suspension was added to each tube. The falcon tubes were

centrifuged at 400 g for 5 minutes, at room temperature. After removal of the supernatant, 12 ml supplemented DMEM media was added to each falcon tube. The suspension was triturated to resuspend the cells, and 6 ml of the suspension was added to each PDL coated flask. An additional 6 ml of fresh media was added to each flask, before placing in the incubator at 37$^{o}$C in 5% $CO_2$ (v/v) until required.

Primary astrocytes and microglia require approximately 10 days in culture before use. Half of the media was removed and replaced with fresh media every seven days. Bright field microscopy was used to observe the progress of the cultures, although during this time microscopic observation was kept to a minimum.

#### 2.2.5.5 Separation of Mixed Astrocyte and Microglia Cultures into Single Cell Populations

When the cultured cells reached confluence, after approximately 10 days, the filter caps of the flasks were replaced with closed caps. The flasks were then placed onto a plate shaker within a 37$^{o}$C incubator at 5 % (v/v) $CO_2$ and air. The caps were loosened to allow $CO_2$ to enter the flasks. When the incubator reached 5% (v/v) $CO_2$ the caps were tightened inside the incubator and the flasks shaken at 150 rpm for four hours. During this time, additional flasks were coated with 4 ml PDL, and allowed to incubate for at least one hour at 37$^{o}$C, as described previously (Section 2.2.5.2). When the flasks containing confluent cells had been shaken for four hours, the media was removed and added to the freshly coated flasks. Fresh supplemented DMEM media (12 ml) was added to the confluent flasks (which now contained predominantly astrocyte cells), and 5 ml fresh supplemented DMEM media was added to the freshly coated flasks (which were now predominantly microglial cells).

### 2.2.6 Cell Maintenance

#### 2.2.6.1 Cell Viability and Cell Counting

Trypan blue was used to detect the approximate level of cell death within isolated cell suspensions. Trypan blue is able to enter dead cells due to a loss of membrane

potential, microscopically resulting in the blue appearance of dead cells, whilst live cells appear colourless.

To perform a cell count, 7 µl cell suspension was added to 7 µl trypan blue, the suspension was mixed and added to a haemocytometer counting chamber, a coverslip was placed over the counting chamber. Using this method, the dilution factor of the cell suspension with trypan blue was 2. A schematic representation of a haemocytometer is shown in Figure 2.3.

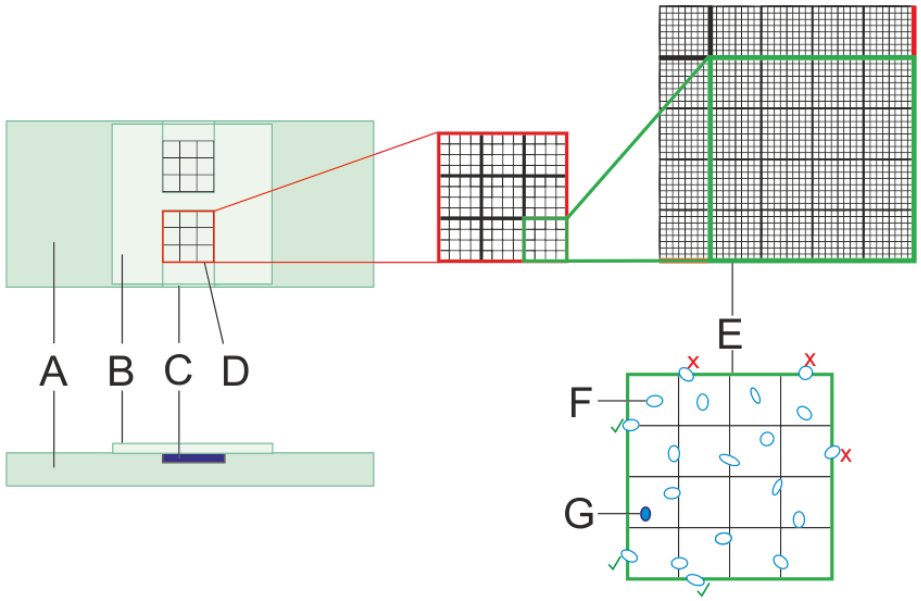


**Figure 2.3: Total Cell Counts using a Haemocytometer.** The trypan blue and cell suspension (1:1 (v/v)) was pipetted into the chamber formed between the counting chamber (C) of the haemocytometer (A) and the coverslip (B). The large grid square (D) was viewed under bright field microscopy, and viable cells (F) were counted within at least four of the medium grid squares (E). Dead cells (G), stained blue, were not counted.

Viable cells (colourless cells) were counted in *n* number of medium grid squares which resulted in a cell count of between 100 to 400 cells. Dead cells (stained blue) were not included in the count. To avoid counting the same cell twice, if cells were located on the top and right-hand grid square boundaries, they were not included in the count. Cells located on the bottom and left-hand grid square boundaries were

included in the count. The total number of cells per ml of suspension was calculated according to Equation 2.1.

$$Number\ of\ cells.ml^{-1} = \frac{Number\ of\ viable\ cells}{n} \times 10^4 \times Dilution\ factor \quad \text{Equation 2.1}$$

- Where *n* = number of grid squares used in cell count; and
- *Dilution factor* = the correction required due to the dilution of the cell suspension with trypan blue.

#### 2.2.6.2 Resurrection of Cell Lines

The cryovials of C6 cell lines were removed from liquid nitrogen storage and thawed at 37°C; 10 ml of fresh Ham's F-12 culture medium was added to the cells before centrifugation at 150 rcf. The pellet was resuspended in 5 ml of fresh culture medium. The cell number was determined and a viability assay performed, as described in Section 2.2.6.1. The cells were incubated in a sterile culture flask (25 $cm^2$) at 37°C in 5 % (v/v) $CO_2$ in air. Once confluent, the cells were transferred to a larger sterile culture flask (75 $cm^2$).

#### 2.2.6.3 Removal of Cells from Tissue Culture Flasks

Cell culture medium was removed from the flasks and the monolayer gently washed with 10 ml PBS without calcium or magnesium. Trypsin/EDTA (3ml) was added to the flask and incubated for 7 minutes at 37°C in 5 % $CO_2$ (v/v) in air, whilst on a rocker at 50 rpm. Flasks were gently tapped to detach cells and 10 ml culture medium was added to suspend cells and inhibit trypsin activity. The cell suspension was added to a sterile universal, and the flask was observed under bright field microscopy, to ensure the majority of cells had been removed. If cells remained in the flask following treatment with trypsin/EDTA, a cell scraper was used to retrieve the remaining cells. A further 5 ml of fresh media was added aseptically to the flask, and a sterile cell scraper was passed across the monolayer surface. The cell suspension was added to the universal, followed by centrifugation for 10 minutes at 150 g, at room temperature. The supernatant was carefully aspirated from the cell pellet, which was then resuspended in 5 ml culture medium.

### 2.2.7 Basic Collagen Gel Mixture

The basic gel mixture was the same throughout the study, with varying concentrations of cells added to the culture media proportion, as described in relevant chapters.

Briefly, 10% (v/v) 10x minimal essential medium (MEM) was added to a sterile vessel of appropriate size for the final gel volume produced. Using a wide bore pipette, 80% (v/v) type-I rat tail collagen (2 mg/ml in 0.6% (w/v) acetic acid) was mixed with the MEM. The mixture was neutralised with 5.8% (v/v) neutralising solution before the addition of 4.2% (v/v) culture medium, containing the appropriate number of cells to achieve the desired cell density, where appropriate.

For example, to produce a 10 ml collagen gel mixture, with a cell seeding density of $4 \times 10^6$ cells per ml, 1000 µl 10 x MEM was added to a sterile universal. Using a wide bore pipette, 8000 µl type-I rat tail collagen (2 mg/ml in 0.6% (w/v) acetic acid) was mixed with the 10 x MEM. The cell suspension was prepared at this stage, to minimise the time that a high density of cells would be in a low volume of media. Cells were removed from the tissue culture flask as described in Section 2.2.6.3, and the cell viability and cell numbers were counted as described in Section 2.2.6.1. The cell suspensions retrieved from several flasks of cells were pooled to acquire a suitable number of cells. The cell suspension containing $4 \times 10^7$ cells was centrifuged for 10 minutes at 150 g, at room temperature. The supernatant was carefully aspirated from the cell pellet, which was then resuspended in 420 µl supplemented DMEM culture medium and triturated thoroughly to mix. The collagen mixture was then neutralised with 580 µl neutralising solution before the addition of the cell suspension. The gel mixture was carefully swirled by hand to mix.

Having made the desired volume of gel mixture, appropriate volumes of gel solution were added to culture-well plates or gel moulds using a wide bore pipette tip. Gels were allowed to set for 10 minutes in a humidified incubator at $37^oC$ in 5 % $CO_2$ (v/v) in air before further gel manipulation occurred.

#### 2.2.7.1 Fully Hydrated Gels

In this study, the term fully hydrated (FH) refers to a 500 µl standard collagen gel solution (Section 2.2.7) that has undergone gelation inside the well of a 24-well plate. The FH gels were approximately 15 mm in diameter.

#### 2.2.7.2 Partially Stabilised Gels

In this study, the term partially stabilised (PS) refers to a 500 µl standard collagen gel solution (Section 2.2.7) that has undergone gelation inside the well of a 24-well plate. A RAFT absorber was applied to each gel for 20 seconds. The PS gels were approximately 15 mm in diameter.

#### 2.2.7.3 Fully Stabilised Gels

In this study, the term fully stabilised (FS) refers to a 500 µl standard collagen gel solution (Section 2.2.7) that has undergone gelation inside the well of a 24-well plate. A RAFT absorber was applied to each gel for 15 minutes. The FS gels were approximately 15 mm in diameter.

### 2.2.8 Staining Methods

Cells were stained using a variety of techniques, as described below and in relevant methods sections of Chapters 3 and 4.

#### 2.2.8.1 Live/Dead® Cell Viability Assay

The fluorescence based Live/Dead® Cell Viability assay was used to qualitatively analyse the numbers of live verses dead cells in given volumes of gel. There are two fluorescent components of the assay: the ethidium homodimer-1 (EH) component is a red-fluorescent dye which binds to DNA. EH is membrane-impermeable, therefore it can only bind to cells with compromised cell membranes, such as those of dead or dying cells; the non-fluorescent acetomethoxy derivate of calcein AM (CAM) is transported through cellular membranes into live cells, once inside the cell, intracellular esterases remove the acetomethoxy group, converting the molecule into the green-fluorescent component, calcein.

To produce 4 mls of Live/Dead® Cell Viability solution, 3999 µl of cell culture media was added to a sterile universal. In the dark, 1 µl of CAM and 3 µl of EH were added to the media and mixed. Samples were covered with at least double their volume of Live/Dead® solution for four hours in a humidified incubator at 37$^{o}$C in 5 % $CO_2$ (v/v) in air. Following incubation, samples were washed three times for 5 minutes each in PBS in the dark. Samples were kept in the dark until visualised using a confocal microscope.

The Live/Dead® solution was used immediately and all related procedures were performed in the dark, where possible.

#### 2.2.8.2 Immunofluorescence staining

*Immunostaining within Gel Matrices*

The following method was used to stain cells within fully hydrated (FH), fully stabilised (FS) and tethered gels. Solutions were added to each gel in volumes double that of the matrix; 1000 µl per FH or FS gel, and 2000 µl per tethered gel.

Following a defined period in culture, gels were rinsed three times in PBS and then fixed in 4 % paraformaldehyde (PFA) overnight at 4$^{o}$C. Following fixation, the PFA was removed and the gels were rinsed three times in PBS for five minutes. The gels were then incubated in 0.1 % Triton X-100 for 30 minutes, before being rinsed three times in PBS, for five minutes. Blocking solution containing 5 % goat serum was added to each gel and the samples were incubated for a further 30 minutes at room temperature, on a rocker at 50 rpm. The gels were then rinsed three times with PBS before a solution of 1:300 primary antibody, made up in PBS, was added to each gel. The gels were incubated overnight at 4$^{o}$C. Following incubation with the primary antibody, the gels were rinsed three times in PBS for five minutes, at room temperature on a rocker at 50 rpm. The gels were then incubated at room temperature, on a rocker at 50 rpm with a solution of 1:300 secondary antibody, and 1:1000 Hoechst 22358 double stranded DNA stain, in PBS in the dark. The gels were then rinsed three times in PBS for five minutes, at room temperature on a rocker at

50 rpm. The gels were stored in PBS in the dark at 4°C until imaging with a confocal microscope.

*Immunostaining Glass Slides*

The following method was used to stain cells cultured on glass slides.

Following a defined period in culture, the slides were rinsed three times in PBS and then fixed in 4 % paraformaldehyde (PFA) overnight at 4°C. Following fixation, the PFA was removed and the slides were rinsed three times in PBS for 30 seconds. A 200 µl solution of 0.1 % Triton X-100 was added to the centre of each slide and the slides were incubated for 15 minutes, before being rinsed three times in PBS, for 30 seconds. A 200 µl solution of blocking solution containing 5 % goat serum was added to each slide and the samples were incubated for a further 15 minutes at room temperature. The slides were then rinsed three times with PBS before a 200 µl solution of 1:300 primary antibody, made up in PBS, was added to each slide. The slides were incubated overnight at 4°C. Following incubation with the primary antibody, the slides were rinsed three times in PBS for 30 seconds, at room temperature. The slides were then incubated at room temperature with a solution of 1:300 secondary antibody, and 1:1000 Hoechst in PBS, in the dark. The slides were then rinsed three times in PBS for 30 seconds, at room temperature. The slides were stored in PBS in the dark at 4°C until imaging with a confocal microscope.

### 2.2.9 Image Analysis

Samples that had been stained with the Live/Dead® stain, fluorescently-tagged antibodies and/or Hoechst 33258 were maintained in a dark environment until imaging could take place. All imaging was performed in a darkened room. A confocal microscope was used to image the samples; the same imaging protocol was followed for each sample type.

To avoid bias and ensure consistent data acquisition, a standardised sampling protocol was adopted.

*Confocal Microscopy Protocol for Circular Gels*

In order to image the circular gels (FH, PS, FS), the 10x objective was used to focus the lasers on the top of the gel, as detected when the cells became visible in the z-plane. The x, y centre of the gel was located using the reported x and y positions on the microscope display. The centre of the gel in the z-plane was located by calculating the height of the gel according to the z-plane position of the first and last cells to come into focus whilst scanning through the gel, as shown in Figure 2.4. The x20 objective was used for subsequent analysis. Images were obtained at the x, y, z centre of the gel, and four locations around the edges of the gels, in the z-plane centre.

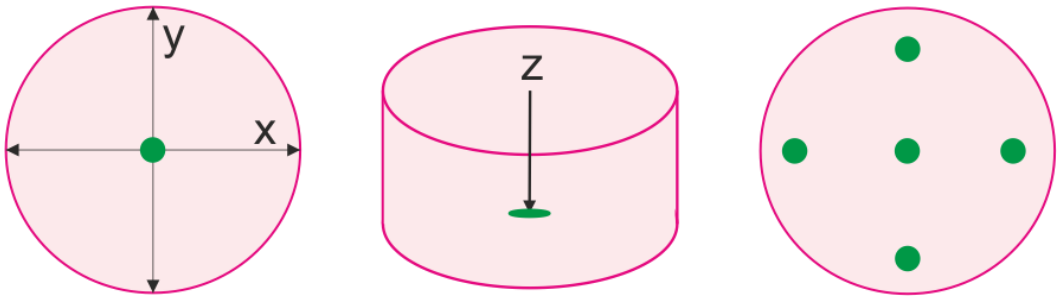


**Figure 2.4: Location of Imaging Regions within Circular Gels.** The centre of the gel was located using the x, y positions on the confocal microscope display. The focal plane was moved from the cell surface to the base of the gel in order to calculate the z-plane centre. Images were obtained at the x, y, z centre of the gel, and four locations (green dots) around the edges of the gels, in the z-plane centre.

*Confocal Microscopy Protocol for Tethered Gels*

In order to image the tethered gels, the 10x objective was used to focus the lasers on the top of the gel, where the first layer of cells became visible in the z-plane. The centre of the gel in the z-plane was located by calculating the height of the gel according to the z-plane position of the first and last cells to come into focus whilst scanning through the gel, as shown in Figure 2.5. The x20 objective was used for subsequent analysis. Images were obtained from the central z-plane in the side, middle and delta regions of the gel.

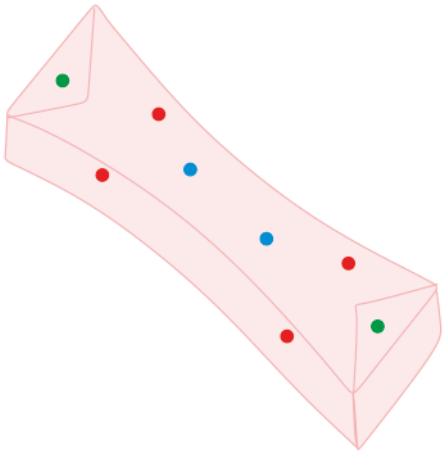

**Figure 2.5: Location of Imaging Regions within Tethered Gels.** The focal plane was moved from the cell surface to the base of the gel in order to calculate the z-plane centre. Images were obtained within the calculated z-plane centre of the gel, at the side (red), middle (blue) and delta (green) locations around the edges of the gels.

*Tile Scans of the Impact Zone*

Tile scans were obtained of the impact zone surface, middle and base, in terms of z-planes through the gel. Firstly, the surface of the impact zone was located, and based on the approximate size of the impact zone the number of tiles per scan was selected. The impact zones varied in size and morphology, so the same tile scan dimensions were not transferable between gels. Occasionally, two tile scans were required per impact zone, in order to image the whole area. In these circumstances, the tiled images were stitched together during subsequent image analysis. Tile scans of the middle of the impact zone were obtained as described previously, in the central z-plane, as calculated by focusing through the gel to locate the surface and base of the gel. The base of the impact zone was imaged turning the gel over and focusing until a plane of cells came into focus.

*Confocal Microscopy Protocol for Glass Slides*

In order to image the glass slides, the x, y centre of the slide was located using the reported x and y positions on the microscope display, as shown in Figure 2.6. The x20 objective was utilised to obtain images from the centre and four surrounding edge regions of the slide.

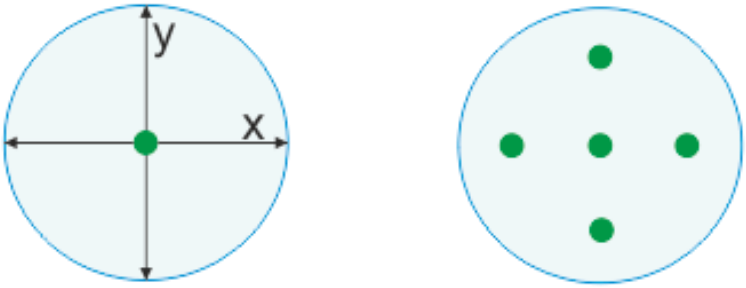


**Figure 2.6: Location of Imaging Regions of Glass Slides.** The centre of the slide was located using the x, y positions on the confocal microscope display. Images were obtained at the x, y, centre of the slide, and four locations (green dots) around the edges of the slide.

### 2.2.10 Enzyme-Linked Immunoabsorbant Assay (ELISA)

An enzyme-linked immunoabsorbant assay (ELISA) was performed on the defrosted media samples in order to determine the levels of extracellular IL-6 that had been secreted by the cells. The quantitative sandwich ELISA was purchased in the form of a kit whereby the wells were pre-coated with antibody.

*ELISA Wash buffer*

A Wash Buffer solution was prepared by adding 50 ml of Wash Buffer Concentrate to a clean 1000 ml graduated cylinder. The final volume was brought to 1000 ml with distilled water. The solution was gently mixed, to avoid foaming. The Wash Buffer solution was transferred to a clean wash bottle and stored at 5$^{o}$C for up to 30 days.

*ELISA Assay Buffer*

The Assay Buffer solution was prepared by adding 5 ml of Assay Buffer Concentrate to 95 ml distilled water; the solution was gently mixed to avoid foaming. The Assay Buffer was stored at 5$^{o}$C for up to 30 days.

*ELISA IL-6 Standard*

A 4000 pg/ml reconstituted solution of IL-6 was prepared by adding 570 µl distilled water to the standard vial. The reconstituted vial was mixed by gentle inversion.

Serial dilutions of the standard were made directly in the assay plate to provide a concentration which ranged from 2000 to 62.5 pg/ml. The pre-coated wells were washed prior to use, as per the first step of the ELISA method, described in Figure 2.7.

A serial dilution of the reconstituted standard was prepared by adding 100 µl Assay Buffer to all standard wells. A volume of 100 µl reconstituted standard was added to the first of two rows (A1 and A2). The contents of wells were mixed before 100 µl of standard solution was transferred from wells A1 and A2, to B1 and B2 respectively. The 1:1 dilution was continued by the transfer of 100 µl standard solution from B1 and B2 through to F1 and F2, providing a serial dilution ranging from 2000 to 62.5 pg/ml. A final volume of 100 µl was maintained in each of the standard wells, therefore 100 µl of solution was discarded from the wells F1 and F2. A volume of 100 µl of Assay Buffer was added in duplicate to the blank wells G1-2 and H1-2.

The reconstituted standard must be used immediately. A fresh standard curve was produced for each assay.

*ELISA Biotin Conjugate*

A 1:100 dilution of Biotin Conjugate was prepared by adding 60 µl Biotin Conjugate solution to 2.97 ml Assay Buffer in a sterile plastic bijou. The Biotin Conjugate must be prepared fresh for each ELISA.

*ELISA Streptavidin-HRP*

A 1:100 dilution of Streptavidin-HRP was prepared by adding 120 µl of concentrated Streptavidin-HRP solution to 12 ml Assay Buffer in a sterile plastic bijou. The Streptavidin-HRP must be prepared fresh for each ELISA.

*Principle of the Method*

Anti-rat IL-6 polyclonal coating antibody was pre-adsorbed onto each microwell of a 96-well plate. Rat IL-6 (rIL-6) present in the sample or standard (standard provided by the kit) was able to bind to the anti-rat IL-6 antibodies adsorbed to the microwells. A biotin conjugated monoclonal anti-rIL-6 antibody was bound to the rIL-6 captured

by the first antibody. Following incubation, unbound biotin conjugated anti-rIL-6 was removed during a wash step. Streptavidin-Horseradish Peroxidase (Streptavidin-HRP) was added which binds to the biotin conjugated anti-rIL-6. Following incubation, unbound Streptavidin-HRP was removed during a wash step, and a substrate solution reactive with HRP was added to the wells. A coloured product was formed in proportion to the amount of rIL-6 present in the sample. The reaction was terminated by addition of acid. The absorbance was measured at 450nm. A standard curve was prepared from seven rIL-6 standard dilutions; the standard curve allowed the rIL-6 sample concentration to be determined. A quantitative sandwich ELISA for rat IL-6 was carried out according to the manufacturer's instructions and the principles described above. The detailed method including the various wash steps and solution applications are explained in detail in Figure 2.7.

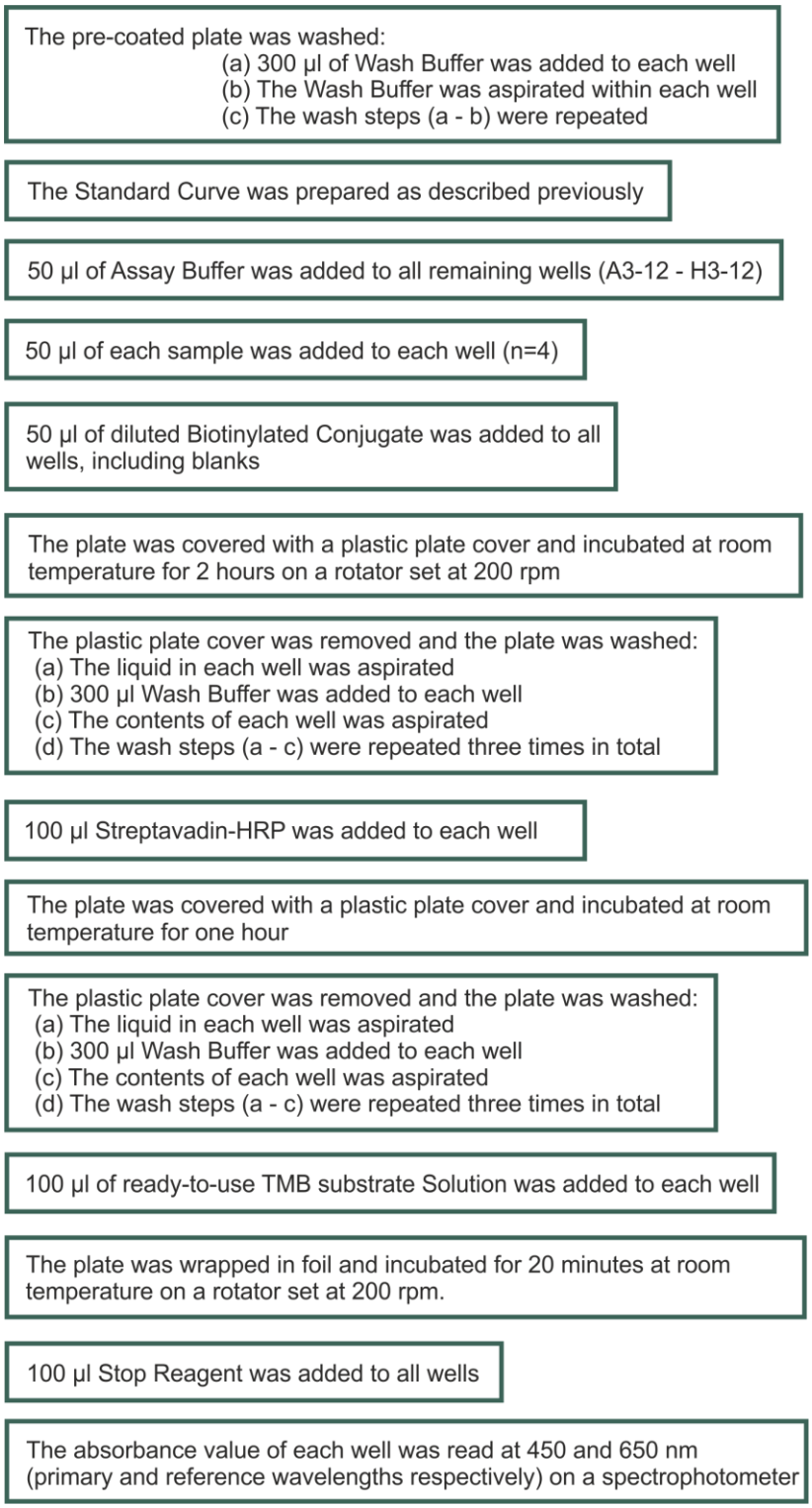


**Figure 2.7: Rat IL-6 ELISA Protocol.** Protocol followed according to manufacturer's instructions. All mixing was by aspiration and ejection, taking care not to scratch the inner surface of the wells. The plate was wrapped in foil during transportation to the spectrophotometer.

# Chapter 3

## Assessment of Reactive Astrogliosis in Response to Matrix Environment within a 3D Cell-Culture Model

### 3.1 Introduction

The glial scar is considered a physiological and physical barrier to regeneration of the injured spinal cord (Kimelberg and Norenberg, 1989). Astrocytes are the principal cells responsible for mediating glial scar formation (Fawcett and Asher, 1999). The glial scar contains reactive, hypertrophic astrocytes which have undergone a spectrum of changes, collectively termed astrogliosis. Astrogliosis can be characterized by morphological changes, such as the up-regulation of intermediate cell filaments vimentin and glial fibrillary acidic protein (GFAP). Astrogliosis can also be characterised by the release of pro-inflammatory cytokines such as interleukin-6 (IL-6) (Farina et al., 2007; Lee et al., 2010; McKillop et al., 2013; Van Wagoner and Benveniste, 1999; Yiu and He, 2006).

Three dimensional (3D) *in vitro* models provide a valuable research tool to investigate the behaviour of specific cell populations involved in glial scar formation. *In vitro* 3D models allow research parameters such as cell type and matrix organisation to be simplified, whilst maintaining cells in a spatial arrangement more representative of the *in vivo* environment, without the complexity and cost associated with animal models (LaPlaca et al., 2007).

An *in vitro* model of SCI could advance the understanding of cellular responses to injury and help inform animal studies which may facilitate the design of therapeutics (Kirkpatrick et al., 2007). The model could theoretically be used as a research tool to advance the understanding of biological, biochemical and biomechanical processes involved in astrocyte reactivity in relation to mechanical loading.

In order to usefully investigate the molecular triggers and cellular mechanisms involved in reactive astrogliosis, it is advantageous if the measurable effects of reactive astrogliosis (for example the measurement of GFAP expression, or cytokine release) are not already at such high baseline levels that it is difficult to determine whether the variation of experimental parameters has had an effect on the level of reactivity of cells in the model.

The collagen gels used throughout this study were polymerised when a solution of acid-soluble, monomer collagen (2 mg/ml in 0.6% (w/v) acetic acid) was neutralised and brought to 37$^{o}$C in 5 % (v/v) $CO_2$ in air. Under these conditions, the monomer collagen proteins rapidly aggregated into their native quarter staggered manner to produce nanometre diameter fibrils. The fibrils elongated and increased in diameter, entwining to form a loose mesh, or lattice (Cheema and Brown, 2013). During gel polymerisation, the collagen fibrils trap the original liquid volume, resulting in a hydrated gel. Cells seeded within the original liquid volume were also trapped when the gel lattice was formed.

The aim of this part of the study was to determine whether stabilisation of a type-I collagen gel would generate a suitable matrix environment for the study of reactive astrogliosis; in particular whether 3D culture of primary astrocytes within stabilised gels would result in astrocyte phenotypes expressing a low baseline level of detectable reactivity in comparison to 2D culture, as has been reported for fully hydrated 3D type-I collagen culture models (East et al., 2009).

Collagen gels have been used as the matrix material for several *in vitro* models, however the stabilisation of gel matrices has been shown to confer advantageous properties in comparison to non-stabilised gels (Braziulis et al., 2012; Brown et al., 2005; East et al., 2009; Engelhardt et al., 2010; Levis et al., 2012). Stabilisation involves the absorption of the liquid component of the gel, in order to concentrate the collagen matrix (including any cells seeded into the matrix), into a sheet of collagen gel. The gel undergoes plastic compression which means it is permanently changed in structure, and even the addition of liquid to the stabilised gel does not rehydrate or reverse the compression of the gel (Brown et al., 2005).

Despite the advantages of gel stabilisation, it was not known if the process would increase the reactivity of astrocytes such that the baseline level of the measurable effects of astrogliosis was higher than in fully hydrated gels, to the extent that the advantages achieved by stabilisation would be negated by the fact that the cells exhibited a highly reactive phenotype. Experimentally, levels of astrogliosis are higher when astrocyte cells are in contact with stiffer substrates (East et al., 2009; Georges et al., 2006). Additionally, the glial scar has been shown to alter the microenvironment of the spinal cord tissue; glial scars are considered to be stiffer than un-injured spinal cord tissue (Franze et al., 2013; Windle and Chambers, 1950).

Based on these observations, an investigation into the changes in astrocyte phenotype in gels of increasing levels of stabilisation and hence increasing stiffness was proposed. Astrogliosis can be detected in several different ways including morphological and chemical changes; a combination of these changes was investigated in order to compare the 'baseline' level of astrogliosis following cell culture within the 3D collagen matrices. Ultimately, it was envisaged that these models would provide a matrix environment for future studies with improved mechanical properties compared to fully hydrated gels, but where the astrocyte cell phenotype would exhibit a baseline level of astrogliosis that was closer to that detected in fully hydrated gels, in comparison to 2D monolayer culture.

## 3.2 Aims

The aims of this chapter were to determine the effects of changing matrix stabilisation on primary astrocyte phenotype in terms of cell viability and expression of reactive astrogliosis markers.

*Specific Objectives:*

(i) To determine the mechanical properties of different stabilised collagen gel matrix environments (as determined by rheological testing methods) over a five day period. This objective includes:
   a. calculation of the linear viscoelastic region (LVER) for each gel type; and
   b. calculation of the elastic and viscous moduli for each gel type across a range of frequencies.

(ii) To assess the viability of primary astrocytes cultured within different stabilised collagen gel matrix environments (as determined by the Live/Dead® Cell Viability assay) over a five day period.

(iii) To assess markers of astrogliosis such as the average area of GFAP expression per cell and cell shape descriptors (as determined by immunocytochemistry and imaging techniques) over a five day period.

(iv) To assess the levels of extracellular IL-6 expression after culture in different stabilised collagen gel matrix environments over a five day period (as determined by an enzyme-linked immunoabsorbant assay (ELISA)).

This part of the study contained two distinct experimental projects. Hence, for ease of presentation, the chapter is divided into two sections. Section A covers the assessment of the mechanical properties for different stabilised collagen gel matrix environments, and Section B covers the studies of cell viability and astrogliosis marker expression for different stabilised collagen gel matrix environments.

## 3.3 General Methods

The experimental approach for this section involved production of astrocyte seeded type-I collagen gel matrices.

All assays were carried out using both cell seeded and acellular gels. The primary astrocyte cells which were seeded within the matrices were from cell cultures pooled from three to six separate animals to account for donor variability. Each experiment was repeated at least three times accounting for variation in the assay reaction ($n \geq 3$).

### 3.3.1 Cell Isolation

Primary astrocytes were isolated from postnatal day-2 or day-3 Wistar rat pups using the protocols described in Section 2.2.5 to 2.2.5.5.

### 3.3.2 Matrix Preparation

The type-I collagen gel matrices were prepared as previously described in Section 2.2.7. The gel matrices were produced in 500 µl volumes using the basic gel mixture. Each gel was produced and cultured within a well of a 24-well cell culture plate.

As described in Section 2.2.7, during the production of cell seeded gel matrices, the cells formed a portion of the gel composition before the gel set. This meant that the cells were evenly dispersed throughout the gel mixture as gelation of the matrix occurred. Confocal microscopy of imunocytochemically stained gels confirmed even cellular distribution. The concentration of primary astrocytes within each cell seeded collagen gel was one million cells per 500 µl gel matrix.

In order to alter the matrix environment of the basic gel matrix, the Real Architecture for 3D Tissue (RAFT) kit was used. The RAFT kit is a 3D culture system designed for the robust and reproducible production of stabilised collagen-based matrices. Stabilisation involves the application of a specially designed absorber to the surface of

the gel matrix. Over a 15-minute incubation period, approximately 98% of liquid component of the gel is absorbed, concentrating the collagen matrix (including any cells seeded into the matrix), into a sheet of collagen gel, as shown schematically in Figure 3.1.

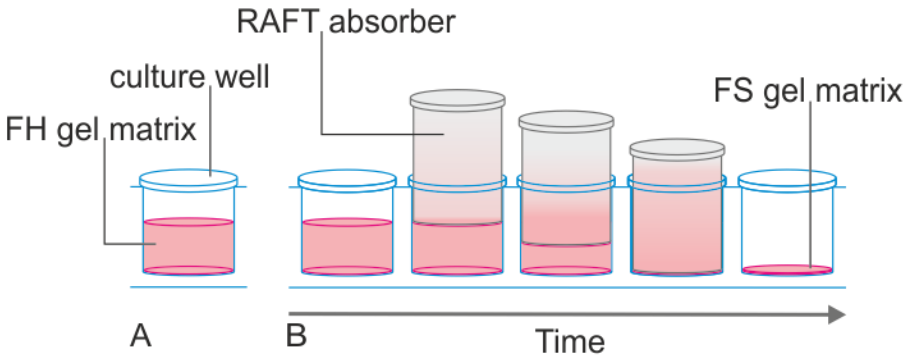


**Figure 3.1: Production of Fully Hydrated and Fully Stabilised Gel Matrix Environments.** (A) a fully hydrated (FH) gel, no RAFT absorber added, and (B) the application of a RAFT absorber to a FH gel removes the liquid component of the gel over time, forming a fully stabilized (FS) gel.

The stabilised gel, termed fully stabilised (FS), is assumed to have differing mechanical properties to a fully hydrated (FH) gel (FH gels are those where no absorber has been applied) due to the removal of the liquid component of the gel. The collagen fibrils within FH gels form a random mesh encapsulating media and cells. The liquid component of FH gels is a result of the gel casting (Brown et al., 2005); in this case the liquid component was made up of cell culture media and neutralised 0.6% (w/v) acetic acid solution which the collagen had been solubilised in. Stabilisation using a RAFT absorber both compresses the gel which expels the liquid component, and absorbs the liquid. The gel undergoes plastic compression; addition of liquid to the stabilised gel does not rehydrate or reverse the compression of the gel (Brown et al., 2005).

An adaption to the RAFT protocol was proposed, in order to produce a partially stabilised (PS) gel type. It was hypothesised that reducing the absorber application time would produce a gel whereby a reduced volume of the liquid component would

be removed, producing a gel with differing mechanical properties to both the FH and FS gels.

Three different matrix environments were produced by varying the liquid component of the initial basic gel mixture through the application of absorbers for differing lengths of time. The process is described more clearly in Figure 3.2.

The FH, PS and FS gel matrices were incubated for either one day or five days at 37$^{o}$C in 5 % (v/v) $CO_2$ and air. The supplemented DMEM media that was added to each gel behaved in a similar way to media that is applied to cultured cells that are adhered to a well of a standard 96-well culture plate; the media was able to flow through the pores of the collagen gel, to provide a supply of nutrients and oxygen, and also remove waste products and metabolites. Fresh supplemented DMEM media was added every three days.

The culture times of one and five days were selected for their comparability to the model and culture times used in the East (2009) study where 3D collagen gels were cultured for 1, 5 and 10 days (East et al., 2009).

Regarding the production of acellular gels, the volume of the gel mixture which contained the cell suspension was replaced with supplemented DMEM media (4.2 % (v/v) of final gel volume). Acellular gels were cultured in the same way as cell-seeded gels; once the gels had set, 1500 µl supplemented DMEM was added to each well, before incubation for either 1 or 5 days inside the incubator at 37$^{o}$C in 5 % (v/v) $CO_2$ in air.

For each batch of gel matrices produced, a proportion of gels were set aside for viability testing as a control. The cell viability Live/Dead assay had to be performed on separate gels to those mechanically tested, because the Live/Dead assay involved lengthy staining and image analysis processes, which could not be performed before mechanical testing. Mechanical testing was too destructive and time consuming for the Live/Dead assay to be performed post-testing.

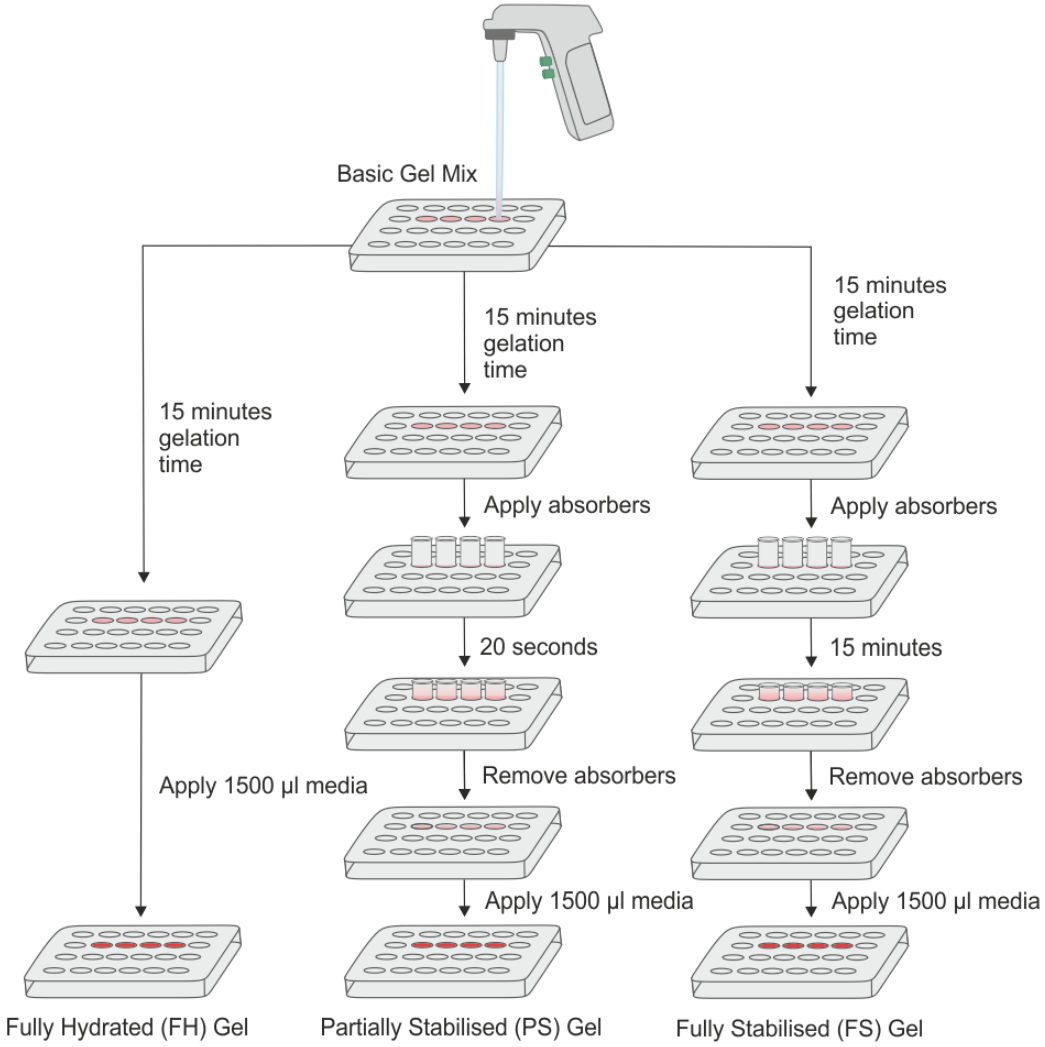


**Figure 3.2: Method for Producing Different Matrix Environments.** The same composition of basic gel mix was used to produce three different matrix environments; fully hydrated (FH), partially stabilised (PS), and fully stabilised (FS) gels. Following 15 minutes gelation, 1500 µl supplemented DMEM (Section 2.2.4.1) was added to each FH gel matrix. In order to stabilise the gels, a RAFT absorber was applied to 500 µl basic gel mix matrices. To produce PS and FS gel matrices, the absorbers were removed after either 20 seconds or 15 minutes respectively, and 1500 µl supplemented DMEM was added to each well before incubation in an incubator at 37$^{o}$C in 5 % (v/v) $CO_2$ in air.

### 3.3.3 Monolayer Two-Dimensional (2D) Cell Culture

Astrocyte cell culture in a 2D monolayer has been shown to generate highly reactive cultures (Wu and Schwartz, 1998), therefore astrocytes were cultured on microscope slides to produce a reactive astrocyte control for cell-related matrix experiments. Monolayer cultures were also used to determine the proportion of astrocytes within the cultured cell population, as described below.

Glass slides were sterilised prior to their preparation for cell culture, by immersion in 70 % (v/v) ethanol for three minutes. The slides were air dried within a class II safety cabinet. One sterile glass slide was placed inside each well of a six-well cell culture plate. Each slide was coated with 200 µl of 1 $\mu g/ml^{-1}$ poly-d-lysine (PDL) solution (Section 2.2.4.10) and allowed to incubate for at least one hour at 37$^{o}$C in 5 % (v/v) $CO_2$ in air. After incubation, the PDL was removed and discarded, before the slides were rinsed twice with 2 ml sterile PBS, and once with 2 ml supplemented DMEM. The slides were left to dry within the six-well plate, inside the incubator at 37$^{o}$C in 5 % (v/v) $CO_2$ in air until required.

Astrocyte cells were added to the PDL coated surface of each slide in 200 µl volumes at a seeding density of $3 \times 10^4$ cells per slide in supplemented DMEM. Cells were counted according to the methods described in Section 2.2.6.1. The cells were allowed to adhere to the PDL coated slide for 10 minutes. The wells were then filled with 5 ml supplemented DMEM before placing in the incubator at 37$^{o}$C in 5% $CO_2$ (v/v). The 2D astrocyte cultures were incubated for 24 hours or until the cells were >75 % confluent. Bright field microscopy was used to observe the progress of the cultures.

When the 2D cultured astrocytes had reached confluence, the media was removed and discarded (or stored in 200 µl aliquots at -70$^{o}$C for future ELISA studies, see Section 2.2.10). The slides were rinsed twice with 2 ml sterile PBS, followed by the addition of 2 ml 4 % (w/v) paraformaldehyde (PFA) solution. The slides were stored at 4$^{o}$C in PFA until required.

### 3.3.4 Determination of Astrocyte Cell Population

The percentage of astrocytes present in the cell suspension used to seed the culture models for each experiment was determined using immunocytochemical analysis of cells grown on slides, as described in Section 3.3.3.

The slides were stained using Hoechst to stain the double stranded DNA within the nuclei and antibodies against GFAP, as described in Section 2.2.8.2. The slides were imaged using a confocal microscope, as described in Section 2.2.9.

Cells isolated using the cell isolation protocol described in Section 2.2.5.4 were most likely to contain contaminating cultures of microglia, which weakly adhere to the cell culture flasks (Kerstetter and Miller, 2012). The proportion of astrocytes within the cell supernatant was estimated by counting the number of nuclei (stained with Hoechst) co-localised with an imunocytochemical stain for the astrocyte marker, GFAP. A population of at least 85 - 90 % of cells staining positively for GFAP was considered an astrocyte population as it has been considered for other studies (East et al., 2009; Kerstetter and Miller, 2012).

### 3.3.5 Determination of Cell Viability

One of the experimental questions considered in this study was whether cell seeded gels differed in their mechanical properties in comparison to acellular gels. Therefore it was necessary to assess the viability of the cells within the different matrices. Gel matrices observed to have a negative effect on cell viability would need to have this taken into consideration when interpreting the results of the experiments.

The viability of astrocytes seeded within the gel matrices was determined using the Live/Dead® Cell Viability assay, as described in Section 2.2.8.1. Briefly, each gel was covered with 1000 µl Live/Dead® Cell Viability solution in the dark. The gels were then incubated for four hours in a humidified incubator at 37$^{o}$C in 5 % $CO_2$ (v/v) in air. Following incubation, samples were washed three times for five minutes each

in PBS in the dark. Samples were kept in the dark until visualised using confocal microscopy.

#### 3.3.5.1 Analysis of Cell Viability Staining

Five fields of view were analysed per gel; the general imaging methods used in this study, with regard to capturing the images using a confocal microscope, can be found in Section 2.2.9.

Images were loaded into the ImageJ software package and analysed using the Cell Counter built in macro. The software places a grid over each image before to aid systematic counting. A 'Type 1' counter was selected, and cells were counted by positioning the computer mouse over a cell and placing a '1' marker to mark and count the cell. Once all 'live' cells (stained green) were counted, the cell counter was switched to 'Type 2' and the process repeated. When the 'Type 2' counter was selected, a click of the mouse deposited a '2' over the cell. This method of counting the cells reduced the possibility of counting a cell more than once, as the cell was marked by a '1' or '2' as it was counted. A representative image is shown in Figure 3.3.

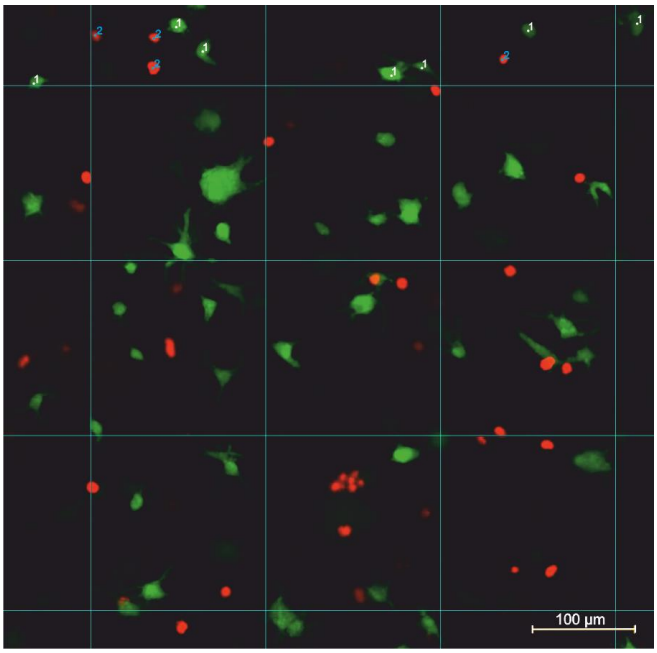


**Figure 3.3: Analysis of Cell Viability using Cell Counter Macro from ImageJ.** The Cell Counter macro from ImageJ assisted in the analysis of cell viability by allowing a grid and cell counter markers to be placed over the image. The computer program kept count of the number of marked cells in each category. The example image shown above has markers placed on stained cells in the first row of the grid. Live cells, stained green, were marked '1' and dead cells, stained red, were marked '2'. Scale bar represents 100 µm.

*Section A: Mechanical Assessments of Different Matrix Environments*

## 3.4 Mechanical Assessment Background Introduction: Section A

Although collagen gels have been mechanically characterised previously (Antoine et al., 2014; Bitar et al., 2007; Busby et al., 2013; Chandran and Barocas, 2004; Evans and Barocas, 2009; Raub et al., 2010) it is rarely possible to compare the measurements of mechanical moduli because of the variation in methods of producing and testing the gels. Compressive, tensile, or shear deformation modes may obtain different mechanical property values; the elastic modulus can refer to either the compressive or tensile modulus, depending on how the value was obtained (Antoine et al., 2014). Parameters involved in the production of collagen gels such as collagen source, solubilisation method, polymerisation pH, polymerisation temperature, and collagen concentration have also been shown to have a significant effect on one or more collagen gel mechanical properties, and these parameters are not always fully reported (Abraham et al., 2008; Gronau et al., 2012; Parenteau-Bareil et al., 2010; Stuart and Panitch, 2008). Care should be taken to avoid drawing comparisons between values for mechanical properties that have not been produced and tested in comparable ways. The mechanical properties of collagen gels produced and tested using a variety of different techniques are presented in Table 3.1 It is clear from this comparison that the reported values span a wide range; from 2 Pa (Velegol and Lanni, 2001) to 1.5 MPa (Brown et al., 2005). Therefore, due to the inconsistencies in the literature, the mechanical properties of the collagen gel matrices were assessed as part of this study in order to report all of the relevant experimental parameters required to draw meaningful comparisons between other studies where possible.

**Table 3.1: Gel Production and Viscoelastic Testing Parameters of Different Collagen Gel Matrices and the Corresponding Mechanical Property Value.**

| Gel Polymerisation Conditions: | | | | | Mechanical Testing Protocol: | | | Mean Modulus Value (Pa*) | Reference |
|---|---|---|---|---|---|---|---|---|---|
| **Collagen Source** | **Solubilisation Method** | **Collagen Concentration** | **pH** | **Temperature** | **Method** | **Temperature** | **Other Test Parameters** | | |
| Rat tail Type-I | DNS | 2 mg/ml | Neutral | DNS | Oscillatory Rheology | 21$^{o}$C | Within the LVER 0.5 % strain 0.1 Hz | **20** | (Miron-Mendoza et al., 2010) |
| Rat tail Type-I | 0.6 % acetic acid (w/v) | 2 mg/ml | Neutral | 37$^{o}$C | Uniaxial Tensile Testing | DNS | Acellular Stabilised gel Spiral assembled constructs Loading Rate: 200 mN min$^{-1}$ | **1.5 ± 0.36 MPa** | (Brown et al., 2005) |
| Rat Tail Type-I | Acid soluble | 2.2 mg/ml | Neutral | DNS | Dynamic Mechanical Analysis (DMA) | DNS | 5 - 30 % tensile strain | **1057 ± 487 kPa** | (Hadjipanayi et al., 2009) |
| Rat Tail Type-I | Acid soluble | 2.2 mg/ml | Neutral | DNS | DMA | DNS | Stabilised gel 5 - 30 % tensile strain | **2305 ± 693 kPa** | (Hadjipanayi et al., 2009) |
| Bovine (dermal) Type-I | 0.012 N HCl | 3.0 mg/ml | DNS | 37$^{o}$C | Oscillatory Rheology | 37$^{o}$C | Mineral oil added 1.0 % shear strain 1 Hz | **15.5** | (Knapp et al., 1997) |

| | | | | | | | | | |
|---|---|---|---|---|---|---|---|---|---|
| Bovine (dermal) Type-I | 0.012 N HCl | 2.3 mg/ml | 7.4 | 37°C | Laser Trap Microrheology | 37°C | 0.01 - 10 Hz Within LVER | **2 to 90** | (Velegol and Lanni, 2001) |
| Bovine (dermal) Type-I | 0.012 N HCl | 3.0 mg/ml | DNS | 37°C | Oscillatory Rheology within LVER | 37°C | Acellular Mineral oil added 10 % shear strain is LVER limit | **15.5** | (Barocas et al., 1995) |
| Sigma Bovine (dermal) Type-I | 0.01 N HCl | 3.0 mg/ml | 7.4 | Ice, then 37°C | Oscillatory Rheology within LVER | 37°C | Shear strain sweep: 0.01 - 5 % strain at 1 Hz (LVER) | **142 ± 11.6** | (Kreger et al., 2010) |
| PureCol (Bovine dermis) | 0.01 N HCl | 3.0 mg/ml | 7.4 | Ice, then 37°C | Oscillatory Rheology within LVER | 37°C | Shear strain sweep: 0.01 - 5 % strain at 1 Hz (LVER) | **37.2 ± 17.5** | (Kreger et al., 2010) |
| Type-I Pig hide | 0.01 N HCl | 2.75 mg/ml | 7.4 | Ice, then 37°C | Oscillatory Rheology within LVER | DNS | Shear strain sweep: 0.01 - 5 % strain at 1 Hz Increasing collagen average polymer molecular weight (APW) increases gel stiffness | **3.3 ± 9 or 20.8 ± 5.4 kPa** | (Bailey et al., 2011) |

All data are for hydrated gels, unless stated otherwise. Modulus values are in Pa unless stated otherwise. DNS = data not shown in study.

Mechanical properties of materials can be assessed by various methods; some are better suited to testing collagen gels than others. For uniaxial tensile testing, samples are placed between two clamps and stretched at constant extension rates in order to determine the Young's modulus of the material. The Young's Modulus is defined as the ratio of tensile stress to tensile strain (Brandl et al., 2007). Tensile measurements are difficult to perform on collagen gels because gripping the gel sample with pneumatic or screw clamps can induce preferential failure at the clamping point (Picout and Ross-Murphy, 2003). In addition, tensile testing predominantly involves the collagen fibre network, rather than testing the bulk properties of the collagen fibre network and liquid component (Chandran and Barocas, 2004).

The compressive modulus is defined as the ratio of compressive stress to compressive strain. Testing is performed by uniaxial compression of specimens between two platens (unconfined compressive testing). The compressive strength is defined as the maximal compressive stress that a sample can withstand until the yield point, at which point the material is plastically deformed (Brandl et al., 2007). Collagen gel behaviour results from the intrinsic properties of and interaction between the network of collagen fibrils and the liquid component. The fibrils form an entangled network that can resist a degree of shear and tensile forces but has little compressive strength. However, the resistance to the flow of the liquid component through the fibril network can allow collagen gels to withstand compressive loads. Thus, when collagen gels are subjected to shear or tension, the physical network supports the load, however under compression, the fibril network transfers much of the load to the liquid component (Knapp et al., 1997). Therefore methods for assessing the compressive modulus of collagen gels are unsuitable for the determination of the bulk properties of collagen gels.

Atomic force microscopy (AFM) is a technique which involves detection of the forces between a sharp stylus and a surface of interest (Meyer and Amer, 1988). Despite the use of AFM for localized tissue and cell mechanical measurements (Brandl et al., 2007; Kloxin et al., 2010), it is poorly suited for assessment of the bulk properties of collagen gels due to the heterogeneity of the gel matrix; the stylus comes into contact with individual fibrils and does not sample the gel as a whole (Thiele et al., 2014).

Complex materials, such as collagen gels, can show both solid and liquid behaviours (the elastic and viscous components, respectively) under deformation; this is known as the viscoelastic properties of a material (Larson 1999). Shear testing can be performed by rheological testing methods. Rheology is the study of the flow and deformation of matter in response to an applied force, measured using a rheometer. Rheology was used to assess the viscoelastic properties of the FH and FS matrices because the rheological shear test accounts for both the fibril network and liquid component of the collagen gels.

A typical rotational rheometer consists of a motor which is able to rotate a geometry, known as a cone or plate, above the sample. The sample is loaded between the top and bottom geometries, as shown in Figure 3.4.

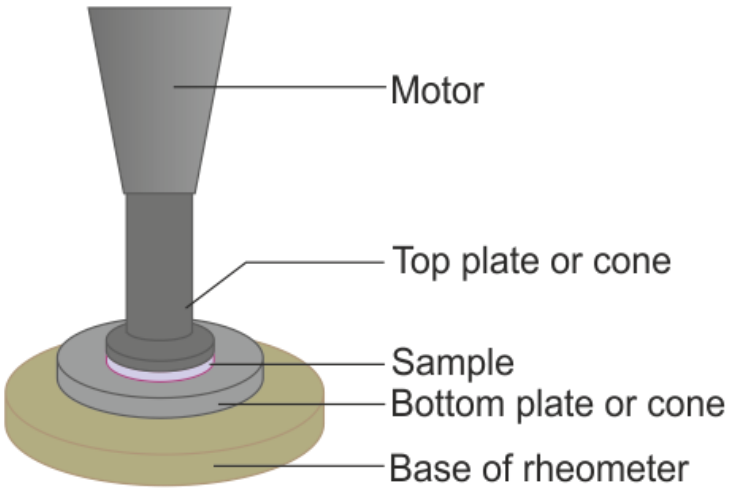


**Figure 3.4: A Rotational Rheometer.** The major components of the rheometer are labelled. The top and bottom plates or cones are removable and can be selected depending on the type and size of sample tested.

A rheometer determines the measure of viscosity by application of shear stress, and measurement of the shear rate, as shown in Equations 3.1 & 3.2.

$$shear\ stress = \frac{force}{area} \qquad \text{Equation 3.1}$$

$$shear\ rate = \frac{velocity}{height} \qquad \text{Equation 3.2}$$

Viscosity can be measured either by rotation of the top plate with application of a set force, in order to measure the velocity of the sample, or rotation of the top plate with a set velocity, in order to measure the force of the sample (Mezger, 2006).

In addition to viscosity, the deformation of a material, allowing the modulus (Equation 3.3), or elasticity, to be measured is required to understand the viscoelastic behaviour. The modulus of a material is calculated by the application of shear stress and measurement of shear strain, as is represented schematically in Figure 3.5. During testing, the top geometry is oscillated back and forth, rather than rotated; controlled stress is calculated by oscillation of the top geometry with a set force in order to measure the displacement (Equation 3.4), whilst controlled strain is calculated by oscillation of the top geometry at a set displacement in order to measure the force (Rohn, 1995).

$$modulus = \frac{shear\ stress}{shear\ strain} \qquad \text{Equation 3.3}$$

$$shear\ strain = \frac{displacement}{height} \qquad \text{Equation 3.4}$$

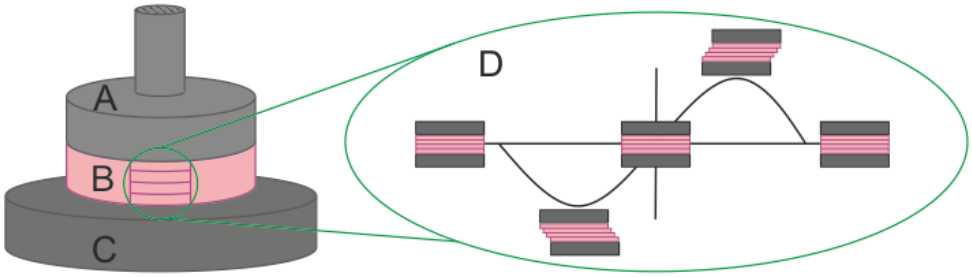


**Figure 3.5: Oscillatory Rheology.** There is a change in strain following the application of shear stress as the top plate (A) oscillates above the sample (B) and the bottom plate (C), which remains fixed in place. Depending on the viscoelastic properties of the sample, oscillation of the top plate causes a degree of shear flow – layers of molecules flow over each other, the bottom layer remaining stationary, the top layer moving the fastest (D). The modulus of a sample is the resistance to movement; stiffer materials resist movement more than less stiff materials and therefore have a higher modulus value. Figure adapted from (Malvern Instruments Ltd., 2016)

The phase angle (δ) is used to determine how solid-like, or liquid-like, a material behaves under certain conditions. The phase angle is calculated by comparing the stress and strain curves in an oscillatory test, for example a purely elastic material would show the stress and strain to be exactly in phase ($\delta = 0^{o}$). When the stress and strain are exactly in phase there is no lag between the two curves, whereas a purely viscous material would show the stress and strain curves to be a quarter of a cycle out of phase ($\delta = 90^{o}$), as illustrated in Figure 3.6 (Larson, 1999; Mezger, 2006).

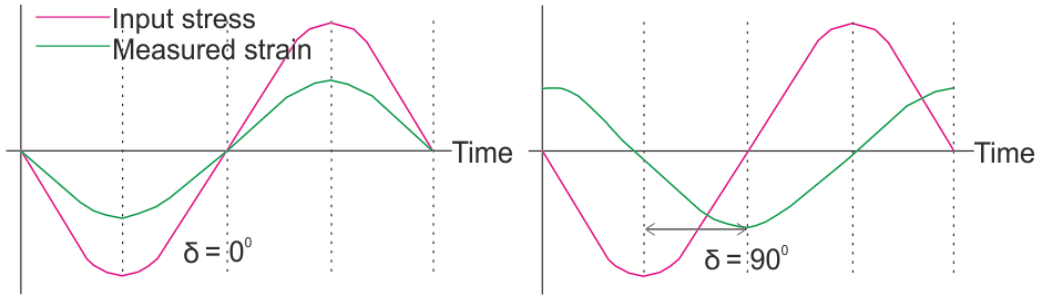


**Figure 3.6: Phase Angle Calculation.** Phase plot of a purely elastic (solid-like) material (left) and a purely viscous (liquid-like) material (right), illustrated are the differences in phase angle between cycles of stress and strain. Figure adapted from (Chaplin, 2016)

The overall stiffness of a material is known as the complex modulus (G*). The complex modulus represents the shear storage (G') and shear loss (G") moduli; it is a measure of the stored energy (elastic portion, G') and the dissipated heat energy (viscous portion, G"). The complex modulus is defined in Equation 3.5 (Larson, 1999; Mezger, 2006).

$$G^* = G' + G^{"} \qquad \text{Equation 3.5}$$

The phase angle for a solid-like material will be less than $45^o$ (G' > G"), whereas the phase angle for a liquid-like material will be greater than $45^o$ (G" > G') (Mezger, 2006).

## 3.5 Methods Specific to Section A

Stabilisation of collagen gel matrices improves the experimental handling of gels (Braziulis et al., 2012); this is thought to be due to changes in mechanical properties, such as increased collagen density and reduced liquid content, which is a result of the stabilisation process (Brown et al., 2005). The experimental approach for this section involved determination of the viscoelastic mechanical properties of astrocyte seeded type-I collagen fully hydrated (FH) and fully stabilised (FS) gel matrices and acellular collagen FH and FS gel matrices, over a five day period. The viscoelastic properties of cell-seeded and acellular FH and FS gel matrices were compared, to determine whether cell seeding and stabilisation affected the viscoelastic properties of the gels over time.

### 3.5.1 Determination of Gel Matrix Mechanical Properties

The viscoelastic properties of the two gel types, FH and FS, were determined to investigate if there was a relationship between the mechanical properties of the gels and astrocyte reactivity. Viscoelastic properties were determined using a rheometer.

All rheological measurements were performed on a Malvern Kinexus Pro+ rheometer with a flat-plate geometry (cone angle: $0^o$, diameter: 1.5 cm, gap: 0.75 mm), at $37^oC$, utilizing a solvent trap ($dH_2O$) to minimise evaporation of the gel samples. The parallel plate geometry (cone angle of $0^o$) was selected as a cone angle is not suitable for use with gel matrices or solid materials, due to the interaction between the cone and the 3D internal network of these materials; for example the collagen fibrils and cells within the collagen gel (Mezger, 2006). The secondary flow generated within the sample by a geometry with a cone angle of greater than $0^o$ can cause aggregations of particles within a sample during testing (Ewoldt et al., 2015). A disadvantage of parallel plate geometries is that the shear rate is inconsistent across the sample because strain rate is dependent on distance, in this case the radius, therefore the strain rate increases from zero in the centre of the plate to a maximum at the plate edge. However, this effect is negligible when tests are performed within the LVER

(Mezger, 2006). An illustration of cone and parallel plate geometries are shown in Figure 3.7.

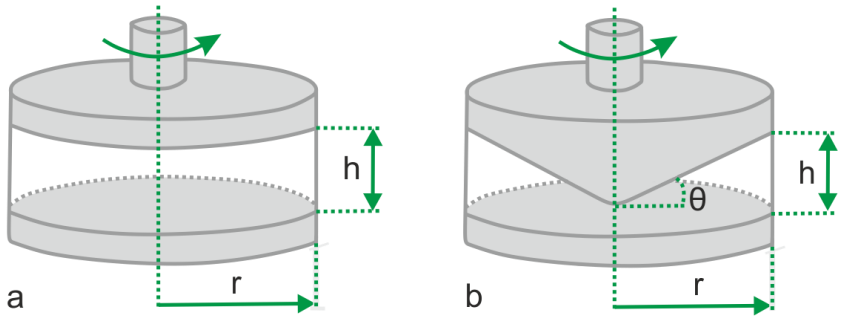


**Figure 3.7: Cone and Plate Geometries of a Rheometer.** A suitable geometry should be selected according to the material being tested. A parallel plate geometry (a) has a cone angle (θ) of $0^o$, a cone plate geometry (b) has a cone angle whereby $\theta > 0^o$. The gap height (h) can be set manually depending on the sample thickness. The radius (r) of the plate geometries dictates the sample size. Adapted from Picout and Ross-Murphy (2003).

Proprietary software (rSpace) for the Kinexus 1.10 Rheometer (Malvern Instruments) was used to control the rheometer and to export the raw data. The GraphPad software package was used to process and plot the results.

### 3.5.2 Solvent Trap Assembly

A solvent trap was utilised during all rheological testing, to minimise the evaporation of samples. Evaporation of the samples was likely to alter their viscoelastic properties, and also lead to under-filling of the sample area as the sample evaporates.

The solvent trap is a removable fixture of the rheometer. Assembly involved placement of a bottom plate comprising a solvent ring component, on the base of the rheometer, and placement of the upper metal ring portion on top of the upper plate, as shown in Figure 3.8. The rings were then filled with $dH_2O$, and the rheometer loaded as instructed by the rSpace software, all software prompts requiring confirmation of

the solvent trap assembly were affirmed. During testing the solvent trap lid was applied over the sample area.

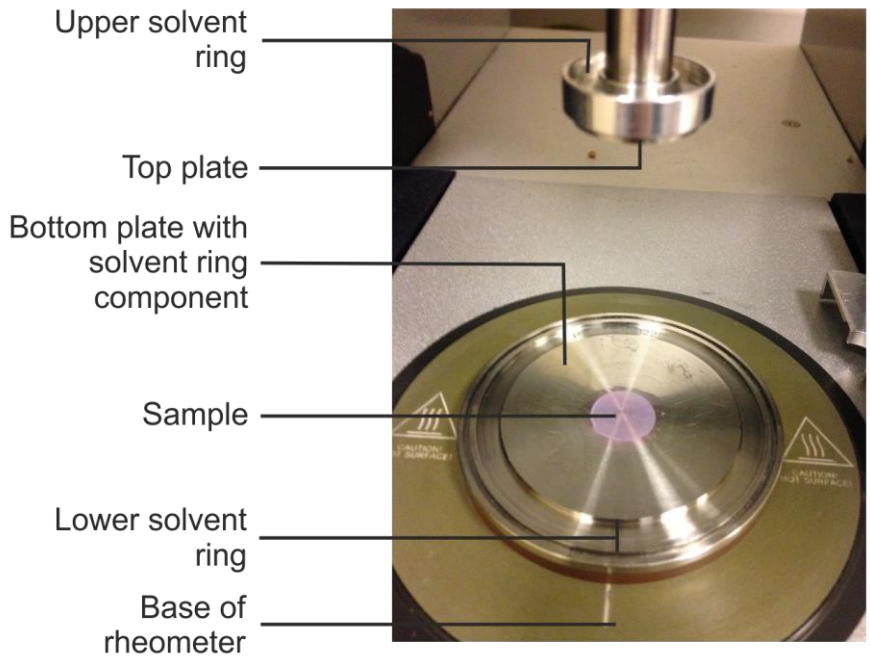


**Figure 3.8: Rheometer Solvent Trap Assembly.** A solvent trap was assembled as part of the rheologial apparatus in order to reduce evaporation of the sample. The key components of the rheometer and the solvent trap are labelled. A solvent, such as $dH_2O$, was placed within the upper and lower ring components of the solvent trap.

All of the rheological testing was performed at 37$^{o}$C. The solvent trap was assembled prior to the application of experimental temperature settings on the computer software, to ensure the solvent trap was brought up to temperature and did not affect the temperature of the experiment.

The volume of $dH_2O$ in the solvent trap was checked before each sample was loaded and refilled if necessary. The rheometer ensured the temperature of the experiment was at 37$^{o}$C before testing began.

### 3.5.3 Loading of Gels Within the Rheometer

The FH and FS gels were polymerised within 24-well plates which resulted in a 1.5 cm gel diameter. During testing, the shear gap (the gap between the top and bottom plate geometries) must be filled completely with the sample. Under- or over-filling the gap can cause variation in results due to the distortion of the instrument reading by the lack of bonding between the gel surface and the metal surfaces of the instrument geometry (Picout and Ross-Murphy, 2003). Following preliminary loading tests, gap heights were selected of 0.75 mm and 0.1 mm for FH and FS gels, respectively. At these gap heights, the gels optimally filled the shear gap without the need to trim excess gel. Examples of optimally filled shear gaps for FH and FS gel matrices are shown in Figure 3.9.

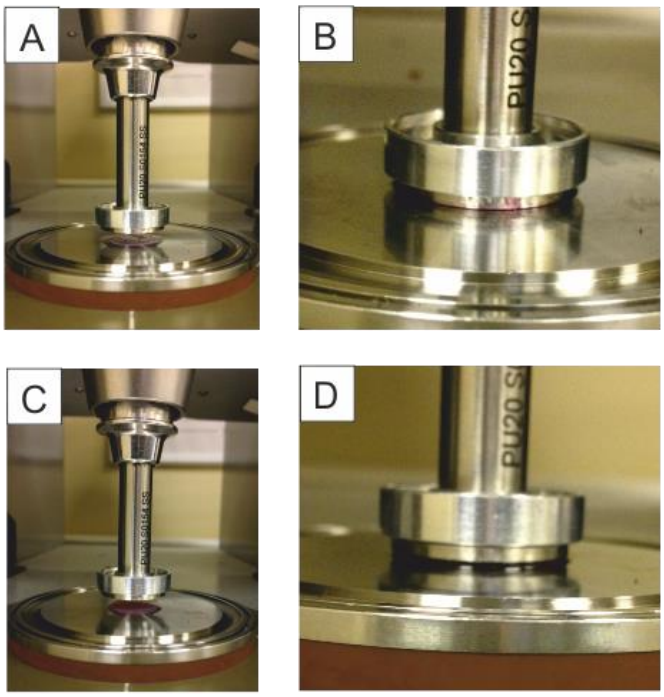


**Figure 3.9: Optimally Filled Gap Height for FS and FH Gels.** Under- or over-filling the shear gap between the top and bottom rheometer plates can cause variation in results. Gap heights were selected of 0.1 mm for FS gels (A & B) and 0.75 mm for FH gels (C & D). At these gap heights, the gels optimally filled the shear gap without the need to trim excess gel and without visible space around the circumference of the gel. A & C are examples of gels in position before loading.

To load a gel sample onto the rheometer for testing, the solvent trap was assembled (Section 3.5.2) and the temperature of the experiment set to 37$^{o}$C using the computer software settings. The plate geometries were cleaned using 70 % (v/v) ethanol and left to air dry before each gel was loaded. A spatula was used to place the gel in the centre of the bottom plate. The gel sample was then loaded using the computer software which lowered the top plate geometry onto the sample to the specified gap height. This step was carefully observed to ensure that the gel did not slip out of the shear gap during loading. Gels that were not correctly loaded were discarded.

Once the gel was loaded into the rheometer, the solvent trap lid was placed over the sample area and the gel was allowed to rest for ten minutes, to reach 37$^{o}$C.

### 3.5.4 Determination of the Linear Viscoelastic Region

Firstly, the Linear Viscoelastic Region (LVER) was determined for each gel environment (FH and FS). The LVER is the rheological testing range in which the strain values are non-destructive. If the LVER range is exceeded (known as exceeding the 'limiting value'), the structure of the sample is irreversibly changed (plastically deformed). It was crucial to determine the LVER range, because results obtained from outside of the LVER range are not based on the basic laws of rheology of Hooke and Newton; strain at any time is directly proportional to the initiating stress (Ewoldt et al., 2015; Macosko, 1994; Mezger, 2006; Parsons and Coger, 2002; Picout and Ross-Murphy, 2003).

The LVER is typically investigated using the strain sweep method which dynamically tests the sample under continuously increasing strain at a fixed frequency, known as an amplitude sweep. The LVER can be analysed by observation of the plotted G' and G" curves, the curves remain on a constant plateau, until they begin to decrease with strain amplitude, as represented by the exemplary curve in Figure 3.10 (Cheng et al., 2008). The last value in the plateau whereby there is noticeable deviation from the constant values is known as the limiting value and is the point at which the LVER range is exceeded (Mezger, 2006).

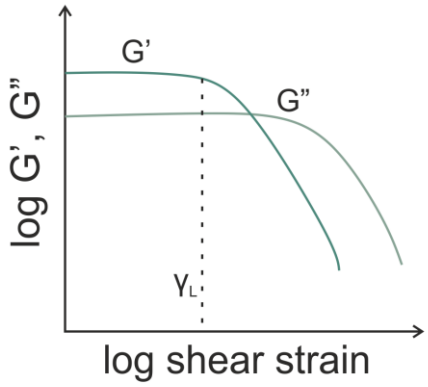


**Figure 3.10: Amplitude Sweep Highlighting the LVER.** Exemplary amplitude sweep, representative of a sample showing solid-like behaviour (G' > G") within the LVER. The limiting value ($Y_L$) is the point at which the values deviate from the plateau; this is highlighted by the dotted line. Adapted from Mezger (2006).

Amplitude sweeps were performed to generate the G' and G" curves for LVER analysis. An amplitude sweep is an oscillatory rheology test which maintains the frequency of the test at a constant value, but is performed at different strain amplitudes. Two amplitude sweeps were carried out for each sample at 1 Hz and 20 Hz, the amplitude sweeps were performed under shear strain controlled mode from 0.01 - 100 %.

Viscoelastic properties of materials are frequency dependent (Antoine et al., 2014), therefore the frequency values of 1 Hz and 20 Hz were selected for their comparability to the frequencies used to determine the viscoelasticity of CNS tissue using a rheometer (Arbogast and Margulies, 1997, 1998; Cheng et al., 2008; Fallenstein et al., 1969; Hirakawa et al., 1981; Lu et al., 2006; Nicolle et al., 2005).

The G' and G" curves were plotted, and a strain value was chosen within the LVER at which the elastic modulus (G') and viscous modulus (G") were independent of strain amplitude at the two different frequency levels; a value was selected from the approximate centre of the curve plateau LVER. The LVER was calculated using cell seeded gel matrices at day 1.

### 3.5.4.1 Confirmation of LVER

A frequency sweep is an oscillatory rheology test which maintains the strain of the test at a constant value (as selected from the LVER), but is performed at different timescales (Cheng et al., 2008).

The LVER, selected using the methods described in 3.5.4, was confirmed by running a frequency sweep test at the strain level selected from within the LVER on a freshly loaded sample. The frequency range related to the two frequencies selected for the initial LVER test (from 1 Hz to 20 Hz). The gel was allowed to equilibrate for 10 minutes once loaded prior to the start of testing, and for 10 minutes between each frequency sweep. The frequency sweep at the lowest frequency was always performed first.

The data obtained from the frequency sweep provided stress values for all of the frequencies tested. The stress values for the highest and lowest frequencies were determined.

For example, the stress value at:

$\sigma 1$ (1 Hz) = 0.87 Pa

$\sigma 2$ (20 Hz) = 1.11 Pa

Stress values over a range which broadly covered both of these values were selected: in this example, 0.05 - 5 Pa.

In order to confirm that the strain value selected during experiments described in Section 3.5.4 was within the LVER, two more amplitude sweeps were carried out in a stress controlled mode, rather than strain controlled mode. The stress values were selected from the higher and lower values of the stress range. For example, if using the values described in the 0.05 - 5 Pa example above, a stress controlled frequency sweep would run under the following conditions: 1 Hz, start stress: 0.05 Pa, end stress: 5 Pa. The test would then be repeated at 20 Hz, start stress: 0.05 Pa, end stress: 5 Pa.

If the values for σ1 and σ2 were found to be independent of stress amplitude (the curve was a plateau), this would confirm that testing was within the LVER.

#### 3.5.4.2 Determination of the LVER: Experiment Design

The determination of the LVER involved several rheological testing methods. The steps involved in determining the testing parameters are presented in the flow diagram in Figure 3.11. The experimental methods displayed in Figure 3.11 are all described in more detail in the previous sections of this chapter.

### 3.5.5 Oscillatory Frequency Sweeps within the LVER

Once the LVER had been determined and confirmed (Sections 3.5.4 & 3.5.4.1), the oscillatory frequency sweeps could be performed at the appropriate strain rate, to determine the viscoelastic properties of the FH and FS gel matrix environments. The determination of the LVER strain rate was performed on cell-seeded FH and FS gels. The same chosen strain rate was applied to gel matrices that were acellular and gel matrices at day 5 for the corresponding FH or FS gel matrices.

Each gel was tested once at the lower frequency and once at the higher frequency at 37$^{o}$C. The gel was allowed to equilibrate for 10 minutes once loaded prior to the start of testing. The gel was discarded and a new sample loaded for each repeat.

For the determination of the viscoelastic properties of FH gels at day 1 and day 5 (cell-seeded and acellular), the oscillatory frequency sweeps were run from 1 Hz to 5 Hz at 1 % strain.

For the determination of the viscoelastic properties of FS gels at day 1 and day 5 (cell-seeded and acellular), the oscillatory frequency sweeps were run from 1 Hz to 20 Hz at 0.3 % strain.

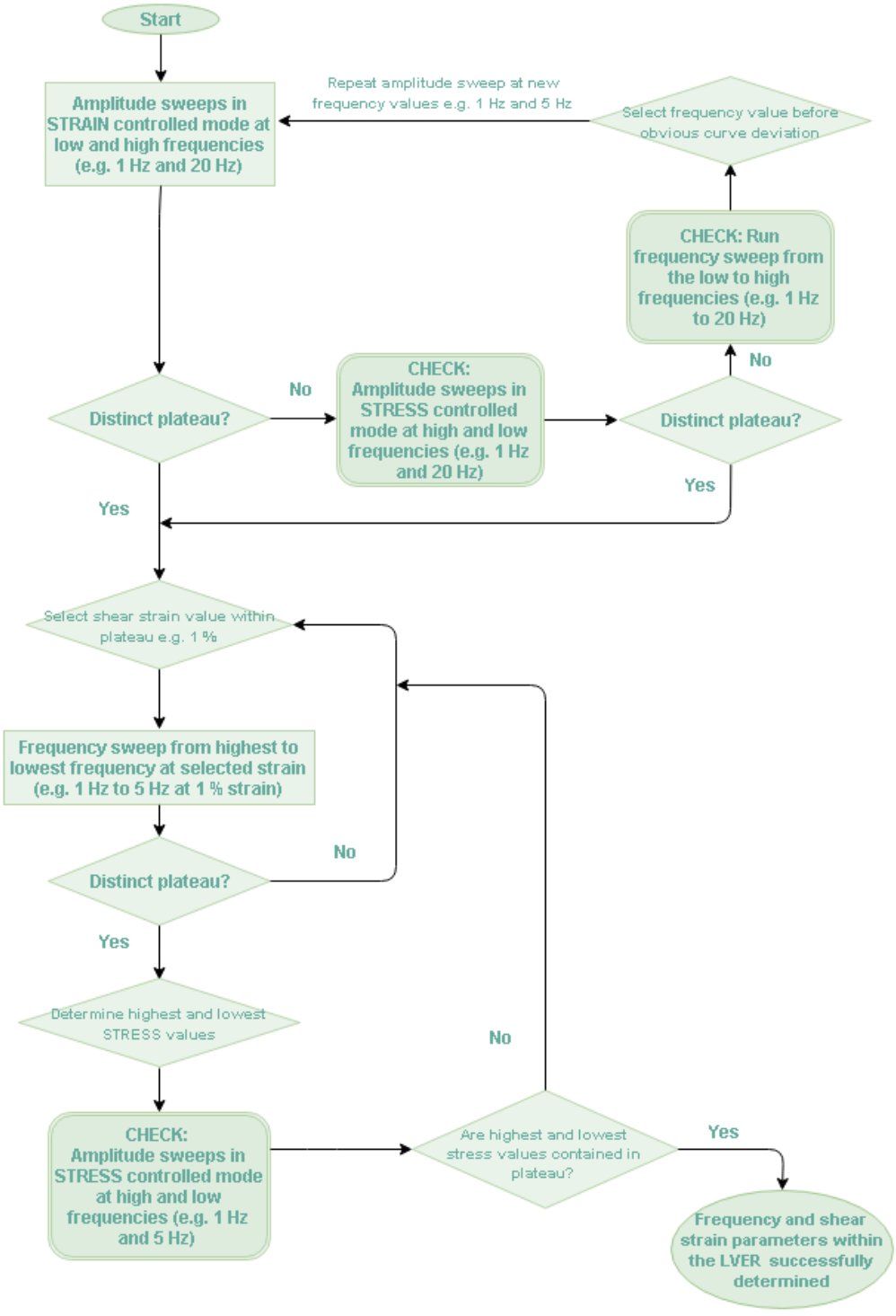


**Figure 3.11: Flow Diagram of the LVER Determination Process.** Rheological testing parameters that were within the Linear Viscoelastic Region (LVER) were selected according to the process outlined in the flowchart. During experiments where stress or strain was controlled, the following parameters were used: shear strain controlled mode, 0.01 – 100%; stress controlled mode, 0.05 – 5 Pa.

## 3.6 Results: Section A

### 3.6.1 Matrix Preparation

During Fully Stabilised (FS) gel matrix production, application of the absorber appeared to remove the majority of the liquid component of the gel within the first minute, based on visual observation of the absorber within the well. However, the manufacturer's instructions stated that the absorber should be applied for 15 minutes.

The absorber application time chosen for the production of the Partially Stabilised (PS) gels was based on a series of timed absorber applications to produce a gel that was approximately half the height of the Fully Hydrated (FH) gels. The objective was to produce a gel matrix environment that would be less stiff than a FS gel, but stiffer than a FH gel, in order to compare a range of environments, rather than two extremes. The difference in height between FH and FS gel matrices was approximately 100-fold (Brown et al., 2005). Although a gel height of exactly half of FH gels would have been preferable, it was assumed unnecessary to investigate the absorber application times which would produce a PS gel that was exactly half the height of FH gels. An absorber application time of 20 seconds was found to be most appropriate, based on visual inspection of the height of the PS gels; this was investigated further using the methodology described below.

#### 3.6.1.1 Assessment of PS Gel Reproducibility

Investigations were made into non-destructive methodology for the assessment of cellular and acellular PS gel production. The proposed methodology was based on measurement of the gel height post-absorber application, on the basis that there would be a relationship between the change in height and the resultant mechanical properties. This relationship was expected due to the removal a proportion of the gels liquid component (Brown et al., 2005). If a 20 second absorber application time could not produce PS gels of reproducible height, it was thought this may produce PS gels of varied mechanical properties which would affect how the cellular response to the PS matrix environment could be interpreted. The results of this method development are shown in Table 3.2.

**Table 3.2: Results of Gel Height Measuring Technique - Method Development**

| Measurement Type: | Result: | Note: |
|---|---|---|
| **Digital Calliper** | Not effective | • Media must be removed from the well in which the gel sits to take the measurement - problematic because evaporation caused gel dehydration<br>• Difficult to visualise surface of the gel<br>• Possibility of compressing gel surface with callipers |
| **Photography** | Not effective | • Media must be removed from the well in which the gel sits to take the measurement - problematic because evaporation caused gel dehydration<br>• Difficult to visualise surface of the gel<br>• Resolution poor, especially with thinner gels |
| **Shadowgraph** | Not effective | • Gel must be completely removed from well to take measurement - problematic because evaporation caused gel dehydration<br>• Gel must be completely flat to record accurate measurement - this is difficult with thin gels such as the FS and PS gels<br>• Location of shadowgraph required 20 minute transportation across campus - not ideal, in particular for cell seeded gels<br>• Difficulty in mounting gels to shadowgraph |

Of the methodologies tried, similar problems were encountered. Removal of the gels from a humidified environment caused dehydration of the samples. The FS gels were too thin to measure accurately using the digital calliper and photography methods, resulting in the callipers disrupting the matrix, and the camera was difficult to focus on the gels whilst they were within a culture well. The shadowgraph was able to resolve the thin FS gels; however it was difficult to get the gels to lie completely flat on a slide for imaging. In addition, mounting the slide on its side within the shadowgraph machine apparatus caused the FH and PS gels to slide off the slide. All of the methods were destructive and were unable to measure all types of FH, PS and FS gel matrices; therefore the methods were deemed unsuitable.

Although it was intended to develop a non-destructive test, it was possible to use confocal microscopy of cellular gels to measure the height of FH, PS and FS gels. The location of the microscope focal plane to the top and bottom gel surfaces (highlighted by the presence of fluorescently labelled cells) provided z-plane values which allowed for calculation of the gel heights.

#### 3.6.1.2 Issues Associated with RAFT Absorber Incubation Time

The RAFT absorber protocol states that for stabilisation of gels, absorbers should not be removed prior to the 15 minute incubation time. It was assumed this was to allow for sufficient time for 96% of the liquid component of the gel to be fully absorbed.

During preliminary experiments to produce PS gels, the absorbers generally behaved in the same way as for FS gel production, and were easily removed after the 20 second incubation time. As larger batches of PS gels were produced, it became apparent that a high proportion of PS gels were not forming correctly. The gels were sticking to the absorbers and could not be removed, as shown in Figure 3.12. Occasionally a sterile metal spatula could be used to remove the gel from the absorber, although often the spatula could not remove the gel at all. Additionally, the extra time that the gel spent in contact with the absorber clearly affected the volume of liquid removed from the gel.

**Figure 3.12: Gel Stuck on RAFT Absorber.** Removal of the absorber from the gel before 15 minutes repeatedly resulted in the gel remaining attached to the absorber resulting in the continued absorption of liquid from the gel.

The PS gels were produced using the same batch of gel mixture that was used for producing FS gels, at the same time, under the same conditions (excluding absorber incubation time). The absorbers did not stick to the FS gels after the 15 minute incubation time. Other troubleshooting experiments included: using absorbers from a different batch, using gel solutions from a different batch, increasing the absorption time (whilst still producing a partially stabilised gel), and measuring the pH of all associated solutions to ensure they were suitable, according to the manufacturer's instructions. No obvious solution could be found. None of the inconsistencies relating to the absorber were found to be an issue for FS gel production. Communication directly with the absorber manufacturer stated that the absorption time of their protocol should not be adapted.

Hence, the study subsequently focussed on FS and FH gel matrices which provided two different matrix environments in which to investigate cellular responses.

### 3.6.2 Determination of Astrocyte Cell Population

Immunocytochemical staining of cells sampled from each cell isolation batch for each experiment and cultured on slides in 2D, provided an estimate that the cultured cells were at least 90 % astrocytes, based on the positive GFAP stain associated with at least 90 % of cell nuclei. A representative image used in this analysis is shown in Figure 3.13.

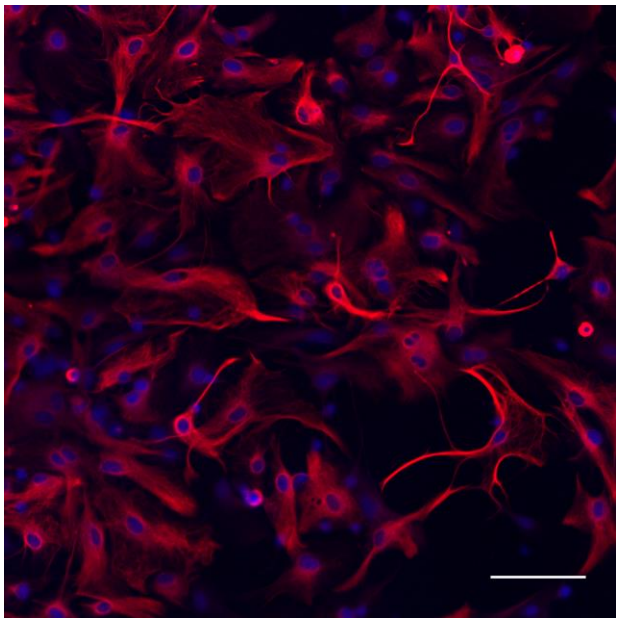

**Figure 3.13: Cells Stained Positive for GFAP in 2D Culture were Assumed to be Astrocytes.** Antibodies with an affinity to the astrocyte marker, GFAP, stained the cells red. Cell nuclei were stained blue with Hoechst. All nuclei in this image were positively associated with the GFAP antibody stain. Scale bar represents 100 μm.

### 3.6.3 Determination of the LVER of Collagen Gel Matrices

The linear viscoelastic region (LVER) is the rheological testing range in which the strain values are non-destructive. The LVER can be determined using amplitude sweeps to determine the LVER strain rate; this can then be confirmed using frequency sweeps in strain-controlled and stress-controlled modes.

#### 3.6.3.1 Fully Stabilised Gel Matrix LVER

The LVER for 500 μl FS gels were determined using a rheometer. Two amplitude sweeps were carried out for each sample at 1 Hz and 20 Hz, the amplitude sweeps were performed under shear strain controlled mode from 0.01 - 100 %.

There was a visible plateau of the G' and G" curves at both frequencies, indicating the range in which the LVER was likely to be found for FS gels, as shown in Figure 3.14. The strain value selected from within the LVER at which the elastic modulus (G') and

viscous modulus (G") were independent of strain amplitude at the two different frequency levels for FS gels was 0.3 % strain.

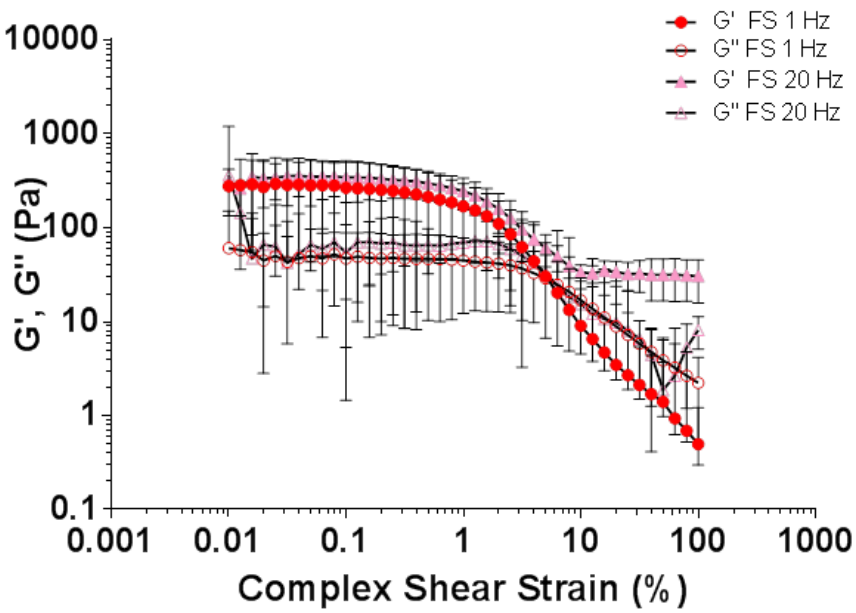


**Figure 3.14: Amplitude Sweep to Allow Determination of LVER in FS (day 1) Gels at 1 Hz and 20 Hz.** Two amplitude sweeps were carried out for each sample at 1 Hz and 20 Hz, the amplitude sweeps were performed under shear strain controlled mode from 0.01 - 100 %. Data are n=4, error bars 95 % confidence limits. Shear gap height 0.1 mm.

The parameters for LVER testing were determined by running two tests. First, by running a frequency sweep test at 0.3 % shear strain, as shown in Figure 3.15. This value was selected as it appeared in the visible plateau of the amplitude sweep curves. At 0.3 % shear strain the curve was not a level plateau, although there was not an obvious deviation from the curve indicative of the limiting value.

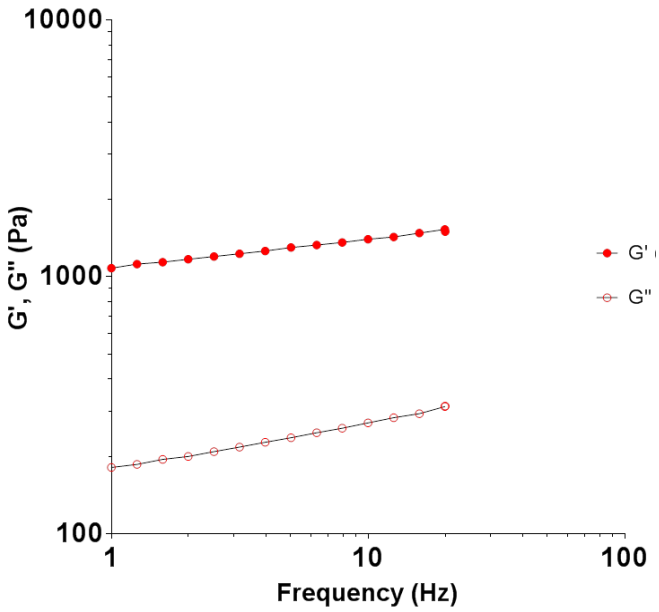


**Figure 3.15: Selection of Frequency Range for FS Gels.** A frequency sweep was performed on day 1, FS gel matrices at 0.3 % strain and a frequency range of 1 Hz to 20 Hz. Shear gap height 0.1 mm.

The frequency sweep at 0.3 % strain (Figure 3.15) provided stress values for all of the frequencies tested. The stress values for the highest and lowest frequencies were:

$\sigma 1$ (1 Hz) = 0.87 Pa

$\sigma 2$ (20 Hz) = 1.109 Pa

In order to confirm that the shear strain value of 0.3 % was within the LVER a stress value range which broadly covered the highest and lowest stress values was selected. The stress range selected was 0.05 - 5 Pa, and a stress controlled frequency sweep was run under the following conditions: 1 Hz, start stress: 0.05 Pa, end stress: 5 Pa and 20 Hz, start stress: 0.05 Pa, end stress: 5 Pa, this is shown in Figure 3.16. The stress values of the highest and lowest frequencies ($\sigma 1$ and $\sigma 2$) were found to be independent of stress amplitude; they are found within a level area of the curve. This confirms that rheological testing performed between 1 Hz and 20 Hz at 0.3 % strain was within the LVER for FS gels.

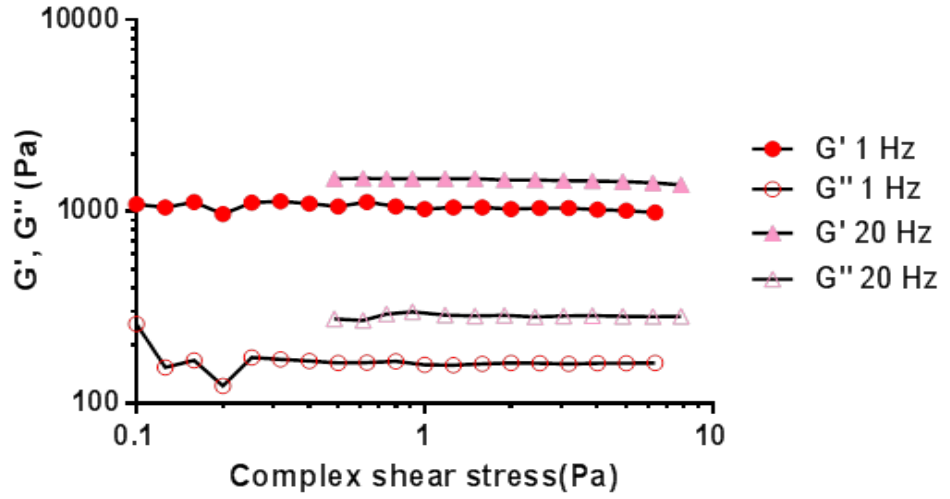


**Figure 3.16: Confirmation of LVER in FS Gels at 0.3 % Strain.** Two amplitude sweeps were carried out for each sample at 1 Hz and 20 Hz, the amplitude sweeps were performed under stress controlled mode from 0.05 - 5 Pa. Shear gap height 0.1 mm.

### 3.6.3.2 Fully Hydrated Gel Matrix LVER

The rheological testing parameters within the LVER for 500 µl FH gels were determined using a rheometer. Two amplitude sweeps were carried out for each sample at 1 Hz and 20 Hz, the amplitude sweeps were performed under shear strain controlled mode from 0.01 - 100 %.

There was a visible plateau of the G' and G'' curves at 1 Hz, however a plateaued region was not distinct in the 20 Hz curve, as shown in Figure 3.17.

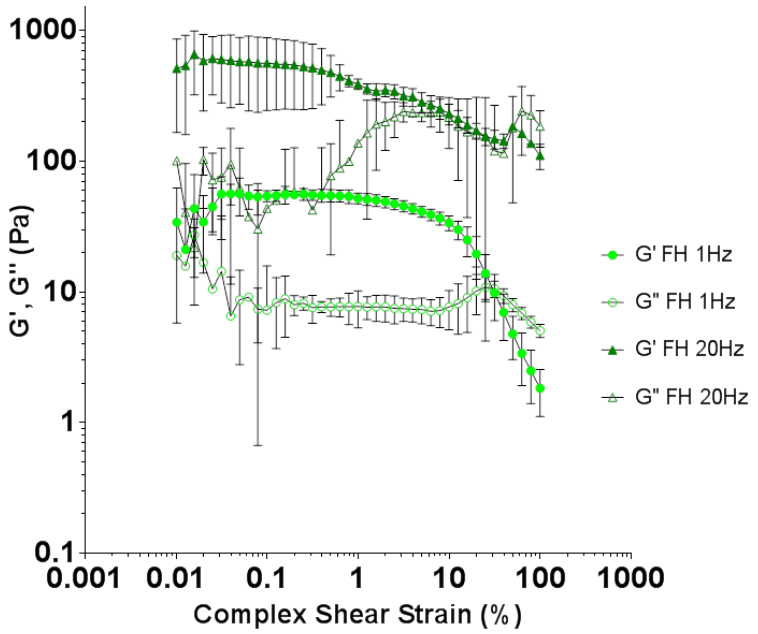


**Figure 3.17: Determination of LVER in FH (day 1) Gels at 1 Hz and 20 Hz.** Two amplitude sweeps were carried out on each sample at 1 Hz and 20 Hz, the amplitude sweeps were performed under shear strain controlled mode from 0.01 - 100 %. Data are n=4, error bars 95 % confidence limits. Shear gap height: 0.75

Due to the non-distinct plateau region a stress controlled amplitude sweep was performed at 1 Hz and 20 Hz to determine if the LVER could be determined at 20 Hz, this is shown in Figure 3.18. The curves at 20 Hz for the G' and G" functions are distorted; the G' and G" curves cross back and forth, indicative of plastic deformation. The rheological testing at 1 Hz appeared to be in the LVER due to the level plateaued appearance of the G' and G" curves.

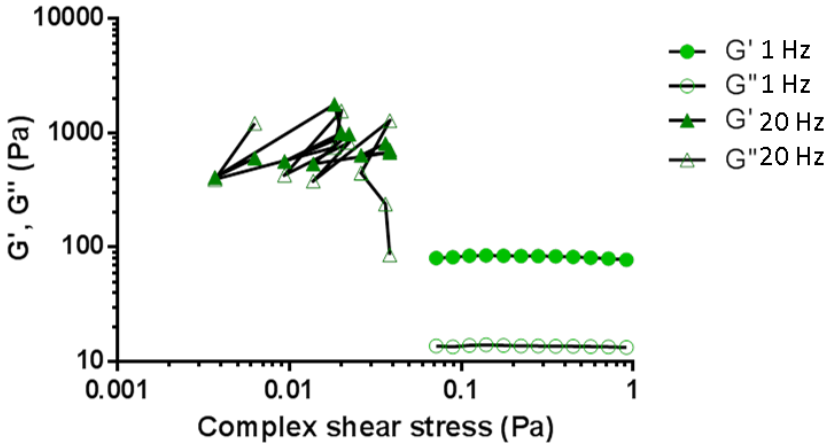


**Figure 3.18: Stress Controlled LVER Test in FH Gels at 1 Hz and 20 Hz.** Two amplitude sweeps were carried out for each sample at 1 Hz and 20 Hz, the amplitude sweeps were performed under stress controlled mode (0.05 - 10 Pa). Shear gap height 0.75 mm.

Due to the destructiveness of testing at a frequency of 20 Hz, a frequency sweep from 1 Hz to 20 Hz was performed on an FH gel at 1% shear strain to determine at what frequency the amplitude sweep was likely to be non-destructive at, and therefore a suitable frequency for LVER determination. The shear strain rate of 1 % was selected because the G' 1 Hz curve in Figure 3.17 plateaued at this strain rate. A frequency of 5 Hz was selected as a potential LVER parameter, as this was the last value in the plateau whereby there was noticeable deviation from the constant values, as shown in Figure 3.19.

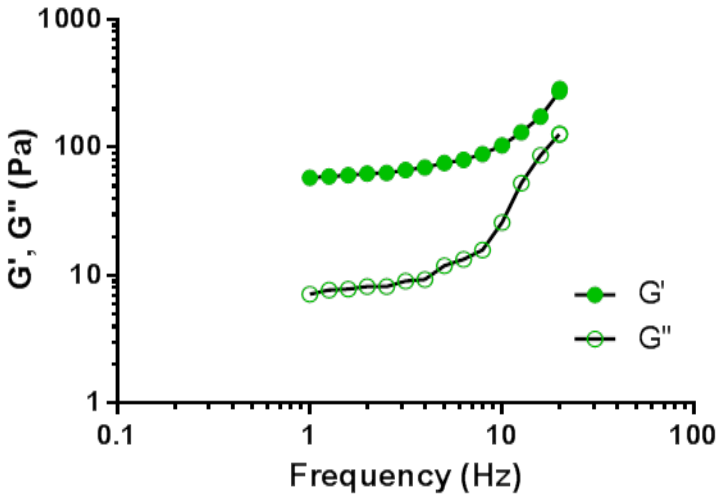


**Figure 3.19: Selection of Frequency Range for FH Gels.** A frequency sweep was performed on day 1, FH gel matrices at 1 % shear strain and a frequency range of 1 Hz to 20 Hz. Shear gap height 0.75 mm.

The two amplitude sweeps were repeated for FH gel matrices at 1 Hz and 5 Hz to determine the possible LVER. The amplitude sweeps were performed under shear strain controlled mode from 0.01 - 100 %. There was a visible plateau of the G' and G" curves at both frequencies, indicating that the LVER frequency parameters had been found for FH gels, as shown in Figure 3.20. The strain value selected from within the LVER at which the elastic modulus (G') and viscous modulus (G") were independent of strain amplitude at the two different frequency levels for FH gels was 1 % strain.

Interestingly, at frequencies of 1 Hz and 5 Hz the curves of the G" functions showed a distinct peak at approximately 20 % and 5 % shear strain respectively, whereby the curves showed a sudden increase and crossed over the G' curves, before decreasing again.

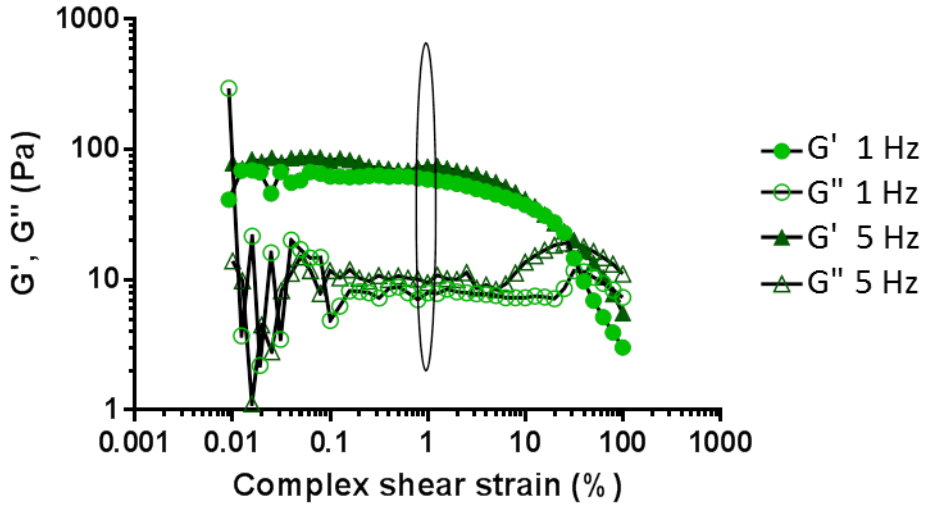


**Figure 3.20: Determination of LVER in FH (day 1) Gels at 1 Hz and 5 Hz.** Two amplitude sweeps were carried out for each sample at 1 Hz and 5 Hz, the amplitude sweeps were performed under shear strain controlled mode from 0.01 - 100 %. The area circled on the graph indicates the location of the strain value that was selected within the LVER. Shear gap height 0.75 mm.

Confirmation that the shear strain value of 1 % was within the LVER was determined by running a frequency sweep test at 1 % strain, as shown in Figure 3.21.

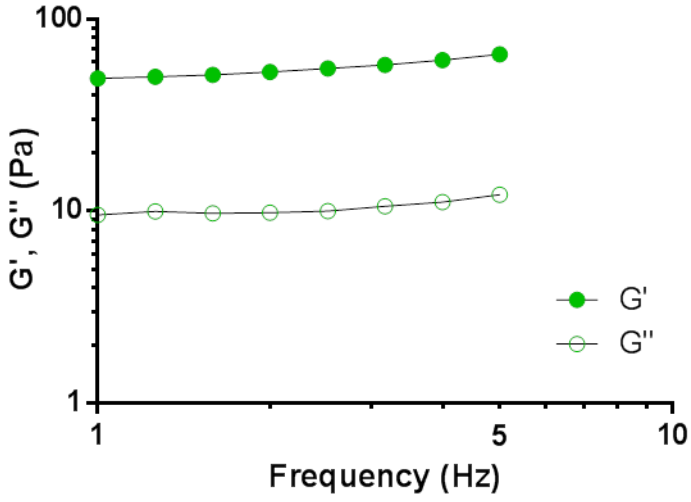


**Figure 3.21: Frequency Sweep of FH Collagen Gels from 1 Hz to 5 Hz at 1 % Shear Strain.** A frequency sweep was performed on day 1, FH gel matrices at 1 % shear strain and a frequency range of 1 Hz to 5 Hz to determine the highest and lowest stress values for the sample. Shear gap height 0.75 mm.

The frequency range related to the two frequencies selected for the initial LVER test (from 1 Hz to 5 Hz). The frequency sweep provided stress values for all of the frequencies tested. The stress values for the highest and lowest frequencies were:

$$\sigma 1 \text{ (1 Hz)} = 0.5101 \text{ Pa}$$
$$\sigma 2 \text{ (5 Hz)} = 0.6203 \text{ Pa}$$

A stress value range which broadly covered both of these values was selected as 0.05 - 5 Pa, therefore a stress controlled frequency sweep was run under the following conditions: 1 Hz, start stress: 0.05 Pa, end stress: 5 Pa and 5 Hz, start stress: 0.05 Pa, end stress: 5 Pa, this is shown in Figure 3.22. The stress values of the highest and lowest frequencies (σ1 and σ2) were found to be independent of stress amplitude (the curve is a plateau), this confirmed that rheological testing performed between 1 Hz and 5 Hz at 1 % strain was within the LVER for FH gels.

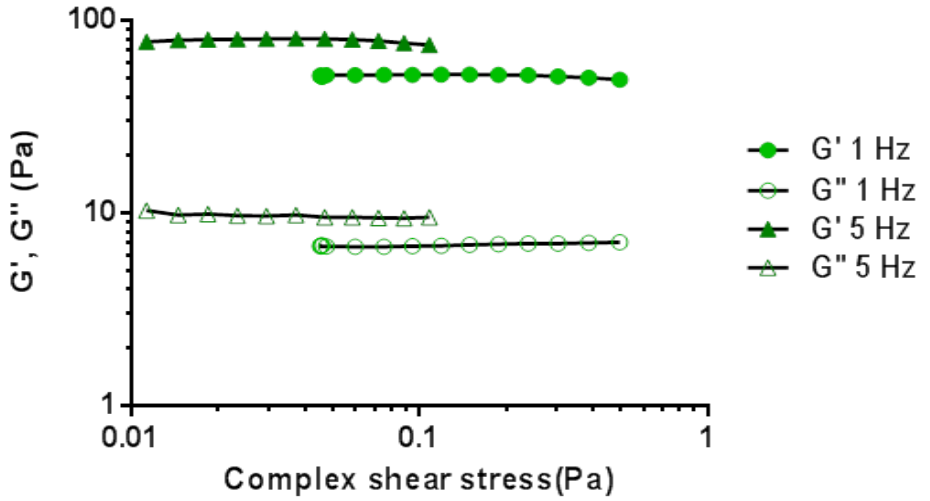


**Figure 3.22: Confirmation of LVER in FH (day 1) Gels at 1 % Strain.** Two amplitude sweeps were carried out for each sample at 1 Hz and 5 Hz, the amplitude sweeps were performed under stress controlled mode from 0.05 - 5 Pa. Shear gap height 0.75 mm.

### 3.6.4 Viscoelastic Properties of Collagen Gel Matrices within the LVER

Once a strain value within the LVER had been determined, the viscoelastic properties of the collagen gels could be determined using oscillatory frequency sweeps. Mechanical testing within the LVER means that the tests do not plastically deform the matrix.

#### 3.6.4.1 Viscoelastic Properties of FS Gels within the LVER

For the determination of the viscoelastic properties of FS gels at day 1 and day 5 (cell-seeded and acellular), the oscillatory frequency sweeps were performed from 1 Hz to 20 Hz at 0.3 % strain. For all FS gel matrices examined, the storage modulus (G') exceeded the loss modulus (G") as shown in Figure 3.23. The results were difficult to interpret using this graphical representation; however a large decrease in the storage modulus between days 1 and 5 was apparent in acellular gels. Cell seeded gels did not show such a large decrease in stiffness over time.

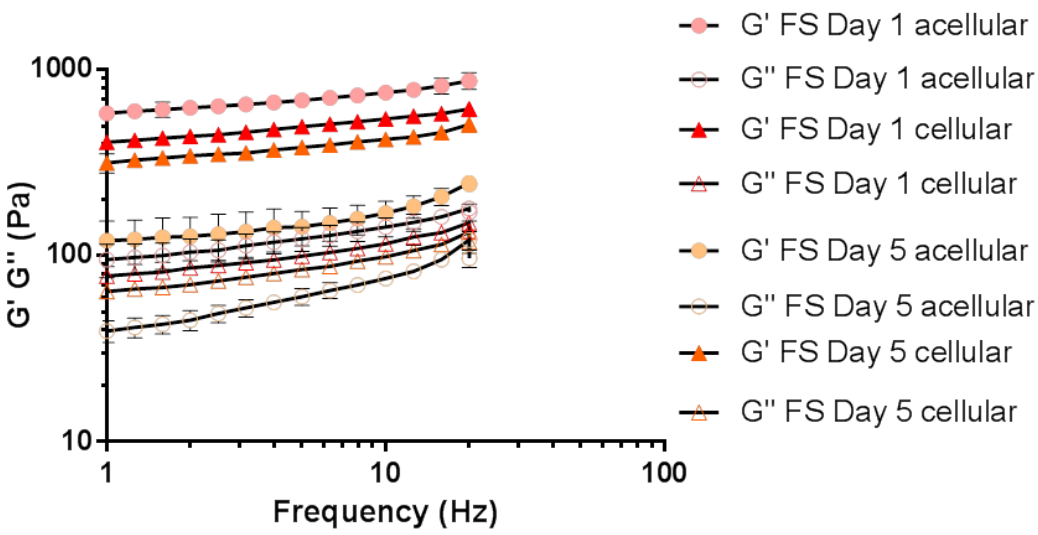


**Figure 3.23: Oscillatory Rheology of FS Gels at 0.3 % Shear Strain.** Oscillatory frequency sweeps between 1 Hz and 20 Hz at 0.3 % shear strain performed on 500 µl FS gels that were either seeded with one million primary astrocytes per gel, or acellular and tested after either one or five days in culture. Shear gap height 0.1 mm. All test conditions n=4, except acellular day 5, n=6. Data are mean plus 95 % confidence limits. All tests performed within the LVER at 37$^{o}$C, using a solvent trap.

### 3.6.4.2 Viscoelastic Properties of FH Gels within the LVER

For the determination of the viscoelastic properties of FH gels at day 1 and day 5 (cell-seeded and acellular), the oscillatory frequency sweeps were performed from 1 Hz to 5 Hz at 1 % strain. For all FH gel matrices examined, the storage modulus (G') exceeded the loss modulus (G'') as shown in Figure 3.24. Differences between test conditions were hard to visualise using this graphical presentation, therefore the results are presented in an alternative format, alongside the FS results for comparison in the following section.

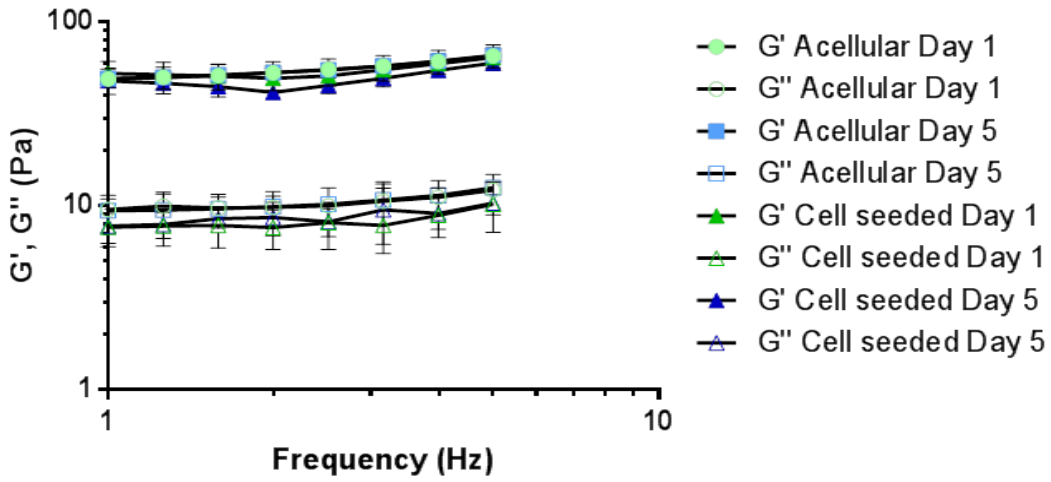


**Figure 3.24: Oscillatory Rheology of FH Gels at 1 % Shear Strain.** Oscillatory frequency sweeps between 1 Hz and 5 Hz at 1 % shear strain performed on 500 µl FH gels that were either seeded with one million primary astrocytes per gel, or acellular and tested after either one or five days in culture. Shear gap height 0.75 mm. Acellular day 1, n=6; acellular day 5, n=8; cell seeded day 1, n=6; cell seeded day 5, n=5. Data are mean plus 95 % confidence limits. All tests performed within the LVER at 37$^{o}$C, using a solvent trap.

### 3.6.4.3 Comparison Between Viscoelastic Properties of FH and FS, Cellular and Acellular Gel Matrices at Days 1 and 5 in Culture

Due to the difficulties of interpreting and comparing the graphical data of the FH and FS rheological gel at day 1 and day 5, in cell-seeded and acellular gels data (presented in Figures 3.23 and 3.24), the data were broken down into a set of comparisons at specific frequencies; 1 Hz, 5 Hz, 10 Hz and 20 Hz, the graphs are shown in Figure 3.25. Statistical analysis was performed on the following data only.

In terms of statistical significance, a one-way ANOVA with a Tukey's un-paired multiple comparisons test was performed to test the effect of each gel type against the other gel types at each frequency. The statistical results of the multiple comparisons test are presented in Table II.I within Appendix II. The ANOVA showed that there was not a statistically significant difference between any of the FH G' values ($p > 0.9999$); time in culture and the presence of cells had no effect on the viscoelastic properties of the FH collagen gels at 1 Hz and 5 Hz.

There was a significant difference between each of the FH gel conditions when compared to their corresponding FS G' value at 1 Hz and 5 Hz. FS gels were significantly stiffer; for example at day 1, the elastic modulus for FH cell-seeded gels was 55.19 Pa (± 8.8), whereas for FS cell-seeded gels at day 1, the elastic modulus was 409.78 Pa (± 14.4). A comparison of the mean elastic modulus values is presented in Table 3.3.

The ANOVA showed a statistically significant difference between each of the FS gel conditions when compared with each of the other FS conditions at all frequencies; 1 Hz, 5 Hz, 10 Hz and 20 Hz ($p < 0.0001$). Therefore, time in culture and the presence of cells had a significant effect on the stiffness of FS gels. Interestingly, in acellular and cellular gels, there was a significant decrease in stiffness over a 5 day period; the elastic modulus for FS acellular gels at day 1 was 585.03 Pa (± 26.2), whereas the elastic modulus for FS acellular gels at day 5 was 125.37 Pa (± 39.5).

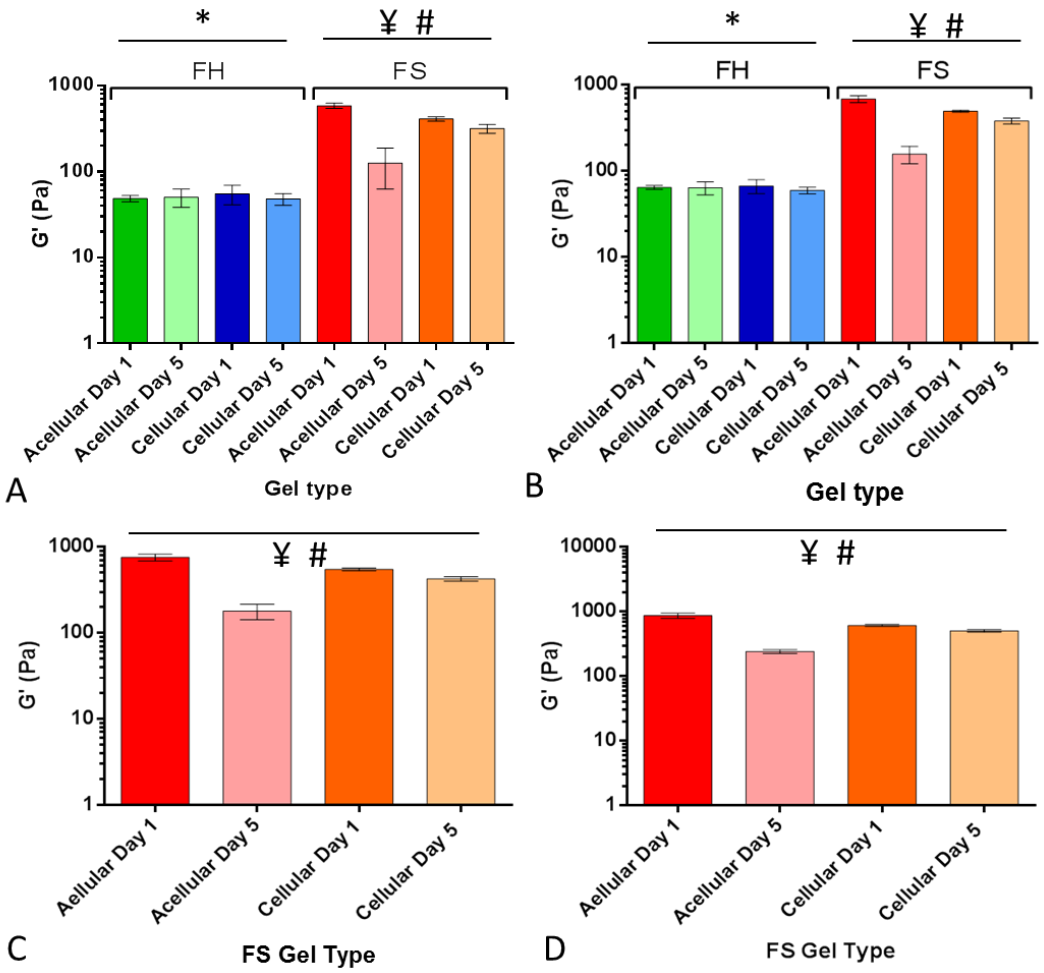


**Figure 3.25: Comparison of the Elastic Modulus for Cell-seeded and Acellular FH and FS gels at Day 1 and Day 5, at 1 Hz, 5 Hz, 10 Hz and 20 Hz.** Comparisons of elastic modulus (G') at specific frequencies, as determined by oscillatory frequency sweeps performed within the LVER (FH: 1 Hz to 5 Hz, at 1 % shear strain, FS: 1 Hz to 20 Hz, at 0.3 % shear strain). Graphs represent frequencies of 1 Hz (A), 5 Hz (B), 10 Hz (C), and 20 Hz (D). FH gels were not tested over 5 Hz. **FH:** shear gap height 0.75 mm, acellular day 1, n=6; acellular day 5, n=8; cell seeded day 1, n=6; cell seeded day 5, n=5. **FS:** shear gap height 0.1 mm, all test conditions n=4, except acellular day 5, n=6. All tests performed within the LVER at 37$^{o}$C, using a solvent trap on 500 µl collagen gels that were either seeded with one million primary astrocytes per gel, or acellular and tested after either one or five days in culture. Data are mean plus 95 % confidence limits. * = Sig. difference from equivalent FS value at same frequency; ¥ = Sig. difference from FS values at same frequency, different condition; # = Sig. difference from equivalent FS value at different frequency ($p < 0.0001$).

**Table 3.3: Viscoelastic Properties of Different Collagen Gel Matrices over 5 Days**

| Gel Type: | | Mean G' Value (Pa) at: | | | |
|---|---|---|---|---|---|
| | | 1 Hz | 5 Hz | 10 Hz | 20 Hz |
| Day 1 Acellular | FH | 48.66 | 64.86 | - | - |
| | FS | 585.03 | 688.79 | 756.25 | 874.00 |
| Day 1 Cellular | FH | 55.19 | 67.16 | - | - |
| | FS | 409.78 | 496.4 | 547.40 | 616.48 |
| Day 5 Acellular | FH | 50.54 | 64.14 | - | - |
| | FS | 125.37 | 157.92 | 179.38 | 243.22 |
| Day 5 Cellular | FH | 47.96 | 59.81 | - | - |
| | FS | 317.03 | 383.90 | 424.15 | 508.15 |

The values presented in Table 3.3 summarise the mean elastic modulus (G') for 500 µl type-I rat tail collagen (2 mg/ml in 0.6% (w/v) acetic acid) FH and FS gels, seeded with one million primary astrocytes per cell-seeded gel. Polymerisation of gels took place at neutral pH, 37$^{o}$C. The viscoelastic analysis took place using parameters within the LVER, which was determined separately for FH and FS gels; oscillatory frequency sweeps between 1 Hz and 5 Hz at 1 % shear strain and between 1 Hz and 20 Hz at 0.3 % strain were performed on FH and FS gels, respectively.

*Section B: Cell-Related Assessments of Astrocyte Culture within Different Matrix Environments*

## 3.7 Methods Specific to Section B

The experimental approach for this section involved production of astrocyte seeded type-I collagen gel matrices.

All assays were carried out using both cell seeded and acellular gels. The primary astrocyte cells which were seeded within the matrices were from cell cultures pooled from three to six separate animals to account for donor variability. Each sample was repeated at least three times accounting for variation in the assay reaction.

### 3.7.1 Analysis of Astrocyte Reactivity

The study of reactive astrogliosis often involves detection of the astrocyte marker, glial fibrillary acidic protein (GFAP), which is part of the cyto-architectural family of intermediate filament proteins (including nestin and vimentin). GFAP is up-regulated during reactive astrogliosis (Pekny and Pekna, 2004). The protein has been shown to be essential for reactive astrogliosis and glial scar formation to occur, but not essential for normal cell functions. GFAP is commonly detected via immunocytochemical techniques, whereby it is observed located along the large astrocyte processes and end feet; it is not present in the cell cytoplasm (Sofroniew and Vinters, 2010). Analysis of immunofluorescence staining for GFAP was performed to determine the extent of astrocyte activation.

The general immunostaining methods used in this study are described in Section 2.2.8.2.

#### 3.7.1.1 Image Processing and Image Analysis of Astrocyte Reactivity

The general imaging methods used in this study, with regard to capturing the images using a confocal microscope, are described in Section 2.2.9.

In order to successfully extract information from fluorescence images, the images can be processed, to overcome limitations in image quality and make content visible to the computer for extraction. The information can then be analysed into meaningful measurements such as shape and size descriptors.

The following steps were applied to each image in order to quantify the levels of fluorescence detected:

- Pre-processing (extracting the desired channel).
- Detection (application of a threshold to locate interesting features and refine the detection).
- Measurement (count pixels to determine areas).

These steps are described in greater detail schematically in Figure 3.26 and in the detailed description that follows.

The fluorescent microscopy images were multichannel images; each pixel value was determined from detected light that had been filtered according to its wavelength and each channel image represented detection at a pre-selected wavelength in order to detect light emitted from one type of bound fluorophore.

The process of detecting interesting image structures (objects) in an image is called segmentation. Manually selecting objects and/or manually selecting threshold values can allow the user to detect more or less of a particular feature, altering the interpretation of data. Using automated threshold detection methods reduces user bias (Bankhead, 2014). Thresholding enables the detection of objects by assuming there are only two classes of pixel in an image, based on pixel fluorescence intensity (hence the term, binary image). The two intensity classes were: (i) pixels that belonged to the object(s), and (ii) pixels that belonged to the background.

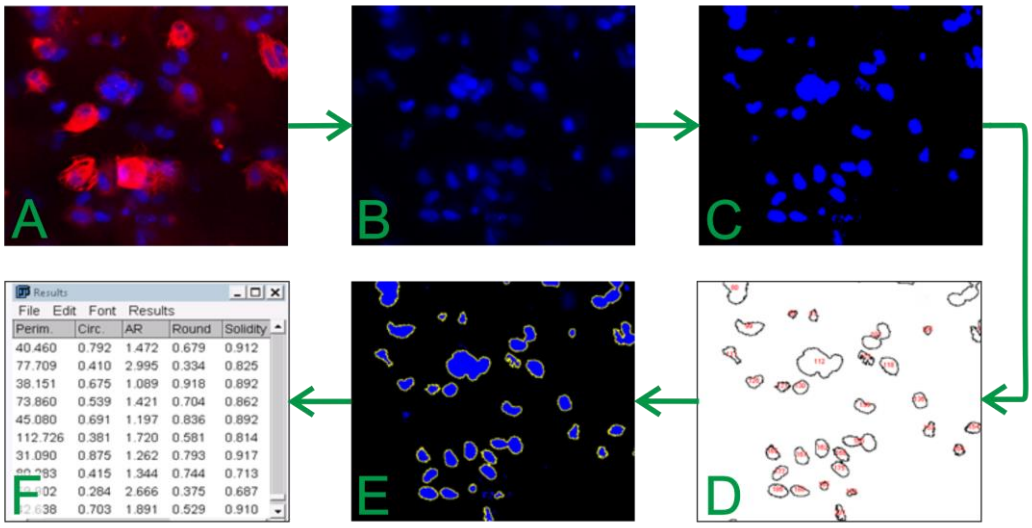


**Figure 3.26: Steps Used to Process and Analyse Fluorescent Images using FIJI.** The fluorescent composite image (A) was formed of two image channels; red, representing GFAP expression, and blue, representing the Hoechst nuclei stain. The first step was to extract the desired channel (B). A mathematical threshold was selected and applied, using the 'Auto Local Threshold' plugin on FIJI, creating a binary image (C). The 'Analyze Particles' FIJI menu option was used to detect and measure objects, each particle was assigned an identification number, shown in red (D). The measurements were then redirected to the original non-binary, single-channel image (E) in order to refine the detection. The measurement results were outputted to a summary table for analysis (F).

Segmentation was performed using the FIJI Is Just ImageJ (FIJI) software program. FIJI is based on the open-source software ImageJ, and is a program focused on biological-image analysis (Schindelin et al., 2012). The 'Auto Local Threshold' plugin was selected, rather than 'Auto Threshold', as local thresholding algorithms are suited to the detection of objects that appear on top of a background that varies in brightness, suffers from noise or contains overlapping cells (Deshmukh and Mankar, 2014; Phansalkar et al., 2011). A local threshold produces a binary image according to the local image characteristics within a radius (r) of each pixel, rather than a global calculation of the image (Bankhead, 2014). In particular, the images of fully stabilised gels could be 'noisy', due to the high proportion of cells and unavoidable

creases in the thin gels, causing some areas of the image to be out of focus. The same auto local threshold method was applied to each image.

The 'Phansalkar' Auto Local Threshold method was chosen due to its suitability for analysis of non-uniform staining (Deshmukh and Mankar, 2014; Phansalkar et al., 2011). The Phansalkar threshold method was calculated according to Equation 3.6, using the default suggested values for the constants *k*, *p*, *q* and *r*.

$$t = mean * \left[1 + p * exp(-q * mean) + k * \left((stdev/r) - 1\right)\right] \quad \textit{Equation 3.6.}$$

Where:

*t* = threshold;

*mean* and *stdev* are the local mean and standard deviation respectively;

the constants, *k*, *p*, and *r*, relate to values within the range of the standard deviation and mean. The constant *p* decides the magnitude to which the exponential term (*exp*) will affect the threshold. The default program settings for the constants were always used: *k* = 0.25; *p* = 0.5; *q* = 2; *r* = 10 (Phansalkar et al., 2011).

Following application of the Phansalkar method to create a binary image, the 'Analyze Particles' menu option was selected. 'Analyze Particles' automates the detection and measurement acquisition of objects in a binary image (Bankhead, 2014). The objects selected by the program were highlighted with an outline and labelled. The image was redirected to the original single-channel image. Although binary images can show the shapes of objects to be measured, generation of a binary image removes the information from the original image that provides meaningful measurements, such as the scale. Therefore the measurements for the Analyze Particles setting were redirected to the original image, creating a segmented image. An additional advantage of this step is that it is possible to run through each object selection in order to refine the selection. Object selection can be refined by various metrics, including size, circularity or fluorescence intensity. Objects with an area below 10 $\mu m^2$ were discounted when counting nuclei (Lundgaard et al., 2015). Deletion of an object selection, deleted the corresponding measurement from the results table. Manually

entering a selection added the measurement to the results table. An example of this refinement is shown in Figure 3.27.

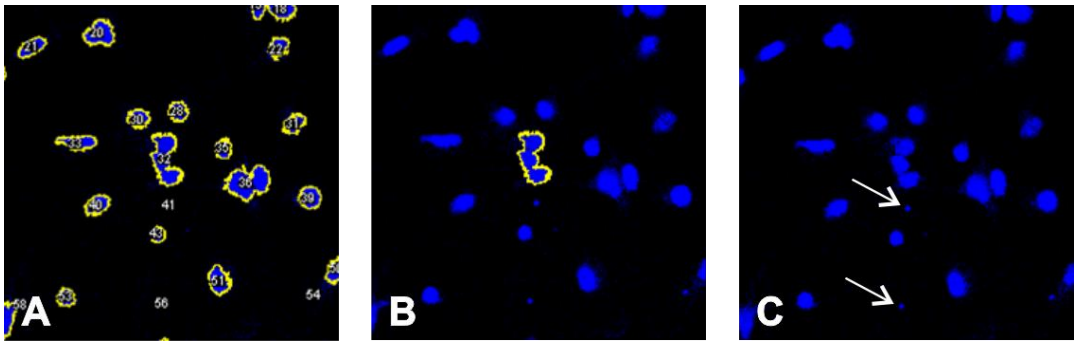


**Figure 3.27: Refinement of the Analyze Particles Object Selection.** The redirected image with each object (Hoechst stained nuclei) labelled and outlined (A). The FIJI program allows the user to move between views of selected (B) and unselected objects (C). In the example highlighted above, the program has combined three objects into one selection; the resolution between the objects is low, therefore causing the gaps between the nuclei to merge in places. The program has also selected objects 41 and 56 (A), highlighted by arrows in (C). These objects were below the chosen size threshold and were discounted.

#### 3.7.1.1.1 Morphological Indicators of Reactive Astrogliosis

The cellular reaction to CNS injury is characterised by changes to the morphological and molecular expression of astrocytes such that the cells become reactive astrocytes; a process known as reactive astrogliosis (Kimelberg and Norenberg, 1989). An increase in what is referred to as the ramification or stellate shape of astrocyte cells has been used as a morphological indicator of reactive astrogliosis (Burgos et al., 2007; East et al., 2009; Ridet et al., 1997; Wilhelmsson et al., 2004).

The cytoskeleton of astrocytes consists of actin, microtubules, and intermediate filaments, of which glial fibrillary acidic protein (GFAP) and vimentin are the most abundant examples (Pekny, 2001). Therefore, it is possible to relate the shape produced by detection of the GFAP-bound fluorophore to the shape of the cell (East et al., 2009).

As part of the process described in Section 3.7.1.1 in which the FIJI software program detected areas of the fluorescence microscopy images containing GFAP expression, it was possible to add a measurement to the 'Analyze Particles' process which would provide information describing the shape of the selected objects, thus the ramification of the astrocyte cells could be quantified.

The formula utilized for this analysis by the FIJI software is shown in Equation 3.7.

$$\frac{(4 \times \pi \times A)}{P^2} \qquad \text{Equation 3.7}$$

Where *A* is the cell area and *P* is the cell perimeter.

A perfectly spherical cell would have a value of 1, whilst smaller values would indicate progressively more irregularly shaped cells, thus providing an indicator of how rounded or ramified the cells were.

### 3.7.2 Determination of Cytokine Release

Astrocytes are known to secrete pro-inflammatory cytokines, such as interleukin-6 (IL-6), as part of their reactive response to SCI (Farina et al., 2007). Therefore increased concentrations of IL-6 in the culture medium may be indicative of increased astrogliosis of the cultured cells.

Following astrocyte (rat) cell culture in the FH and FS matrix environments for one day or five days (as described in Section 3.3.2), 200 µl of supernatant was harvested from the well of each replicate. The samples were transferred to a non-treated 96-well plate which was stored at - 70$^{o}$C until required. The samples were stored for up to 12 months and defrosted at room temperature when required.

An enzyme-linked immunoabsorbant assay (ELISA) was performed on the defrosted media samples as described in Section 2.2.10, in order to determine the levels of extracellular IL-6 that had been secreted by the cells.

### 3.7.3 Experimental Design

The aims and objectives of Part B of this chapter were investigated by experiments that were designed to minimise the use of primary astrocyte cells. The experiments were designed according to the process presented in Figure 3.28. The experimental methods displayed in Figure 3.28 are all described in more detail in the previous sections of this chapter.

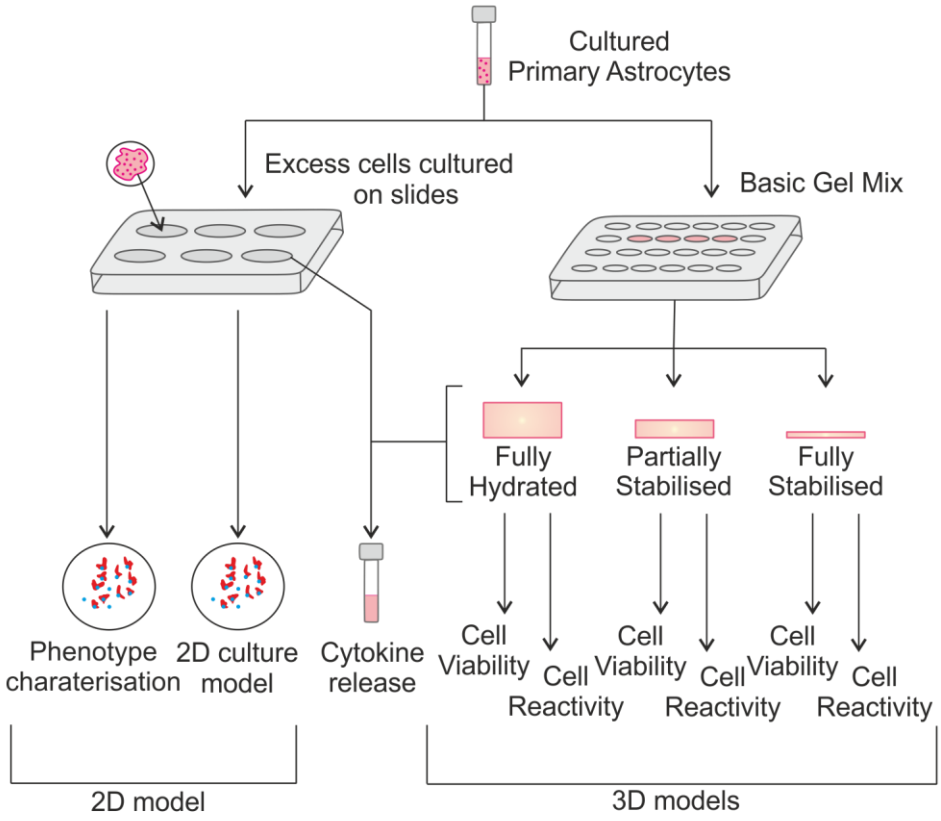


**Figure 3.28: Experimental Plan for the Completion of Chapter 3B.** In order to minimise wastage of primary astrocyte cells, 2D experiments were performed with the excess cells from the 3D matrix experiments. The 2D model additionally provided a means of checking the percentage of cells which stained positive for GFAP in order to characterise the phenotype of cultured cells. With each batch of gels that were produced, the batch was split into gels for cell viability analysis and cell reactivity analysis. (Note: The number of cells available dictated the number of gels that could be produced at one time. A minimum of n=3 for each batch and type of gel matrix that was produced were tested.) Media was sampled from 2D and 3D models to provide supernatant for analysis of cytokine release.

## 3.8 Results: Section B

### 3.8.1 Matrix Environment Effect on Cell Viability

Primary astrocyte cells were cultured within fully hydrated (FH) or fully stabilised (FS) gels for 1 or 5 days. The concentration of primary astrocytes within each cell seeded collagen gel was one million cells per 500 µl gel matrix. The Live/Dead assay determined the percentage of cell death within the matrix environments. Gels were stained with the Live/Dead solution (Section 2.2.8.1) and imaged using the defined imaging protocol (Section 2.2.9). The images were analysed as described in Section 3.3.5.1, five fields of view were analysed per gel.

Representative images of Live/Dead stained FH and FS gels are shown in Figure 3.29 at day 1 and day 5 in culture. The images were analysed using ImageJ software, to calculate the percentage cell death for each condition.

Cells cultured in FH gels showed very little difference in cell viability between time points. There were more dead cells present in the FS gels compared to FH gels at both time points. Due to the way the FS gels were formed, there were a higher number of cells per image in the FS gels, and the cells appeared more crowded together, in comparison to FH gels. FS gels were formed by removing the liquid component of FH gels, therefore the FS gels had the same number of cells per gel as the FH gels, but manipulated into a smaller area.

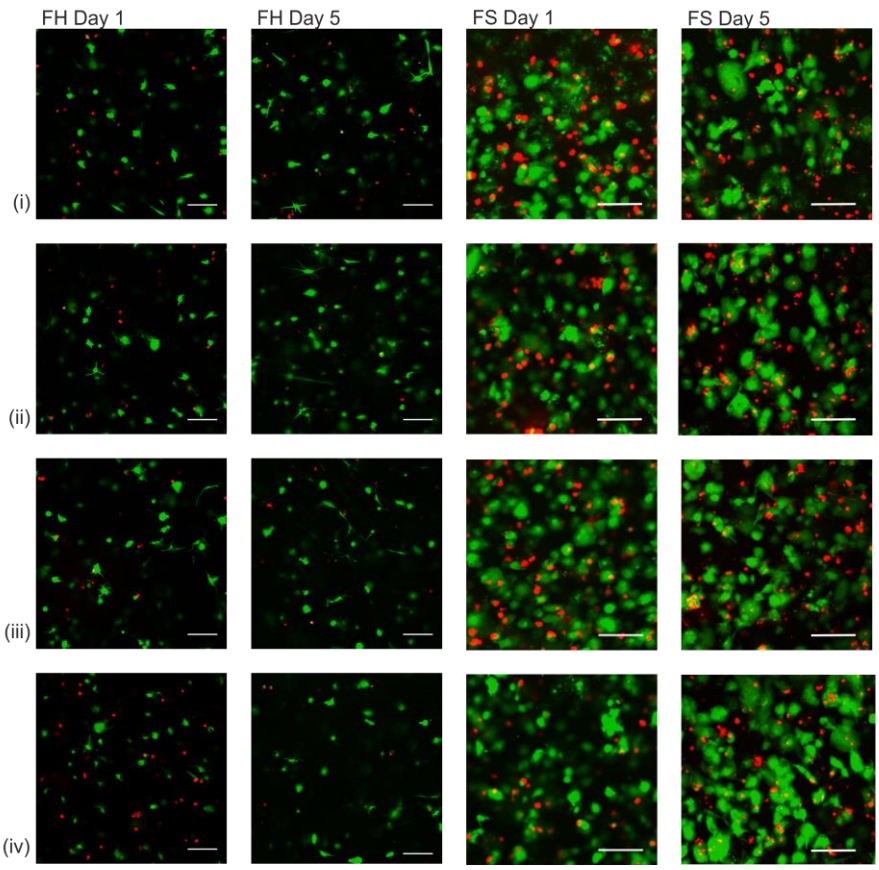


**Figure 3.29: Viability of Primary Astrocytes Seeded in Fully Hydrated (FH) and Fully Stabilised (FS) Gel Matrix Environments.** Images of Live/Dead stained gels whereby cells stained red with ethidium homodimer (EH) were dead and cells stained green with calcein AM (CAM) were alive. Gels were cultured for either 1 or 5 days before Live/Dead staining. Images (i) to (iv) are representative images of different gel repeats of the same gel type and culture length to highlight the reproducibility of the method. Scale bars represent 100 μm.

The percentage of cell death in FH and FS gel matrix environments at day 1 and day 5 in culture is shown in Figure 3.30. The percentage cell death is lower in FH gels in comparison to FS gels at both day 1 and day 5. The percentage death decreases from day 1 to day 5 within FH gels. The percentage cell death increases from day 1 to day 5 within FS gels.

In terms of statistical significance, to test the effect of matrix environment and culture length on % cell death, measurements were the raw percentage data were arcsine

transformed before analysis using a 2x2 independent ANOVA. The first factor was matrix environment (FH, FS) and the second factor was the culture length (day 1, day 5). The ANOVA revealed that the matrix environment had a significant impact on % cell death ($p<0.001$); a higher % cell death was observed in FS gels compared to FH gels. The main effect of the culture length was significant $p<0.01$; cell death increased over time in culture. The interaction between the matrix environment and the culture length stage was also significant $p<0.001$. In this case, there was no need for follow-up tests regarding the nature of the interaction because each significant effect only had two levels. A Tukey post-hoc test revealed that FS gels had significantly increased % cell death (31.9±1.6) compared to FH matrix environments (24.08±1.8) ($p<0.001$) at day 1 and at day 5 the % cell death was significantly higher (45.3±1.3) compared to day 1 within FS gels (31.9±1.6) ($p<0.01$) (mean ± standard deviation).

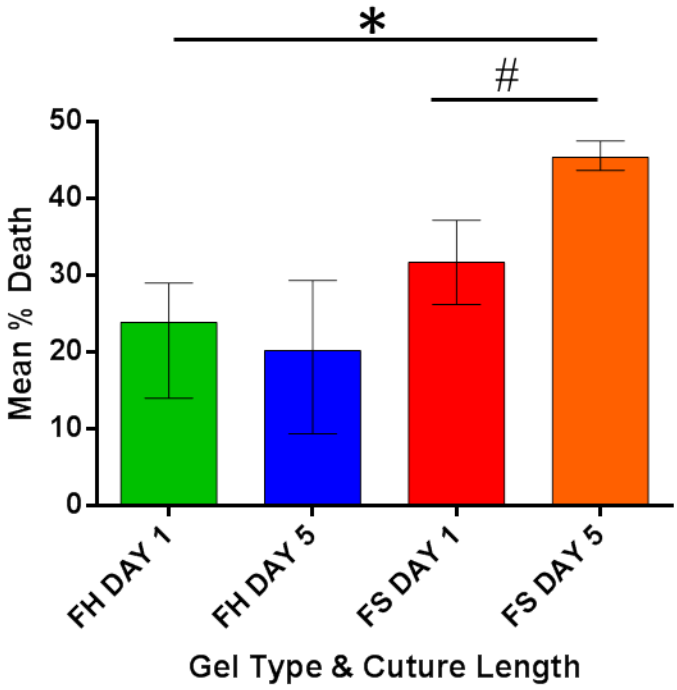


**Figure 3.30: Percentage Death of Primary Astrocytes Seeded in Fully Hydrated (FH) and Fully Stabilised (FS) Gel Matrices after 1 or 5 Days in Culture.** Two-way ANOVA with post-hoc Tukey test; *$p<0.001$ FS vs FH, #$p<0.01$ DAY 5 v DAY 1 in FS gels. Data are shown as the mean (n=5) ± arcsine transformed error bars.

### 3.8.2 Auto Local Threshold Method Selection

The Phansalkar method was selected as the Auto Local Threshold for image analysis of immunohistochemical staining for its suitability for analysis of non-uniform staining. Some of the available Auto Local Threshold methods are shown in Figure 3.31.

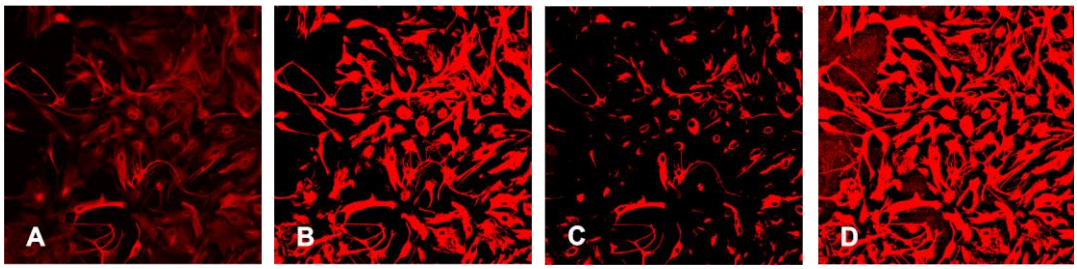


**Figure 3.31: Comparison of Several FIJI Auto Local Threshold Methods.** Original fluorescence image (A) showing astrocyte cells stained for GFAP (red); binary image resulting from thresholding using the Phansalkar method (B); binary image resulting from thresholding using the Bernsen method (C); and binary image resulting from thresholding using the Median method (D).

As shown in Figure 3.31, Phansalkar provides the optimal method in this comparison because the cellular projection detail has not been lost. Capturing all of the detail of the cellular projections was important for the morphological analysis of reactivity. The Bernsen method has rejected pixels, losing much of the detail of cellular projections, in particular the finer projections. The Median method resulted in too many background pixels being picked up as foreground objects; this increased the size of the objects in the image and created noise. The image analysis methods which were used to quantify GFAP expression, focussed on shape descriptors such as cell area and circularity. The intensity of fluorescence was not analysed, therefore the creation of a binary image whereby all pixels represented either an object for analysis (e.g. red pixels) or did not represent an image (e.g. black pixels), resulting in all cells being represented as a solid object, was suitable (see Figure 3.31 (A) cells compared to Figure 3.31 (B) cells).

### 3.8.3 Total Cell Number Per Field

The total number of cells per field was used to calculate the area of GFAP expression per cell. This calculation was based on counting nuclei positively stained with Hoechst. The Hoechst stain does not allow discrimination between live and dead cells. The percentage change in total cells per field was normalised to the respective day 1 total cells per field in order to correct for the difference in cells/field between FS and FH gels.

The total number of cells per field showed a non-significant percentage increase between day 1 and day 5 for FH gel matrix environments. The total number of cells per field showed a non-significant percentage increase between day 1 and day 5 for FS gel matrix environments. This is shown graphically in Figure 3.32.

In terms of statistical significance, to test the effect of matrix environment and culture length on the total number of cells per field, measurements were analysed using a one way independent ANOVA. The ANOVA showed no significant effect in the percentage increase of cells between matrix environments ($p>0.05$).

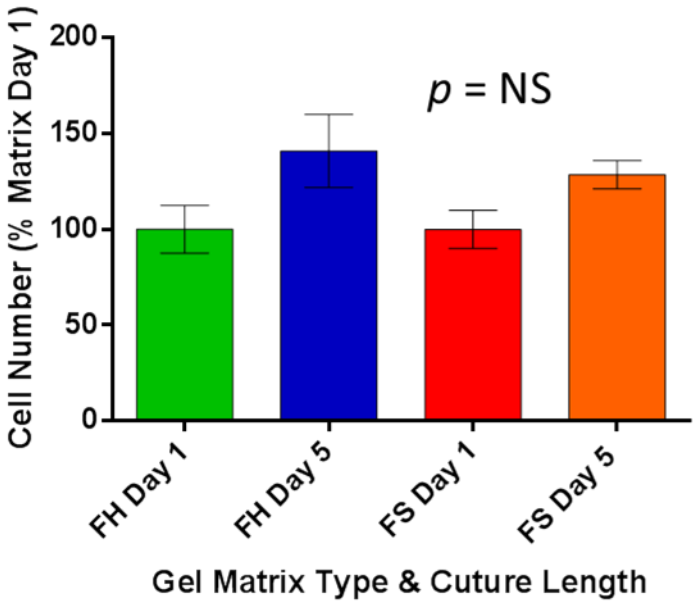


**Figure 3.32: Total Cell Number per Image Field.** The total number of primary astrocytes detected in Fully Hydrated (FH) and Fully Stabilised (FS) gel matrices after 1 or 5 Days in culture. The data were normalised to the respective day 1 total, in order to highlight the percentage increase of cells over time. One-way independent ANOVA showed no significant difference between matrix types (p=NS). Data are shown as the mean (FH day 1, n=5; FH day 5, n=6; FS day 1, n=3; FS day 5, n=6), ±95 % confidence intervals.

### 3.8.4 Effect of Different Matrix Environment on Astrocyte Phenotype

Primary astrocyte cells were cultured within FH or FS gels for 1 or 5 days. The concentration of primary astrocytes within each cell seeded collagen gel was one million cells per 500 µl gel matrix. The gels were fixed and GFAP was detected using immunocytochemical techniques, as a way of determining the astrocyte phenotype associated with reactive astrogliosis. Gels were imaged using the imaging protocol (Section 2.2.9); five fields of view were imaged per gel. The images were analysed as described in Section 3.7.1.1.

### 3.8.4.1 Effect of Matrix Environment on Expression of GFAP

Representative images of immunocytochemical staining for GFAP in FH and FS gels are shown in Figure 3.33 at day 1 and day 5 in culture. The images were analysed using FIJI software, to calculate the area of GFAP expression for each condition. The expression of GFAP was quantified on the basis of the mean area of GFAP-immunofluorescence per cell in the field of view.

Cells cultured in FH gels showed very little difference in the mean area of GFAP expression between time points. There were a higher number of cells per image in the FS gels, and the cells appeared more crowded together. More GFAP expression was visible in the FS matrix environments at both time points, in comparison to FH matrix environments. In addition, cells appeared ramified in the FS gels; many filaments extended from the cells and overlapped within clusters of cells. All data were normalized to the number of cells/field in order to correct for the difference in cells/field between FS and FH gels, and also to account for any potential cell proliferation over the 5 day time period of the experiment. Cells cultured in 2D monolayer as a control showed a high level of reactivity, with almost all cells presenting as highly ramified cells with overlapping GFAP positive filaments.

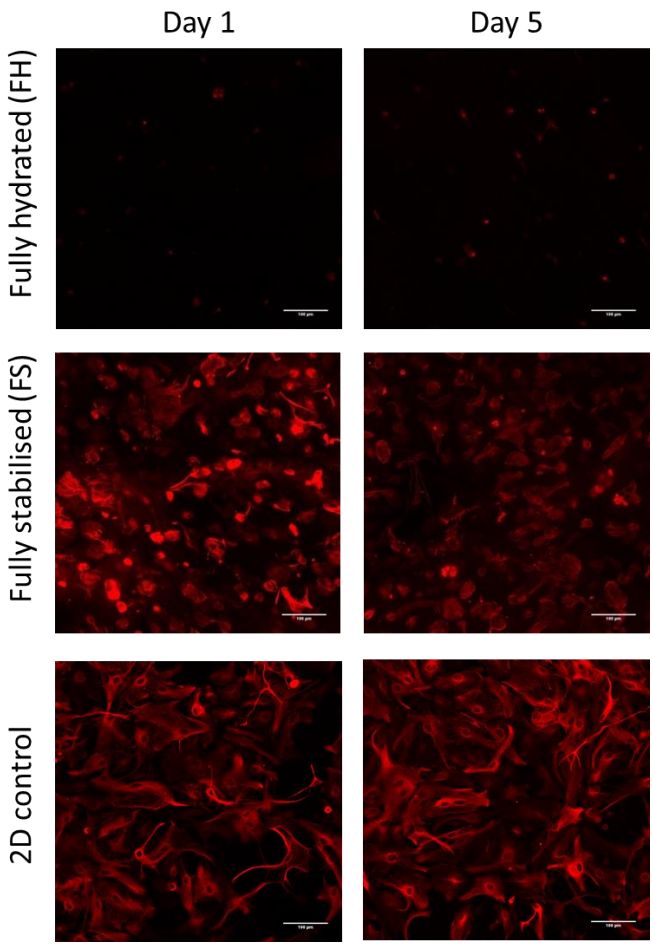


**Figure 3.33: Immunofluorescence of Reactivity Marker, GFAP within Fully Hydrated (FH), Fully Stabilised (FS) Gel Matrix Environments.** Astrocytes in FS gels expressed increased levels of GFAP (red) in comparison to FH gels. 2D astrocyte cultures on PDL-coated coverslips were used as the positive control for reactive astrogliosis. Scale bars 100 μm.

The area of expression per matrix environment, normalised to cell number is shown in Figure 3.34. The area of GFAP expression per cell was lower in cells cultured in FH gels at both time points, in comparison to cells cultured in FS gel environments. In terms of statistical significance, to test the effect of matrix environment and culture length on the area of GFAP expression per cell, measurements were analysed using a 2x2 independent ANOVA with Tukey post-hoc. Cells in the FS matrix environments expressed a significantly increased area of GFAP per cell ($134.37 \pm 45.6$ $\mu m^2$) compared to cells in the FH matrix environments ($50.42 \pm 21.3$ $\mu m^2$) ($p<0.001$). Within both gel matrix environments, the area of GFAP expression decreased over the

5 day culture period, however this was not significant. The area of GFAP expression per cell was significantly higher when cells were cultured in a 2D environment in comparison to a 3D environment ($p<0.001$). The cells within the 2D control expressed significantly increased areas of GFAP expression ($827.99 \pm 63.16\ \mu m^2$) in comparison to cells within FS ($134.37 \pm 45.6\ \mu m^2$) and FH ($50.42 \pm 21.3\ \mu m^2$) gel matrix environments ($p<0.001$) (mean ± SEM).

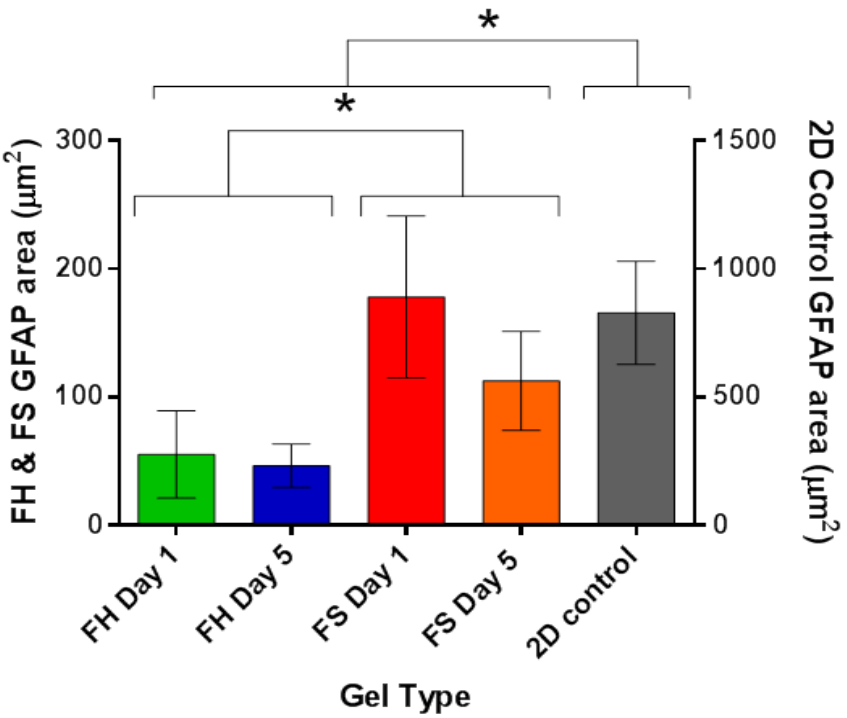


**Figure 3.34: Area of GFAP Immunofluorescence per Cell within Fully Hydrated (FH), Fully Stabilised (FS) Gel Matrix Environments.** The area ($\mu m^2$) of GFAP fluorescence detected per astrocyte cell in each field of view was significantly higher in FS gels in comparison to FH gels. 2D astrocyte cultures on PDL-coated coverslips were used as the positive control for reactive astrogliosis. Two-way ANOVA with post-hoc Tukey test; *$p<0.001$ FS vs FH, *$p<0.001$ 2D control v FH, *$p<0.001$ 2D control v FS. Data are shown as the mean ± 95 % confidence intervals FH day 1, n=5, FH day 5, n=6, FS day 1, n=3, FS day 5, n=6, 2D control, n=4.

### 3.8.4.2 Morphological Indicators of Reactive Astrogliosis

Primary astrocyte cells were cultured within FH or FS gels for 1 or 5 days. The concentration of primary astrocytes within each cell seeded collagen gel was one million cells per 500 µl gel matrix. The gels were fixed and immunocytochemically stained as a way of determining the expression of glial fibrillary acidic protein (GFAP) within the matrix environments. Five fields of view per gel were imaged using the imaging protocol (Section 2.2.9). The images were analysed as described in Section 3.7.1.1 in order to calculate the circularity of the astrocyte cells. Cells that were circular had a value close to 1, whereas irregularly shaped cells, such as ramified astrocytes, had smaller values, close to 0.

The circularity of the cells did not appear to change over time within the different matrix environments. The cells in the FS gels were more ramified than the FH gels. The cells cultured within FS gels showed a similar level of ramification compared to those in the 2D monolayer controls. Representative images of astrocyte cell shape within the different matrix environments are shown in Figure 3.35.

As shown in Figure 3.36, GFAP-positive cells cultured within FH gel matrices tended to be more circular than ramified in appearance. Conversely, GFAP-positive cells cultured within FS gel matrices and in 2D monolayer culture tend to be more ramified in appearance than circular. The length of time in culture did not seem to affect the circularity of cells cultured within gels of the same type.

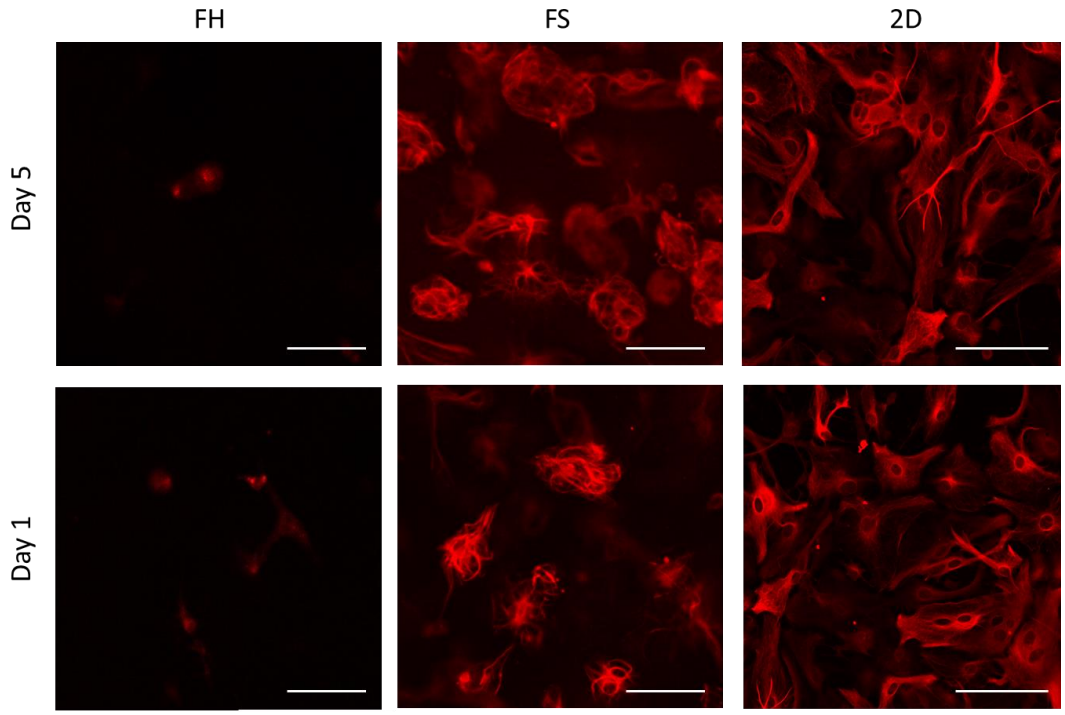


**Figure 3.35: Representative Images of GFAP Immunofluorescence Highlighting the difference in Cell Shape within Fully Hydrated (FH), Fully Stabilised (FS) Gel Matrix Environments.** The ramification of astrocyte cells, as detected using GFAP fluorescence (red) was higher in FS gels in comparison to FH gels. 2D astrocyte cultures on PDL-coated coverslips were used as the positive control for reactive astrogliosis represented by cellular ramification. Scale bars represent 50 μm for FH and FS images and 100 μm for 2D control.

In terms of statistical significance, to test the effect of matrix environment and culture length on the circularity of GFAP-positive astrocyte cells, measurements were analysed using a non-parametric, unlinked, multiple comparison, Kruskal-Wallis test. The Kruskal-Wallis test was used following the results of a D'Agostino & Pearson omnibus normality test, in which each matrix condition was found not to be normally distributed ($p<0.001$). The Kruskal-Wallis test showed a significant difference between all matrix environments in comparison to the control; the cells were significantly more ramified in 2D matrix environments in comparison to FH environments at both time points ($p<0.001$), the cells were also significantly more ramified in 2D matrix environments in comparison to FS environments at both time points ($p<0.001$). There was a significant increase in ramification in cells cultured in

FS environments in comparison to FH environments at both time points ($p<0.001$). The culture length had a significant effect on the circularity of cells between factors, but not between matrix environments of the same type; FH day 1 v FS day 5 ($p<0.001$), FH day 5 v FS day 1 ($p<0.001$), FH day 1 v FH day 5 ($p>0.05$), FS day 1 v FS day 5 ($p>0.05$).

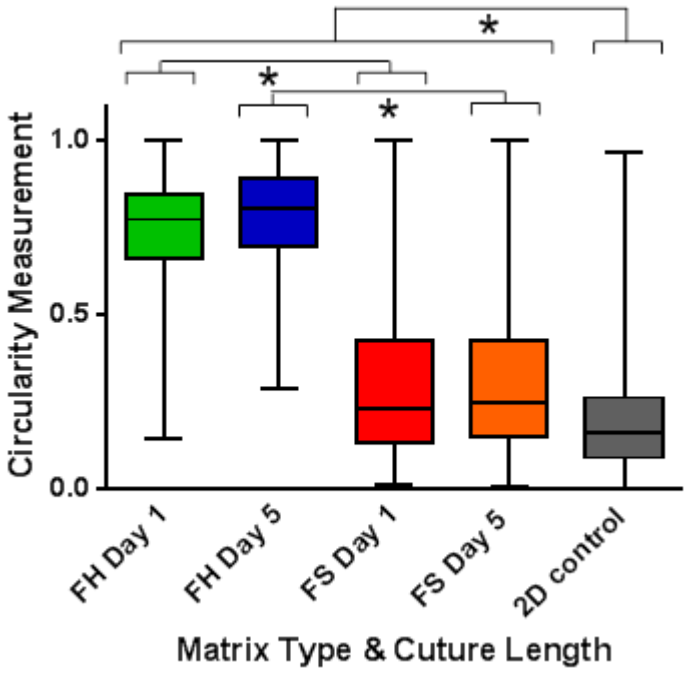


**Figure 3.36: Circularity of Primary Astrocytes within Fully Hydrated (FH) and Fully Stabilised (FS) Gel Matrix Environments.** The shape of primary astrocytes was determined by analysing the shape of GFAP fluorescence per cell in each field of view. Ramification (reactivity) was significantly higher in FS gels in comparison to FH gels at day 1 and day 5. 2D astrocyte cultures on PDL-coated coverslips were used as the positive control for reactive astrogliosis; 2D cultures were significantly more ramified than all test conditions. Kruskal-Wallis test; *$p<0.001$ FS day 1 vs FH day 1, *$p<0.001$ FS day 5 vs FH day 5, *$p<0.001$ 2D control v all test conditions. FH day 1, n=5, FH day 5, n=6, FS day 1, n=3, FS day 5, n=6, 2D control, n=4.

### 3.8.4.3 Extracellular Release of Cytokines

Supernatants were collected from each gel type at either day 1 or day 5 in culture in order to investigate the extracellular release of the rat interleukin-6 (rIL-6) cytokine. Controls included supernatant from astrocytes in 2D monolayer culture whereby high levels of reactive astrogliosis were visible following immunocytochemical staining for GFAP.

An Enzyme Linked Immunoabsorbant Assay (ELISA) was performed according to the protocol in Section 2.2.10.

The standard curve was plotted according to the readings from the ELISA kit standards. The amount of rIL-6 in each sample could not be determined by extrapolating the absorption readings against the readings of the standard curve because the level of rIL-6 detected was below the lowest reading on the standard curve. Despite a visible colour change occurring within all sample wells, the ELISA was not sensitive enough to detect IL-6 in the supernatant.

The standard curve which was produced as a result of this assay is shown in Figure 3.37.

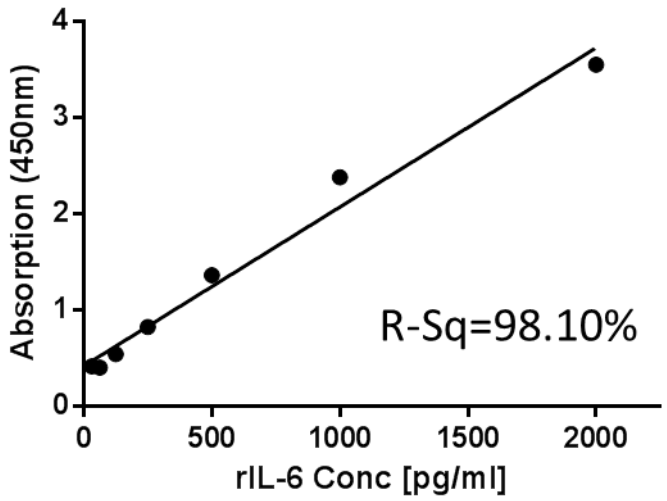


**Figure 3.37: Standard Curve for Rat Interleukin-6 ELISA.** The standard curve produced using the ELISA kit rat interleukin-6 (rIL-6) standards.

## 3.9 Discussion

The aim of this part of the study was to determine the mechanical properties of different collagen gel matrix environments over a five day period, and to relate the mechanical properties of the gels to the phenotypic changes observed in cells cultured within gels of differing mechanical properties, in order to investigate the suitability of the matrix environments as a 3D *in vitro* model to compare cellular responses to mechanical loading with *in vivo* models of SCI.

Following a spinal cord injury (SCI), the damaged tissue undergoes an injury response termed reactive gliosis (Fawcett and Asher, 1999). After initial cell death caused by the physical impact of the injury, the cells of the spinal cord undergo a series of reactive changes which can be both neuro-protective, and neuro-inhibitory. The consequence of reactive gliosis is often the formation of a glial scar. The glial scar is a physical and physiological barrier to regeneration of the spinal cord tissue (Silver and Miller, 2004), which often results in compromised neural function for the affected individual.

The glial scar forms over several days, reaching maturity at about two weeks post-injury (Anderson et al., 2016; Faulkner et al., 2004; Herrmann et al., 2008; Wanner et al., 2013). The main cells involved in the scar formation are astrocytes, oligodendrocytes and microglia. The final structure of the glial scar is predominantly made up of a dense network of overlapping processes of ramified, hypertrophic astrocytes (Fitch and Silver, 2008; Silver and Miller, 2004; Wanner et al., 2013).

The glial scar is not just a physical barrier (Fitch and Silver, 1997); therefore investigations into the molecular and cellular interactions that inhibit regeneration are important research directions which may help to answer questions regarding the causes of glial scar formation, the inhibitory nature of the glial scar, and if the glial scar be manipulated such that functional axonal regeneration can occur (Fawcett and Asher, 1999).

The glial scar is formed of several different cell types such as neurons, astrocytes, oligodendrocytes, and microglia. For the purposes of developing a preliminary model for the investigation of reactive astrogliosis, it was deemed appropriate to seed the gel matrix with only one cell type; astrocytes. The study of a single cell type allowed for simplification of the model whereby it was possible to study the direct relationship between the matrix environment and astrocytes, without adding the additional layer of complexity of cell-cell interactions.

The simplicity and adaptability of the gel matrix formation would allow future studies to incorporate several different cell types within the matrix; cells can be added during gelation such that they are evenly distributed throughout the matrix (as was the case in this study), and/or they can be seeded on a surface of the gel, and allowed to migrate into the gel.

Whilst there are many positives to using *in vitro* models as a method of simplifying an investigation in comparison to *in vivo* models, there are limitations to the usefulness of 2D models due to the highly reactive nature of astrocytes cultured in this way. The level of reactivity in 2D models inhibits the study of further astrocyte activation as the base line levels of astrocyte markers are too high (East et al., 2009). The high level of detectable reactivity was the reason that 2D monolayer culture was selected as a control for this study. Therefore the design and utilisation of a 3D *in vitro* environment, similar to the model developed in this study, which aims to maintain astrocytes in a less reactive state than a comparative 2D model, is advantageous.

The study was initially designed to have three different 3D gel matrix environments that would each have different mechanical properties due to the degree of stabilisation the matrix had received. Reactive astrogliosis was quantifiable through detection of reactivity markers and cytokines. It was thought that the change in matrix stiffness due to differing degrees of gel stabilisation, in addition to other factors, would cause an increase in detectable reactivity. This was linked to an observation by East et al. (2009) whereby astrocytes at the edges of 3D collagen gel matrices showed elevated GFAP levels and increased ramification where the cells were in contact with the stiff plastic of the culture wells, at the edges of the gels (East et al., 2009). However, the

method of producing a partially stabilised (PS) gel was not reproducible and communication directly with the absorber manufacturer stated that the absorption time of their protocol should not be adapted. It was decided to continue with the gel matrix model using a non-stabilised, fully hydrated (FH) gel matrix environment and a fully stabilised (FS) gel matrix environment.

In addition to the problems associated with reproducibly producing a PS gel matrix, there were also problems encountered quantifying the degree of partial stabilisation. Quantification of PS gel height was necessary due to the variation in liquid absorption that would occur when applying the absorber for a comparatively short time (20 seconds for PS, 15 minutes for FS). Despite the use of several different methods for measuring gel height, such as digital callipers, a shadowgraph and photography, these methods either involved exposing the gel to a non-humidified environment (callipers, shadowgraph, photography), which resulted in the evaporation of the liquid component of the matrix, or did not achieve sufficient resolution to allow accurate measurements (photography and callipers). Methods used in the literature to quantify the level of stabilisation have included weighing gels before and after application of absorbers (Braziulis et al., 2012; Brown et al., 2005), however again this would have necessitated the use of a non-humidified environment and similar problems with evaporation would have been encountered.

The viability of cells within the different matrix environments was important because the model would be of most use as a research tool if cells could be maintained in culture for several days and preferably up to two weeks, in order to study the effects of astrogliosis over time (East et al., 2009). The length of culture time necessary would depend on the desired outcome of the model; future development of this model might include study of the interaction between astrogliosis and myelination of axons by oligodendrocytes. Oligodendrocytes typically need to be cultured for at least 30 days before substantial myelination occurs (Barres, 2008).

For this study, the models were analysed after one or five days in culture. The addition of a longer time frame would have been useful, however due to the time restraints and primary astrocyte availability; this was not possible within the time

frame of this study. The five day time frame was selected for comparison to the results of the TGF-β1 induced astrogliosis model used by East et al (2009) which utilised the equivalent of the FH gels used in this study.

The mechanical testing of the viscoelastic properties of the collagen gels found that in FH and FS gel matrices, the elastic modulus (G') was greater than the viscous modulus (G") which suggests that the solid-properties of the gel were dominant over the liquid properties; both types of collagen gel matrices behaved as viscoelastic solids. Gels typically exhibit elastic behaviours due to the physical network of fibrils. The curves for the G' and G" functions showed almost parallel lines throughout the entire frequency range tested (1 Hz - 5 Hz (FH) and 1 Hz - 20 Hz (FS)), showing only a slight increase with frequency. This behaviour is typical of gel-like structures under oscillatory rheological testing (Mezger, 2006).

The loss modulus (G") of a sample represents the energy lost due to friction; therefore when the linear viscoelastic region (LVER) is exceeded, there is typically a distinct peak in the G" curve (Mezger, 2006). The cross-over point between the G' and G" curves represented a strain dependency of the elastic modulus and “softening” under higher deformation, characterised by the reduction in the elastic modulus (Taheri and Samyn, 2016). A G" peak was present in the FH frequency sweep; the G" peak appeared after the G' curve deviated from the plateaued region, this indicated that the collagen fibrillary network structure had not been completely deformed until the G" curve crossed the G' curve (Mezger, 2006). A G" peak was not observed in the FS frequency sweep, this was probably due to the stabilisation induced increase in collagen fibre density and reduced fluid content causing an increase in the maximum deformation rate.

The testing parameters were determined using frequency sweeps and strain- and stress-controlled amplitude sweeps. The LVER parameters for FH gels corresponded to those found by other rheological studies of non-stabilised collagen gels; 1 Hz, 1 % shear strain (Bailey et al., 2011; Kreger et al., 2010). Although several studies report that stabilisation of gels improved the mechanical properties and handling of the collagen gels, the mechanical properties were not reported (Braziulis et al., 2012;

Cheema and Brown, 2013; Engelhardt et al., 2010; Levis et al., 2012; Mi et al., 2010; Serpooshan et al., 2011). The studies which report mechanical properties of stabilised gels used different testing methods (tensile) and therefore did not investigate the LVER (Brown et al., 2005; Hadjipanayi et al., 2009). Therefore no comparisons could be drawn between the LVER parameters used in this study.

FS gels were significantly stiffer than the FH gels in all conditions tested ($p < 0.0001$): in gels seeded with astrocytes, acellular gels and at day 1 and day 5. The increased mechanical integrity of the FS gels could overcome some of the mechanical limitations involved in the handling and application of FH collagen gels, such as mechanical instability (Braziulis et al., 2012), matrix contraction, volume loss and degradation over time (Brown et al., 2005; Cheema and Brown, 2013; Mi et al., 2010).

There was no significant difference ($p > 0.9999$) between the elastic moduli reported for FH gels under any of the conditions. The gels appeared to maintain their stiffness over time and under the presence or absence of cells. For example, a range of 47.96 to 55.19 Pa was recorded at 1 Hz, across all conditions. This result suggests that the FH gels are stable over time and any cellular remodelling of the matrix which might have occurred over the five day culture period had not had an effect on the stiffness of the matrix.

Conversely, there were significant differences between each of the FS gel conditions. Both with and without the presence of cells, the stiffness significantly decreased over five days in culture; for example in acellular FS gels at 20 Hz, the mean stiffness decreased from 874 Pa to 243.2 Pa after five days. The presence of cells lessened the decrease in stiffness over five days in comparison to acellular gels, although the decrease was still significant. For example, in cell-seeded FS gels at 20 Hz, the mean stiffness decreased from 616.47 Pa to 508.15 Pa after five days. This result suggests that the presence of cells provided a positive mechanical effect, possibly through remodelling of the matrix. Cells can improve the mechanical properties of gel constructs through the reorganisation of fibres, production of extracellular matrix products (e.g. collagen), and the application of intrinsic strains (Ahearne et al., 2008;

Drury et al., 2004; Hu and Athanasiou, 2005; Kazakia et al., 2006; Wakatsuki and Elson, 2003). The glial scar has been reported as a stiffer environment in comparison to the surrounding spinal cord tissue (Franze et al., 2013; Windle and Chambers, 1950), this is thought to be due to the reactive astrocytes laying down extracellular matrix such as collagen (Liesi and Kauppila, 2002; Okada et al., 2007) and remodelling the scar environment, for example by collagen cross-linking (Gilad et al., 2001; Rolls et al., 2009). Interestingly, Brown found that the modulus of stabilised collagen gels seeded with fibroblasts reduced by a third in comparison to the same gels without cells. However, after two-weeks in culture the cellular and acellular moduli were similar, indicating cellular remodelling of the matrix had improved the mechanical properties (Brown et al., 2005).

The variable parameters associated with the production of collagen gels such as collagen source, solubilisation method, polymerisation pH, polymerisation temperature, and collagen concentration have been shown to have a significant effect on one or more collagen gel material properties, and these parameters are not always fully reported (Abraham et al., 2008; Gronau et al., 2012; Parenteau-Bareil et al., 2010; Stuart and Panitch, 2008). Therefore comparisons between mechanical property values for collagen gels that have not been produced and tested in comparable ways should be avoided.

It was not possible to locate viscoelastic property values for type-I rat tail collagen gels, which had been tested using oscillatory rheology, under the exact same testing parameters that were used in this study. Reported values for the mean elastic moduli of hydrated type-I collagen gels range from 20 Pa (Miron-Mendoza et al., 2010) to 1057000 Pa (Hadjipanayi et al., 2009). The mean elastic modulus of 47.96 Pa for an acellular FH gel found in this study is similar to the mean elastic modulus reported by Kreger (2010) of 37.2 $\pm$ 17.5 Pa. The testing parameters were very similar; polymerisation at neutral pH and 37$^{o}$C, and mechanically tested using oscillatory rheology, at 37$^{o}$C within the LVER, between 0.01 - 5 % strain, at 1 Hz, parameters that differed were use of PureCol, bovine dermis in 0.01 N HCl at 3 mg/ml. The differences in the collagen type, concentration and solubilisation method are likely to account for the difference in the reported modulus (Antoine et al., 2014). The Kreger

(2010) study also compared a different brand of bovine dermis (Sigma), using the same production and testing parameters. Changing this parameter alone resulted in a modulus of 142 $\pm$ 11.6 Pa in comparison to 37.2 $\pm$ 17.5 Pa using the PureCol brand (Kreger et al., 2010).

The presence of cells, time in culture and testing frequency of FS gels all had a significant effect on the elastic modulus, resulting in a range from 874 Pa (day 1, acellular) to 125.35 Pa (day 5, acellular). The elastic modulus of stabilised collagen gels found in this study was different in comparison to much of the literature. Values reported in the literature are bigger by orders of magnitude; 2.3 MPa (Hadjipanayi et al., 2009) and 1.5 MPa (Brown et al., 2005). However, these studies utilised tensile testing methodologies to record the mechanical properties, and the Brown study also tested the gels after they had been rolled into spiral constructs. Therefore the stabilised collagen gel moduli reported by Brown and Hadjipanayi should not be directly compared to the results of this study (Antoine et al., 2014; Brown et al., 2005; Hadjipanayi et al., 2009).

Neural tissue has been reported to have a modulus of between 100 - 1000 Pa, depending on the source of the tissue, and testing methods used (Cheng et al., 2008; Elkin et al., 2007; Engler et al., 2006; Flanagan et al., 2002; Lu et al., 2006). The same issues associated with comparing the reported mechanical properties of collagen gels in the literature are also relevant when comparing them to CNS tissue. For example, the mechanical testing method and testing parameters, type of tissue, age of tissue, dissection method, have all been shown to affect the reported mechanical properties (Cheng et al., 2008).

In terms of selecting a matrix of a similar stiffness to neural tissue for use within a 3D injury model, both FH and FS gels would seem appropriate, as neither were stiffer than neural tissue. Although, FS gels fall within the range of mechanical stiffness values, the FS gels were more variable over time, especially without the presence of cells. There was no significant change in the stiffness properties of FH gels over the five days in culture, which may indicate the matrix is more predictable and reliable as a matrix component for a 3D model. Longer term mechanical studies would need to

be carried out to investigate the change in mechanical properties over longer time points for both gel types. The cell-related matrix investigations discussed below allowed a matrix type to be selected for future investigations based on the interaction between the mechanical properties of the gel matrix environment and the primary astrocyte cells in terms of the effect on cell viability and the expression of reactive astrogliosis markers.

The cells in FH gels were viable over a 5 day period with an average percentage death of 19.95 % at day 5. There was a significant increase in percentage death in FS gels at both time points. The average percentage death was 45 % at day 5 in FS gels; this should be taken into account when interpreting other results; a high level of cell death could increase the reactivity of the surrounding cells. Gels seeded with fibroblasts stabilised using a similar method (compression and removal of the expelled liquid component) have reported a reduction in viability of only 10 % (Brown et al., 2005). The reduction in viability was approximately twice this level in this study. It is possible that astrocytes are more sensitive to the stabilisation process in comparison to fibroblasts; astrocytes may be more easily damaged by the rapidity of the fluid flow as the absorber removes the liquid component from the gel. Another factor which may increase the percentage of cell death is the susceptibility of the thin FS gels to desiccation due to their low mass; the fibroblast seeded gels mentioned above reported 70 % to 100 % cell death when FS gels were exposed to laminar air-flow for 20 or 60 seconds, respectively (Brown et al., 2005). Care was taken during the production of gels to add media to the wells containing the gels as soon as possible after the absorbers were removed, however it is likely that desiccation was a contributing factor to the lower viability observed in FS gels.

Additionally, the concentration of cells per area may have increased the percentage cell death in FS gels due to cellular competition for nutrients. Stabilisation of the gels reduced the gel height by orders of magnitude, resulting in the concentration of cell and collagen density within the gel in comparison to FH gels (Brown et al., 2005). The effect of reduced cell density within FS gels could have been investigated by reducing the cell seeding density of gels in the basic gel mixture before stabilisation. Unfortunately, there was not enough time to investigate this further in this study.

There may have been some variation in cell death throughout different regions of the gel; only a central z-slice portion of each gel was analysed in this study. For example, a study by Engelhardt used stabilised collagen gel constructs as a scaffold for human bladder cells. Although the overall cell viability was 90 % across the time course of the experiment (including all gel regions), in some sections, such as the surface and bottom of the gel, cell death was as high as 37 % (Engelhardt et al., 2010).

Studies have shown that passive diffusion of oxygen can occur in collagen gels up to 2 mm thick, depending on the cell seeding density (Griffith et al., 2005; Schechner et al., 2000). Therefore, diffusion of oxygen should not be a physical problem in the gel matrix environments used in this study which had a maximum thickness of around 1000 μm (as determined by confocal analysis of the z-planes).

The total cells per field were counted using a nuclear stain that did not discriminate between live or dead cells. The percentage increase in total cells per field from day 1 to day 5 was not significant in FH and FS gels. This indicates that the cells were not proliferating. The cell viability assay showed the percentage death in FS gels was on average 45 % at day 5; the slight increase in total cell number between days 1 and 5 is explained by the fact that both live and dead cells have been included in the cell count. To determine cellular proliferation in more detail in future experiments, an alternative assay, such as a proliferation assay, could be performed (Engelhardt et al., 2010).

The area of GFAP expression per cell was calculated using image analysis techniques. It was easy to determine whether the image to be analysed was a FH or FS gel from visual inspection of the images, based on the number of cells per image. Therefore in order to minimise bias, an image analysis protocol was designed such that the same mathematical thresholds and the same exclusion criteria, based on the size of particles (i.e. size of the cells) measured, could be applied to each image. Reactivity of astrocytes in relation to the expression of GFAP has been reported in the literature via a range of parameters such as area, perimeter, circularity, and fibril extension length (Burgos et al., 2007; Cullen et al., 2007; East et al., 2009; Moshayedi et al., 2010).

The area per cell and circularity were selected as the measurement parameters in this study as they were suitable for use with the thresholding technique and covered two different morphological indicators of reactive astrogliosis.

Astrocytes expressed significantly higher levels of markers of reactivity (area of expression and ramification) in 2D monolayer culture in comparison to 3D culture. There was a significant increase in the area of GFAP expression per cell in astrocytes cultured in FS gel matrix environments in comparison to FH gel matrix environments, this is indicative of the hypertrophic, morphological response of reactive astrocytes (Kimelberg and Norenberg, 1989) and has been observed in other studies of astrocytes cultured in different matrix environments (East et al., 2009; Georges et al., 2006; Moshayedi et al., 2010).

The increase in ramification was clear from analysis of the immunocytochemically stained images. The box and whisker plots showed a clear skew in the data whereby FS gels were significantly more ramified (less circular) in comparison to the astrocytes within FH gels. Cells in 2D monolayer culture were significantly more ramified compared to both FS and FH gels. These observations are supported by other studies of astrocyte morphologies following culture on substrates with differing stiffness properties whereby culture on stiffer substrates resulted in increased ramification (East et al., 2009; Georges et al., 2006; Moshayedi et al., 2010).

In terms of explaining the difference between the matrix environments, the increase in markers of astrocyte reactivity could be due to the response of astrocytes to culture within a stiffer matrix environment. The FS gels were approximately an order of magnitude stiffer than the FH gels. Additionally, the FS matrix remained stiffer over 5 days when seeded with cells in comparison to acellular FS gels. This could be explained by the highly reactive phenotype present within the FS gels. Cytoskeletal filaments contribute to the mechanical strength of cells (Silver and Miller, 2004), therefore up-regulation of GFAP, which is an intermediate cytoskeletal filament, could maintain the stiffness of the FS gels.

Astrocytes have been reported to become more reactive when cultured on stiff matrices; Georges et al (2006) reported that astrocyte growth on soft gels resulted in rounded morphologies, whilst cells cultured on the surface of stiffer gels showed a significantly increased cell area. East et al (2009) noted that within soft gels, the cells that were near the stiffer tissue culture plastic were more reactive than those away from the plastic. Similarly, Moshayedi et al (2010) showed astrocytes cultured on stiff polyacrylamide gels presented with a significantly increased perimeter, area, diameter and number of extremities compared to those cultured on compliant substrates.

Importantly, regardless of the change in mechanical properties of the matrix environments, several other factors of the matrix environment had also been altered to generate the FS gels matrices, which could have affected the expression of astrocyte reactivity markers. The cells in the FS gels had a greater degree of manipulation in comparison to the FH gels; the gels had been compressed by an absorber and the cells subjected to fluid shear flow as the liquid component of the gel was absorbed by the absorber from the top surface of the gel.

The higher rate of death in the FS gels may have stimulated the surrounding cells to become reactive. It is likely that non-apoptotic cell death stimulates reactivity in astrocytes, as it is a mechanism of cell death during the initial stages of spinal cord trauma (Balentine, 1978; Faulkner et al., 2004).

The higher cell density following stabilisation may have increased the local cell competition for nutrients and exposure to cellular waste products, which may have stimulated the astrocytes to become reactive. Astrogliosis has been shown to be triggered by low nutrient levels in cultured cells (Iglesias et al., 2016), and astrogliosis itself is an energy intensive process (Allaman et al., 2010).

Interestingly, there was a significant decrease in the area of GFAP expression per cell between the day 1 and day 5 time points within FS gels. This result cannot be explained by variations in cell number, as the expression was normalised to cell number per image. It may be that the cells were highly reactive in the initial stages of

cell culture due to the processes involved in seeding the cells; in particular the increased manipulation involved in production of FS gels. Following a mild to moderate trigger of astrogliosis, astrocytes have been seen to reduce their reactivity (Silver and Miller, 2004), and this may be the case here. The decrease in reactive phenotype might also be related to the significant decrease in stiffness observed in FS gels at day 5. Additional time points would help investigate this trend further.

Unfortunately the investigation into the effect of matrix environment on cytokine release using an ELISA was unsuccessful due to the sensitivity of the kit purchased. The suitability of the kit was based on the 60 - 100 pg/ml IL-6 values reported at day 1 to day 5 of primary astrocytes in collagen gels in another study (East et al., 2009). The kit that was purchased was sensitive down to 62.5 pg/ml IL-6. It was assumed that the supernatant from the 2D monolayer controls would contain an elevated amount of IL-6 in comparison to the levels observed in the fully hydrated gels of the East (2009) study; however the readings from the controls were also undetectable. It is possible that the cytokines were heavily diluted in the culture medium; large volumes of media were applied to each gel (1500 - 2000 µl), and fresh media was added every three days, further diluting cytokines. Unfortunately, due to time pressures, this experiment could not be repeated.

In summary, the detection of astrocyte markers was generally significantly higher in FS gels in comparison to FH gels. However astrocytes present in both the FH and FS matrix environments were at a significantly less reactive phenotype in comparison to 2D monolayer cultures. Several possibilities have been discussed above regarding the mechanism of astrogliosis stimulation; the mechanism is likely to be a combination of these. Stiffness of the gel matrix environment was of particular interest due to the reported influence that stiffness has on reactive astrogliosis (East et al., 2009; Georges et al., 2006; Moshayedi et al., 2010) and neuron and glial cells (Kleiman et al., 2011; Lantoine et al., 2016; Sundararaghavan et al., 2009; Willits and Skornia, 2004; Yeung et al., 2005). The stiffness properties of the different gel matrix environments were significantly different. Although the stiffness properties of the FH and FS gel types were lower than or within the range reported for neural tissues; FS gels were significantly stiffer than FH gels in all conditions.

The overall aim of this chapter was to select a gel matrix for future investigations into the effect of mechanical injury on primary astrocytes within a 3D collagen matrix. The improved experimental handling of FS gels in comparison to FH gels that had been reported in the literature influenced the investigation (Braziulis et al., 2012; Brown et al., 2005; East et al., 2010; Engelhardt et al., 2010; Georgiou et al., 2013; Levis et al., 2012; Micol et al., 2011). Although the astrocytes present in both the FH and FS matrix environments were at a significantly less reactive phenotype in comparison to 2D monolayer cultures, the reactive astrocyte phenotype within the FS gels was significantly increased in comparison to FH gels. A matrix which stimulated a low level of reactivity was desirable for future investigations, such that increases in reactivity in response to mechanical injury could be more readily observed. In addition, the image analysis of the FS gels was more time-consuming and complex, due to the density of cells and the overlapping processes made full resolution of each cell difficult. For these reasons, FH gel matrices were selected as the most suitable for future investigations.

# Chapter 4

## Assessment of Reactive Astrogliosis in Response to Mechanical Impact within a 3D Cell-Culture Model

### 4.1 Introduction

Spinal cord injury (SCI) occurs when the load applied to the cord is greater than the mechanical tolerances that the cells and tissue can allow. The rate of loading and the degree of deformation or the magnitude of the load are important factors and are thought to affect the outcome of the injury (Oxland et al., 2011). Injury is most commonly caused by fracture and dislocation of the spinal column; 80% of injuries are high energy spinal fractures such as fracture-dislocations and burst fractures (Pickett et al., 2006; Sekhon and Fehlings, 2001). Injuries to the spinal cord are generally classed as complete or incomplete; the majority of clinical cases are incomplete injuries (Engesser-Cesar et al., 2007), this means that the nerve fibre bundles that convey ascending sensory and descending motor information have not been completely transected; some nerve signals can still pass, but the signals are likely to be distorted, leading to additional neurological complications, such as chronic pain or spasticity (Raineteau and Schwab, 2001).

SCI involves primary and secondary injury mechanisms. The functional outcome for the patient is determined by the location of injury, type of load, force and duration of impact, and the mechanism of treatment. Although the primary injury causes tissue damage, it is the secondary injury which both increases this damage, and prevents the regeneration of tissue (Faulkner et al., 2004; Fehlings and Baptiste, 2005). Therefore investigations into the secondary injury response may provide new treatment targets for SCI regeneration.

Animal models of SCI have been an important tool in advancing our understanding of the secondary injury response (Kwon et al., 2004). Most SCI models were initially

described and characterised in rat models, and they are frequently used to study the effects of primary mechanisms of injury such as laceration, contusion and compression (Bresnahan et al., 1991; Fehlings et al., 1989; Ichiyama et al., 2009; Scheff et al., 2003; Siriphorn et al., 2012; Soubeyrand et al., 2013; Stokes, 1992; Taoka and Okajima, 1998; Wrathall et al., 1985; Zhang et al., 2014, 2008). Animal models allow manipulation of parameters such as the velocity and type of impact, types of treatments, time of sacrifice and even genetic modification, whilst preserving much of the tissue complexity associated with human tissue (LaPlaca et al., 2007). Many techniques have been developed to mimic human SCI in animal models; though most techniques require a laminectomy, which causes pathology that would be unlikely to occur in a clinical setting (Fukuda et al., 2005).

Contusion models of SCI are thought to be the most relevant models (Zhang et al., 2014). A comparison of the commonly used contusion devices used to model SCI *in vivo* is shown in Table 4.1. Some devices are more advanced than others, for example the Weight Drop device suffers from impaction rod rebound, affecting the reproducibility of results (Sharif-Alhoseini and Rahimi-Movaghar, 2014). The aneurysm clip is unreliable due to variable clip positioning and lack of standardisation of the clip release (Zhang et al., 2014). The other contusion devices listed tend to offer better control over the experimental parameters resulting in greater reproducibility and the possibility of producing graded injuries, so that animals can be studied after mild-, moderate-, or severe-impactions (Scheff et al., 2003; Sharif-Alhoseini and Rahimi-Movaghar, 2014; Vialle et al., 2007; Zhang et al., 2014). The viscoelastic properties of the matrix allow the material to respond to deformation during impaction; the amount of energy absorbed or dissipated during deformation has been shown to be proportional to the severity of injury, therefore it is important to carefully control the experimental parameters during SCI modelling and understand the mechanical properties of the model as much as possible (Choo et al., 2007; Kearney et al., 1988).

**Table 4.1: Contusion Devices for use *in vivo* (Table adapted from** (Zhang et al., 2008)**)**

| Device | Injury Parameter | Calibration method | Dwell-time | Velocity (m/sec) | Output Data | Reference |
|---|---|---|---|---|---|---|
| New York University (NYU) | Velocity (± 5 %) | Contact (closed circuit) | Variable depending on operator | 0.3 - 0.9 | Velocity Height Movement of vertebra | (Basso et al., 1996; Gruner, 1992; Vialle et al., 2007) |
| Weight Drop | Velocity | Contact (visual observation) | Variable depending on operator | 0.3 - 0.9 | Strain Force | (Gale et al., 1985) |
| Modified aneurysm clips | Clip tension | N/A | Variable depending on operator | N/A | None | (Fehlings and Nashmi, 1997; Rivlin and Tator, 1978) |
| Electro-mechanical SCI device (ESCID) | Displacement (± 0.008 mm) | Contact | Immediately <5 ms | 0.148 | Velocity Force Momentum | (Stokes, 1992) |
| Louisville Injury System Apparatus (LISA) | Displacement (± 0.007 mm) | Non-contact laser sensor | 50 ms to 5 sec (± 5 ms) | 0.5 - 2.0 | Velocity Force Duration of compression | (Zhang et al., 2008) |
| Hatteras Cortical Impactor | Velocity Depth (0 - 5 mm) Dwell time | Contact | Input in ms | 0 - 3 | Velocity Force Duration of compression | (Bilgen, 2005) |
| Infinite Horizons Impactor | Force | Contact | Input in seconds up to one minute | 0.1 - 0.13 | Force Displacement Velocity Dwell time | (Scheff et al., 2003) |

Despite the abundance of SCI animal model studies and the understanding that investigations using these models have provided, this has not been translated to the successful discovery of neuroprotective regenerative drugs in clinical trials (Macaya and Spector, 2012; Yu et al., 2009). Therefore, the use of *in vitro* models to help inform animal studies may help in the design of therapeutics. Some of the advantages of *in vitro* models include the adaptability of models to different cell types, including human stem cells and cell lines; models that can adapt to be more or less complex through the addition or removal of components; choice of matrix; potential for industrial scale up; reduction of *in vivo* testing; live cell monitoring; maintenance of cells in a 3D spatial arrangement more representative of the *in vivo* environment; and reduced cost in comparison to animal models (East and Phillips, 2008; LaPlaca et al., 2007). A simplified SCI model could theoretically be used as a research tool to advance the understanding of biological, biochemical and biomechanical processes

occurring in the spinal cord in relation to mechanical loading. Such a model could be used as a research tool alongside animal models in order to inform experiments and investigate the response of different cell types (Kirkpatrick et al., 2007).

The spinal cord is an aligned structure; the white matter is organized into tracts of aligned axons (Duval et al., 2015), therefore it would be preferential to include alignment as a feature of a 3D cellular model for the investigation of the effects of simulated SCI. Additionally, the effect of aligned astrocytes and aligned matrix components on the regeneration of neurites has been investigated using *in vitro* models (Davies et al., 2006; East and Phillips, 2008; East et al., 2010; Hsiao et al., 2015; Kofron et al., 2009; Vahidi et al., 2008; Weightman et al., 2014). This is important as it is thought that the physical barrier of disorganised astrocytes in the glial scar may contribute to the overall inhibition of regenerating axons by disrupting the guidance of the cells (Davies et al., 2006; Geller and Fawcett, 2002; Hofstetter et al., 2002; Li et al., 1998; Reier, 1979). Therefore a SCI model is more likely to be clinically relevant if an aligned model is impacted, rather than a non-aligned model, particularly if the regeneration of axons is investigated.

East et al. (2010) produced a tethered 3D collagen gel model of aligned astrocytes, for use as a spinal cord repair conduit. These authors found that when neurons were seeded on and within astrocyte gels, neurite length was greatest in the areas of astrocyte alignment (East et al., 2010). Tethered gel models generate tension in the longitudinal axis of the matrix as the gel contracts due to astrocyte remodelling of the matrix as the cells form stable integrin-mediated attachments with the fibrils of the collagen gel (Phillips et al., 2005). The astrocytes self-align along the longitudinal axis in order to reduce the tensile forces that they experience, resulting in the alignment of both cell and collagen filaments within the gel matrix (Phillips, 2014). Other self-aligned collagen gel models have seeded gels with Schwann cells (Georgiou et al., 2013) and human dental pulp stem cells, which were differentiated into Schwann cells and were shown to myelinate DRG neurites within the tethered matrix (Martens et al., 2014).

Therefore, the use of a tethered, self-aligned construct showed good potential as an *in vitro*, 3D aligned collagen gel matrix, for use as an SCI model. Advantageously, the complexity of the model can be increased following further development to include additional cell types, for example. In addition, it was hypothesised that the contusion devices used to simulate SCI in animal models can be easily transferred to the impaction of gels, allowing the *in vitro* 3D collagen gel model to be compared with *in vivo* models.

The previous chapter investigated the effect of matrix environment, in particular increased matrix stiffness, on the phenotype of astrocytes. This was investigated in order to select an appropriate matrix environment for an *in vitro* SCI model, whereby the astrocytes cultured within the 3D matrix would not develop a reactive phenotype. It was hypothesised that astrocyte cells would undergo reactive astrogliosis over time following mechanical impaction of the cell culture environment. In order to investigate the response to injury, it would be beneficial if the measurable effects of reactive astrogliosis (for example the measurement of GFAP expression, or cytokine release) were not expressed above baseline levels so that it would be difficult to determine whether the mechanical impaction had had an effect on the phenotype of primary astrocytes within the model. It is possible to stabilise tethered gel matrices (East et al., 2010; Georgiou et al., 2013); stabilised gels are thought to be mechanically stable in comparison to non-stabilised (fully hydrated) gels, due to the concentration of collagen fibres which improves the handling of the gels (Braziulis et al., 2012; Brown et al., 2005). However, it was proposed that all investigations involving mechanical impaction in the present study were performed on fully hydrated gels, due to the previous investigation (Chapter 3) which found that astrocytes were significantly more reactive in the fully stabilised gels in comparison to the fully hydrated gels.

## 4.2 Aims

The aims of this part of the study were to determine the suitability of *in vivo* methods of simulating spinal cord injury, in an *in vitro* environment by replicating the experimental parameters used to cause traumatic SCI in animal models within the constraints of the 3D tethered gel models.

*Specific Objectives:*

(i) To determine the suitability of *in vivo* contusion devices for use with an *in vitro* 3D tethered collagen gel model. This objective includes:
   a. investigating the effect of impaction on gel matrices using the parameters used *in vivo*; and
   b. defining an impaction protocol for use with 3D tethered collagen gels.

(ii) To assess the viability of primary astrocytes after impaction within 3D models over a ten day period.

(iii) To assess the effect of impaction on the markers of astrogliosis such as the average area of GFAP expression per cell and cell shape descriptors (as determined by immunocytochemistry and imaging techniques) over a ten day period.

(iv) To assess the effect of impaction on the alignment of astrocyte filaments, in particular alignment in relation to the impact zone (as determined by immunocytochemistry and imaging techniques) over a ten day period.

(v) To assess the effect of impaction on the levels of extracellular IL-6 expression after culture in different stabilised collagen gel matrix environments over a ten day period (as determined by an enzyme-linked immunoabsorbant assay (ELISA)).

## 4.3 General Methods

The experimental approach for this section involved production of tethered primary astrocyte seeded type-I collagen gel matrices.

The primary astrocyte cells which were seeded within the matrices were from cell cultures pooled from three to six separate animals to account for donor variability. Each experiment was repeated at least three times accounting for variation in the assay reaction ($n \geq 3$).

### 4.3.1 Cell Isolation

Primary astrocytes were isolated from postnatal day-2 or day-3 Wistar rat pups using the protocols described in Section 2.2.5 to 2.2.5.5.

### 4.3.2 Determination of Astrocyte Population

The percentage of astrocytes present in the cell suspension used to seed the culture models for each experiment was determined using immunocytochemical analysis of cells cultured on slides, as described in Section 3.3.4.

### 4.3.3 Tethered Gel Cell Culture Medium

A 1000 ng/ml stock solution of transforming growth factor-beta 1 (TGF-β1) was prepared by dissolving 2 μg of TGF-β1 powder in 2 ml of water which had been filter sterilised. The TGF-β1 stock solution was stored in 10 ml aliquots, at -20$^{o}$C, until the expiration date shown on the manufacturers packaging. Prior to use, the TGF-β1 stock solution was defrosted at room temperature.

A working dilution TGF-β1 of 10 ng/ml was prepared when required, by adding 10 μl/ml of the TGF-β1 stock solution to supplemented pre-warmed DMEM (Section 2.2.4.1). Approximately 7 ml of TGF-β1 supplemented media was required per tethered gel matrix.

### 4.3.4 Contraction Assay: Optimisation of Astrocyte Cell Seeding Density For Self-Aligned Tethered Gels

The effect of cell seeding density on the contraction properties of collagen gels was investigated before preparing a tethered gel model for the first time (O'Rourke et al., 2015; Phillips and Brown, 2011). The cell seeding density is an important parameter in tethered gel models because higher densities tend to cause faster contraction, which may be advantageous in terms of increased cellular alignment, or may result in the gel breaking during the experiment (Phillips and Brown, 2011). The contraction profile depends on the cell type to be used; some cell populations are slow at contracting and can be supplemented with other cells or chemical stimulants to influence the contraction rate. For example, in East's 3D collagen gel model (2010), neural fibroblasts were added to the astrocyte and dorsal root ganglia cell populations at a seeding density of 5 % in order to ensure consistent gel contraction. The use of chemical stimulants, such as TGF-β1, have been used to aid contraction of collagen gels seeded with cardiac fibroblasts (Lijnen et al., 2003), and a primary astrocyte seeding density of four million cells per ml in the presence of TGF-β1 has been used previously to provide between 60 and 80 % contraction in collagen gels (O'Rourke et al., 2015).

A multi-well plate assay using free-floating gels was used to quantify the contraction of primary astrocyte seeded type-I collagen gels over a range of cell densities, in order to relate this to the extent of cellular alignment generated in tethered aligned gels of equivalent seeding density. A free-floating gel is a gel which has been gently released from the material in which it was polymerised and allowed to float within the surrounding cell culture medium. O'Rourke (2015) showed that the percentage contraction in free-floating gels was related to the extent of cellular self-alignment achieved using the equivalent cell seeding density in tethered gels.

Cell seeded gel solutions, as described in Section 2.2.7, were prepared at increasing cell densities of 0.5, 1, 2, 4, and 5 million cells per ml. The cell-seeded gel solutions were added to the wells of a 96-well plate, in volumes of 75 µl (n = 6). The gels were

incubated for 15 minutes at 37°C, in 5 % $CO_2$ (v/v) in air to allow polymerisation of the gels. A sterile 21 gauge needle was used to detach the polymerised gel from the side of the well plate so that the gels became free-floating. The gels were then overlaid with 100 µl TGF-β1 supplemented media (10 ng/ml) and incubated at 37°C, in 5 % $CO_2$ (v/v) in air for 24 hours to allow gel contraction to occur.

After 24 hours in culture, the culture medium was removed from each well and images of each gel were taken. In order to measure the percentage contraction of each gel, the Fiji Is Just ImageJ (FIJI) software program was used to trace the circumference of a culture well, this was then measured using the 'Measure' setting. The perimeter of the gel was traced and measured in the same way, as shown in Figure 4.1, and the percentage change in area was calculated.

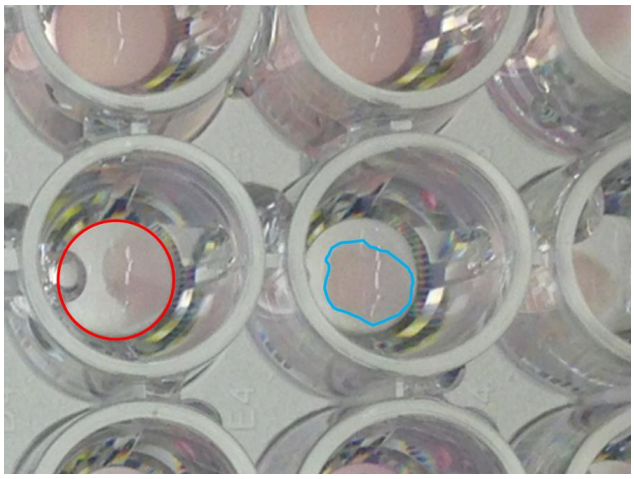

**Figure 4.1: Image Analysis of Gel Contraction.** The percentage contraction of gels was calculated by measuring the area of the culture well base (red) and calculating the percentage change in area in comparison to the area of the gel (blue). Image analysis software (FIJI) was used to analyse the images.

### 4.3.5 Matrix Preparation

As described in Section 2.2.7, during the production of cell seeded gel matrices, the cells formed a portion of the gel composition before the gel set. This meant that the cells were evenly dispersed throughout the gel mixture as gelation of the matrix occurred. Confocal microscopy of immunocytochemically stained gels confirmed

even cellular distribution. The concentration of primary astrocytes within each cell seeded collagen gel was four million cells per 1000 µl gel matrix.

The gel matrices were produced in 1000 µl volumes using the basic gel mixture described in Section 2.2.7. However, rather than polymerising the gels within circular wells of a tissue culture plate, each gel was polymerised and cultured within a polyether ether ketone (PEEK) tethering gel mould, the shape and dimensions of which are presented in Figure 4.2.

The tethering moulds required specific preparation prior to gel production. Cells within the tethering systems self-align along the long axis of the gel as a result of the tension generated between the two tethering sites (East et al., 2010; Georgiou et al., 2013; Phillips et al., 2005). The dimensions of the moulds were based on the methods described by Phillips & Brown (2011) which recommend that the gel mould opening was rectangular with the distance between the tethering bars three times the width of the gel. The arrangement of tethering the gel at either end influences the contractile forces that cause the cells to align to the direction of principal strain.

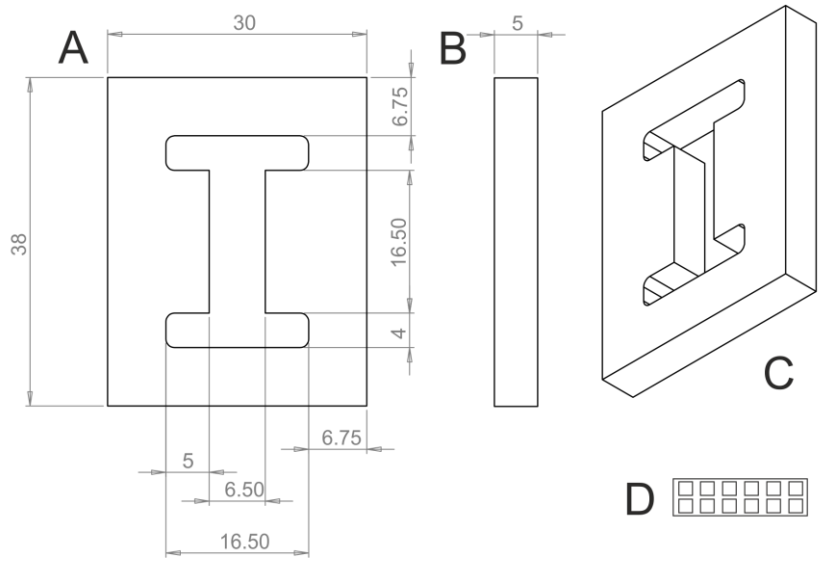


**Figure 4.2: Shape and Dimensions of the Tethered Gel Moulds and Tethering Bars.** The tethered gel mould (A-C) was manufactured from polyether ether ketone to the dimensions presented above (A,B), all measurements shown are in millimetres. Two nylon tethering bars (D) were inserted at each end of the mould within the tethering sites. Technical drawing courtesy of Philippa Clarkson.

The following method as described, allows to the production of four tethered gels; however the number produced at any one time varied throughout the study depending on factors such as cell availability, therefore the materials were scaled appropriately.

#### 4.3.5.1 Tethered Gel Mould Preparation

The preparation of the tethered gel mould equipment involved sterilisation of apparatus and assembly of the mould components. An approximately 40 x 80 mm piece of parafilm and four tethering bars were required per gel mould. The moulds and tethering bars were washed and scrubbed under hot tap water, then soaked in 1 % (v/v) Trigene for approximately 30 minutes to remove any debris. The following procedures were performed inside a class II safety cabinet. The moulds, tethering bars, and parafilm (paper removed) were then submerged in 70 % (v/v) ethanol and left to incubate for a minimum of 30 minutes. The apparatus was then removed from the ethanol using sterile tweezers and air dried.

Once dry, the parafilm was wrapped tightly around one face of the mould using sterile blunt tweezers, in order to create a seal underneath the opening of the mould. Sterile tweezers were then used to insert two tethering bars across each end of the mould at the tethering sites, as shown in Figure 4.3. Each assembled tethered gel mould was placed inside a sterile tissue culture dish until required. Assembled tethered gel moulds were used immediately.

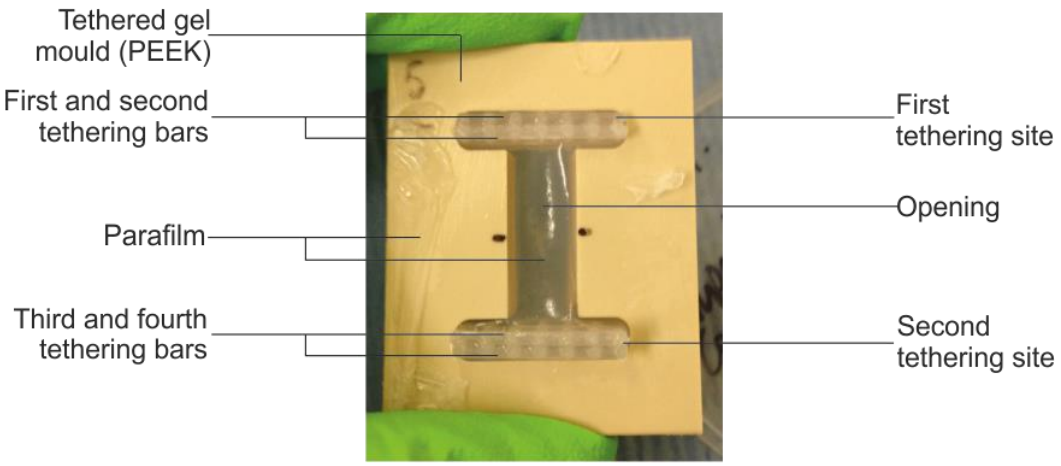


**Figure 4.3: Tethered Gel Moulds Assembly.** The tethered gel mould was assembled by placement of sterilised parafilm across one face of the mould in order to create a seal underneath the opening of the mould. First and second tethering bars were inserted into the first tethering site, and third and fourth tethering bars were inserted into the second tethering site.

#### 4.3.5.2 Preparation of Gel Solution

To prepare a 4 ml collagen gel solution, with a cell seeding density of $4 \times 10^6$ primary astrocyte cells per ml, 400 µl 10 x MEM was added to a sterile universal. Using a wide bore pipette, 3200 µl type-I rat tail collagen (2 $mg.ml^{-1}$ in 0.6% (w/v) acetic acid) was mixed with the 10 x MEM. The cell suspension was prepared at this stage, to minimise the time that a high density of cells would be in a low volume of media. Cells were removed from the tissue culture flask as described in Section 2.2.6.3, the cell viability was assessed and the cell numbers were determined as described in Section 2.2.6.1. The cell suspensions retrieved from several flasks of cells were pooled to acquire a suitable number of cells. The cell suspension containing $1.6 \times 10^7$

primary astrocyte cells was centrifuged for 10 minutes at 150 g, at room temperature. The supernatant was carefully aspirated from the cell pellet, which was then resuspended in 168 µl supplemented DMEM culture medium (not supplemented with TGF-β1) and triturated thoroughly to mix. The collagen mixture was then neutralised with 232 µl neutralising solution before the addition of the cell suspension. The gel mixture was carefully swirled by hand to mix.

To prepare a 4 ml collagen gel solution, with a cell seeding density of $2 \times 10^6$ C6 cells per ml, the same volume of supplemented DMEM culture medium (not supplemented with TGF-β1) was used, but $8 \times 10^6$ C6 cells were suspended within it. To prepare 4 ml of acellular gel solution, the same volume of supplemented DMEM culture medium (not supplemented with TGF-β1) was used, but no cells were added to the suspension.

The gel solutions were used immediately following preparation.

#### 4.3.5.3 Tethered Gel Polymerisation

Once an astrocyte seeded, C6 seeded, or acellular gel solution (Section 4.3.5.2) had been prepared, it was immediately transferred to the assembled tethered gel moulds (Section 4.3.5.1). A volume of 1 ml gel solution was added to the opening of each mould using a wide bore pipette. The gel solution was integrated with the tethering bars using a 200 µl Gilson pipette. Integration was sufficient when the pink gel solution could be seen throughout the tethering bars and throughout the entirety of the opening of the mould.

The gels were incubated for 15 minutes at 37°C, in 5 % $CO_2$ (v/v) in air to allow polymerisation of the gels. The gels were then overlaid with 7 ml TGF-β1 (10 ng/ml) supplemented media before replacing the lid of the tissue culture dish. The gels were incubated at 37°C, in 5 % $CO_2$ (v/v) in air for 24 hours to allow gel contraction and cellular self-alignment to occur in the cell seeded gels. Gel contraction and self-alignment did not occur in acellular gels; acellular gels were produced for preliminary investigations into the impaction parameters. Examples of a contracted

primary astrocyte seeded collagen gel and an acellular collagen gel after three days in culture are shown in Figure 4.4.

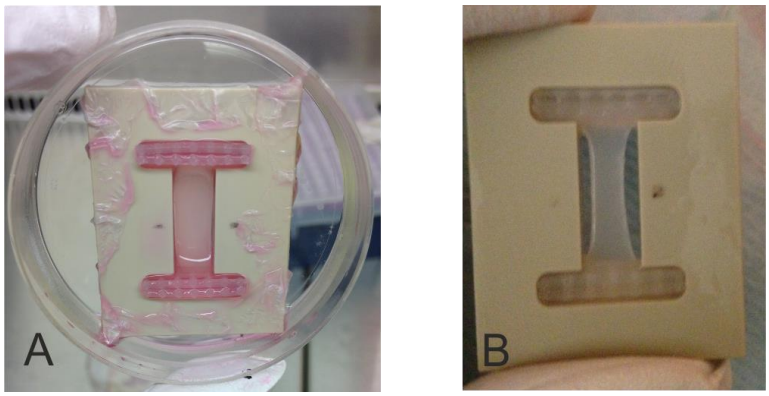


**Figure 4.4: Tethered Acellular and Cellular Collagen Gels.** Representative images of an acellular collagen gel (A) in comparison to a contracted tethered collagen gel (B), highlighting the characteristic tapered shape of the contracted gel.

### 4.3.6 Optimisation of Impaction Protocol

In order to apply a mechanical impact to the 3D tethered gel models, an impaction rig was required. Impactors are used frequently to replicate CNS injuries in animal models (Carter et al., 2000; Gattlen et al., 2016; Hooshmand et al., 2014; Lam et al., 2014; Michael-Titus and Priestley, 2014; Nishi et al., 2007; Scheff et al., 2003; Visavadiya et al., 2016; Zhang et al., 2014), therefore it was hypothesised that the methodology would be easily transferrable to the impaction of gels, allowing the 3D cellular model to be compared with *in vivo* models.

#### 4.3.6.1 Pilot Impaction Study

A pilot impaction study was undertaken at University College London (UCL) using a Hatteras PCI3000 Precision Cortical Impactor™ (Hatteras impactor). The Hatteras impactor was being used as part of a collaboration between (UCL) and Queen Mary University of London (QMU). At QMU, the Hatteras impactor was used as part of research to replicate traumatic brain and spinal cord injuries in animal models (Michael-Titus and Priestley, 2014). Impactors such as this were investigated due to the comparisons that might be drawn between the *in vivo* animal models and the

*in vitro* 3D tethered gel models. Therefore the aim was to replicate the experimental parameters used to generate traumatic SCI in animal models within the constraints of the 3D tethered gel models, in order to investigate the suitability of impactors for investigations into the effect of mechanical loading on primary astrocytes within tethered gels.

Tethered C6 seeded (2 x $10^6$ cells per ml) collagen gels were prepared and allowed to contract and self-align for 24 hours, as described in Sections 4.3.5.2 and 4.3.5.3. The impactions took place inside a class II safety cabinet. All of the components of the Hatteras impactor were sprayed with 1 % (w/v) Virkon, followed by 70 % (v/v) ethanol before being placed inside the class II safety cabinet.

In order to reduce culture media splashes which might increase the risk of infection of cultured gels, the media was removed from the surface of the gels before the impaction. Gels were prepared for impaction individually to minimise the time the gels were spent without media coverage. All of the media was removed from the surface of the gel and the gel was placed on the impaction platform. The gel was aligned so that the impaction tip would impact the centre of the tethered gel, as shown in Figure 4.5, by carefully lowering the tip towards the gel, and adjusting the gels position on the platform by eye.

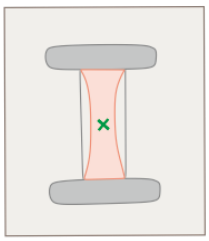

**Figure 4.5: Impaction Location in Tethered Gel Models.** The impaction tip of the impactor was aligned with the centre (X) of the tethered gels before each impaction. Alignment was performed by eye.

Computer software was used to operate the Hatteras impactor and input the impact parameters. The experimental set-up of the Hatteras impactor is shown in Figure 4.6. The parameters selected were those used by the QMU research group when generating

SCI *in vivo*: impactor tip 2 mm diameter, impact speed 1.5 m/s, depth 1.8 mm and dwell time 100 ms (Tremoleda et al., 2016). After impaction, the gels were overlaid with 7 ml TGF-β1 supplemented media before replacing the lid of the tissue culture dish. The gels were incubated at 37$^{o}$C, in 5 % $CO_2$ (v/v) in air for a further 24 hours or 3 days.

The impaction tip was removed, sprayed with 70 % (v/v) ethanol, and allowed to air dry within the class II safety cabinet before impaction of a fresh gel. Impaction using the Hatteras impactor was quick; the procedure took approximately two to three minutes from removal of media to the gel being returned to the incubator following impaction.

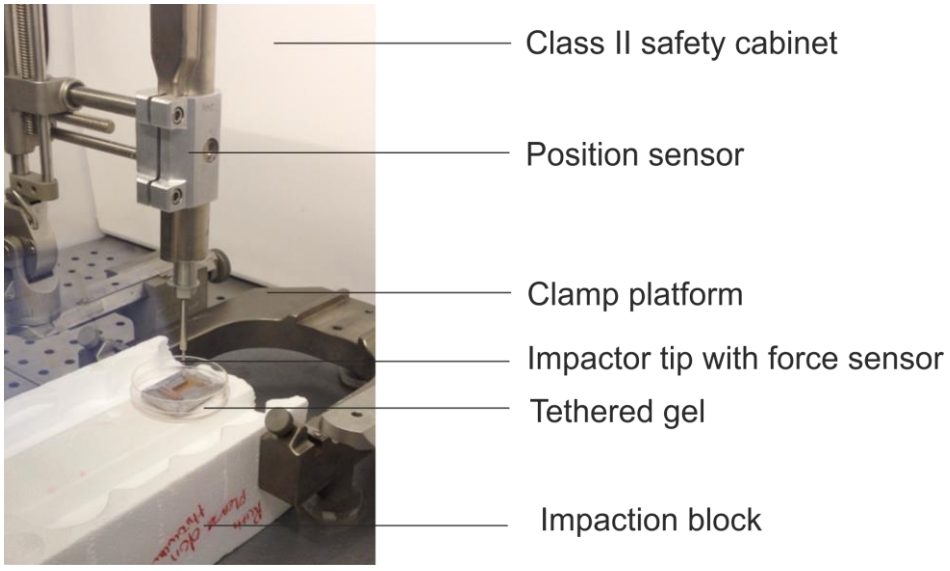


**Figure 4.6: Experimental Set-up of the Hatteras Impactor at UCL.** The Hatteras impactor was situated within a class II safety cabinet during the impactions, in order to maintain sterility. The tethered gel was positioned on top of a polystyrene impaction block because the clamp platform was unsuitable for positioning a tissue culture dish, due to the impactor being designed for animal model use. The software controlled the position sensor and the force sensor in order to impact the gel with the impactor tip.

After 24 hours in culture, the media was removed from the impacted gels and discarded whilst inside a class II cabinet. The gels were then rinsed with sterile

phosphate buffered saline (PBS) three times before the gels were fixed by the addition of 7 ml 4 % paraformaldehyde (PFA) solution (Section 2.2.4.8). The tissue culture dish was sealed with parafilm before the gels were placed at 4$^{o}$C for 24 hours, for fixation to occur.

#### 4.3.6.1.1 Removal of Gels from Mould and Transportation

The gels were removed from the fridge after 24 hours had passed. The PFA was removed and discarded. The gels were then rinsed three times with PBS before the gels were removed from the moulds. Using tweezers, the parafilm was removed from the underside of the moulds. The moulds were then placed in a clean tissue culture dish containing 5 ml PBS. A scalpel was used to release the gel from the tethering bars. The mould was lifted using the tweezers, which left the collagen gel floating in the PBS. The released gels were then transferred to bijous containing 4 ml PBS (one gel per bijou) and stored at 4$^{o}$C until required. The gels were transported to the University of Leeds for immunocytochemical staining and imaging.

### 4.3.6.2 Investigations into Impactor Parameters using University of Leeds Impactor

Following the results of the pilot study at UCL, a similar impactor to the Hatteras impactor was located at the University of Leeds. This type of impactor was also regularly used to simulate traumatic CNS injury in *in vivo* models (Carter et al., 2016; Gattlen et al., 2016; Hooshmand et al., 2014; Lam et al., 2014; Nishi et al., 2007; Scheff et al., 2003; Visavadiya et al., 2016; Zhang et al., 2014).

The impactor used throughout the rest of the study was an Infinite Horizons IH-0400 Impactor (IH impactor) which was a contusion device designed for medical research into spinal injury of rats and mice through reproducible replication of graded contusion injuries (Nishi et al., 2007; Scheff and Roberts, 2008; Scheff et al., 2003). The impactor enabled application of a standard-force which could be manually selected in order to produce graded injuries, i.e., mild, moderate and severe (Hooshmand et al., 2014). However, unlike the Hatteras impactor, the displacement and velocity parameters could not be controlled.

The key components of the IH impactor are shown in Figure 4.7; instead of using a polystyrene block as the substitute impaction platform, a custom-made platform was produced out of trespa sheet material, which had an anti-microbial surface, in order to reduce the risk of infection.

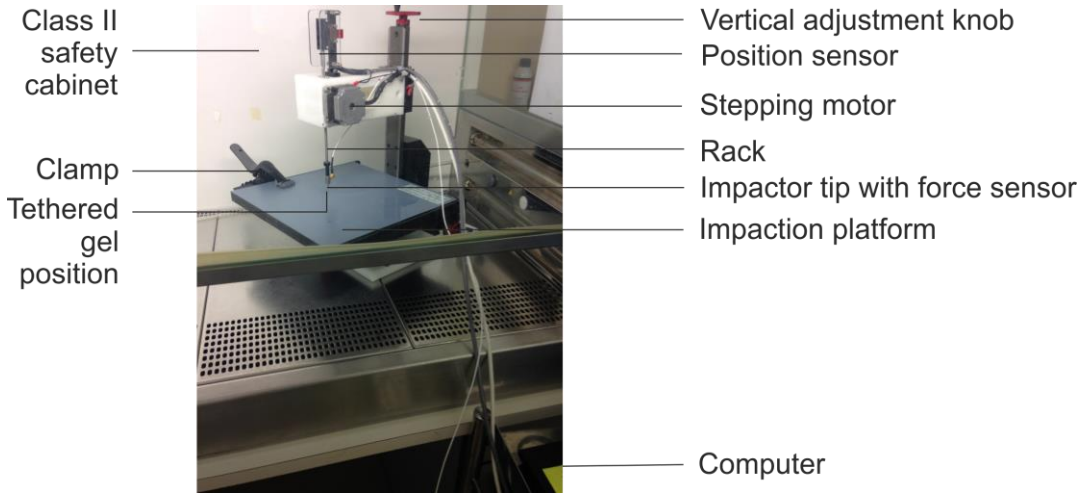


**Figure 4.7: Experimental Set-up of the IH Impactor at Leeds University.** The IH impactor was situated within a class II safety cabinet during the impactions, in order to maintain sterility. The tethered gel was positioned on a custom made impaction platform which was clamped in position. The computer controlled the position sensor and the force sensor in order to impact the gel with the impactor tip at the desired impaction parameters. The vertical adjustment knob was used to position the impaction tip above the gel.

The IH impactor is designed to monitor the injury using a force-driven sensor, which measured the actual force and the resulting displacement delivered to the spinal cord *in vivo* (Scheff et al., 2003). The user is able to select a force, known as the 'desired' force, and the dwell time of the tip at the injury site after the application of force, in order to model extended compression injuries. Following impaction, the impactor software presents the desired force value and the actual force value; the actual force value is the actual experimentally acquired value after the impact (Scheff et al., 2003). The 'PSI IH Spinal Cord Impactor v5.0' impactor software (version 5.0) was able to calculate the displacement and velocity of the impaction after it had occurred, it was not possible to input these parameters for the experimental set up.

Tethered aligned collagen gels, seeded with C6 cells (Sections 4.3.5.2 and 4.3.5.3) with a cell seeding density of 2 x $10^6$ C6 cells per ml, were prepared for the initial experiments to optimise the IH impactor parameters.

#### 4.3.6.3 Impaction Tip Diameter

The impactor was assembled inside a class II safety cabinet, as was shown in Figure 4.7. Tethered aligned C6 seeded collagen gels were impacted using the experimental parameters used in the simulation of SCI in *in vivo* studies at the University of Leeds, i.e. 200 kdyn (desired), 0 ms dwell time (personal communication, Yazi Al'Joboori). However, it was found that the impactor tip travelled the entire way through the gel and impacted the tissue culture plastic underneath.

Upon further research into how the IH impactor was programmed, it transpired that upon initiation of an injury sequence, the motor applies a torque to the rack, thus moving the rack with the attached tip and force sensor in a vertical direction, towards the sample. After each step, the force between the impactor and the specimen is sampled by the microcontroller. The microcontroller commands another step if the force level does not exceed the threshold level of the user-defined desired force. Therefore, due to the low elastic modulus of the fully hydrated gels, which are less stiff than the CNS tissue that the IH impactor is designed to detect, it was hypothesised that the impactor might not be able to detect the presence of the gel, and therefore was passing through the entire gel matrix before impacting the tissue culture plastic. The displacement setting could not be manually set; this meant that the actual force applied to the gel was unknown. The experiment was repeated on acellular fully stabilised (FS) gels (Section 3.3.2), which have a significantly higher elastic modulus in comparison to hydrated collagen gels.

It was proposed that increasing the diameter of the impaction tip might improve the detection of the gel by the impactor by increasing the surface area of the tip. The increase in tip size was restricted by the dimensions of the tethered gel mould. Although it would be possible to increase the size of the moulds, an increase in mould dimensions would significantly increase the number of cells required per experiment.

Due to the use of primary astrocyte cells in this study, minimising the number of cells required per experiment was a priority; therefore increasing the size of the moulds was avoided.

Stainless steel impaction tips were manufactured in diameters of 4 mm and 6.5 mm, as shown in Figure 4.8. An impaction experiment was set up to investigate the effect of increasing impaction tip size on the actual force reading and the displacement reading. In order to minimise error in these experiments, the same 'test block' was used for each impaction. The test block was a sorbothane test sample provided with the IH impactor as a reference sample for each machine. The test block was part of the IH impactor kit and was intended to give an indication of the relative health of the impactor.

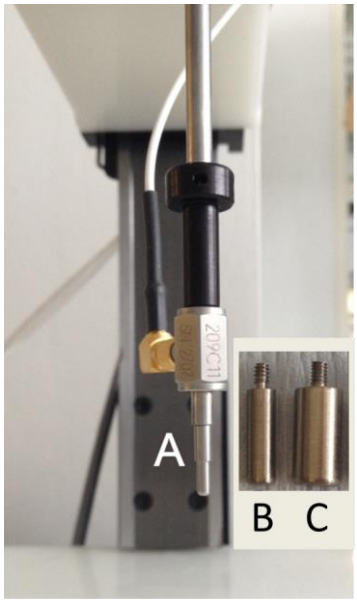


**Figure 4.8: Impaction Tips of Increasing Diameter.** Impaction tips of three different diameters were tested; 2.5 mm (A), 4 mm (B) and 6.5 mm (C). The 2.5 mm diameter impaction tip (A) was the tip provided with the IH impactor for impaction of rat spinal cords, shown in position on the rack of the IH impactor. Impaction tips B & C were manufactured at the University of Leeds.

The test block was placed underneath the impaction tip, on the impaction platform. The experiment was set up according to the manufacturer's instructions for impaction

*in vivo*; briefly, the sample was placed underneath the impaction tip and the tip was lowered using the vertical adjustment knobs, to within a few millimetres of the sample surface. The position of the sample was then adjusted by viewing the location of the sample from several different angles. For experiments involving the test block, alignment involved locating the impaction tip at the centre of the test block, as shown in Figure 4.9. Once the test block was aligned, the impaction tip was raised by approximately 5 mm by rotating the vertical adjustment knob by two full turns. The impaction parameters were then input into the software, and the impaction was initiated. The three tip sizes were each tested at 30, 100 and 300 kdyn, and a dwell time of 0 ms was selected.

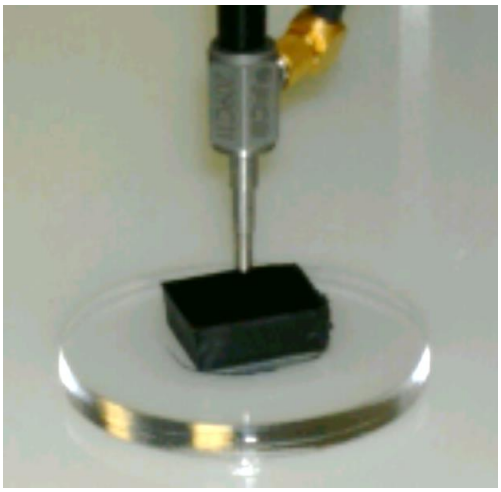

**Figure 4.9: IH Test Block in Aligned Position with Impaction Tip.** The sorbothane test block in position with a 2.5 mm diameter impaction tip aligned centrally, a few millimetres above the sample. The test block was mounted on plastic.

#### 4.3.6.4 Impaction Depth

The displacement of the IH impactor could not be controlled by the computer software, therefore in addition to the unavailability of the actual force reading following an impaction, the impactor tip was travelling all of the way through the gel to the base of the mould. This was apparent due to the noise of the tip hitting the plastic of the culture well dish in which the tethered gels were contained, and also

through visual inspection of the gels following impact, whereby a through-hole was visible in the gels.

The gel matrix surrounding the impact zone was of interest; it was envisaged that imaging techniques would be used to sample areas at the surface, sides and base of the impact zone, and at distances from the impact zone, to investigate differences in cell behaviour within different gel locations. A mechanism of controlling the displacement manually, without the computer program, was investigated.

It was hypothesised that increasing the distance that the tip started the impaction from, once it had been aligned, might overcome the computer operated displacement which was forcing the tip to impact the tissue plastic. This was investigated using acellular tethered gels; the impactor tip was lowered one complete turn of the vertical adjustment knob at a time, while maintaining all of the other parameters at 200 kdyn, dwell time 0 ms, tip size of 2.5 mm. The gels were analysed under the bright field microscope, where it was possible to see if the impaction tip had pierced through to the tissue culture plastic or not.

### 4.3.7 Impaction Protocol

Following the investigations carried out into the impactor parameters such as impaction tip diameter and impaction depth, the following protocol was developed. All impaction experiments took place inside a class II safety cabinet.

#### 4.3.7.1 Impactor Reference Check with Test Block

At the start of each experiment, before gels were impacted, the test block was impacted as a reference. The test block was placed centrally underneath the impaction tip, on the impaction platform, and the tip was lowered using the vertical adjustment knob, until the tip was approximately 1 mm away from the sample surface. The impaction tip was then raised by rotating the vertical adjustment knob by five full turns. The test block was then impacted at 200 kdyn, 0 ms dwell time, using the 2.5 mm diameter tip. The shapes of the force versus time and displacement versus time graphs that were produced immediately by the software were compared to previous

test block graphs produced under the same settings to check for any obvious deviations that might have indicated that the IH impactor was not functioning correctly.

#### 4.3.7.2 Impaction of Tethered Collagen Gels

The astrocyte-conditioned media was removed from the surface of the gels before impaction; therefore gels were prepared for impaction individually to minimise the time the gels were spent without media coverage. The media that was removed from the gel was stored in a sterile bijou whilst the impaction took place to be replaced afterwards. The tethered gel, which was contained within the tissue culture dish, was placed centrally underneath the impaction tip and the tip was lowered using the vertical adjustment knobs, to within a few millimetres of the gel surface in order to calibrate the tip. Alignment with the centre of the gels was aided by markers that were placed onto the moulds using a permanent marker, as shown in Figure 4.10. The markings were added before the moulds were sterilised. The marking highlighted the approximate centre of the gel, which made alignment possible. The impaction tip was then raised from the calibration point by rotating the vertical adjustment knob by five full turns. The gel was then impacted at 200 kdyn, 0 ms dwell time, using a 2.5 mm diameter impaction tip. The media was removed from non-impacted control gels and the test block was then impacted, to simulate the time taken for the gel to be impacted, before the media was replaced over the non-impacted control.

After impaction, the gels were overlaid with the conditioned media that had been removed from the gel (TGF-β1 supplemented media). The dishes were topped up with fresh TGF-β1 supplemented media to ensure the media was fully covering the whole mould, before replacing the lid of the tissue culture dish. The gels were incubated at 37$^{o}$C, in 5 % $CO_2$ (v/v) in air for the remaining time course of the experiment; either one, five, or ten days after impaction. The gels were topped up with fresh TGF-β1 supplemented media as required, at least every three days. The impaction tip was removed and sprayed with 70 % (v/v) ethanol between the impaction of each gel. Impaction using the IH impactor was quick; the procedure took approximately two to three minutes from removal of media to the gel being returned to the incubator following impaction.

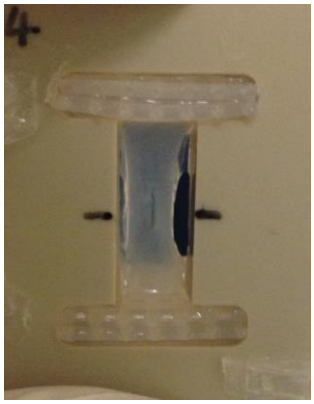

**Figure 4.10: Tethered Gel Mould Alignment Marking.** The approximate centre of the mould was marked with permanent marker before the moulds were sterilised in order to aid the visual alignment of the impaction tip with the centre of the gel. The impaction site is visible in this impacted gel as an axial slit in the gel centre.

### 4.3.8 Experimental Design

The tethered gels were time-consuming to produce and required relatively large numbers of primary astrocyte cells. In order to minimise the number of cells required for each experiment, the number of assays that could be performed on one gel was optimised. Initially it was thought that the tethered impacted gels could be sliced in half after the experimental time course had elapsed, before performing cell viability assays on one half of the gel, immunostaining on the other half, and collecting the media for analysis of extracellular cytokine release. However, the shape of the impact zone, and in particular how this might change over time, was of interest. It was uncertain whether slicing the gels in half would affect the analysis of the impact zones because it was unknown how symmetrical the impact zones would be. In addition, slicing the gels in half would cause cell death along the incision which would interfere with the results of the cell viability stain in particular.

The cell viability assay that had been used previously in this study was the Live/Dead® Cell Viability assay which immunofluorescently labelled live and dead cells green and red, respectively. The determination of astrocyte phenotype that had been used previously in this study involved immunofluorescently labelling the

reactive astrogliosis marker, glial fibrillary acidic protein (GFAP), and staining the double stranded DNA of the cell nuclei with the fluorescent stain, Hoechst, the stains were red and blue, respectively. It was not practical to fluorescently stain one gel with more than three different fluorescent stains. In their paper, East et al., (2009) describe using propidium iodide (PI) staining in combination with Hoechst to assess the cell viability of primary astrocytes seeded within collagen gels; dead cells were those with co-localised nuclear staining of PI and Hoechst, live cells were those stained only with Hoechst. Therefore, it was hypothesised that a combination of the Dead-component of the Live/Dead® Cell Viability assay (ethidium homodimer-1 (EH)) and Hoechst would be suitable for the assessment of cell viability of primary astrocytes in the impacted tethered gel model. The combination of these stains would enable immunocytochemical staining of GFAP to be performed on the same gel as cell viability analysis, therefore the full gel could be analysed without being split into separate components for different assays. The aims and objectives of this chapter were investigated by implementing experiments that were designed according to the process presented in Figure 4.11.

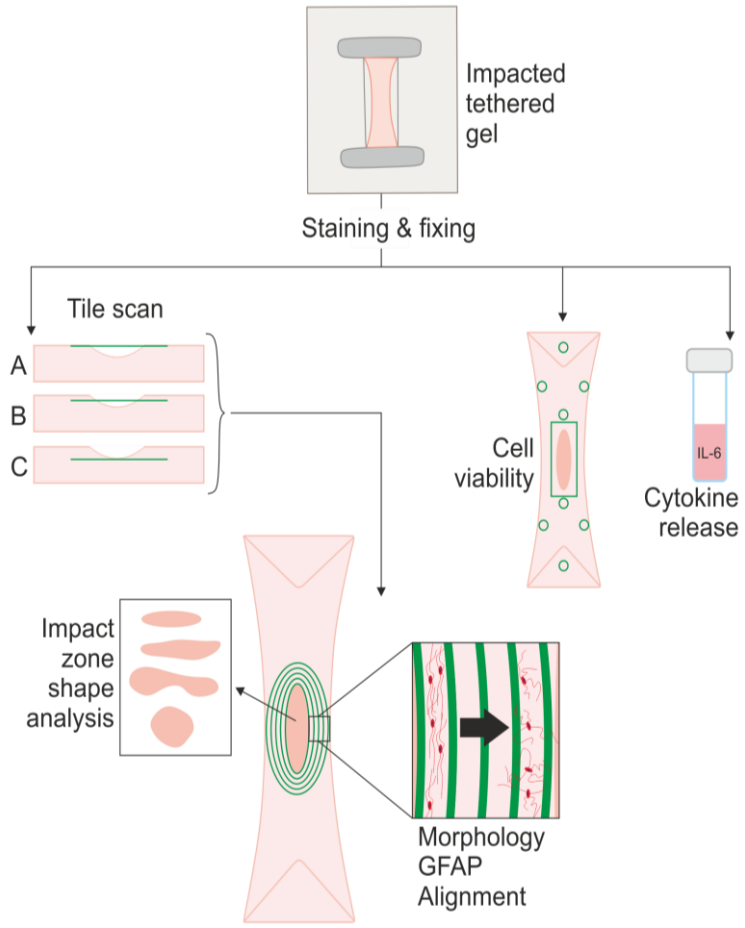


**Figure 4.11: Assay Plan for Each Tethered Gel.** The number of assays and types of analysis performed on each gel was optimised in order to reduce the number of primary astrocyte cells required. Gels were imaged using tile scanning on the confocal microscope to analyse the impact zone at its surface (A), middle (B) and base (C). Tile scans allowed the area around the impact zone to be analysed in increasing increments (green contours) to investigate differences in cell morphology, GFAP expression and cellular alignment at defined distances away from the impact. The shape of the impact zone was analysed. Cell viability was determined at specific locations around the gel, highlighted in green. Media was sampled in order to investigate extracellular cytokine release.

### 4.3.9 Determination of Cell Viability

The viability of astrocytes seeded within the gel matrices was determined using the EH (Dead) component of the Live/Dead® Cell Viability assay in combination with the Hoechst stain.

An experiment to investigate the efficacy of the combination of these stains was performed prior to use on the impacted tethered gels. The preliminary experiment was performed on type-I collagen gel matrices which were prepared as previously described in Section 2.2.7. The gel matrices were produced in 500 µl volumes using the basic gel mixture; each having a seeding density of one million primary astrocytes per gel. The gels were polymerised within a well of a 24-well cell culture plate. Once the gels had set, 1500 µl supplemented DMEM was added to each well, before incubation for either one or five days at 37$^{o}$C in 5 % (v/v) $CO_2$ in air. The Live/Dead® Cell Viability assay described in Section 2.2.8.1 was adapted to include only the dead stain, EH. The Dead solution was prepared by defrosting the EH kit component at room temperature (Live/Dead® kit components were stored at -20$^{o}$C). A volume of 3 µl EH and 4 µl Hoechst was added to 3993 µl supplemented DMEM cell culture medium. The Dead solution was protected from light and used immediately.

Having tested the efficacy of the adapted cell viability method, the adapted method was used on tethered gels thereafter. Each tethered gel was overlaid with 2000 µl Dead cell viability solution containing 1.5 µl EH per 2998.5 µl supplemented DMEM cell culture medium. The gels were then incubated for four hours in a humidified incubator at 37$^{o}$C in 5 % $CO_2$ (v/v) in air. Following incubation, samples were washed thoroughly three times for five minutes each in PBS in the dark. The gels were then fixed by the addition of 7000 µl paraformaldehyde (PFA) solution; tethered gels remained within the tethered moulds at this stage. Gels in PFA were stored in the fridge at 4$^{o}$C for at least 12 hours before staining for nuclei and GFAP using Hoechst and immunostaining techniques, respectively. Once fixed, the tethered gels were removed from their moulds as described in Section 4.3.6.1.1, before further staining.

The nuclei and immunostaining methods used in this study are described in Section 2.2.8.2. Gels were stored in the dark, at 4$^{o}$C until required for imaging.

#### 4.3.9.1 Analysis of Cell Viability Staining

Eight fields of view were analysed per gel, as highlighted in Figure 4.12. The general imaging methods used in this study, with regard to capturing the images using a confocal microscope, can be found in Section 2.2.9. The regions analysed were all within the central z-plane of the gel, unless stated otherwise. In order to locate the central z-plane, the confocal microscope was used to focus on the surface of the gel, where the first cells came into focus. The recording of the microscope z-position was noted, before focussing through the gel until the last plane of cells were in focus. The z-position was noted at this focal plane. The two z-position readouts were used to calculate the central z-plane of the gel. The z-plane was recalculated at each region, to account for changes in the gel height at different locations.

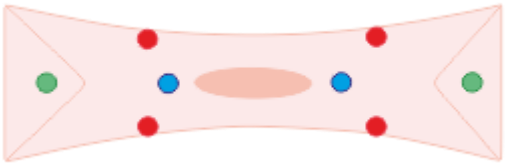

**Figure 4.12: Analysis of Tethered Gel Regions.** The different regions analysed for each contracted, self-aligned collagen gel, after impaction. Regions labelled (in terms of their x,y location): red regions represent the sides of the gel; blue regions represent the middle of the gel; and green regions represent the delta zones. These regions were analysed within the central z-plane of the gel. A tile scan was taken of the impact zone region, labelled pink. Tile scans were analysed at the gel surface, central z-plane of the impact zone, and base of the impact zone.

Images were loaded into the Fiji Is Just ImageJ (FIJI) software package and analysed using the Cell Counter built in macro. The software places a grid over each image to aid systematic counting. A 'Type 1' counter was selected, and cells were counted by positioning the computer mouse over a cell and placing a '1' marker to mark and count the cell. Once all 'live' cells, which were stained blue with the Hoechst nuclear stain,

were counted, the cell counter was switched to 'Type 2' and the process repeated. When the 'Type 2' counter was selected, a click of the mouse deposited a '2' over the dead cells, which were stained red and blue due to the co-localisation of the Hoechst and EH dead viability stain. This method of counting the cells reduced the possibility of counting a cell more than once, as the cell was marked by a '1' or '2' as it was counted. A representative image is shown in Figure 4.13.

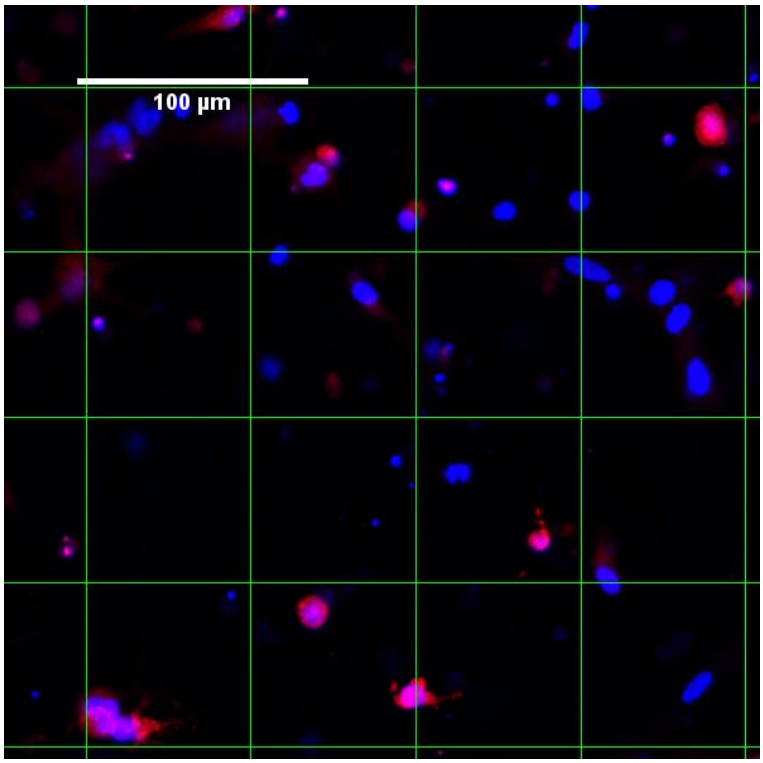


**Figure 4.13: Analysis of Cell Viability using Cell Counter Macro from ImageJ.** The Cell Counter macro from FIJI assisted in the analysis of cell viability by allowing a grid and cell counter markers to be placed over the image. The computer program kept count of the number of marked cells in each category. Live cells, stained blue, were marked '1' and dead cells, stained red AND blue, were marked '2'. Scale bar represents 100 µm.

### 4.3.10 Analysis of Astrocyte Reactivity

As described in the previous chapter, the analysis of immunofluorescence staining for GFAP was performed to determine the extent of astrocyte activation. The general immunostaining methods used in this study are described in Section 2.2.8.2. The

secondary antibody used in this study was conjugated to a green fluorophore, rather than the red fluorophore used in the previous sections. This was due to the requirement for multiple assays to be performed on one gel, and in particular because the cell viability Dead stain resulted in red fluorescence.

#### 4.3.10.1 Image Processing and Image Analysis of Astrocyte Reactivity

The general imaging methods used in this study, with regard to capturing the images using the confocal microscope, are described in Section 2.2.9.

The images that were captured for the analysis of astrocyte reactivity were tiled images from across the entire impact site. The tiled images were large and depended on the size of the impact zone (which varied); the images represented a scan of approximately 7 x 2 mm of the gel. The size of the tiled images meant that additional methodology had to be developed in order to quantify astrocyte reactivity in a meaningful way.

*Stitching Tiled Images*

The impact zones were difficult to image using the confocal microscope because estimating a suitable number of tiles for each scan did not always result in a scan of the right dimension to capture the entire impact zone in one scanned image. Therefore it was sometimes necessary to join two tiled images together before performing image analysis techniques.

The FIJI plugin 'Pairwise Stitching' was used to stitch the tiled images together (Preibisch et al., 2009; Schindelin et al., 2012). Two tiled images before and after pairwise stitching is shown are Figure 4.14. The stitched images remained multi-channel images that could be analysed in the same way as before they were stitched.

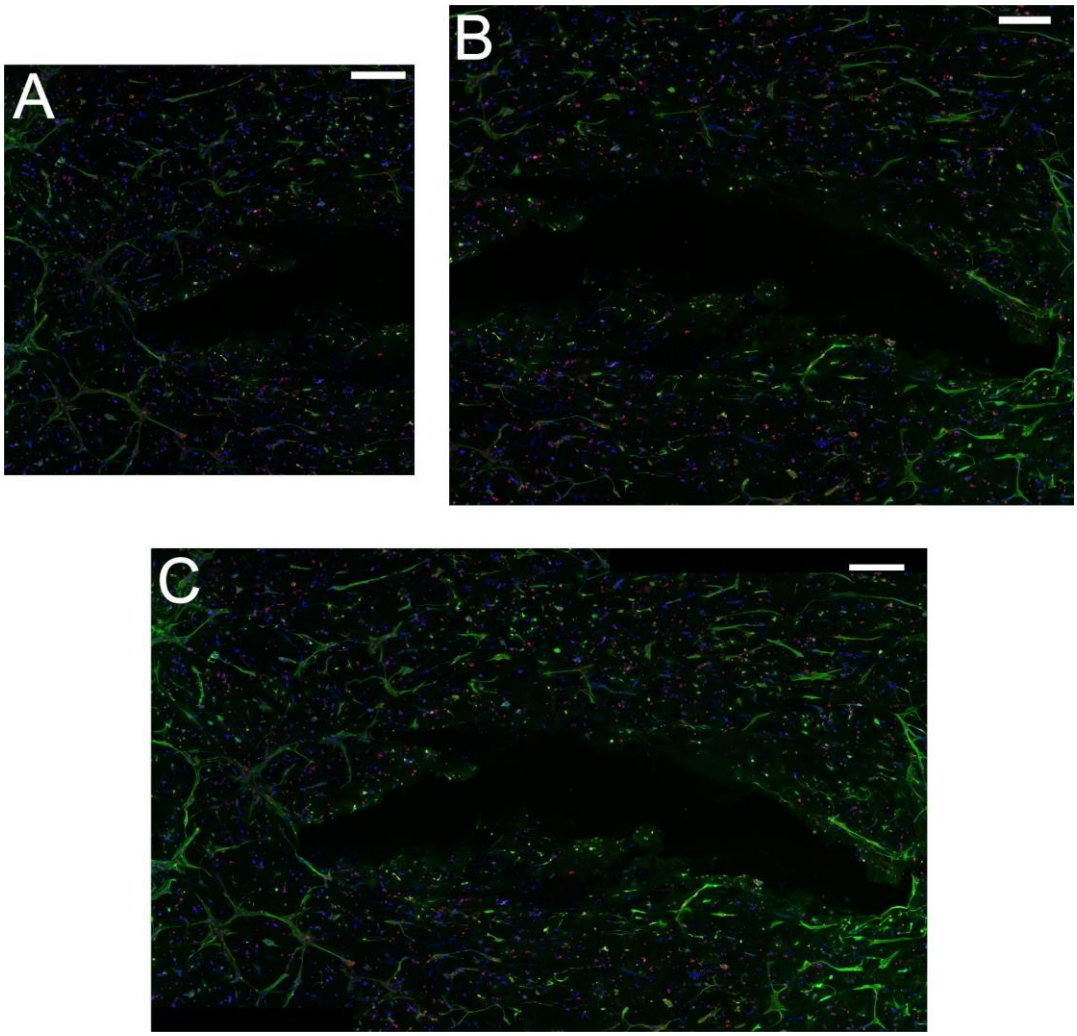


**Figure 4.14: Stitching Tiled Images Using FIJI.** The Pairwise Stitching plugin was used to stitch two tiled images together when required. Images (A) and (B) contain the left and right portions of the impact zone, respectively. Following Pairwise Stitching, a multi-channel stitched imaged of (A) and (B) was created (C). Primary astrocyte cells (4 x $10^6$ cells per gel) were stained for GFAP (green), nuclei (Hoechst – blue) and dead nuclei (Dead viability stain – red) following impaction of the gel using an IH impactor. Confocal optical sections of the gel sampled in an xy-plane on the gel surface (z = 0 µm for A, B, C). Scale bars each represent 500 µm.

*Image Analysis of the Morphological Indicators of Astrogliosis*

The FIJI image analysis software was used to analyse the tiled images using the same thresholding techniques that were described in Sections 3.7.1.1 and 3.7.1.1.1.

However, rather than analysing the image in its entirety, methodology was developed to analyse the images in zones around the impact zone.

Firstly, the impact zone was traced using the FIJI 'Freehand Selection' tool. The perimeter of the impact zone was clearly visible due to the void left behind by the impaction. A Phansalkar threshold was then applied to the images, as described in Section 3.7.1.1. The impact zone perimeter was then measured and saved as a Region of Interest (ROI), as shown in Figure 4.15.

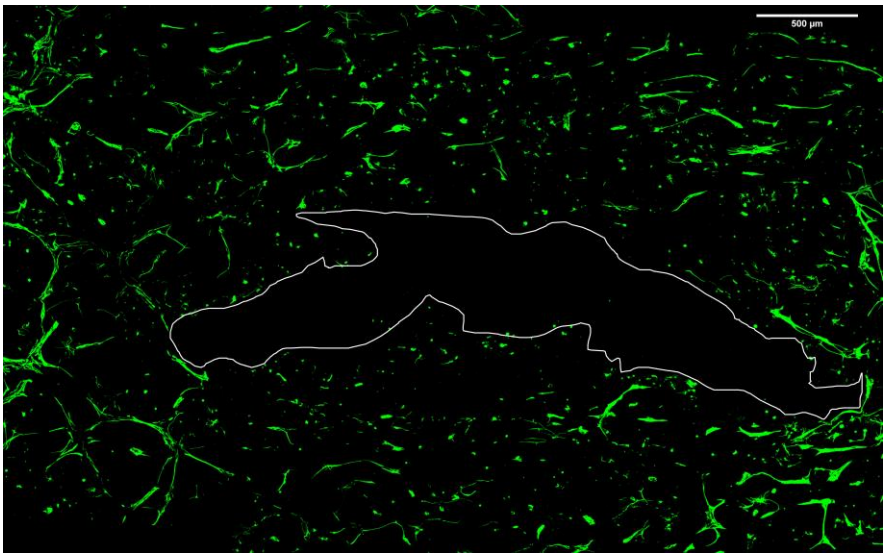


**Figure 4.15: Impact Zone Trace Using FIJI.** The impact zone was traced using the FIJI freehand selection tool. Primary astrocyte cells (4 x $10^6$ cells per gel) were stained for GFAP (green). The image shown above shows the impact zone trace (white line) overlaid onto a single-channel (GFAP) image with the Phansalkar threshold applied. Confocal optical section of the gel sampled in an xy-plane on the gel surface (z = 0 µm). Scale bar represents 500 µm.

After the impact zone had been traced and saved as a ROI, the 'Analyze Particles' tool was used to measure the area of GFAP expression and the circularity of the cells, as described in Section 3.7.1.1.1. Once the measurements had been recorded, the objects inside the ROI were deleted. Therefore the same cells were not counted twice. The ROI was then enlarged by 100 µm and saved as a second ROI. The Analyze Particles tool was used to analyse the cells within a 100 µm radius of the impact zone. These

steps were repeated until a 1000 μm radius had been analysed, as shown by the complete impact zone area trace shown in Figure 4.16.

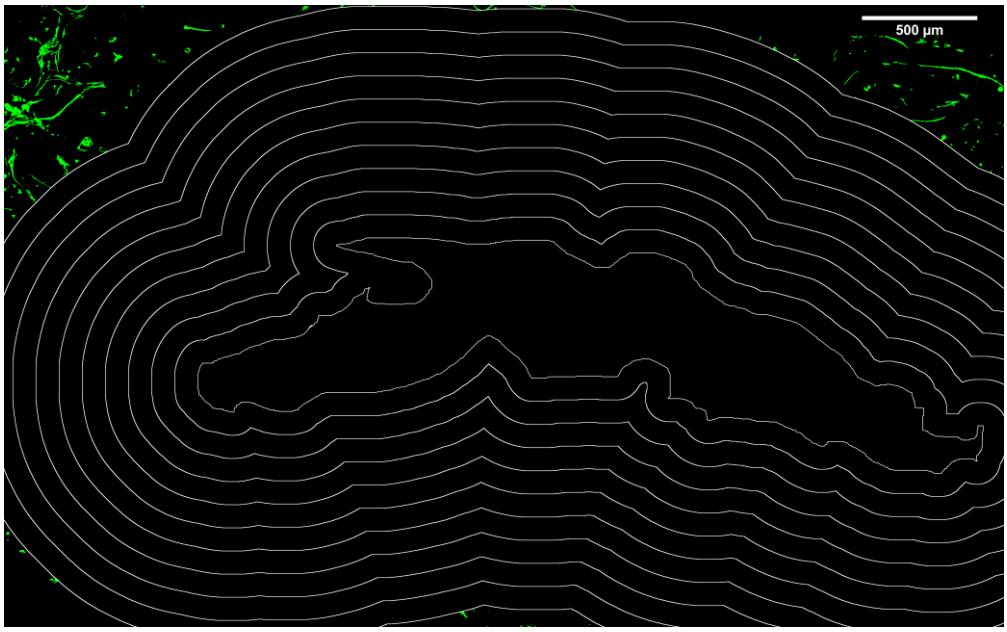


**Figure 4.16: Complete Impact Zone Trace Using FIJI.** Primary astrocyte cells (4 x $10^6$ cells per gel) were stained for GFAP (green) following impaction of the gel using an IH impactor. The impact zone was traced using the FIJI freehand selection tool. The contents of the impact zone were analysed, then deleted and the impact zone trace was increased by 100 μm. This process was repeated in 100 μm increments until 1000 μm surrounding the impact zone had been analysed. The image shown above shows the impact zone trace (white line) overlaid onto a single-channel (GFAP) image with the Phansalkar threshold applied. Areas of GFAP expression that have not been measured because they fall outside of the 1000 μm analysis area are visible at the corners of the image in green. Confocal optical section of the gel sampled in an xy-plane on the gel surface (z = 0 μm). Scale bar represents 500 μm.

As is visible in Figure 4.16, the 100 μm zones surrounding the impact zone were not always complete, depending on the position of the impact zone within the tiled image. The measurements taken from each image were normalised to cell number, therefore variation in cell numbers between zones, between images, and between time-points was accounted for.

*Image Analysis of Impact Zone Shape*

The dimensions and circularity of the impact zones were measured using the impact zone trace described in the methods above. The trace of the impact zone was saved as an image so that these could be compared. The circularity of the impact zones was measured according to the method described in Section 3.7.1.1.1.

*Image Analysis of Cellular Alignment*

This study investigated the effect of mechanical injury simulating SCI on primary astrocyte seeded tethered collagen gels. The tethered gels stimulated the cells to self-align along the long axis in response to the tension within the gels as a result of the tethering bars (East et al., 2010; Georgiou et al., 2013; Phillips and Brown, 2011; Phillips et al., 2005). It was hypothesised that the alignment of cells within the gels might be affected by the impaction due to the possible changes in gel shape and astrocyte phenotype. The alignment of cells surrounding the impact zone was determined using the 'Angle tool' on FIJI. First, the impact zone was traced and saved as a ROI, the impact zone trace was then enlarged in 100 μm increments which were each saved as ROI. The angle tool was used to draw along astrocyte cytoskeletal filaments, as highlighted by the GFAP staining, and the edge of the impact zone to which the cell was located, as is shown in Figure 4.17. This method provided an angle of deviation from the impact edge. Angles of $0^o$ indicated a filament that was completely aligned with the impact zone edge, for example ran parallel to it, whereas angles of $90^o$ indicated filaments perpendicular to the impact zone, which were assumed to not be aligned with the impact zone.

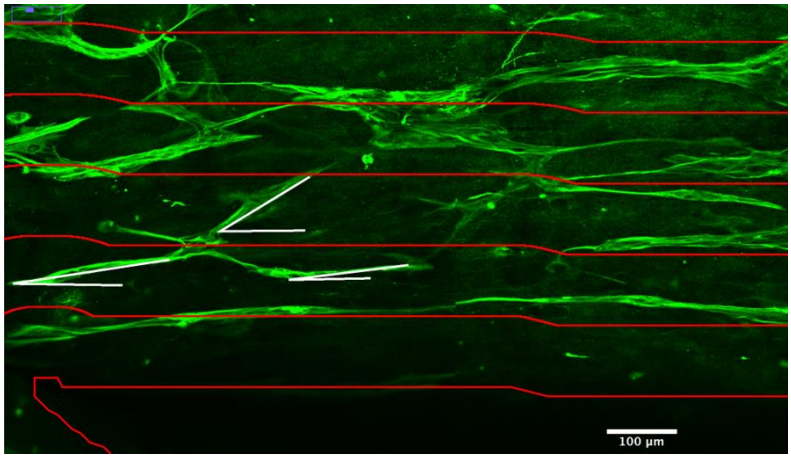


**Figure 4.17: Analysis of Cellular Alignment.** Primary astrocyte cells (4 x $10^6$ cells per gel) were stained for GFAP (green) following impaction of the gel using an IH impactor. The angle between cellular filaments and the impact zone edge was determined using the FIJI 'Angle tool'. Red lines indicate the impact zone trace at 100 µm increments. White lines indicate representative measurements of 30.8°, 9.5° and 5.9° using the Angle tool. Scale bar represents 100 µm.

## 4.4 Results

### 4.4.1 Determination of Astrocyte Population

Immunocytochemical staining of cells that were sampled from each cell isolation batch for each experiment and cultured on slides in 2D, provided an estimate that the cultured cells were at least 90% astrocytes, based on the positive GFAP stain associated with at least 90 % of cell nuclei.

### 4.4.2 Contraction Assay

The contraction properties of the primary astrocytes were investigated before selecting the seeding density for tethered self-aligned gels, in order to achieve optimal cellular self-alignment (O'Rourke et al., 2015; Phillips and Brown, 2011). The percentage contraction of collagen gels seeded at a range of cell densities was quantified using free-floating gels in a multi-well plate assay. The percentage contraction in the free-floating gels was used to select a suitable seeding density for tethered aligned gels. The percentage contraction of collagen gels increased linearly as the cell seeding density was increased from 0.5 x $10^6$ cells per ml to 4 x $10^6$ cells per ml, reaching 70.7 % contraction. The rate of percentage contraction plateaued from 4 x $10^6$ cells per ml to 5 x $10^6$ cells per ml, as shown in Figure 4.18.

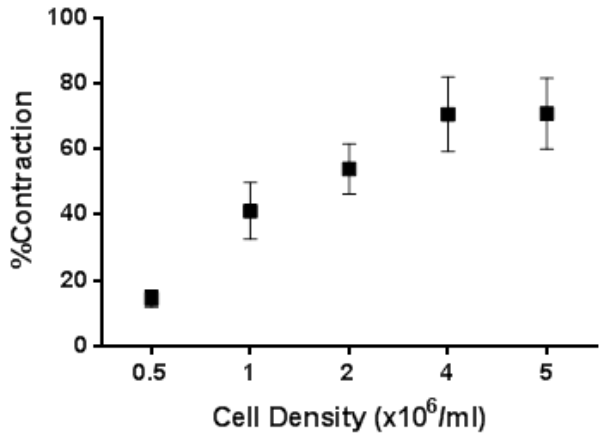


**Figure 4.18: Percentage Contraction of Collagen Gels Containing Primary Astrocytes at Increasing Seeding Densities.** The percentage contraction was calculated using image analysis of contracted gels to produce a contraction profile. Data are mean plus 95 % confidence limits, n = 6.

The cell seeding density for tethered self-aligned gels was dependant on cell type. The study by O'Rourke (2015) showed that a cell seeding density which would provide a contraction profile of approximately 70 % in a free-floating gel would be appropriate to stimulate cellular self-alignment in a tethered gel. The study by O'Rourke (2015) showed that a seeding density of 2 x $10^6$ C6 cells per ml was sufficient to provide 68 % contraction within type-I collagen gels. However, the contraction profile of free-floating type-I collagen gels seeded with primary astrocyte cells indicated that an increased seeding density of 4 x $10^6$ cells per ml was required to provide 70.7 % contraction.

### 4.4.3 Pilot Impaction Study at UCL

The pilot impaction study was undertaken at University College London (UCL) using a Hatteras PCI3000 Precision Cortical Impactor™ (Hatteras impactor). Tethered C6 seeded (2 x $10^6$ cells per ml) collagen gels were prepared and allowed to contract and self-align for 24 hours before impaction using a 2 mm diameter impactor tip at an impact speed of 1.5 m/s, to a depth of 1.8 mm into the gel, and with a dwell time of 100 ms.

#### 4.4.3.1 GFAP Expression Within Impacted Gels - Pilot Study

Representative images of the immunostaining for GFAP, which is a marker of astrogliosis, are shown in Figure 4.19. An increase in GFAP expression was observed after three days in culture from impaction, in comparison to gels 24 hours after impaction. The C6 cells appeared to be more ramified at the later time point, as indicated in Figure 4.19 by the increased number of filaments and irregular shape.

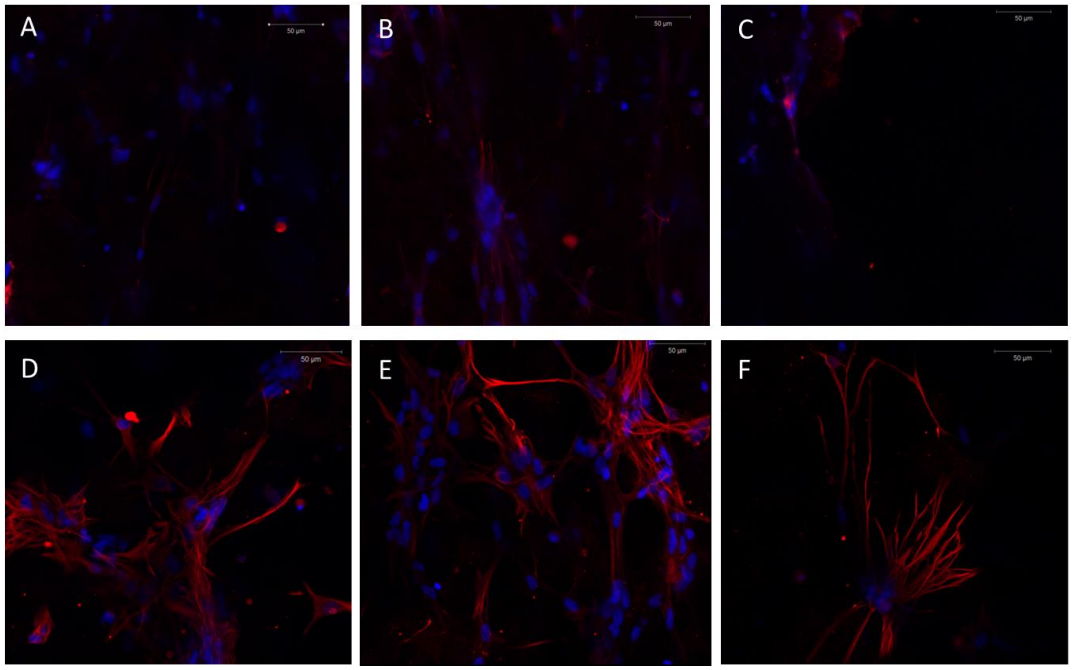


**Figure 4.19: Immunostaining for GFAP in C6 Seeded Gels (Pilot Study).** The C6 cells seeded within impacted tethered gels were immunostained for GFAP (red) and the nuclei were stained using Hoechst (blue). Images A to C represent astrocytes in tethered gels 24 hours after impaction. Images D to F represent astrocytes in tethered gels three days after impaction. Scale bars represent 50 µm.

### 4.4.4 Impaction Investigations at the University of Leeds

The remainder of this part of the study focussed on results obtained using the Infinite Horizons IH-0400 Impactor (IH impactor) at the University of Leeds.

#### 4.4.4.1 Impactor Tip Diameter

The impactor software was programmed to calculate the displacement and velocity of the impaction after it had occurred, however it was not possible to select these parameters for the experimental set up.

Tethered aligned collagen gels, with a cell seeding density of 2 x $10^6$ C6 cells per ml, were impacted according to the experimental parameters used to create SCI in *in vivo* models by the research group in Leeds (personal communication, Yazi Al'Joboori). During *in vivo* experiments, Al'Joboori impacted rat spinal cord at 200 kdyn (desired), 0 ms dwell time, however under these conditions using the tethered aligned gels, the actual force value was reported as 391 kdyn. Repeating the test at 100 kdyn (desired) input force, 0 ms dwell time, resulted in an actual force value output of 337 kdyn. These results indicated that the impactor was not controlling the force of the impaction as expected. In order to investigate the reason behind the actual force outputs being approximately 200 to 300 kdyn higher than expected, an experiment was designed to investigate the upper and lower thresholds of the impactor. The sorbothane test block was utilised in order to minimise variation that might have been associated with the collagen gels. The results of this experiment are shown in Figure 4.20.

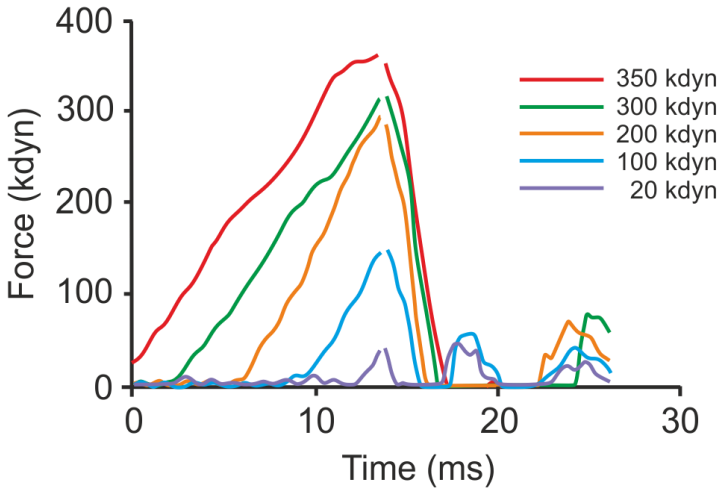


**Figure 4.20: Determination of Upper and Lower Thresholds of the IH Impactor using the Test Block - Force Graph.** The IH impactor was used to impact the sorbothane test block at increasing desired force inputs ranging from 20 to 350 kdyn.

The force graph plots the force value recorded by the force sensor on the impactor tip against the time of the impact experiment. A typical force graph consists of background noise as the tip is translated towards the sample and a large peak as the tip impacts the sample. Background noise was present after the impact peak due to the residual forces experienced as the tip retracted. There was a break in the curve after the maximum force was applied, at the tip of the impact peak, which represented the change in direction of the tip (Scheff et al., 2003). The force plots represented in Figure 4.20 represented the stereotypical force plot shape for inputs of 100 - 300 kdyn. However, at 350 kdyn no background readings were recorded, and at 20 kdyn the background peaks were of the same height or smaller than the impact peak. The results of this experiment indicated that when the test block was used as the impact sample, the desired and actual force readings were similar.

The force graph was repeated using C6 tethered gels, the lower force range of 20 - 50 kdyn was selected due to the high actual force readouts previously observed at 100 and 200 kdyn. As is shown in Figure 4.21, when the IH impactor impacted collagen gels, the actual force detected was much higher in comparison to the desired force; for example, a desired force of 50 kdyn resulted in an actual force of 395 kdyn.

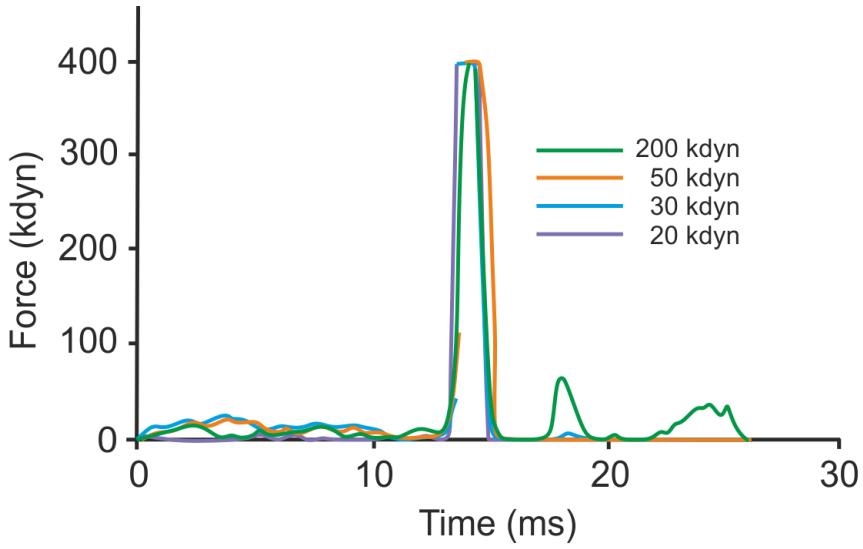


**Figure 4.21: Determination of Upper and Lower Thresholds of the IH Impactor using C6 Seeded Gels - Force Graph.** The IH impactor was used to impact C6 seeded (2 x $10^6$ per ml) tethered collagen gels at increasing desired force inputs ranging from 20 to 200 kdyn.

The experiment was repeated using acellular fully stabilised (FS) gels, to determine whether the stiffness of the gel would have an effect on the actual force readouts. As is shown in Figure 4.22, when the IH impactor impacted FS collagen gels, the actual force detected was much higher in comparison to the desired force. The force output readings from the FS gels were similar to the results obtained from impactions of the less stiff C6 seeded gels.

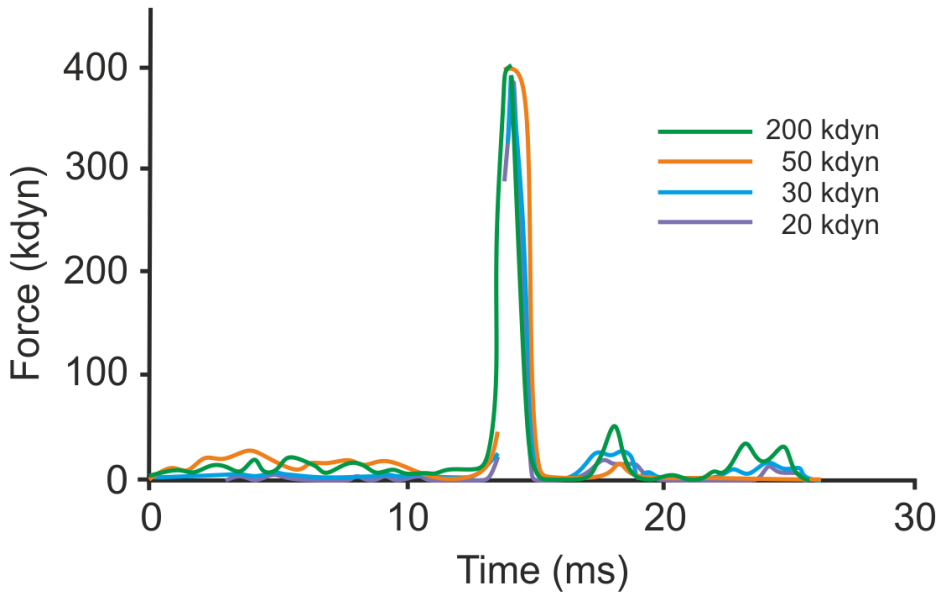


**Figure 4.22: Force Graph of the Actual Force Recording from Impacted Fully Stabilised Gels.** The IH impactor was used to impact acellular fully stabilised collagen gels at increasing desired force inputs ranging from 20 to 200 kdyn.

Whilst performing these experiments on the C6 seeded collagen gels, it was noted that the impactor tip was travelling the entire way through the gel and impacting the tissue culture plastic underneath. It was proposed that increasing the diameter of the impaction tip might improve the accuracy of the output measurements by increasing the surface area of the tip. An experiment was designed to investigate the effect of increasing impaction tip diameter on the actual force output reading and the displacement reading of the IH impactor. Impaction tips with diameters of 2.5 mm, 4 mm and 6.5 mm were used. In order to minimise error in these experiments, the sorbothane test block was used for each impaction. The effect of increasing tip diameter is shown in Figure 4.23.

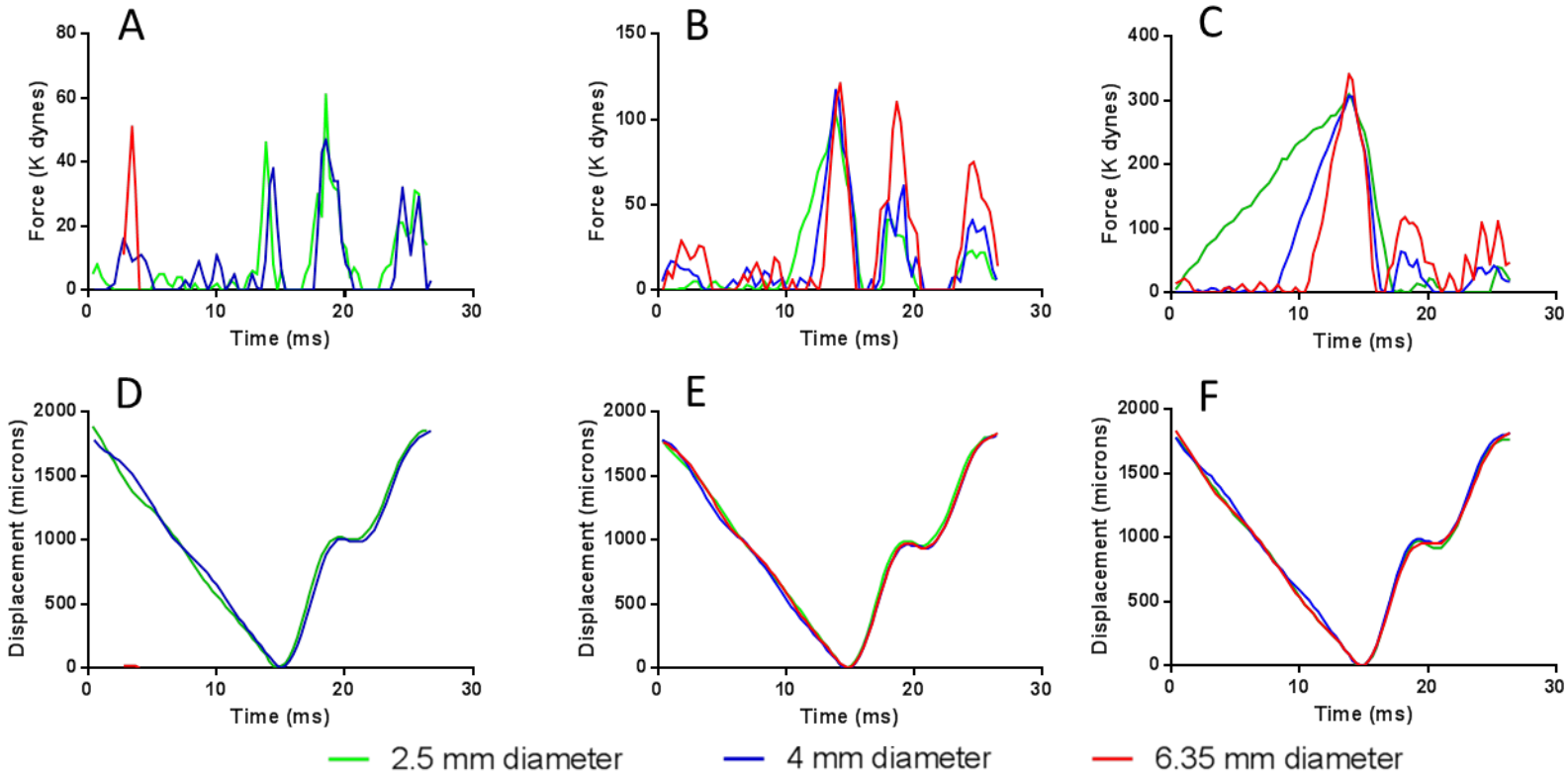


**Figure 4.23: Increasing Impaction Tip Diameter - Effect on Actual Force and Displacement Outputs.** Impaction tips of either a 2.5 mm (green), 4 mm (blue), or 6.5 mm (red) diameter were loaded into the IH impactor which impacted a sorbothane test block at the desired force of 30 kdyn (A & D), 100 kdyn (B & E) or 300 kdyn (C & F) to produce the actual force readings (A to C) and the displacement readings (D to F).

Increasing the tip diameter had no effect on the peak actual force when comparing 2.5 mm to 4 mm diameter impaction tips at 100 and 300 kdyn. At a 30 kdyn desired force the 6.5 mm tip showed a single actual force peak at 51 kdyn at 3.4 ms, however the corresponding displacement graph showed that the tip had not been displaced. At a desired force of 30 kdyn, a difference in the actual force peak of approximately 10 kdyn was observed between the 2.5 mm and 4 mm impaction tips, although the difference between the peak value and the background peaks was also approximately 10 kdyn for both tips.

The displacement graphs are a plot of displacement (microns) of the tip relative to the deepest point it reaches in the sample, against time (milliseconds). The graph was inverted to correspond to the physical movement of the tip as an impact occurred. The characteristic plateaued area in the second half of the curve represented the tip retraction slowing down (Scheff et al., 2003). The displacement curves showed no difference in displacement when tips of 2.5 mm, 4 mm, or 6.5 mm diameter were tested at a desired force of 100 or 300 kdyn. This indicated that increasing the impactor tip diameter had no effect on the distance the tip travelled through the sample. These results indicated that the force sensor of the IH impactor was not sensitive enough to detect changes in impact surface area with regard to the displacement or actual force readings.

#### 4.4.4.2 Impaction Depth Control

The displacement of the IH impactor could not be controlled by the impactor software, which resulted in the impactor tip travelling all of the way through the gel to the base of the mould. A mechanism of controlling the displacement manually, without the computer program, was investigated using acellular tethered gels. The impactor tip was lowered by one full turn of the vertical adjustment knob at a time, while maintaining all of the other parameters at 200 kdyn, dwell time 0 ms, and a 2.5 mm diameter impaction tip.

A tethered acellular gel was positioned on the impaction platform and aligned centrally underneath the impaction tip. The vertical adjustment knob was turned eight full turns before impaction; the impactor tip did not reach the gel at this height. The

initial impactor tip height was reduced to seven full turns of the vertical adjustment knob, but again the impactor tip did not reach the gel. At six full turns the gel was impacted. The gels were analysed using a bright field microscope, where it was possible to confirm if the impaction tip had pierced through to the tissue culture plastic or not. At six full turns, the impaction site was barely visible using the bright field microscope. At five full turns the impaction site was clearly visible, yet the gel had not been pierced through entirely. At four full turns, the gel was pierced all of the way through to the base. Therefore all subsequent impaction experiments were performed with the impactor tip starting point at five full turns from the surface of the gel.

#### 4.4.4.3 Test Block Reference Graph

The sorbothane test block was used as a reference before each impaction session, in order to check that the impactor was performing as expected. The actual force plots for the test block reference checks are shown in Figure 4.24 with the exemplary actual force plot from the IH impactor User Manual overlaid. This shows that the test block repeatedly showed a typical actual force plot shape, when impacted at 200 kdyn, 0 ms dwell time and five full turns of the vertical adjustment knob; although the background peaks appear more variable, the actual force peak remained in the same position and within 10 kdyn of the same actual force input of approximately 110 kdyn.

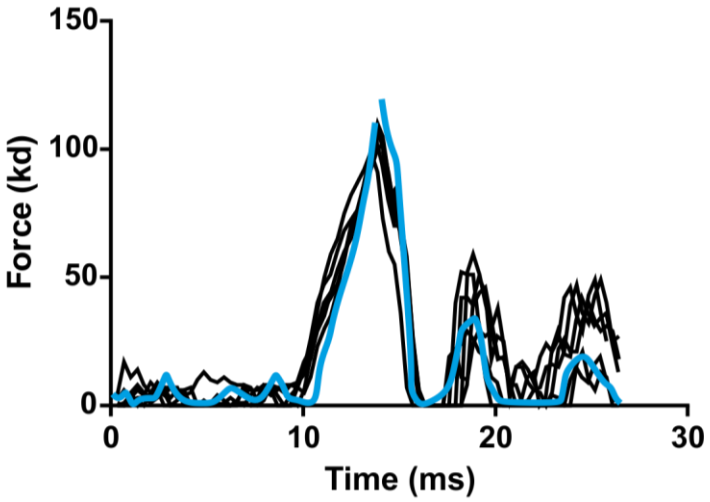


**Figure 4.24: Test Block Reference Graph.** Plots of the test block reference checks are shown in black, whilst the IH impactor manual exemplary reference plot is shown in blue.

### 4.4.5 Contraction of Tethered Gels

The chemical stimulant, TGF-β1, has been used to aid contraction of collagen gels seeded with primary astrocytes (O'Rourke et al., 2015). At a seeding density of $4 \times 10^6$ primary astrocyte cells per ml, with the addition of 10 ng/ml TGF-β1 supplemented DMEM media, the tethered collagen gels showed contraction profiles of 28.2 % (± 1.3 SEM) after 24 hours in culture, as shown by the representative gel pictured in Figure 4.25. The gels were impacted after 24 hours in culture.

**Figure 4.25: Gel Contraction after 24 hours.** The 1000 µl type-I collagen gels, seeded with 4 x $10^6$ primary astrocyte cells per ml, with the addition of 10 ng/ml TGF-β1 supplemented DMEM media, contracted by an average of 28.2 % (± 1.3 SEM) after 24 hours in culture.

Cellular self-alignment was detected in the gels, as shown in the representative images in Figure 4.26. The primary astrocyte cells within the delta zones of the gel showed relatively few filamentous processes, as highlighted by immunocytochemical staining for GFAP. The filaments that were detected showed random orientation. The primary astrocyte filaments in the side regions of the tethered gels were numerous and aligned in the direction of the longitudinal axis of the tethered gels.

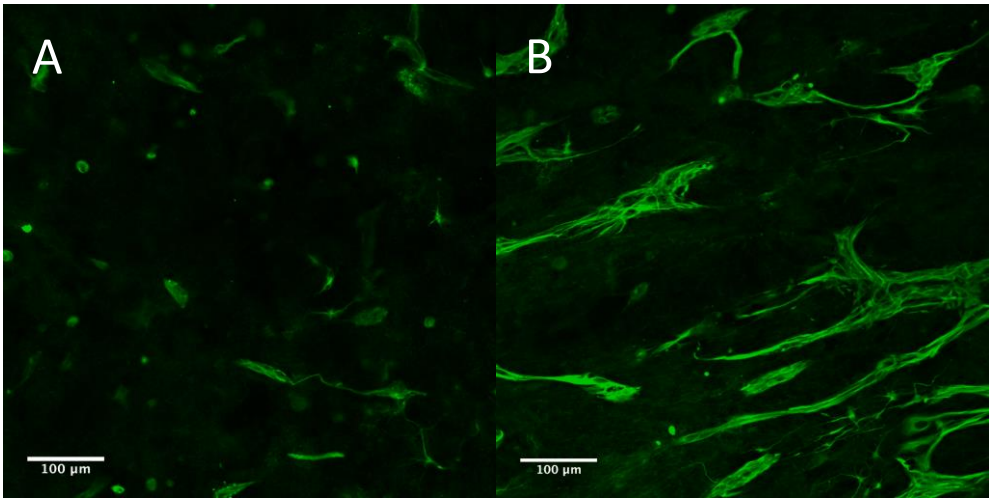


**Figure 4.26: Cellular Alignment within Tethered Gels.** Primary astrocyte cells (4 x $10^6$ cells per gel) were imaged following contraction and self-alignment of tethered type-I collagen gels. Cellular alignment differed within different regions of the gels due to the properties of the tethered environment, as highlighted by immunocytochemical staining of primary astrocytes for GFAP (green). The alignment was least prominent in the delta zones (A) and most prominent at the sides of the gels (B). Increased ramification of the cells and increased expression of GFAP was detected at the sides of the gel in comparison to the delta zones. Scale bars represent 100 µm.

### 4.4.6 Impact Zone Morphology

The impact zone morphology was analysed using FIJI image analysis software; the impact zones were variable in shape and size at all time points, as shown by the impact zone traces in Figure 4.27. At later time points, the impact zones appeared more elongated in the direction of the longitudinal axis of the tethered gels. At day 10, one of the impact zones was significantly smaller and more rounded in comparison to the other impact zones.

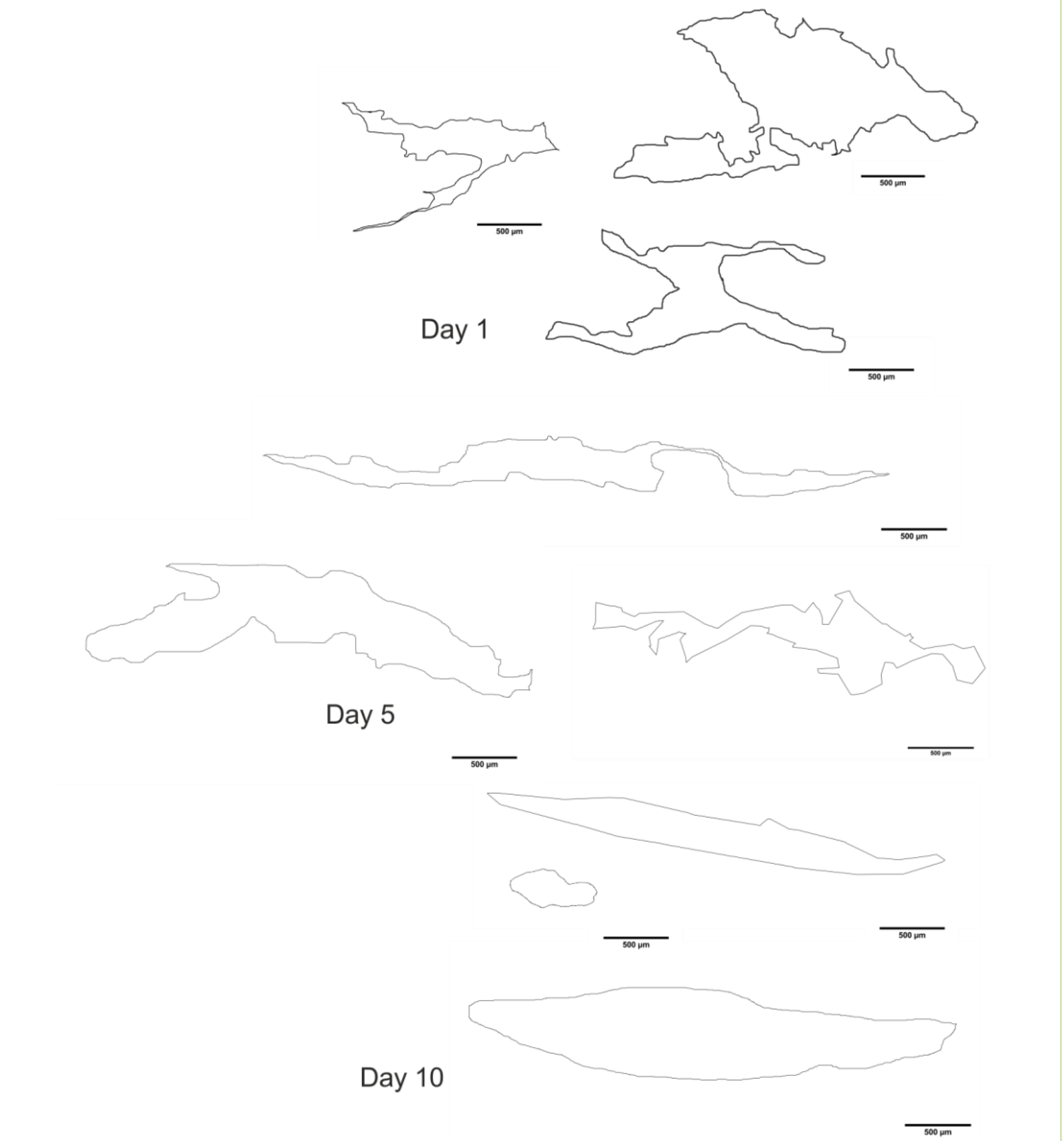


**Figure 4.27: Impact Zone Morphology after Impaction.** The impact zones were traced using the FIJI freehand selection tool. The image shown above shows the surface impact zone trace of three impacted tethered gels 1, 5 and 10 days after impaction, different gels were tested at each time point.

The circularity of the impact zones was analysed using the FIJI software. A perfectly spherical impact zone would have a value of 1, whilst smaller values would indicate progressively more irregularly shaped impact zones, thus providing an indicator of how rounded or irregular the impact zones were. The circularity analysis showed that

the impact zones one day after impaction were significantly more irregular than the impact zones at ten days after impaction, as shown in Figure 4.28.

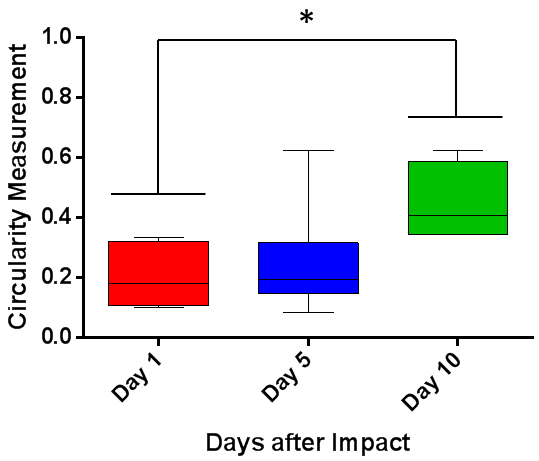


**Figure 4.28: Circularity of Impact Zone Morphology.** Tethered self-aligned type-I collagen gels, seeded with primary astrocyte cells (4 x $10^6$ cells per gel) were impacted using an IH impactor. The circularity of the impact zones of the impacted tethered gels was determined at 1, 5 and 10 days after impaction (n=3), by analysing the shape of the impact zone traces using FIJI.
* = $p<0.05$ (Kruskal-Wallis with Dunn's post hoc).

In terms of statistical significance, to test the effect of culture length after mechanical impact on the circularity of tethered gel impact zones, measurements were analysed using a non-parametric, unlinked, multiple comparison, Kruskal-Wallis test with Dunn's post-hoc, this showed a significant difference between day 1 and day 10 impact zone circularities ($p<0.05$). The impact zones were statistically more circular ten days after impaction, in comparison to one day after impaction.

### 4.4.7 The Effect of Mechanical Impaction on Cell Death

The percentage of dead primary astrocytes within the impacted cells was determined using the Dead (ethidium homodimer-1) stain from the Live/Dead® Cell Viability Assay, and the Hoechst nuclear stain. Images of the gels were analysed at eight locations around the gel; in the delta zones, side zones, middle, and on the impact

zone edges. The percentage cell death ranged from 31 % to 38 % across all conditions tested, except within gels at ten days after impaction, where cell death was higher at 45 % (± 2.7 SEM). The percentage death of primary astrocytes within impacted gels was not significantly different compared to the cell viability of non-impacted control gels ($p>0.05$) at one and five days after impaction, as shown in Figure 4.29. There was a significant increase in the percentage cell death at ten days after impaction (45 % ± 2.7) compared to the non-impacted control (31 % ± 2.6), however there was not a significant difference in cell death when impacted gels were compared over the ten day period ($p>0.05$). In order to determine if there was any statistical significance, the raw percentage data were arcsine transformed before analysis using a 2x2 independent ANOVA.

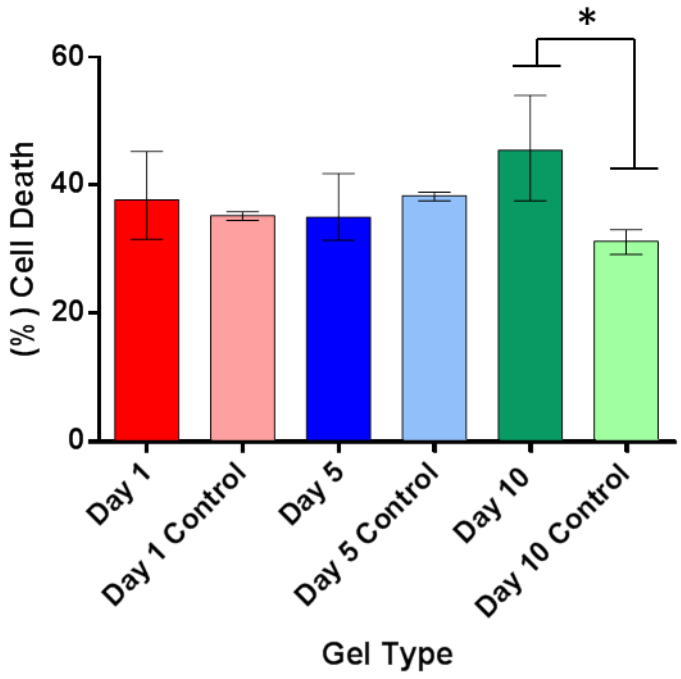


**Figure 4.29: Effect of Mechanical Impaction on Cell Viability.** The percentage cell death of primary astrocytes (4 x $10^6$ cells per gel) within tethered self-aligned collagen gels was determined by co-localisation of the Live/Dead cell viability Dead stain with Hoechst nuclear stain. Gels impacted using the IH impactor after 24 hours in culture, at 200 kdyn desired impact force. Control gels were not impacted. Cell viability was determined after 1, 5 or 10 days in culture following impaction. The % cell death was high across all samples tested, including the non-impacted control samples. Data presented as mean ± arcsine transformed error bars (n = 3). Two-way ANOVA with post-hoc Tukey test; * $p<0.05$ Day 10 vs Day 10 control.

### 4.4.8 Imaging the Impact Zones

It was initially intended to analyse cellular alignment at several locations throughout the gel; the surface of the impact, middle of the impact, and base of the impact. The impaction protocol was designed to limit the depth of the impaction tip through the gel, so that there would be a volume of gel underneath the impact zone which could be analysed. Tiled image scans were taken of the surface and middle of the gel impact zones; the middle of the impact zone was determined by focussing through the

gel in order to calculate the gel centre using the confocal microscope x, y, z positioning readout. However, the base of the impact zones was not easily located or imaged; there was not an obvious base to the empty impact zone when using the confocal microscope. Initial attempts to image the base of the impact zone were time consuming, and in some cases the impact tip had pierced the entire way through the gel. It was decided to focus the imaging on the surface and middle regions due to the adverse photobleaching effects that repeated attempts to image the base of the impact zone would have on the fluorescently labelled cells.

However, it was possible to image the effects of the impaction on the very base of some of the gels by focussing the microscope onto the non-impacted side of the gel; in some gels the impaction depth resulted in a hole in the gel spanning the entire thickness of the gel, in others, a fluorescently visible outline of the impact zone was detected on the base of the gel, this is shown in Figure 4.30.

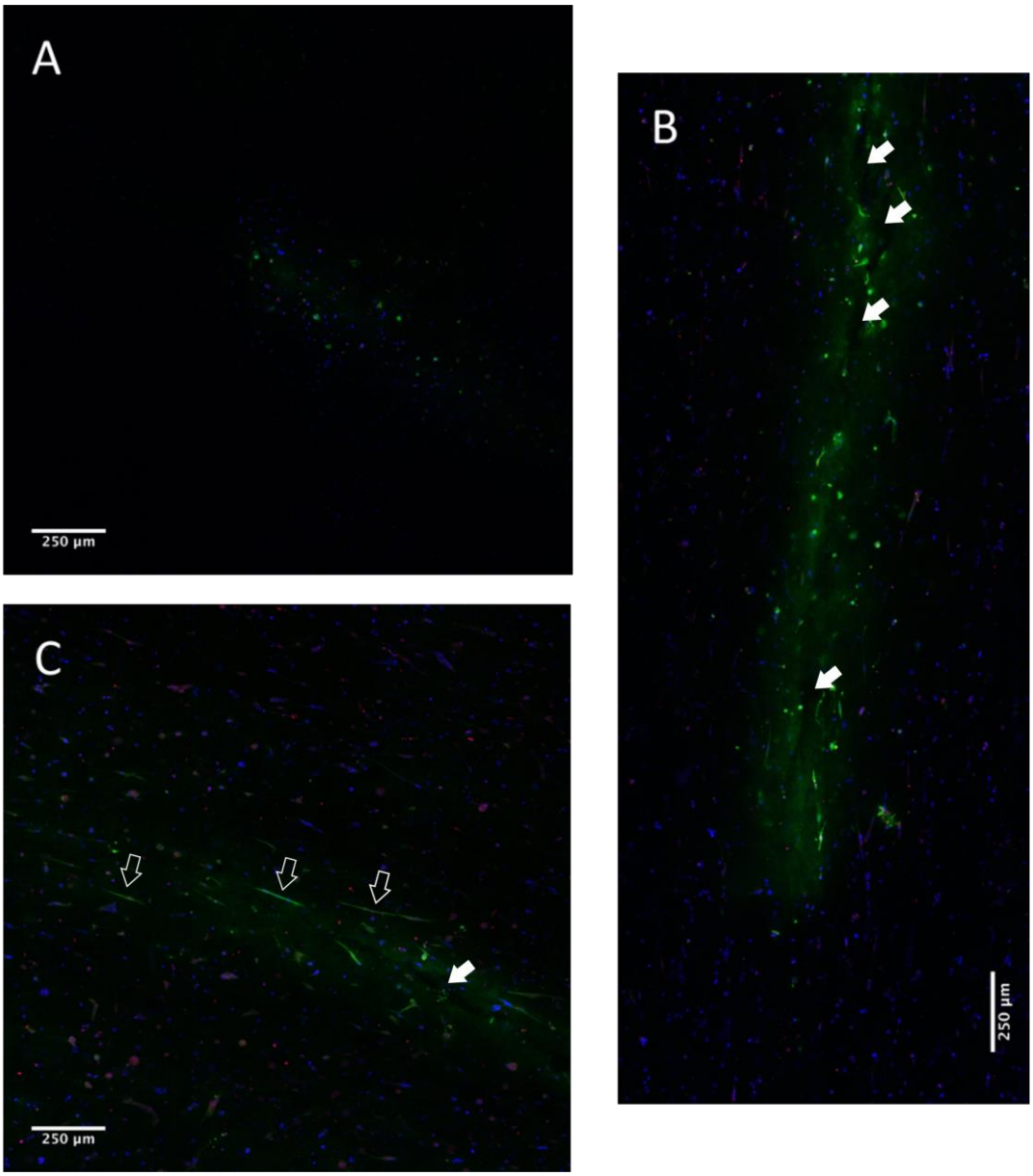


**Figure 4.30: Imaging the Base of Impacted Collagen Gels.** Tiled images of the base of the impact zone at one (A), five (B) and 10 days (C) after impaction. Tiled images of the impact zone base were difficult to acquire, however in some cases, the impact zone was detectable on the base of the gel (non-impacted side) due to an increased level of fluorescence in one particular area. Solid arrows indicate areas where the impact void extends through to the base of the gel. Outlined arrows indicate aligned astrocyte filaments. An increase in GFAP expression was observed from day one to day ten after impaction. Primary astrocyte cells ($4 \times 10^6$ cells per gel) were stained for GFAP (green), nuclei (Hoechst - blue) and dead nuclei (Dead viability stain - red). Scale bars represent 250 µm.

### 4.4.9 The Effect of Mechanical Impaction on Astrocyte Alignment

The alignment of astrocyte filaments was determined using image analysis of impacted tethered collagen gels, immunocytochemically stained for the cytoskeletal protein, glial fibrillary acidic protein (GFAP). Cellular filaments were analysed in 100 μm increments from the impact zone edge.

Cellular filaments were found to be aligned with the impact zone at each time point, as shown in Figure 4.31. The smaller the angle reported, the more aligned the filament was considered to be.

The alignment measurements were analysed using an independent, one-way ANOVA. A Tukey's multiple comparisons post-hoc test revealed that there was a significant increase in angle of deviation at the 200 μm and 300 μm increments from one day to ten days after impaction ($p<0.05$). At one day after impaction, there was a significant increase in the angle of deviation between the area closest to the impact zone (100 μm), outwards to the 500 μm, 600 μm and 800 μm increments ($p<0.05$, $p<0.001$, $p<0.01$ respectively). At five days after impaction, there was a significant increase in the angle of deviation from the 100 μm increment and each of the 300 μm to 1000 μm increments, there was also a significant increase in the angle of deviation from the 200 μm increment compared to the 600 μm and each of the 800 μm - 1000 μm increments, and a significant increase in the angle of deviation from the 300 μm increment to the 900 μm increment. At ten days after impaction, there was a significant increase in the angle of deviation from the filaments in the 100 μm increment in comparison to each of the 300 μm to 1000 μm increments ($p<0.0001$ at each comparison). The p-values of each of the significant comparisons are presented in full in Table II.II of Appendix II. Whilst performing the alignment measurements, it was noted that the alignment appeared most prevalent at the tips of the impact zone, the tips being the narrowest parts at each end of the impact zone.

An increase in the expression of GFAP was observed over the time course of the experiment; this was particularly evident in the images of the impact zones ten days after impaction, in comparison to days one and five.

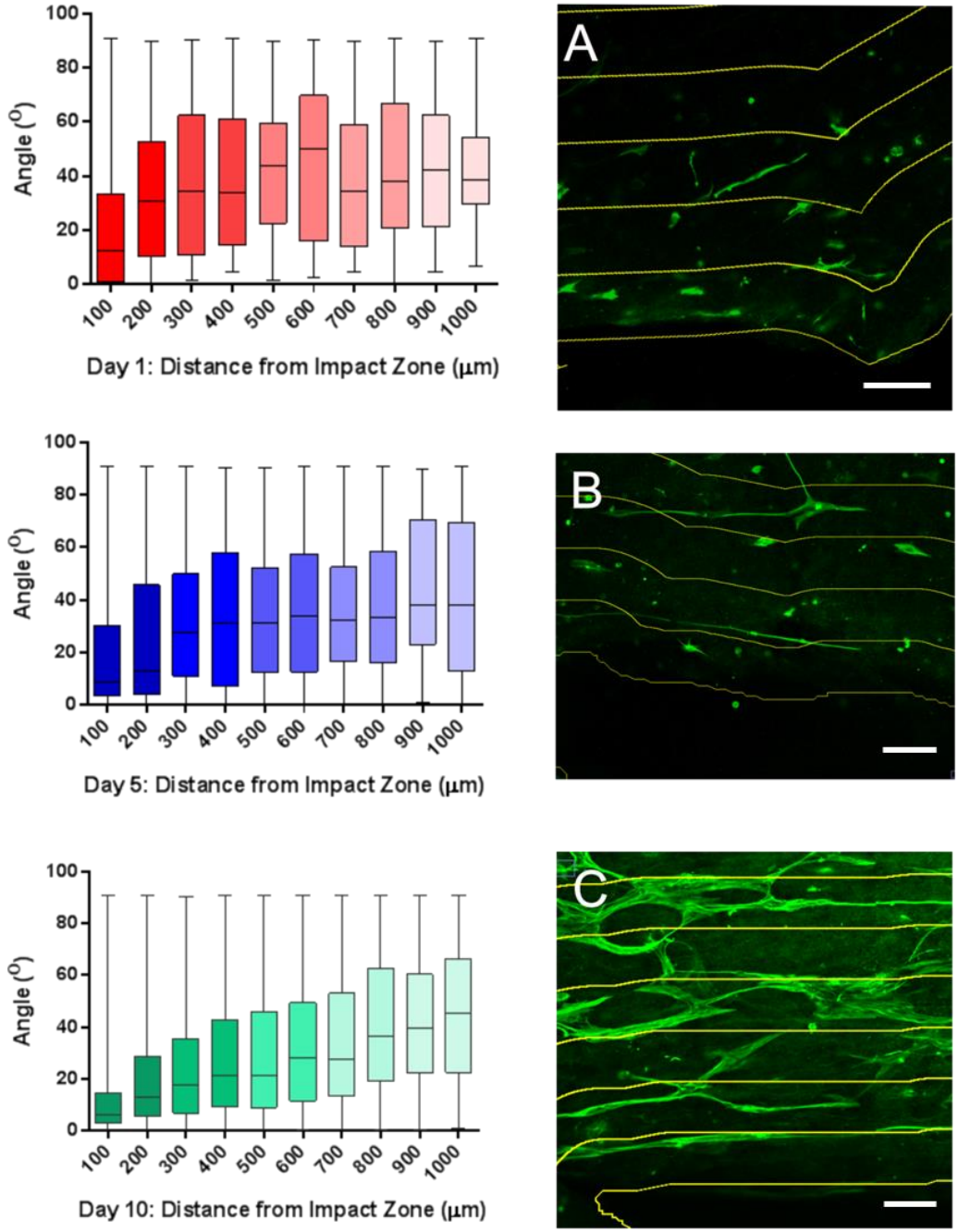


**Figure 4.31: Alignment of Cellular Filaments within Impacted Gels.** The distribution of cellular alignment determined at 100 µm distances from the impact zone at one, five and ten days after impaction. Exemplary images of the first 500 µm increments (yellow lines spaced at 100 µm increments from the impact zone) at one day (A), five days (B) and 10 days (C) after impaction. Primary astrocyte cells (4 x $10^6$ cells per gel) were immunocytochemically stained for GFAP (green). An increase in the expression of GFAP was observed over time. Scale bars represent 100 µm.

### 4.4.10 The Effect of Mechanical Impaction on Markers of Reactive Astrogliosis

Primary astrocyte cells were cultured for 24 hours within tethered self-aligning collagen gels before impaction using the IH impactor at a desired impaction force of 200 kdyn. After impaction, the gels were cultured for one, five, or ten days before analysis. The concentration of primary astrocytes within each tethered collagen gel was four million cells per 1000 µl gel matrix. The gels were fixed and GFAP was detected using immunocytochemical techniques, in order to detect the reactive astrocyte phenotype associated with reactive astrogliosis. The double stranded DNA marker, Hoechst, was used to detect nuclei. Gels were imaged using the imaging protocol (Section 2.2.9). The images were analysed in 100 µm increments from the impact zone, as described in Section 4.3.10.1.

The total number of cells per 100 µm increment was used to calculate the area of GFAP expression per cell in each region. This calculation was based on counting the nuclei that were positively stained with Hoechst. The Hoechst stain does not allow discrimination between live and dead cells.

#### 4.4.10.1 Effect of Mechanical Impaction on Expression of GFAP

Representative images of immunocytochemical staining for GFAP in impacted gels following one to ten days in culture after impaction are shown in Figures 4.32 to 4.36 and non-impacted controls in Figure 4.37. As discussed previously, the morphology of the impact zones varied between impactions, as is visible in the images where cross-shaped (Figure 4.32), elongated (Figures 4.33, 4.34 and 4.36), and circular (Figure 4.35) morphologies of the impact zone are present. In each case, the impact zone was smaller when imaged at the middle of the impact zone, compared to the surface. Comparative images of the middle and surface of the same gels are presented in Figures 4.32 and 4.33. The area of GFAP expression detected varied, depending on the time after impact, and whether the gel was imaged at the impact surface or the middle region of the impact zone. Visually, there appeared to be a higher concentration of background fluorescence associated with the first 100 µm of the impact edge in the impacted gels. Similar intense localisations of background fluorescence were not observed in the non-impacted controls, or at other locations in

the impacted gels. The amount of GFAP expression detected appeared to be lower in the non-impacted control gels at all time points that were investigated, as can be observed in Figure 4.37. There was no obvious increase in cell death in any particular area of the impacted gels.

*One Day after Impaction*

A representative tiled image of the surface and middle impaction regions of a gel one day after impaction is shown in Figure 4.32. At this time point, the GFAP staining appeared to be localised around the impact zone edge, spreading outwards in the shape of the impact zone. At a higher magnification, ramified astrocyte cells were observed around the impact zone. The impact zone of this gel had a cross-shaped morphology; the shape is visible in the image of the impact zone middle region, however the impact zone is smaller (Figure 4.32 (B)). There were no cells visible in the impact zone itself, which appeared to be void of cells and gel matrix.

*Five Days after Impaction*

Representative tiled images of the surface and middle impact of two gels five days after impaction is shown in Figure 4.33. The detection of GFAP associated fluorescence was greater in surface images compared to middle images. There was a greater detection of GFAP associated fluorescence compared to the gels one day after impaction. GFAP fluorescence increased around the impact zone edge, outwards and in the middle regions of the impact zone, GFAP staining outlined the shape of the impact zone but was not expressed in as high proportions throughout the surrounding area. Highly ramified astrocytes were visible, in particular on the surface images of the impact zones (Figure 4.33 (A & C); long entangled filaments appeared to align along the impact zone edge. No cells were visible in the impact zone itself, which appeared to be void of cells and gel matrix.

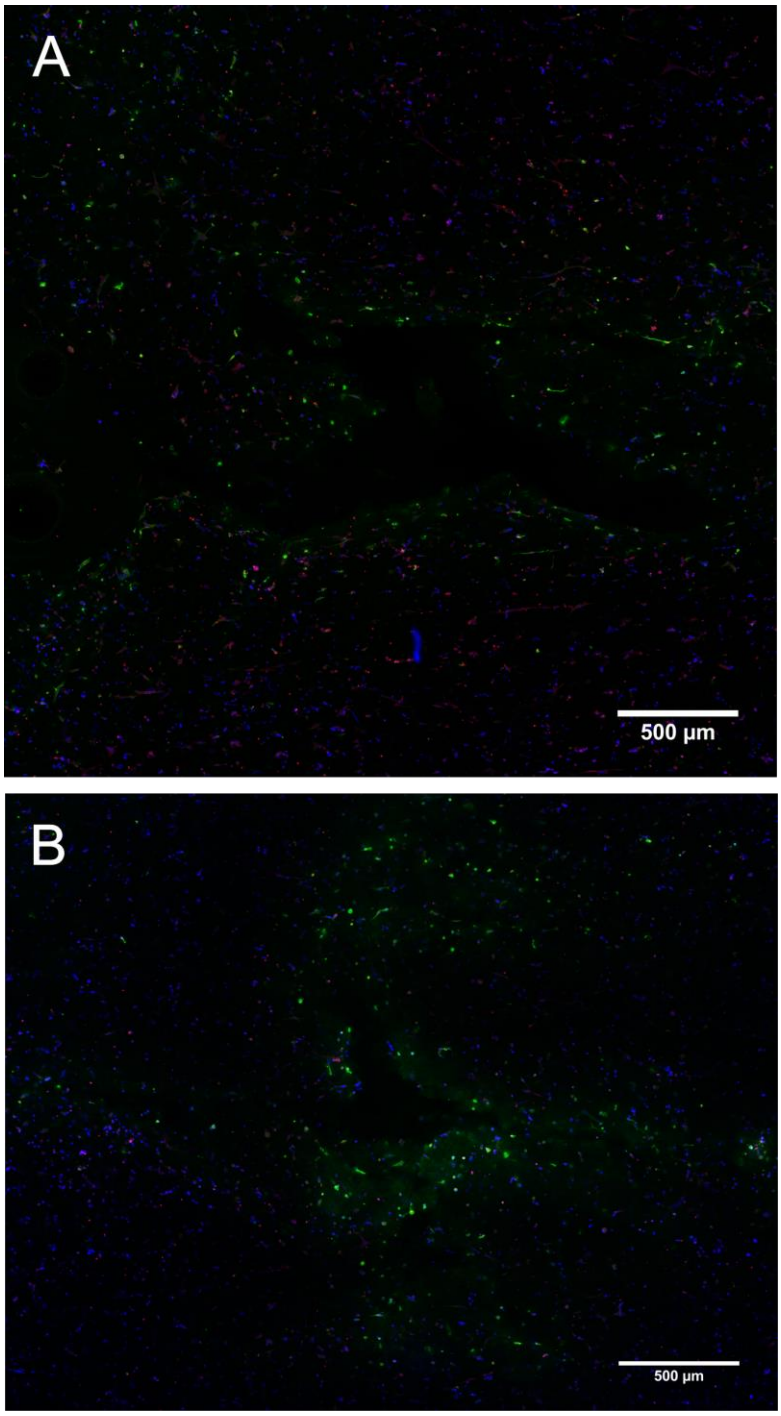


**Figure 4.32: Images of Tethered Collagen Gels One Day after Impaction.** The impacted gels were imaged one day after impaction at the impact surface (A) and middle of the impact (B). A & B are images from the same gel. Primary astrocyte cells (4 x $10^6$ cells per gel) were immunocytochemically stained for GFAP (green) and stained for nuclei using Hoechst (blue) and dead cells (red co-localised to blue). Scale bars represent 500 µm. Confocal optical sections of the gels were sampled in an xy-plane at a depth (z) of 0 µm (A) and 244 µm.

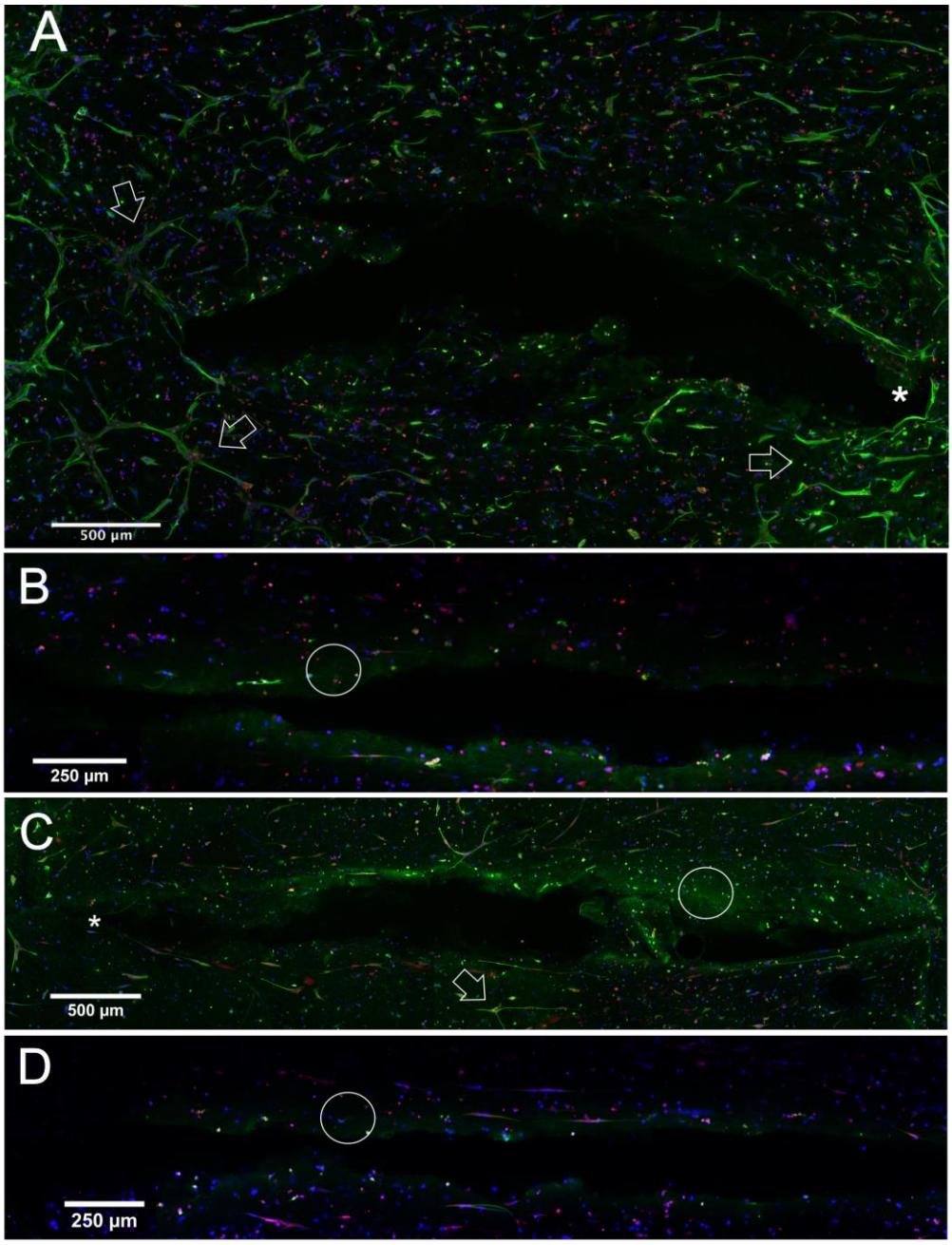


**Figure 4.33: Images of Tethered Collagen Gels Five Days after Impaction.** Gels were imaged 5 days after impaction; A & B and C & D are images from the same gel at the surface (A & C) and middle (B & D) regions of the impact zone. Primary astrocyte cells ($4 \times 10^6$ cells per gel) were immunostained for GFAP (green), nuclei were stained blue, dead cells were stained red (co-localised to blue). Filaments aligned to the impact zone edge, particularly at the tips of the impact zone (*). Examples of highly ramified cells (arrows), staining localised to impact zone edge (circles) and high background fluorescence. Scale bars 500 µm (A & C) and 250 µm (B & D). Confocal optical sections of the gels were sampled in an xy-plane at a depth (z) of 0 µm (A & C), 215 µm (B) and 357 µm (D).

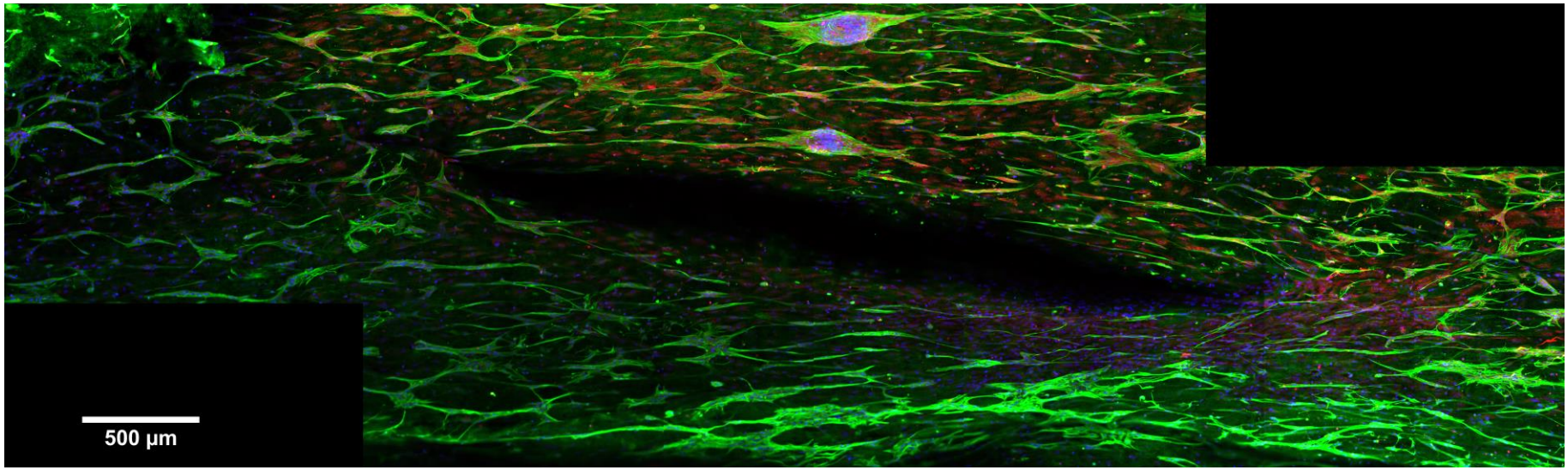


**Figure 4.34: Image of Tethered Collagen Gel Surface Ten Days after Impaction.** The impacted gel was imaged ten days after impaction at the impact zone surface. Primary astrocyte cells (4 x $10^6$ cells per gel) were immunocytochemically stained for GFAP (green) and stained for nuclei using Hoechst (blue) and dead cells (red co-localised to blue). Two large clumps of cells were observed (top, centre). Scale bar represents 500 µm. Confocal optical sections of the gel sampled in an xy-plane on the gel surface (z = 0 µm).

*Ten Days after Impaction*

Two large clumps of cells were observed located near to the impact zone at ten days after impaction (Figure 4.34) the cells appeared highly ramified and aligned both within the clump of cells and with the impact zone. The alignment of the cellular filaments in the direction of the impact zone edge was clear in the day-ten images. Cells appeared highly ramified across the entirety of the tile scan. No cells were visible in the impact zone itself, which appeared to be void of cells and gel matrix.

The impact zone in the gel shown in Figure 4.35 was much smaller than all of the other impact zones investigated. Alignment of the ramified astrocyte filaments was visible near the impact zone, although there appeared to be less alignment away from the impact zone in comparison to the surface images at five and ten days after impact. No cells were visible in the impact zone itself, which appeared to be void of cells and gel matrix.

The middle of the gel at ten days after impaction is shown in Figure 4.36. The cells within the middle region showed very little GFAP staining throughout the gel as a whole, however there was a distinct area of GFAP staining and background fluorescence on the impact zone edge. Where cellular filaments were visible, the filaments were aligned with the impact zone edge. No cells were visible within the impact zone itself, which appeared to be void of cells and gel matrix.

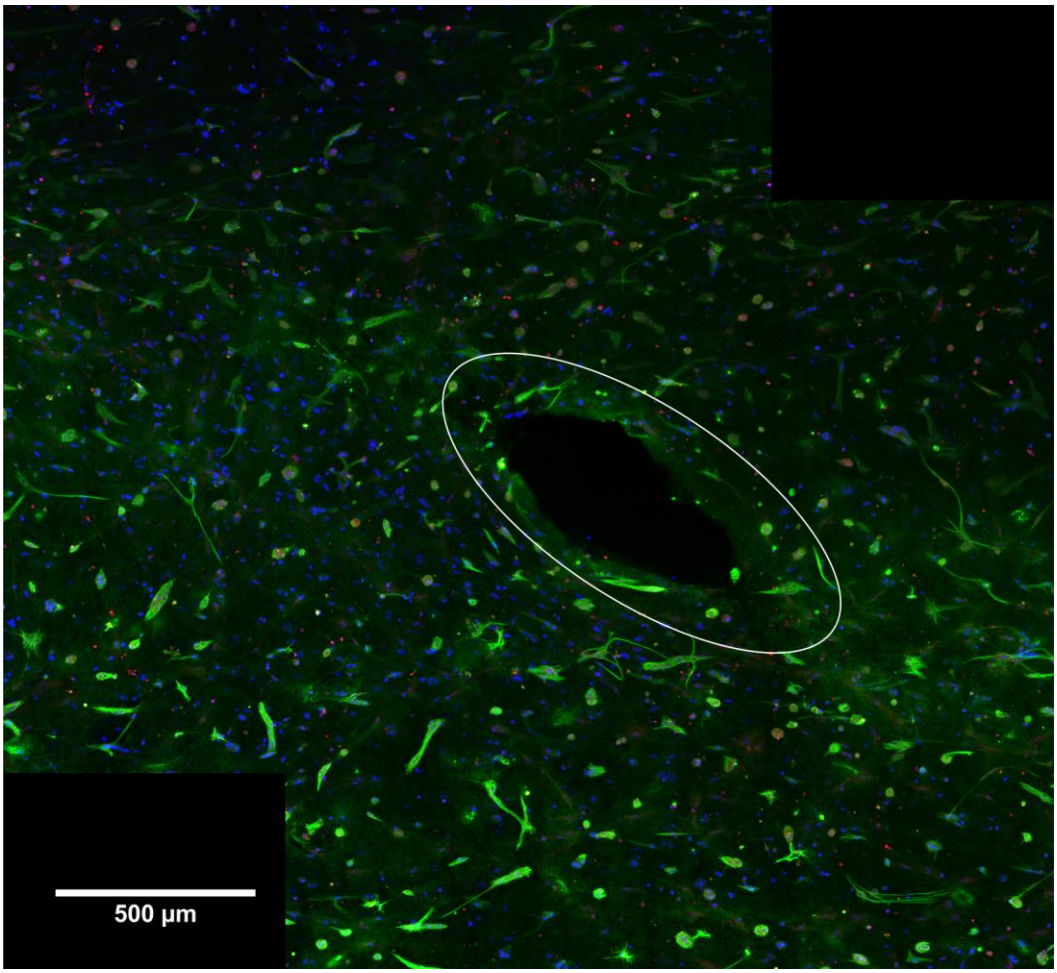


**Figure 4.35: Surface of Tethered Collagen Gel Ten Days after Impaction.** The impacted gel was imaged ten days after impaction at the impact zone surface. Primary astrocyte cells (4 x $10^6$ cells per gel) were immunocytochemically stained for GFAP (green) and stained for nuclei using Hoechst (blue) and dead cells (red co-localised to blue). Cellular alignment was observed at the impact zone edge, as indicated by selection on figure (white outline). Minimal cellular alignment was observed elsewhere. Scale bar represents 500 µm. Confocal optical sections of the gel sampled in an xy-plane on the gel surface (z = 0 µm).

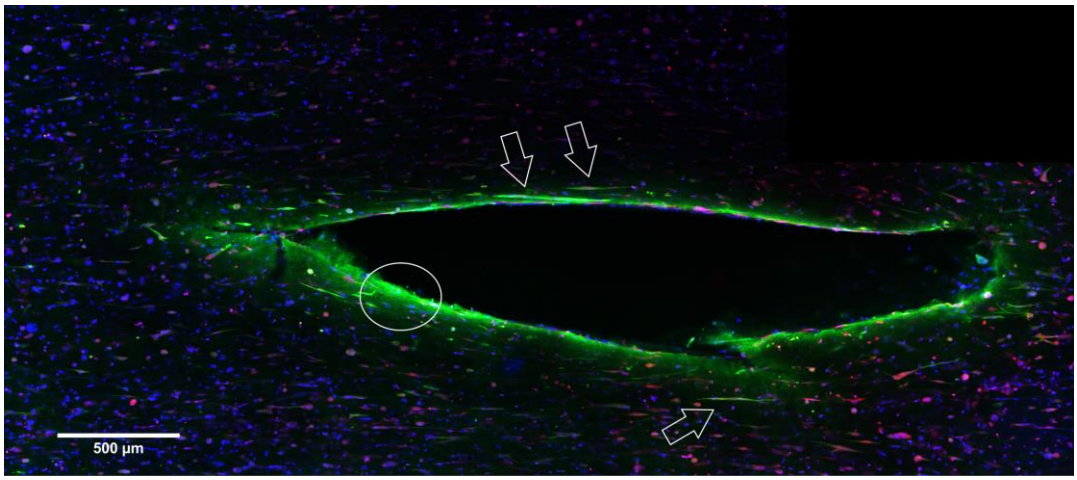


**Figure 4.36: Middle of Tethered Collagen Gel Ten Days after Impaction.** The impacted gel was imaged ten days after impaction at the middle region of the impact zone. Primary astrocyte cells ($4 \times 10^6$ cells per gel) were immunocytochemically stained for GFAP (green) and stained for nuclei using Hoechst (blue) and dead cells (red co-localised to blue). Arrows indicate examples of aligned cells. Circle indicates staining localised to impact zone edge and high background fluorescence. Scale bar represents 500 µm. Confocal optical sections of the gel sampled in an xy-plane at a depth (z) of 280 µm.

*Non-Impacted Controls*

There was no observable increase in cell death or GFAP staining over the ten day culture period in the non-impacted control gels, shown in Figure 4.37. A slightly increased level of GFAP staining and astrocyte ramification was observed when comparing the surface images to the middle images, which was similar to the staining observed in the impacted gels.

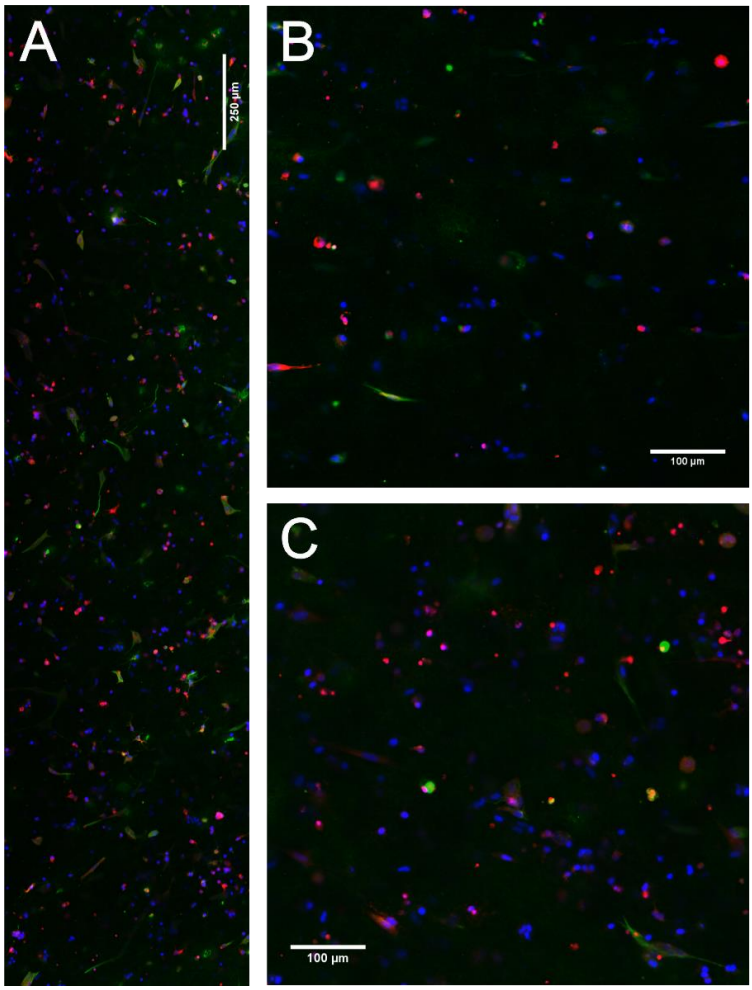


**Figure 4.37: Non-Impacted Control Images of Tethered Collagen Gels.** The non-impacted control gels were imaged at one (A, gel surface), five (B, gel middle) and ten (C, gel middle) days after the test gels were impacted. Primary astrocyte cells (4 x $10^6$ cells per gel) were immunostained for GFAP (green) and stained for nuclei using Hoechst (blue) and dead cells (red co-localised to blue). Scale bars represent 250 µm (A) and 100 µm (B & C). Confocal optical sections of the gels were sampled in an xy-plane at a depth (z) of 0 µm (A), 257 µm (B), and 154 µm.

The tiled images of the impacted gels were analysed using FIJI software, to calculate the area of GFAP expression at distances from the impact zones. The expression of GFAP was quantified on the basis of the mean area of GFAP-immunofluorescence per cell in each 100 µm increment. Due to time constraints, only one of the gels was imaged in the middle region at the ten-day time point; representative GFAP area data are presented for this time point out of interest, however no statistical analysis was

performed using these data. For all of the other time points, middle and surface scans were imaged and analysed for each gel (n = 3). The area of GFAP expression at each time point and at each 100 μm increment, normalised to cell number is shown in Figure 4.38. The GFAP area measurements were analysed using a non-parametric, unlinked, multiple comparison, Kruskal-Wallis test. The Kruskal-Wallis test was used following the results of a D'Agostino & Pearson omnibus normality test, in which each condition was found to not be normally distributed. The Kruskal-Wallis test showed that there was no significant difference between any of the measurements.

At one day after impaction, there was a large increase in the area of GFAP expression per cell within the first 100 μm (259.7 μm2 ± 60.9 SEM) compared to all of the other distances from the impact zone in which the mean area of GFAP expression per cell ranged from 61 μm2 to 18.3 μm2 from 200 μm to 1000 μm, respectively. The area of GFAP expression per cell was greater within the first 100 μm of the surface of the impact zone (259.7 μm2 ± 60.9) compared to the control (36.8 μm2 ± 14.7). The area of GFAP expression per cell was greater between the first 100 μm of the surface of the impact zone (259.7 μm2 ± 60.9) and the first 100 μm of the middle of the impact zone (82.8 μm2 ± 26.5). The area of GFAP expression per cell was greater within the first 100 μm of the middle of the impact zone (82.8 μm2 ± 26.5) compared to the non-impacted control (36.8 μm2 ± 14.7) (mean ± SEM).

At five days after impaction, the area of GFAP expression per cell was higher in comparison to the area of expression detected one day after impaction at the impact zone surface. The area of GFAP expression appeared fairly constant across all distances measured, ranging from 98.6 μm2 (± 20.3 SEM) within the first 100 μm to 88.63 μm2 (± 26.3 SEM) within the furthest distance of 1000 μm from the impact zone surface. The area of GFAP expression per cell was greater at the surface of the impacted gels compared to the non-impacted control (32.9 μm2 ± 10.2 SEM). In the middle of the impact zone, the area of GFAP expression per cell decreased as the distance increased from the impact zone edge; within the first 100 μm the mean GFAP area per cell was 153.8 μm2 (± 32.8 SEM) compared to all of the other distances from the impact zone in which the mean area of GFAP expression per cell ranged from 89.5 μm2 to 0 μm2 from 200 μm to 1000 μm, respectively. The area of GFAP

expression per cell was greater between the first 100 μm of the middle of the impact zone (153.8 μm2 ± 32.8 SEM) and the first 100 μm of the surface of the impact zone (98.6 μm2 ± 26.3 SEM). The area of GFAP expression per cell was greater within the first 100 μm of the middle of the impact zone (153.8 μm2 ± 32.8 SEM) compared to the non-impacted control (32.9 μm2 ± 10.2 SEM).

At ten days after impaction, the mean area of GFAP expression was higher in comparison to the mean area of GFAP detected at the corresponding distance at one and five days after impaction at the impact zone surface. At ten days after impaction, the pattern of GFAP expression across the impact zone tile was similar to that observed at five days after impaction; the area of GFAP expression at the impact zone surface appeared fairly constant across all distances measured, ranging from 160.3 μm2 (± 50.5 SEM) within the first 100 μm to 148.2 μm2 (± 61.8 SEM) within the furthest distance of 1000 μm. The area of GFAP expression per cell was greater at the surface of the impacted gels compared to the non-impacted control (45.3 μm2 ± 12.9 SEM). There was only an n-number of one for the middle tiled images at ten days after impaction, therefore these data were not included in the statistical analysis, and are shown in Figure 4.38 for qualitative purposes only. Within the middle of the impact zone, the area of GFAP expression per cell increased from 100 μm (82.9 μm2) to 200 μm (296.4 μm2) before decreasing towards the impact zone edge; within the first 300 μm the area of GFAP expression per cell was 102.7 μm2 and at 1000 μm the area of GFAP expression per cells was 17.4 μm2. The area of GFAP expression per cell was greater compared to the non-impacted control (45.3 μm2 ± 12.9 SEM).

Overall, the area of GFAP expression per cell increased over the ten day period following impaction. The expression of GFAP was highest and covered a greater distance from the impact zone at the impact zone surface, compared to the middle of the impact zone; in the middle region, the expression of GFAP tended to be concentrated within the first 100 to 300 μm of the impact zone.

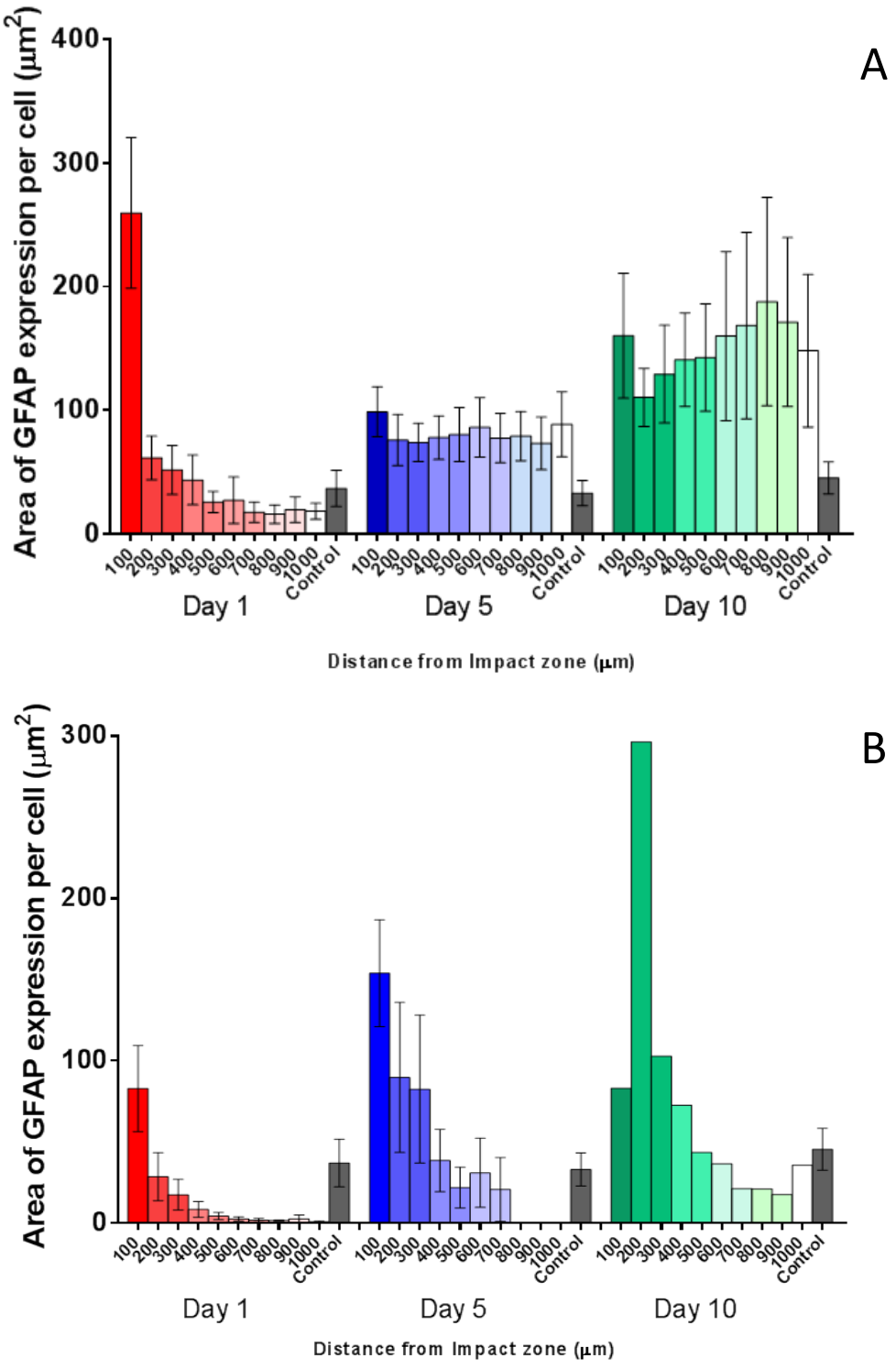


**Figure 4.38: Area of GFAP Expression per Cell at Distances from the Impact Zone.** The area of GFAP expression per cell was determined within 100 µm increments from the impact zone at one, five and ten days after impaction at the impact surface (A) and middle (B). Primary astrocyte cells (4 x $10^6$ cells per gel) were stained for GFAP (green) and analysed using FIJI. Data are shown as the mean (n = 3) ± standard error of the mean, except day 10 of (B) where n = 1.

### 4.4.11 The Effect of Mechanical Impaction on the Extracellular Release of Cytokines

Supernatants were collected from each gel one, five, and ten days after impaction in order to investigate the extracellular release of the rat interleukin-6 (rIL-6) cytokine. Controls included supernatant from astrocytes in 2D monolayer culture whereby high levels of reactive astrogliosis were visible following immunocytochemical staining for GFAP and tethered gels that had not been impacted.

An Enzyme Linked Immunoabsorbant Assay (ELISA) was performed according to the protocol in Section 2.2.10.

Despite a visible colour change occurring within all sample wells, the ELISA was not sensitive enough to detect IL-6 in the supernatant.

## 4.5 Discussion

The aim of this part of the study was to determine the suitability of *in vivo* methods of simulating spinal cord injury, within an *in vitro* environment by replicating the experimental parameters used to simulate traumatic SCI in animal models within the constraints of the 3D tethered gel models.

Spinal cord injury (SCI) can cause life-long physical, emotional, and social problems such as paralysis, loss of sensation, and respirator dependency (Spinal Research, 2011). Following hospital discharge, less than 1 % of US patients experience complete neurologic recovery (NSCISC, 2011). The functional outcome for the patient is determined by the location of injury, type of load, force and duration of impact, and the mechanism of treatment. Although the primary injury causes tissue damage, the cells of the spinal cord undergo a series of reactive changes over time which can be both neuro-protective, and neuro-inhibitive, known as the secondary response. One of the consequences of secondary response is often the formation of a glial scar. The glial scar is a physical and physiological barrier to regeneration of the spinal cord tissue, which often results in compromised neural function for the affected individual (Silver and Miller, 2004). Therefore investigations into the secondary injury response may provide new treatment targets for SCI regeneration.

Animal models of SCI allow manipulation of various parameters such as the velocity and type of impact, whilst preserving much of the tissue complexity of human tissue (LaPlaca et al., 2007). However, it is thought that *in vitro* models could better inform animal studies, in order to provide a useful step between animal models and clinical trials, which may increase therapeutic success (Kirkpatrick et al., 2007).

In the present study, the decision was made that the SCI model should feature cellular alignment in order to mimic the natural cellular alignment of the spinal cord and because the disorganisation of the naturally aligned spinal cord following injury is thought to be one of the contributing factors that inhibits regeneration of axons

(Davies et al., 2006; Duval et al., 2015; Geller and Fawcett, 2002; Hofstetter et al., 2002; Li et al., 1998; Reier, 1979).

The glial scar is formed of several different cell types such as neurons, astrocytes, oligodendrocytes, and microglia. For the purposes of developing a preliminary model for the investigation of cellular responses to mechanical injury, and the suitability of *in vivo*-type contusion devices, it was deemed appropriate to seed the gel matrix with only one cell type; astrocytes. The study of a single cell type allowed for simplification of the model, whereby it was possible to study the direct relationship between the mechanical impact and the response of the astrocytes, without adding the additional layer of complexity of cell-cell interactions. The simplicity and adaptability of the gel matrix formation would allow future studies to incorporate several different cell types within the matrix; cells can be added during gelation such that they are evenly distributed throughout the matrix (as was the case in this study), and/or they can be seeded on a surface of the gel, and allowed to migrate into the gel.

For this study, the models were analysed one, five and ten days after impaction. The ten day time frame was selected because clinically, the glial scar forms over several days, reaching maturity at about two weeks post-injury (Anderson et al., 2016; Faulkner et al., 2004; Herrmann et al., 2008; Wanner et al., 2013), therefore it was hypothesised that a ten day time frame would allow detection of a range of phenotypic changes within the cells.

The investigations involving mechanical impaction were performed on fully hydrated gels, as a result of the previous investigation described in Chapter 3, which determined that astrocytes were significantly more reactive in the fully stabilised gels, in comparison to the fully hydrated gels. An initially non-reactive phenotype within non-impacted gels would be beneficial when determining whether the mechanical impaction had an effect on the phenotype of primary astrocytes within this 3D model.

The tethering gel moulds were produced at the University of Leeds for this study. Tethering gel moulds have been manufactured from stainless steel and PEEK in previous studies (East et al., 2010; O'Rourke, 2015). The choice of mould material

should be biocompatible, resistant to cell-generated tensile forces, suitable for sterilisation and suitable for use as a collagen gel polymerisation environment (able to entrap collagen gel solution) (Shi et al., 2005). Therefore PEEK was selected for producing the tethered gel moulds in this study, as it fulfilled the above criteria, has been used for tissue engineering applications in the spine (Toth et al., 2006), and was readily available for manufacture of the moulds.

The contraction of primary astrocytes within type-I collagen gels was determined using a free-floating gel contraction assay. The cell seeding density is an important parameter to control in tethered gel models, as higher cell densities tend to cause faster contraction, which may be advantageous in terms of increased cellular alignment, or may result in the gel being disrupted during the experiment (Phillips and Brown, 2011). O'Rourke et al. (2015) showed that the percentage contraction in free-floating gels was related to the extent of cellular self-alignment achieved using the equivalent cell seeding density in tethered gels. The percentage contraction in the free-floating gels was used to select a suitable seeding density for tethered aligned gels, the primary astrocyte cells were cultured for 24 hours in the presence of TGF-β1 (10 $ng.ml^{-1}$) supplemented DMEM media. The addition of TGF-β1 to cell culture media has been shown to increase the contraction of gels containing primary astrocytes, although it has also been shown to increase the adoption of a more reactive phenotype (East et al., 2009, 2010). The percentage contraction of collagen gels increased to 70.7 % at a seeding density of $4 \times 10^6$ cells per ml. Increasing the seeding density above this caused the contraction to plateau. At the same cell seeding density, in the presence of TGF-β1, O'Rourke found that cells were highly aligned in both the middle and side regions of tethered gels. Highly aligned astrocytes were also detected within the side regions of the tethered gels used in this study, with the astrocytes in the middle and delta regions becoming increasingly less aligned, as was predicted due to the location of maximum tension throughout the gel matrix (East et al., 2010; Eastwood et al., 1998; O'Rourke et al., 2015).

In order to reduce the use of primary cells, the rat C6 ATCC® CCL-107™ glial cell line (C6) which is used as an astrocyte-like cell line (Quincozes-Santos et al., 2013), was utilised for the pilot studies and preliminary work, where possible. The seeding

density of C6 cell seeded tethered gels was based on a previous study by O'Rourke et al. (2015), which found that a C6 cell seeding density of 2 x $10^6$ cells per ml was sufficient to provide 68 % (± 3.3) contraction within type-I collagen gels. The C6 cell line expresses the astrocyte marker, glial fibrillary acidic protein (GFAP) (Kim et al., 2008). Cell lines can be advantageous because they are able to be passaged many times and stored in liquid nitrogen, to create a relatively unlimited supply. However, cell lines are not a true representation of the natural cell phenotype; for example they are often derived from cancerous tissue or immortalised, meaning that they have inherent changes in their genetic and proteomic expression which must be taken into account when using them within culture models simulating SCI (Morrison et al., 1998). For example, C6 cells do not replicate some of the primary astrocyte behaviours investigated in this study; the addition of TGF-β1 is not required in tethered gels seeded with C6 cells due the difference in cell behaviour which allows the C6 cells to contract the collagen gel at a lower cell concentration and without TGF-β1. The ability to contract gels without the addition of a chemical stimulant may indicate that the C6 cellular response to injury could differ, in particular in terms of alignment around the impact zone.

Contusion models of SCI are thought to be the most relevant models (Zhang et al., 2014). Therefore the availability of contusion devices was investigated. The pilot impaction study at University College London (UCL) used the Hatteras impactor to impact tethered C6 seeded collagen gels. The gels were incubated for one to three days after impaction, before the gels were fixed and immunostained for GFAP. Qualitative analysis showed that there was an increase in GFAP over the three day period. The impactor appeared to be an effective method of simulating injury within the tethered gels; the *in vivo* methodology did not have to be altered in order to impact the gels, following impaction an impacted area of gel was clearly visible, and in terms of minimising the infection risk to the cell cultures, the time spent out of the incubator and gel handling was minimal. Therefore it was decided to pursue mechanical impaction using an *in vivo* contusion device at the University of Leeds.

The investigations at the University of Leeds used the IH impactor to impact tethered collagen gels. The impactor software was able to calculate the displacement and

velocity of the impaction tip after the impaction had occurred, however it was not possible to input these parameters into the experimental set up. For example, if the impactor was programmed to apply 100 kdyn of force (desired value) to a rat spinal cord, the actual value applied might be 112 kdyn, with a displacement of 405 μm at a velocity of 115 mm/sec, 0 ms dwell time. The actual force output was dependent on the mechanical properties of the tissue that the tip contacted during the impaction; if the tip contacted bone instead of the spinal cord, the actual force output would be greater than the desired force. Determining the velocity of the impact in addition to the force of the impact would enable comparisons to be drawn between clinical injuries, animal models and other injury models; various studies utilising *in vivo* models have found that there is a strong correlation between the type of mechanical insult and the neurological outcome (Choo et al., 2007, 2008, 2009; Clarke et al., 2008; Persson et al., 2010).

Using the experimental settings utilised by Al'Joboori *in vivo*, the IH impactor was used to impact tethered aligned collagen gels, with a cell seeding density of $2 \times 10^6$ C6 cells per ml at 200 kdyn, 0 ms dwell time. Previous studies utilising the IH impactor within an *in vivo* setting impacted rat spinal cords at 200 kdyn (Cao et al., 2005; Hooshmand et al., 2014; Lee et al., 2012; Loy et al., 2005; Park et al., 2016). The impactor tip travelled the entire way through the gel and impacted the base of the tissue culture dish, rather than impacting the gel approximately mid-way through the gel, as was desired. In addition, the output of the actual force was 397 kdyn, rather than the desired 200 kdyn. An experiment was devised to investigate the actual force outputs of the IH impactor when impacting the sorbothane test block; these revealed that the actual force output increased in line with the desired force that was input into the software program. However, when this experiment was repeated with the C6 seeded tethered gels, the actual force output was recorded at >390 kdyn, regardless of how low the desired force input was. The IH impactor software is designed to detect the force experienced by the impaction tip throughout the impaction procedure. The impactor microcontroller is programmed to command another step deeper into the tissue if the force level does not exceed the threshold level of the user-defined desired force (Scheff et al., 2003). The fully hydrated gels had a lower elastic modulus (48 Pa) than the CNS tissue that the IH impactor was designed to detect; neural tissue

has been reported to have a modulus of between 100 - 1000 Pa, depending on the source of the tissue, and testing methods used (Cheng et al., 2008; Elkin et al., 2007; Engler et al., 2006; Flanagan et al., 2002; Lu et al., 2006). It was thought that the impactor might not be able to detect the presence of the gel, and therefore was passing through the entire gel matrix before impacting the tissue culture plastic. The experiment was repeated on acellular fully stabilised (FS) gels which have a significantly higher elastic modulus (874 Pa) in comparison to hydrated collagen gels, and which falls within the range reported for CNS tissue. The impaction of FS gels did not alter the desired force reading; the actual force output was recorded at >390 kdyn regardless of the desired force input.

Determining the velocity of the impact in addition to the force of the impact would enable comparisons to be drawn between clinical injuries, animal models and other injury models; for example, Park et al. (2016) investigated which parameters would yield equivalent SCI using different *in vivo* impactors; the New York University (NYU) impactor and the Infinite Horizon (IH) impactor. At equivalent impactions of the 25 mm injuries generated by the NYU impactor, and the 200 kdyn injuries generated by the IH impactor, there were differences in ladder rung test scores, magnetic resonance imaging (MRI) scans, anterograde tracing using biotinylated dextran amines (BDA) (BDA tracing is used to trace axonal projections from their source), and differences in the anti-PKC-γ antibody, used for detecting axons in the corticospinal tract, at eight weeks post-injury. These results demonstrated that the two devices exerted qualitatively different impacts on the spinal cord (Park et al., 2016). Therefore it was thought worthwhile to investigate a mechanism of determining the actual injury parameters that were being used on the gels; it was proposed that increasing the diameter of the impaction tip might improve the accuracy of the outputs by increasing the surface area of the tip. The increase in tip size was restricted by the dimensions of the tethered gel mould. Although it would be possible to increase the size of the moulds, an increase in mould dimensions would significantly increase the number of cells required per experiment. Due to the use of primary astrocyte cells in this study, minimising the number of cells required per experiment was a priority; therefore increasing the size of the moulds was avoided. Stainless steel impaction tips were manufactured in diameters of 4 mm and 6.5 mm, in

addition to the IH impactor 2.5 mm tip, which was used for *in vivo* testing. The impactor tips of increasing diameter were used to impact the sorbothane test block at 30, 100 and 300 kdyn, with a dwell time of 0 ms. The increase in diameter did not result in any significant change in the actual force outputs. From this experiment, it was concluded that the force sensor of the IH impactor was not sensitive enough to detect changes in impactor tip diameter. It was unfortunate that the actual force outputs were unknown, because the magnitude, rate, duration, contact velocity and compression are principle biomechanical SCI inputs that have been shown to affect the severity of the injury (Allen, 1911; Choo et al., 2007, 2009; Fiford et al., 2004; Hung et al., 1975; Kearney et al., 1988; Kwon et al., 2002; Onifer et al., 2007; Rivlin and Tator, 1978; Somerson and Stokes, 1987; Tarlov, 1954, 1972).

Although it was not possible to record the actual force outputs of the impaction, it was proposed that the IH impactor might be manipulated so that the impactor tip did not travel the entire way through the gel. The variation of impact depth in contusion injuries has been shown to lead to differences in injury morphology in animal models, resulting in larger spinal cord lesions and larger areas of demyelination (Behrmann et al., 1994; Lam et al., 2014; Pearse et al., 2005). The displacement setting could not be manually altered via the software, therefore an investigation into the manual control of the initial start height of the impactor tip was proposed, in order to increase the distance between the tip and the gel and override the software, thus restricting the depth the impactor tip travelled through the gel. Five turns of the vertical adjustment knob was found to be sufficient to produce a visible impaction zone in the gel, but not impact all of the way to the base of the gel.

Despite being unable to retrieve the actual force outputs for each impaction, the impactor was validated using the test block before each impaction session. It was assumed that any problems with the impactor would be detected by this validation; if the actual force plot using the test block matched that of a typical force plot set out in the user manual, then the impactor was assumed to be performing as expected. No problems were detected with the impactor at any stage.

In order to simulate the *in vivo* injuries generated by the IH impactor as closely as possible, the experimental parameters for the remainder of the study were 200 kdyn, 0 ms dwell time, using a 2.5 mm diameter tip, in order to replicate previous studies (Cao et al., 2005; Hooshmand et al., 2014; Lee et al., 2012; Loy et al., 2005; Park et al., 2016). However, the initial start height of the impaction tip was raised by five turns, rather than the recommended two turns.

The tethered gels were impacted after 24 hours in culture. At this point the gels had visibly contracted into a recognisably tapered shape; the gels were narrower at their centre in comparison to the tethered ends. The contraction of tethered gels is related to the level of cellular self-alignment (O'Rourke et al., 2015); the cells were visibly aligned at the sides of the gel in particular, as detected by immunostaining for the astrocyte cytoskeletal protein, GFAP. Cellular alignment in relation to the impact zone was determined by image analysis of the tiled image scans of the impacted gels. Tiled images of the impact zone were taken at the gel surface and the middle (z-plane) of the impact zone.

The morphology of the impact zones was variable; the size and shape of the impact zones were not similar within the same time points, which indicated that the impaction of the gels was not consistent. A possible explanation for the inconsistency may be related to the manual calibration of the impactor tip above the gel surface prior to each impaction experiment. It was sometimes difficult to distinguish the difference between culture media and the gel surface; therefore the tip might not have been lowered close enough to the gel surface if a volume of media remained over the gel surface. The media was carefully removed before each impaction, however the handling of the moulds was minimised in order to reduce the chance of infection, and care was taken to not touch the surface of the gel with the pipette tip as media was removed. Contact with the pipette tip could have damaged the gel matrix, which could have triggered an injury-type response from the cells. Reducing the chance of damage and infection was deemed to be a priority over complete removal of the media from the gel surface. This may have led to some underestimations regarding the positioning of the impaction tip with respect to the gel surface, which may explain the variation in size of the impact zones. In particular, the impact zone of one of the gels

at the ten-day time point was particularly small; measuring approximately 500 μm in length, in comparison to the other impaction zones at the same time point, which were approximately 3500 - 4000 μm in length. It should be noted that each gel was macroscopically analysed following each impaction, and no obvious differences in the appearance of the impaction zones was observed at the time of impaction. The variation in impact zone morphology was likely to have an effect on the data collected regarding the cellular response; some gels may have experienced a greater impact, or been impacted over a greater surface area, which would lead to an increased number of cells affected by the impaction. This variation should be taken into consideration when interpreting the results of this study. It is expected that future investigations into the impaction of the tethered gels using the IH impactor, or similar contusion device would be able to improve the reliability of the impaction procedure; for example, the Louisville Injury System Apparatus (LISA) comprises a non-contact laser in order to zero the impaction tip above the sample (Zhang et al., 2008).

The morphology of the impact zones was observed to become significantly less irregular over the ten days following impaction, however due to the obvious variation in impaction zone morphology, this result may be an artefact of experimental set up. It would be interesting to image the morphology of the impact zone over time within the same gel. For example, tethered gels could be seeded with fluorescently labelled cells suitable for live image analysis, such as those from a β-actin-green fluorescent protein (GFP) reporter animal line (East et al., 2010), in order to image the impact zone and cellular response to impaction over time.

The complete lack of cells and gel material within the impact zone was useful for analysis as it meant that the impact zone edge was clearly defined. Gel matrix was not visibly attached to the impactor tip after impaction. It is possible that at least some of the impacted gel matrix may have floated away into the surrounding media, although it was macroscopically observed that there was a loss of material at the impact zone site immediately after impaction and before media was reapplied to the gels. The gels were polymerised against the parafilm that encased the base of the moulds and were not floating; therefore it was assumed that the matrix material could not be forced out of the base of the gel during impaction, as it was restricted against

the parafilm and tissue culture dish. The matrix material may have been forced into the surrounding area by the impaction tip during impaction. It was interesting to note that whilst imaging the base of the gels, one of the gels appeared to have an impact zone-shaped matrix protrusion at its base. The confocal microscope images were obtained at specific z-planes through the sample, and whilst imaging the base of the gel, the first cells to come into focus were those in a circular clump in the centre of the base of the gel; the position of the cells was in a similar x, y location to the impact zone above it. No other cells were visible in the same z-plane, which suggested a protrusion of matrix material was present at the base of the gel. Advancing the focal plane deeper into the sample brought cells into focus in the surrounding gel. A protrusion at the base of the gel was not observed in the other impacted gels. In the future it would be important to investigate where the matrix material and cells from the impact zone, were transported to if this model were to be developed further.

In terms of a model of SCI, the void space created during the impaction was reminiscent of the fluid-filled cystic cavity that is a prominent pathological feature of SCI in humans (Bresnahan et al., 1991; Guth et al., 1999; Hooshmand et al., 2014). Rat models of SCI also develop large fluid-filled cystic cavities at the injury site (Lee and Lee, 2013). For example, the cyst-like impaction zone could be used as an *in vitro* model for investigating the regeneration of axons, or the success of grafts or cellular transplantation within cysts, in order to inform similar *in vivo* investigations (Bunge, 2016; Bunge and Pearse, 2003; Cheng et al., 1996; Fortun et al., 2009; Teng et al., 2001; Tetzlaff et al., 2011; Tukmachev et al., 2016). It would also be interesting to investigate if the impaction zones increased in size over a time period; cystic cavities often increase over time in animal models, as the cells continue to die and infiltrating macrophages clear the site (Popovich et al., 1997). This model could be adapted to include multiple cell types, for example astrocytes, microglia and macrophages; vascular damage during injury causes the recruitment of macrophage cells from the blood; the macrophages persist in injury sites for many weeks after injury, and in addition to clearing damaged and degenerated tissues after injury, they are also known to contribute to matrix remodelling and regeneration (Condeelis and Pollard, 2006; Greenhalgh and David, 2014; Zhou et al., 2014).

The impact zone decreased in area as it progressed vertically into the gel matrix from the surface towards the middle of the gel. A similar decrease in damage away from the impact epicentre is seen clinically and in animal models, for example quantification of tissue sparing assessed by staining for myelin-based proteins in injured rats, found the white and grey matter damage spread out as far as 3 mm, both rostral and caudal to the epicentre, seven days post injury. However, the percentage spared white and grey matter was over 95 % at this distance (Lam et al., 2014). Therefore this model could be developed to enable comparisons with *in vivo* models in terms of the dimensions and morphology of the impact zone, and the influence this has on axon regeneration.

The cells within the non-impacted controls were viable for the time course of the experiment; the percentage cell death did not significantly alter over the time course of the experiment, however there was a decrease in cell death between five and ten days from 38.4 % to 31.3 %, respectively. In comparison to the cell viability within the models previously investigated (Chapter 3), the percentage cell death in non-impacted controls was higher than the percentage cell death observed in fully hydrated gels at a similar time point (19.5 % death at day 5), but lower than the fully stabilised gels at a similar time point (45 % death at day 5). Within the tethered gels at one and five days following impaction, there was no significant increase in percentage cell death compared to non-impacted controls. One explanation for the similarities in percentage cell death between the impacted gels and non-impacted gels is that the area of the matrix where cell death would be expected to be at its highest (the impaction zone) did not contain any cells; instead the location of the impaction was a void. It is possible that cell death that occurred immediately following impaction resulted in mechanically dissociated cells that immediately dispersed within the overlaid cell culture medium, therefore these dead cells were not included in the analysis. It is also possible that the gel matrix from the impact zone was forced into the surrounding matrix, however if this was the case then a higher proportion of cell death might be expected around the impact zone edge; this was not observed and neither was an obvious increase in cell number around the impact zone, although this was not quantified. Staining for cell death immediately after an impaction might help to identify the location of the cells and gel matrix. The stain used in this study was

prepared in cell culture medium and required a four-hour incubation time, therefore an alternative viability stain with a reduced incubation time, involving minimal rinsing of the gel (therefore reduced removal of dead cells from within the impaction zone) might be more appropriate. Interestingly, at ten days after impaction, the percentage cell death increased to 45.5 %, which was significantly higher than the non-impacted control at the same time point (31.3 %). The significance of this difference is probably attributable to the combination of a slight increase in cell death in the impacted gels, and a decrease in cell death in the non-impacted controls, since there was no significant difference between percentage death in the impacted gels at five and ten days after impaction. The cell viability data were collected from several regions around the gel matrix, and calculated as percentage death within the gel as a whole. Although the data collected included regions on the edge of the impact zone, it would perhaps have been be more appropriate to quantify the cell death at distances from the impact zone, similar to the methods used to collect cellular alignment and GFAP expression data.

It was hypothesised that the alignment of cells within the gels might be affected by the impaction due to the possible changes in gel shape and changes in astrocyte phenotype potentially leading to remodelling of the matrix. Injury was simulated within tethered gels whereby the cells had self-aligned along the long axis in response to the tension within the gels as a result of the tethering process (East et al., 2010; Georgiou et al., 2013; Phillips and Brown, 2011; Phillips et al., 2005). The alignment of cells surrounding the impact zone was determined using the 'Angle tool' on FIJI within 100 μm increments from the impact zone. The angle tool was used to draw along astrocyte cytoskeletal filaments, as highlighted by the GFAP staining, and the edge of the impact zone to which the cell was located in order to provide an angle of deviation from the impact edge. Angles of $0^o$ indicted a filament that was completely aligned with the impact zone edge, for example ran parallel to it, whereas angles of $90^o$ indicated filaments perpendicular to the impact zone, which were assumed to not be aligned with the impact zone. As observed in the box and whisker plots, the overall trend was for the astrocyte filaments to be aligned against the impact zone edge within the first 100 μm of the impact zone; the mean angles of deviation were $22.2^o$ ($\pm$ 3.1), $21.7^o$ ($\pm$ 2.2) and $12.9^o$ ($\pm$ 1.4) at one, five and ten days after

impaction, respectively. The increased alignment at the impact zone edge was visible in the immunostained gels, particularly at ten days after impaction. The alignment decreased at distances further away from the impact zone edge; within 300 μm of the impact zone; the mean angles of deviation had increased to $38.1^{o}$ (± 3.3), $32.8^{o}$ (± 1.9) and $24.3^{o}$ (± 1.2) at one, five and ten days after impaction, respectively. At 1000 μm from the impact zone edge, which was the furthest distance quantified, the mean angles of deviation had increased to $43.0^{o}$ (± 4.7), $40.5^{o}$ (± 2.8) and $44.5^{o}$ (± 2.1) at one, five and ten days after impaction, respectively. This analysis showed that cells that were positioned the furthest away from the impact zone were significantly less likely to align their filaments with the impact zone edge. Whilst performing the analysis, it was noted that the alignment was particularly apparent on the 'tips' or 'ends' of the impact zones, where the gels were effectively split in two. A study by Sharpe et al., (1997) used a finite element model to investigate the mechanical properties of dog-bone shaped polysilicon films that contained etch holes. The etch holes were square-shaped, with rounded corners. Under a uniaxial stress field, the stress concentrated at the edges of the holes and the maximum stress was where the straight boundary of the hole joined with the quarter circle of the corner of the etch hole (Sharpe et al., 1997). There are similarities between the shape, dimensions and uniaxial stress field of Sharpe's model, and the tethered impacted gels. Therefore it was hypothesised that the stress would also concentrate around the edges of the impaction zone within the impacted gel model. As observed previously, astrocytes have been shown to align parallel to the maximum stress in non-impacted tethered gels (East et al., 2010; Eastwood et al., 1998; Phillips and Brown, 2011; Phillips et al., 2005), therefore the increased alignment with the impact zone edge over the ten days following impaction suggests the cells were responding to changing forces within the tethered gels, specifically increased stress around the edge of the impact zone. In addition, the impact zone tended to longitudinally extend along the long axis of the tethered gels, in line with the alignment already present prior to impaction. This meant that the gels were more likely to be aligned in the direction of the impact zone edge before the impaction. Future work could include the impaction of non-aligned matrices, in order to compare the alignment of astrocytes around the impact zone.

The area of GFAP expression per cell followed a similar trend to the level of alignment; there was a larger area of GFAP expressed per cell at the impact zone edge in comparison to the furthest distances analysed. Increased GFAP expression is an indicator of reactive astrogliosis (East et al., 2009; Georges et al., 2006; Kimelberg and Norenberg, 1989; Moshayedi et al., 2010). There was an increase in the area of GFAP expression per cell in astrocytes over the ten days following impaction, this is indicative of the hypertrophic, morphological response of reactive astrocytes (Kimelberg and Norenberg, 1989). The area of GFAP expression was higher in cells on the surface of the impact zone in comparison to the middle of the impact zone. The expression of GFAP was mainly concentrated to cells within the first 300 μm of the impact zone at the middle of the impact zone, whereas on the surface of the gels, the expression of GFAP tended to be high across all of the 1000 μm increments analysed. The area of GFAP expression was greatest at ten days following impaction; this is representative of *in vivo* models, where reactive astrocytes are more prominent at 7 to 28 days post-injury, compared to earlier time points (Popovich et al., 1997).

The increase in GFAP expression in the area surrounding the impact zone is similar to results seen clinically and within *in vivo* models; Wanner et al. (2013) demonstrated that astrocytes showed phenotypic and proliferative changes which varied with respect to the distance from the injury lesion in their mouse contusion model. The edge of the lesion was bordered with newly proliferated, elongated astrocytes, as the scar matured over 14 days, the astrocytes exhibited distinctive elongated morphologies with extensively overlapping processes (Wanner et al., 2013). An additional similarity between Wanner's *in vivo* model and the results of this *in vitro* model, was the reactivity of astrocytes one millimetre away from the impact zone; at 14 and 28 days after SCI, Wanner observed that the astrocyte morphology was similar to that in uninjured tissue, however there was evidence of increased expression of GFAP and cellular hypertrophy. Choo et al. (2008) compared the secondary pathology following contusion, dislocation, and distraction SCI within rat models. The study found that contusion, dislocation and distraction injury mechanisms resulted in reactive astrogliosis near the boundary of the lesion. In the contusion injury model, reactive astrocytes were mainly contained within 2 mm of the lesion epicentre (Choo et al., 2008).

Within non-impacted controls, the expression of GFAP was greater at the side of the gel in comparison to the middle, this could to be due to the increased tensile strain within this region of the gel (O'Rourke et al., 2015; Phillips and Brown, 2011); as was shown in Chapter 3, and as has been shown previously, astrocytes adopt a more reactive phenotype when cultured in matrices of increased stiffness (East et al., 2009; Moshayedi et al., 2010). However within *in vivo* injury models, GFAP expression associated with cells on the sides of the spinal cord was observed within the sham controls in addition to the injured models (Choo et al., 2008).

Due to the variation in impact zone size, the effect of the distance of the impact zone edge to the side of the gel was investigated. In gels where the impact zone was larger, it was hypothesised that the impact zone edge was closer to the sides of the gel, relative to gels with a smaller impact zone. Therefore, this may have skewed the data; causing an apparent increase in GFAP expression in comparison to gels with smaller impact zones. However, the variation in the width of the impact zones was not as great as the variation in length, and the difference in size relative to the size of the gel and distance to the side of the gels was not thought to be significant. Further development of this model would involve reducing the variability in size and morphology of the impact zones, therefore this may not be an issue, although it should be taken into consideration.

In summary, the *in vivo* contusion devices utilised to simulate SCI within 3D tethered collagen gels resulted in a promising 3D *in vitro* model of SCI. The model requires further development in order to improve the consistency of the impaction, in particular the morphology and depth of the impaction zone, and the recording of the actual force output. Although significant differences between the expression of GFAP at different time points and locations with the gels were not observed, the trend of increased expression within cells bordering the impact zone were reminiscent of those observed within *in vivo* models (Anderson et al., 2016; Choo et al., 2008; Fawcett and Asher, 1999; McKeon et al., 1991; Ridet et al., 1997; Wanner et al., 2013). It is anticipated that improvement of the consistency of the impaction and increasing the number of repeats would influence the significance of these results.

There are many areas for further development linked to this study, for example, the morphological changes in astrocytes were investigated in terms of the filament alignment, however the changes in cellular ramification were not investigated in this study. As was observed previously, an increase in cellular ramification is a marker of reactive astrogliosis. The cavity created by at the impaction site could have been investigated in more detail; 3D z-stacks through the impaction zone could be used to investigate the differences in cellular responses to injury throughout the full thickness of the model. An advantage of collagen gels as a 3D matrix material over *ex vivo* or *in vivo* investigations is the ability to image samples of greater thicknesses. The effect of mechanical impaction on cell death within the 3D model requires further investigation; in particular into the location of the cells from within the impact zone following impact, and a more thorough analysis of cell death around the impact zone. The utilisation of a different contusion device, or adaption of the IH impactor to include software which is able to control the displacement of the device, may increase the reproducibility of this model.

In summary, the use of an *in vivo* type contusion device and impaction protocol was successfully applied to a preliminary 3D *in vitro* collagen gel model. Following impaction, the 3D model simulated *in vivo* models of SCI in the formation of a cavity, bordered by reactive astrocytes *in vitro*. Models of SCI lesions to date have included *in vivo* animal models (Choo et al., 2008; Hooshmand et al., 2014; Nishi et al., 2007) and *ex vivo* organotypic slice models (Weightman et al., 2014), however these models lack the adaptability of an *n vitro* 3D self-aligned collagen gel matrix. The astrocytes seeded within the impacted gel matrices showed increased levels of reactivity over the ten days following impaction; the area of GFAP expression per cell increased, although more repeats are required to investigate this further, and the alignment of astrocyte filaments around the impact zone significantly increased over ten days, forming a dense border of reactive astrocytes at the impact zone edge. Several possibilities have been discussed regarding the future development of this model; in particular investigations involving additional cell types, applications of treatments and regeneration therapies, such as those involving regeneration across SCI lesions, and the adaption of further assays for use within the model. 3D *in vitro* tethered collagen

gel models such as this could provide valuable insights into the cellular mechanisms which may progress the translation of treatments into the clinic.

# Chapter 5

# Overall Discussion

## 5.1 General Discussion

The underpinning hypothesis of this study was that it was possible to simulate *in vivo* injuries within a 3D *in vitro* model of spinal cord injury (SCI) within a tethered, self-aligned, type-I collagen gel. An *in vitro* model of SCI could advance the understanding of cellular responses to injury and help inform animal studies which may facilitate the design of therapeutics (Kirkpatrick et al., 2007). SCI can cause paralysis, loss of sensation, and respirator dependency (Spinal Research, 2011) which has a significant impact on the quality of life of patients, their life expectancy and is an economic burden due to the high costs associated with primary care and loss of income (Thuret et al., 2006). Injuries to the spine occur at an incidence of 11.5 to 53.4 people per 1 million of the population in developed countries (Burney, 1993; Bydon et al., 2014; DeVivo and Vogel, 2004; Sekhon and Fehlings, 2001); worldwide, an estimated 2.5 million people are living with SCI (Thuret et al., 2006).

The most common causes of SCI in the UK are traumatic incidents occurring over a very short space of time, such as falls and car accidents; these injuries can result in compression, contusion, laceration or stretching of the spinal cord (Thuret et al., 2006). The functional outcome for the patient is determined by the location of injury, type of load, force and duration of impact, and the mechanism of treatment. SCI is a two-phase process involving primary and secondary injury mechanisms (Silver and Miller, 2004). The primary injury causes tissue damage such as vascular disruption and the death of cells, including neurons, oligodendrocytes, and astrocytes. However, the secondary mechanisms of injury amplify the primary damage; additional structure and function are lost through the ongoing apoptosis of cells and demyelination of axons (Guest et al., 2005), reorganisation of the extracellular matrix removes guidance cues for regenerating axons (Schwab and Bartholdi, 1996), resulting in the

formation of cystic cavities, and the release of inhibitive factors, which prevent the regeneration of damaged tissue (Fawcett, 2006; Jones et al., 2003). The outcome of the primary and secondary mechanisms of injury is a glial scar comprising cells such as reactive astrocytes, microglia and macrophages (Bunge et al., 1993; Fawcett and Asher, 1999; Jones et al., 2002; Kakulas, 1999; Klapka and Müller, 2009; Norenberg et al., 2004; Silver and Miller, 2004; Sofroniew and Vinters, 2010).

Although the spinal cord demonstrates plasticity after injury (Bareyre et al., 2004; Weidner et al., 2001), limited axon sprouting occurs and the axons are rarely able to bridge the lesion site (Raineteau and Schwab, 2001). Despite the numerous clinical trials that have been conducted for the treatment of SCI, no therapeutic intervention has been effective in improving functional outcome (Fehlings et al., 2011; Kwon et al., 2004; Sayer et al., 2006; Tator, 2006; Wanner et al., 2013). Following hospital discharge, less than 1% of US patients experienced complete neurologic recovery (NSCISC 2011). Thus, there is a need for the development of therapeutics to improve the regenerative capacity of the spinal cord. A better understanding of the cellular mechanisms and molecular regulation, in particular the cellular contributions to the glial scar, could progress the development of therapeutic treatments (Bush et al., 1999; Faulkner et al., 2004; Fawcett and Asher, 1999; Klapka and Müller, 2009; Silver and Miller, 2004; Sofroniew, 2009; Sofroniew and Vinters, 2010; Wanner et al., 2013). One of the difficulties in establishing a treatment method is the heterogeneity of SCI; there are many different types and severities of traumatic primary injury, across different ages of patient and different locations within the spinal cord, whilst at a cellular level, there are multiple, interacting secondary injury cascades that amplify the primary damage inflicted during the traumatic insult (Pleasant et al., 2011).

Many techniques have been developed to mimic particular injuries found in human SCI, however surgical procedures to create animal models can be extremely costly and time consuming, particularly in larger animals (Jones et al., 2012). The time and cost implications increase further when the development of SCI from an acute injury to a chronic injury is studied; long follow-ups are expensive and ethical considerations prevent the long-term study of cervical SCI in rats and primates (Choo

et al., 2007; Zurita et al., 2012). The modest translation of therapeutic treatments from animal models to successful clinical trials suggests that there is a need for simplified models of SCI, in which the complex secondary cascade can be broken down into specific cellular interactions under controlled injury parameters (Choo et al., 2008; Hopkins et al., 2015; Pleasant et al., 2011; Tator, 2006; Thuret et al., 2006).

Current *in vitro* models of injury are designed to simplify the investigation of cellular responses to specific aspects or outcomes of SCI, for example the effect of high rate shear strain on neural cell cultures (LaPlaca et al., 2005a; Pfister et al., 2003), the responses of primary rat microglial cells and astrocytes to increasing matrix stiffness in comparison to physiological values (Moshayedi et al., 2014), and the inhibition of DRG outgrowth when DRGs were seeded onto a monolayer of reactive astrocytes (Wanner et al., 2008). However, various *in vitro* models of SCI have been developed with the specific focus of simulating animal models of SCI within a simplified *in vitro* setting. For example Boomkamp et al. (2012) made a single cut with a scalpel blade across monolayer cultures of dissociated rat embryonic spinal cord cells in order to specifically simulate *in vivo* transection injuries, rather than clinically presenting mechanisms of injury (Boomkamp et al., 2012), Balentine et al. (1988) dropped weights onto explanted whole foetal mouse spinal cords in order to simulate weight drop contusion models (Balentine et al., 1988), and the *in vitro* model utilised by Weightman et al. (2014) simulated transection injuries by slicing organotypic slice cultures of mouse spinal cord with a double-bladed scalpel (Weightman et al., 2014b).

The use of whole spinal cords and organotypic slices as models of SCI is advantageous because the *in vivo* 3D structure of the tissue is maintained, in addition to the spatial orientations of heterogeneous cell types, tissue architecture and neuronal connections at a synaptic level. For this reason, these models are useful for the study of extracellular matrix molecules, cell-cell interactions including neuronal networks, and for investigating treatment efficacy (Cavaliere et al., 2010; Morrison et al., 1998; Ravikumar et al., 2012). Matrices such as collagen gels, have been utilised within 3D models that allow modelling of cells within a 3D environment that is relatively simple, whereby highly controlled experimental methods can be investigated and the intra- and extra- cellular environments can be manipulated, without the complexity of

animal tissues (Willits and Skornia, 2004). The physiological environment of a cell involves cellular interactions and responses to mechanical stimuli, adjacent cells and extracellular matrix in a 3D microenvironment; these factors can influence cellular proliferation, morphology, migration and differentiation (Kofron et al., 2009; LaPlaca et al., 2005b; Li et al., 2007; Sundararaghavan et al., 2009). In contrast, cells grown in 2D are often cultured on a solid-liquid interface between the matrix substrate and the culture media, a situation which is unlikely to occur *in vivo* (Bard and Hay, 1975; Greenburg and Hay, 1982; Yeung et al., 2005).

The ability to culture CNS cells within a gel matrix in order to generate a 3D model offers an intermediate degree of complexity in comparison to 2D models. Depending on the orientation of cells within the matrix, there is the ability to apply bulk forces to the model resulting in heterogeneous strain fields at the cellular level. This type of modelling is more relevant to the application of forces during SCI *in vivo*, whilst allowing the researcher flexibility to simplify the model in relation to the physiological environment and mechanical parameters (Cullen and LaPlaca, 2006; LaPlaca et al., 2005b, 2007).

The spinal cord is an aligned structure; the white matter is organized into tracts of aligned axons (Duval et al., 2015), therefore it would be preferential to include alignment as a feature of a 3D cellular model for the investigation of the effects of simulated SCI. Additionally, the effect of aligned astrocytes and aligned matrix components on the regeneration of neurites has been investigated using *in vitro* models (Davies et al., 2006; East and Phillips, 2008; East et al., 2010; Hsiao et al., 2015; Kofron et al., 2009; Vahidi et al., 2008; Weightman et al., 2014a). This is important as it is thought that the physical barrier of disorganised astrocytes in the glial scar may contribute to the overall inhibition of regenerating axons by disrupting the guidance of the cells (Davies et al., 2006; Geller and Fawcett, 2002; Hofstetter et al., 2002; Li et al., 1998; Reier, 1979). Therefore, a SCI model is more likely to be clinically relevant if an aligned model is impacted, rather than a non-aligned model, particularly if the regeneration of axons is to be investigated.

East et al. (2010) produced a 3D collagen gel model of aligned astrocytes, for use as a spinal cord repair conduit. These authors found that when neurons were seeded on and within astrocyte gels, neurite length was greatest in the areas of astrocyte alignment (East et al., 2010). In order to stimulate alignment of astrocytes within the gel, a tethered self-aligning model was used. Tethered gel models generate tension in the longitudinal axis of the matrix as the gel contracts due to astrocyte remodelling of the matrix. Cells are able to form stable integrin-mediated attachments with the fibrils of collagen gels (Brakebusch and Fässler, 2003; Kagami et al., 1999; O'Rourke et al., 2015). Astrocytes self-align along the longitudinal axis in order to reduce the tensile forces that they experience, resulting in the alignment of both cell and collagen filaments within the gel matrix (Phillips, 2014). East et al. (2010) seeded their model with primary astrocytes, dorsal root ganglia (DRG) and neural fibroblasts. Other self-aligned collagen gel models been seeded with Schwann cells (Georgiou et al., 2013) and human dental pulp stem cells, which were differentiated into Schwann cells and were shown to myelinate DRG neurites within the tethered matrix (Martens et al., 2014).

The aim of the current study was to modify the model created by East et al. (2010) in order to create a 3D *in vitro* model that simulated *in vivo* SCI contusion-type models such as those described by Cao et al. (2005), Loy et al. (2005), Lee et al. (2012), Hooshmand et al. (2014) and Park et al. (2016).

It was imperative that the 3D *in vitro* model would be simple, without restricting the scope for future development; a single cell type meant it was possible to study the direct relationship between the mechanical impact and the response of the cells, without adding the additional layer of complexity of cell-cell interactions. For example, it is anticipated that future investigations which will utilise this model would be able to adapt the model to include additional cell types. Primary rat astrocytes were selected for use within the *in vitro* model because the rat is the most commonly used and widely accepted animal model of SCI (Stokes and Jakeman, 2002; Tetzlaff et al., 2011), and astrocytes were selected in particular due to their role in glial scar formation (Fawcett and Asher, 1999; Fleming et al., 2006; Norenberg et al., 2004). Contusion models of SCI are thought to be the most relevant animal models of SCI

(Zhang et al., 2014), therefore the suitability for use as a contusion injury mechanism within a 3D cellular model was investigated. Several devices have been designed specifically for the simulation of contusion within *in vivo* models. Some devices are more advanced than others, for example the Weight Drop device suffers from impaction rod rebound, affecting the reproducibility of results (Sharif-Alhoseini and Rahimi-Movaghar, 2014), whilst the aneurysm clip is unreliable due to variable clip positioning and lack of standardisation of the clip release (Zhang et al., 2014). Some contusion devices offer better control over the experimental parameters resulting in greater reproducibility and the possibility of producing graded injuries. This enables animals to be studied after mild-, moderate-, or severe-impactions (Scheff et al., 2003; Sharif-Alhoseini and Rahimi-Movaghar, 2014; Vialle et al., 2007; Zhang et al., 2014).

The type-I collagen matrix used by East et al. (2010) consisted of a hydrated gel matrix which was allowed to contract and undergo cellular self-alignment before being stabilised. The gel was stabilised because the model was developed as a potential implantable spinal cord repair conduit (East et al., 2010). Stabilisation involves the application of an absorbent material to the surface of the gel matrix, sometimes in combination with a weight. The liquid component of the gel is absorbed, concentrating the collagen matrix (including any cells seeded into the matrix), into a sheet of collagen gel. The gel undergoes plastic compression which means it is permanently changed in structure (Brown et al., 2005). Due to the concentration of collagen fibres, stabilised gels are thought to be mechanically stable in comparison to non-stabilised (fully hydrated) gels, which improves the handling of the gels (Braziulis et al., 2012; Brown et al., 2005). Additional advantages of gel matrix stabilisation include rapid and simple production which is reproducible, and produces easily manipulated, cell-seeded, membrane-like constructs (Braziulis et al., 2012; Brown et al., 2005; Levis et al., 2012).

Despite the advantages of gel stabilisation, it was not known what effect this would have on the cells seeded within the matrix; levels of astrogliosis have been reported to be higher when astrocyte cells are in contact with stiffer substrates (East et al., 2009; Georges et al., 2006).

Therefore, the first aim of this study was to determine whether the stabilisation of type-I collagen gels would generate a suitable matrix environment for the study of the astrocyte responses to SCI. In order to investigate the astrocyte response to injury, it would be beneficial if the measurable effects of reactive astrogliosis (for example the measurement of GFAP expression, or cytokine release) were not expressed above baseline levels, in such a way that it would be difficult to determine whether the mechanical impaction had an effect on the phenotype of primary astrocytes within the model.

In the current study, three different type-I collagen matrix environments were investigated, based on the hydration of the gels; fully hydrated (FH), partially stabilised (PS), and fully stabilised (FS). The PS gels could not be produced reliably due to problems with the stabilisation absorber. For this reason, partially stabilised gels were abandoned as a potential matrix environment. The biomechanical properties of the FS and FH matrix environments were investigated using oscillatory rheometry. The linear viscoelastic region (LVER) was determined for each gel type; the LVER is the rheological testing range in which the strain values are non-destructive. It was crucial to determine the LVER range, because measurements obtained from outside of the LVER range are not based on the basic laws of rheology (Ewoldt et al., 2015; Macosko, 1994; Mezger, 2006; Parsons and Coger, 2002; Picout and Ross-Murphy, 2003). The LVER was determined using amplitude sweeps to determine the LVER strain rate; this was then confirmed using frequency sweeps in strain-controlled and stress-controlled modes. The LVER for the FS gels was between 1 Hz and 20 Hz at 0.3 % strain. The LVER for FH gels was between 1 Hz and 5 Hz at 1 % strain. The LVER parameters for FH gels corresponded to those reported in other rheological studies of non-stabilised collagen gels; 1 Hz, 1 % shear strain (Bailey et al., 2011; Kreger et al., 2010). Although several studies report that stabilisation of gels improved the mechanical properties and handling of the collagen gels, the mechanical properties were not reported (Braziulis et al., 2012; Cheema and Brown, 2013; Engelhardt et al., 2010; Levis et al., 2012; Mi et al., 2010; Serpooshan et al., 2011). The studies which have reported mechanical properties of stabilised gels used different testing methods (tensile) and therefore did not investigate the LVER

(Brown et al., 2005; Hadjipanayi et al., 2009). Therefore no comparisons could be drawn between the LVER parameters used in this study and those in the literature.

The biomechanical properties of the matrix environments were significantly different; for example, within astrocyte-seeded gels at day 1, FS gels were significantly stiffer than FH gels, with an elastic modulus of 409.78 Pa (± 14.4) at 1 Hz, compared to an elastic modulus of 55.19 Pa (± 8.8) at 1 Hz, respectively. There was no significant difference ($p > 0.9999$) between the elastic moduli reported for FH gels under any of the conditions investigated, a range of 47.96 to 55.19 Pa was recorded at 1 Hz, across all conditions; the gels appeared to maintain their stiffness over time and in the presence or absence of cells. This suggests that the FH gels are stable over time and any cellular remodelling of the matrix which might have occurred over the 5 day culture period did not affect the stiffness of the matrix. Conversely, there were significant differences between each of the FS gel conditions. In the presence and absence of cells, the stiffness significantly decreased over five days in culture; for example in acellular FS gels at 20 Hz, the mean stiffness decreased from 874 Pa to 243.2 Pa after 5 days. It was not possible to locate viscoelastic property values in the literature for type-I rat tail collagen gels, which had been tested using oscillatory rheology, under the exact same testing parameters that were used in this study. Reported values for the mean elastic moduli of hydrated type-I collagen gels range from 20 Pa (Miron-Mendoza et al., 2010) to 1.06 MPa (Hadjipanayi et al., 2009). The elastic modulus of 47.96 Pa for an acellular FH gel found in this study was similar to the mean elastic modulus reported by Kreger (2010) of 37.2 Pa.

Neural tissue has been reported to have a modulus of between 100 - 1000 Pa, depending on the source of the tissue, and testing methods used (Cheng et al., 2008; Elkin et al., 2007; Engler et al., 2006; Flanagan et al., 2002; Lu et al., 2006). However, the mechanical testing method and testing parameters, type of tissue, age of tissue, dissection method, have all been shown to affect the reported mechanical properties (Cheng et al., 2008) therefore direct comparisons are difficult.

The cells in FH gels were viable over a five day period with an average percentage death of 19.95 % at day five. There was a significant increase in percentage death in

FS gels at day 1 and day 5. The average percentage death was 45 % at day five in FS gels; this should be taken into account when interpreting other results; a high level of cell death could increase the reactivity of the surrounding cells. It is possible that astrocytes may be more easily damaged by the rapidity of the fluid flow, as the absorber removed the liquid component from the gel in comparison to other cell types that have been studied within stabilised gels (Brown et al., 2005). In addition, increased cell density and the susceptibility of FS matrices to desiccation was likely to have contributed to a higher percentage death in this condition.

The astrocytes cultured within FS gels expressed significantly higher levels of reactive astrogliosis markers, such as an increased area of GFAP expression and increased cellular ramification. The increase in markers of astrocyte reactivity could be due to the response of astrocytes to culture within a stiffer matrix environment. The FS gels were approximately an order of magnitude stiffer than the FH gels. However, a limitation of this study was that the increased reactivity of astrocytes could not be directly attributed to the stiffness of the matrix environments, because the FS gels had undergone a greater degree of manipulation in comparison to the FH gels.

Although the astrocytes present in both the FH and FS matrix environments were of a significantly less reactive phenotype in comparison to 2D monolayer cultures, the astrocyte reactivity within the FS gels was significantly increased and there were elevated levels of cell death in comparison to FH matrices. A matrix which stimulated a low level of reactivity was desirable for future investigations, such that increases in reactivity in response to mechanical injury could be more readily observed. For these reasons, FH gels were selected as the most suitable matrix environment for continued development of the 3D *in vitro* tethered gel model of SCI.

The second aim of this study was to determine whether *in vivo* contusion devices were suitable for the impaction of 3D *in vitro* tethered collagen gels, and whether a model of SCI could be developed that had the potential to inform future animal studies.

The contraction of primary astrocytes within type-I collagen gels was determined using a free-floating gel contraction assay. The cell seeding density was an important parameter to control within tethered gel models, as higher cell densities tend to cause faster contraction, which may be advantageous in terms of increased cellular alignment, or may result in the gel being disrupted during the experiment (Phillips and Brown, 2011). O'Rourke et al. (2015) showed that the percentage contraction in free floating gels was related to the extent of cellular self-alignment achieved using the equivalent cell seeding density in tethered gels. The percentage contraction in the free-floating gels was used to select a suitable seeding density for tethered aligned gels. The primary astrocyte seeded gels were cultured for 24 hours in the presence of TGF-β1 (10 $ng.ml^{-1}$) supplemented DMEM media. The addition of TGF-β1 to cell culture media has been shown to increase the contraction of gels containing primary astrocytes, although it has also been shown to increase the adoption of a more reactive phenotype (East et al., 2009, 2010). The percentage contraction of collagen gels increased to 70.7 % at a seeding density of $4 \times 10^6$ cells per ml. Increasing the seeding density above this caused the contraction to plateau. At the same cell seeding density, in the presence of TGF-β1, O'Rourke et al. (2015) found that cells were highly aligned in both the middle and side regions of tethered gels. Highly aligned astrocytes were also detected within the side regions of the tethered gels used in the present study, with the astrocytes in the middle and delta regions of the gel becoming increasingly less aligned, as was predicted due to the location of maximum tension throughout the gel matrix (East et al., 2010; Eastwood et al., 1998; O'Rourke et al., 2015).

Following the preliminary results of a pilot study, which utilised the Hatteras contusion device to impact tethered collagen gels at University College London, the subsequent study was continued at the University of Leeds using an Infinite Horizons (IH) impactor. The tethered gels were impacted after 24 hours in culture. At this point the gels had visibly contracted by approximately 28 % and demonstrated a tapered shape. The development of an impaction protocol involved different approaches to improving the accuracy of the force outputs; this included variation of impaction tip diameter, impaction tip starting height and sample material. The impactor tip diameter and sample material did not affect the actual force output of the

IH impactor. Variation of the impaction tip starting height provided some control over the depth of the impaction, preventing the impactor tip from impacting the entire depth of the gel. Following a number of iterations, a protocol was optimised to impact tethered collagen gels, however the actual force output remained unknown, due to the limitations of the IH impactor. The method comprised removal of media from tethered collagen gels, seeded with 4 x $10^6$ primary astrocytes, which had self-aligned and contracted following 24 hours in culture. The gels were positioned centrally underneath a 2.5 mm diameter impaction tip. The 2.5 mm diameter tip is used to simulate injury in rat models (Hooshmand et al., 2014). The impactor tip was then zeroed to the surface of the gel, before being raised to the starting impaction height, following five-turns of the vertical adjustment knob. The impactor was programmed to impact the gels at 200 kdyn with 0 ms dwell time. Following impaction, the media was replaced over the surface of the gel before incubation for the desired culture length, of one, five or ten days. The impaction parameters were based on those described by Cao et al. (2005), Loy et al. (2005), Lee et al. (2012), Hooshmand et al. (2014) and Park et al. (2016). A major limitation of the IH impactor was that it could not record the actual force of impaction, and therefore the force, velocity, and impaction depth of the impaction were unknown.

Upon analysis of the impaction zones, it was apparent that the impactions were not consistent, as the impaction zones varied considerably in size and shape. It was hypothesised that the cells within the gels would have experienced a different range of forces due to this inconsistency; therefore this should be taken into consideration whilst interpreting the data.

The percentage of dead primary astrocytes within the impacted cells was determined using co-localisation of the Dead (ethidium homodimer-1) stain from the Live/Dead® Cell Viability Assay with the Hoechst nuclear stain. Images of the gels were analysed at eight locations around the gel; in the delta zones, side zones, middle, and on the impact zone edges. The percentage cell death ranged from 31 % to 38 % across all conditions tested, except within gels at ten days after impaction, where cell death was higher at 45 % ($\pm$ 2.7 SEM). The percentage death of primary astrocytes within

impacted gels was not significantly different compared to the cell viability of non-impacted control gels ($p>0.05$) at one and five days after impaction.

The impaction zone did not contain cells or matrix material which may have affected to the reported percentage death within impacted gels; the impact zone was the area of the matrix where cell death would be expected to be at its highest. It is possible that cell death that occurred immediately following impaction resulted in mechanically dissociated cells that immediately dispersed within the overlaid cell culture medium, therefore these dead cells were not included in the analysis. It is also possible that the gel matrix from the impact zone was forced into the surrounding matrix, however if this was the case then a higher proportion of cell death might be expected around the impact zone edge; this was not observed and neither was an obvious increase in cell number around the impact zone, although this was not quantified. The cell viability data were collected from several regions around the gel matrix, and calculated as percentage death within the gel as a whole. Although the data collected included regions on the edge of the impact zone, it would perhaps have been be more appropriate to quantify the cell death at distances from the impact zone, similar to the methods used to collect cellular alignment and GFAP expression data.

It was hypothesised that the alignment of cells within the gels might be affected by the impaction due to the possible changes in gel shape and changes in astrocyte phenotype, potentially leading to remodelling of the matrix. Injury was simulated within tethered gels, whereby the cells had self-aligned along the long axis in response to the tension within the gels as a result of the tethering process (East et al., 2010; Georgiou et al., 2013; Phillips and Brown, 2011; Phillips et al., 2005). The alignment of cells surrounding the impact zone was determined using the 'Angle tool' on FIJI, within 100 μm increments from the impact zone. The angle tool was used to draw along astrocyte cytoskeletal filaments, as highlighted by the GFAP staining, and the edge of the impact zone to which the cell was located in order to provide an angle of deviation from the impact edge. Angles of $0^{o}$ indicted a filament that was completely aligned with the impact zone edge, for example ran parallel to it, whereas angles of $90^{o}$ indicated filaments perpendicular to the impact zone, which were assumed not to be aligned with the impact zone. The astrocyte filaments were aligned

with the impact zone edge within the first 100 μm of the impact zone; the mean angles of deviation were 22.2$^{o}$ (± 3.1), 21.7$^{o}$ (± 2.2) and 12.9 $^{o}$ (± 1.4) at one, five and ten days after impaction, respectively. The alignment significantly decreased at distances further away from the impact zone edge. At 1000 μm from the impact zone edge, which was the furthest distance quantified, the mean angles of deviation had increased to 43.0$^{o}$ (± 4.7), 40.5$^{o}$ (± 2.8) and 44.5$^{o}$ (± 2.1) at one, five and ten days after impaction, respectively. This analysis indicated that cells that were positioned the furthest away from the impact zone were significantly less likely to align their filaments with the impact zone edge. As observed previously, astrocytes have been shown to align parallel to the maximum stress in non-impacted tethered gels (East et al., 2010; Eastwood et al., 1998; Phillips and Brown, 2011; Phillips et al., 2005), therefore the increased alignment with the impact zone edge over the ten days following impaction suggests the cells were responding to changing forces within the tethered gels, specifically increased stress around the edge of the impact zone.

The area of GFAP expression per cell followed a similar trend to the level of alignment; there was a larger area of GFAP expressed per cell at the impact zone edge, in comparison to the furthest distances analysed. Increased GFAP expression is an indicator of reactive astrogliosis (East et al., 2009; Georges et al., 2006; Kimelberg and Norenberg, 1989; Moshayedi et al., 2010). There was an increase in the area of GFAP expression per cell in astrocytes over the ten days following impaction, this is indicative of the hypertrophic, morphological response of reactive astrocytes (Kimelberg and Norenberg, 1989). The area of GFAP expression was higher in cells on the surface of the impact zone in comparison to the middle of the impact zone. The expression of GFAP was mainly concentrated to cells within the first 300 μm of the impact zone at the middle of the impact zone, whereas on the surface of the gels, the expression of GFAP tended to be high across all of the 1000 μm increments analysed. The area of GFAP expression was greatest at ten days following impaction; this is representative of *in vivo* models, where reactive astrocytes are more prominent at 7 to 28 days post-injury, compared to earlier time points (Popovich et al., 1997).

Regrettably, the ELISA kit that was utilised to detect extracellular interleukin-6 (IL-6) release by astrocytes within the FH, FS and impacted models was not sensitive

enough to detect any extracellular release of IL-6 from the models. It was assumed that the supernatant from 2D controls and gels containing a high proportion of reactive astrocytes would contain IL-6, as has been reported previously by East et al. (2009), however IL-6 was not detected in the present study. It is possible that the cytokines were heavily diluted in the culture medium; large volumes of media were applied to each gel, and fresh media was added every three days, further diluting cytokines. Conversely, there may not have been a change in the extracellular expression of IL-6 in any of the samples to detect. Unfortunately, due to time pressures, these experiments could not be repeated with a more sensitive kit.

The main limitations of this study were the lack of mechanical output data from the IH impactor, and the inconsistent impaction morphology. It was not possible to conclude that the 3D tethered gels had been subjected to the same mechanical impact as *in vivo* models, despite the impactions being performed under the same parameters, with the exception of the starting height of the impactor tip. It was clear that the impaction was not consistent between gels due to the morphology of the impaction zones. Previous *in vivo* studies have reported an excellent correlation between the force and displacement of the spinal cord in mouse (Ghasemlou et al., 2005) and rat models (Scheff et al., 2003) whilst using the IH impactor, therefore the inconsistency within this study is likely to be due to operator error in the initial calibration of the impactor tip against the gel surface.

In terms of the development of a 3D *in vitro* model of SCI within a tethered, self-aligned, type-I collagen gel that simulated *in vivo* SCI, the outcome of the study was positive. The results of the study were comparable to those observed *in vivo*, for example the border of reactive astrocytes that surrounded a cavity, the decrease in GFAP expression over an increasing distance from the impact zone, and the time frame of the expression of markers of astrogliosis. For example, the cavity of the impaction zone could be used as an *in vitro* model for investigating the regeneration of axons, or the success of grafts or cellular transplantation within cysts, in order to inform similar *in vivo* investigations. The model showed potential for improvement in terms of the consistency of impaction and types of assays investigated, such as live cell imaging and cytokine analysis. The model could be adapted further through the

addition of additional cell types to study cell-cell interactions and include different modes of injury. Particular advantages of this model were the 3D nature and cellular alignment within the matrix, as this mimicked the spatial arrangement of astrocytes *in vivo.*

An *in vitro* model of SCI has the capacity to complement *in vivo* models of SCI. Advantages include cost, ease of use, fewer ethical issues (in particular for longer time points), and the control over experimental variables. As a direct comparison to *in vivo* models there are distinct limitations, such as the lack of a circulation system in this model which influences inflammation, bleeding, ischemia, and therefore has a complex effect on the secondary responses involved in SCI. Although the model could be utilised as a mechanism of studying regeneration or graft integration, the practical outcomes of these experiments that can be studied *in vivo,* such as behavioural studies, clinical improvement, and side-effects to treatments, are not possible *in vitro.* However, used in conjunction with *in vivo* models, 3D *in vitro* tethered collagen gel models could provide valuable insights into cellular mechanisms which may progress the translation of treatments into the clinic.

## 5.2 Further Work

There were many aspects of this study that would have been developed further, had there been time. In particular, the investigations related to the IH impactor would have been expanded, had the impaction of the gels been more consistent, and had the impactor generated the expected force and displacement outputs.

### 5.2.1 Detailed Approach to Future Work

Several key objectives should be met in the further development of a 3D *in vitro* model of SCI, in order to enable progress to a model that functions as a clinical tool. Firstly, the mechanism of injury simulation should be fully investigated. Secondly, the location of the cells and matrix material from the impaction cavity should be investigated. Thirdly, further assays and mechanisms of analysis should be

investigated; in particular those suited to best inform *in vivo* studies. Finally, the model should be further optimised for use with alternative and/or additional cell types.

#### 5.2.1.1 Mechanism of Injury

Several different types of contusion devices are available; this study utilised two different contusion devices designed to apply different input parameters. The Hatteras impactor used velocity or depth inputs, whilst the IH impactor was force controlled. Although different instruments are able to offer various injury inputs and outputs, such as height, force, velocity, and tissue compression depth (Zhang et al., 2008), the equivalence of the input parameters, in terms of lesion severity, has not yet been precisely and systematically assessed (Park et al., 2016). Therefore this would need to be considered for future comparisons with *in vivo* models.

Generally, the IH impactor was able to successfully simulate injury within the 3D tethered gels. However, due to the inconsistency of the impaction, and the lack of the impact force output, it would be appropriate to investigate the suitability of different contusion devices for the continuation of this model. When selecting a suitable impactor, several factors should be considered: the availability of the impactor and the frequency of use within an *in vivo* setting, to allow research to be compared from a wide range of research groups; the inputs and outputs of the device, preferably these would also be relevant to a clinically presenting injury, in addition to *in vivo*; and the mechanism of calibration with the gel surface, for example the Louisville Injury System Apparatus (LISA) uses a laser position sensor, which could improve the accuracy and consistency of impactions.

#### 5.2.1.2 Impact Zone Cavity Investigation

The location of the cells and matrix material from the impaction cavity should be investigated, as this will affect the interpretation of results. For example, if the cells from the impaction zone are forced into the surrounding gel matrix upon impaction, assays investigating the proliferation of astrocytes around the impact zone would need to take this into account (proliferation is an indication of reactive astrogliosis). As discussed previously, the location of the directly impacted cells is of interest in terms of the effect of impaction on cell death.

#### 5.2.1.3 Further Assays

Further assays and mechanisms of analysis should be investigated; in particular those suited to best inform *in vivo* studies. The collagen gel matrix material was selected for its compatibility with a variety of assays and modes of investigation. It would be particularly interesting to analyse the cells within the impacted gels using live cell imaging. This is a particular advantage of the *in vitro* model over *in vivo* models, and has the potential to provide new insights into the cellular mechanisms involved in SCI. Another advantage of this model over tissue that has been sectioned following an *in vivo* investigation is the optical clarity of collagen gels; z-stacks of through the periphery of the impact zone could inform investigations into alignment, graft interfaces and cellular interactions at different locations through the cavity, for example. The model could be utilised for the screening of drug treatments and the effects of cytokines.

In addition, the results gained from the *in vivo*, and *in vitro* models could serve as a basis for *in silico* models which could further inform *in vivo* models. An *in silico* model has been developed by Goode (2015) in parallel to this study and it is anticipated that the parameters of this model could be input into the *in silico* model in order to relate the forces involved in the impaction with the cellular responses at different locations within the gel.

#### 5.2.1.4 Alternative Cell Types

This model has the potential to be optimised for investigations into the injury response of alternative and/or additional cell types. As mentioned previously, collagen gels have been utilised as a matrix material for a variety of different cell types including neurons and microglia. The aligned nature of this model would be suited to a model including neuronal cell types; either as a single cell culture or in combination with another cell type, such as astrocytes. The effects of impaction and the formation of a cavity within an *in vitro* aligned neuronal culture model would be interesting to compare to those observed within *in vivo* models.

## 5.3 Conclusion

In conclusion, this study represents a step forward in the development of a 3D *in vitro* model of *in vivo* SCI. The main findings of the study were as follows:

- The LVER for rheological testing of FH gels was between 1 Hz and 5 Hz at 1 % shear strain.
- The LVER for rheological testing of FS gels was between 1 Hz and 10 Hz, at 0.3 % shear strain.
- The mean elastic modulus (G') for 500 µl type-I rat tail collagen (2 mg/ml in 0.6% (w/v) acetic acid) gels, seeded with one million primary astrocytes per cell-seeded gel after one day in culture was FH: 55.19 Pa and FS: 409.78 Pa.
- The mean elastic modulus (G') for 500 µl type-I rat tail collagen (2 mg/ml in 0.6% (w/v) acetic acid) acellular gels after one day in culture was FH: 48.66 Pa and FS: 585.03 Pa.
- The mean elastic modulus (G') for 500 µl type-I rat tail collagen (2 mg/ml in 0.6% (w/v) acetic acid) gels, seeded with one million primary astrocytes per cell-seeded gel after five days in culture was FH: 47.96 Pa and FS: 317.03 Pa.
- The mean elastic modulus (G') for 500 µl type-I rat tail collagen (2 mg/ml in 0.6% (w/v) acetic acid) acellular gels after five days in culture was FH: 50.54 Pa and FS: 125.37 Pa.
- The level of astrogliosis, as determined by analysis of astrocyte ramification and the expression of GFAP, was significantly higher in astrocytes cultured in FS gels in comparison to FH gels.
- Self-aligned 3D collagen gel matrices were produced, in which the expression of markers of reactive astrogliosis were low before impaction, allowing investigation into the astrocyte response to impaction.
- The experimental parameters implemented throughout the study were 200 kdyn, 0 ms dwell time, using a 2.5 mm diameter tip. The initial start height of the impaction tip was raised by five turns (rather than the two turns used *in vivo*). Therefore, using the IH impactor, it was possible to simulate *in vivo* injury parameters as closely as possible.
- The methods presented for the injury produced by the IH impactor simulated some of the well-documented responses of astrocytes to SCI *in vivo*. In

particular, this contusion model generated a 3D cavity bordered by reactive astrocytes within an *in vitro* setting. Current *in vitro* models of the lesion or cavity have focussed on transection models, often utilising explanted tissue such as organotypic slice models, rather than the highly adaptable, simplified collagen gel model presented in this study.

- The cells that were positioned the furthest away from the impact zone were significantly less likely to align their filaments with the impact zone edge. The increased alignment at the impact zone edge was visible in the immunostained gels, particularly at ten days after impaction.
- There was a larger area of GFAP expressed per cell at the impact zone edge in comparison to the furthest distances analysed. GFAP expression per cell increased in astrocytes over the ten days following impaction. The area of GFAP expression was higher in cells on the surface xy-plane ($z = 0$ μm) of the impact zone in comparison to the middle xy-plane ($z = \geq 150$ μm) of the impact zone.
- However, issues with the consistency of the impaction need to be resolved in order to directly compare *in vivo* and *in vitro* SCI using the IH impactor.
- More detailed analysis of the cellular responses, over longer time courses, and perhaps with the additional complexity of multiple cell types would complement investigations within *in vivo* models.
- 3D *in vitro* tethered collagen gel models such as this could provide valuable insights into the cellular mechanisms which may progress the translation of treatments into the clinic.

# References

Abraham, L.C., Zuena, E., Perez-Ramirez, B., and Kaplan, D.L. (2008). Guide to collagen characterization for biomaterial studies. J. Biomed. Mater. Res. B. Appl. Biomater. *87*, 264–285.

Abreu, E.L., Palmer, M.P., and Murray, M.M. (2010). Collagen density significantly affects the functional properties of an engineered provisional scaffold. J. Biomed. Mater. Res. A *93*, 150–157.

Ahearne, M., Yang, Y., and Liu, K.-K. (2008). Mechanical Characterisation of Hydrogels for Tissue Engineering Applications. Top. Tissue Eng. Tissue Eng. *4*.

Allaman, I., Gavillet, M., Belanger, M., Laroche, T., Viertl, D., Lashuel, H.A., and Magistretti, P.J. (2010). Amyloid- Aggregates Cause Alterations of Astrocytic Metabolic Phenotype: Impact on Neuronal Viability. J. Neurosci. *30*, 3326–3338.

Allen, A.R. (1911). Surgery of Experimental Lesion of Spinal Cord Equivalent to Crush Injury of Fracture Dislocation of Spinal Column: A Preliminary Report. JAMA J. Am. Med. Assoc. *LVII*, 878.

Anatomycorner (2015). Neuroglial Cells | Anatomy Corner.

Anderson, M.A., Burda, J.E., Ren, Y., Ao, Y., O'Shea, T.M., Kawaguchi, R., Coppola, G., Khakh, B.S., Deming, T.J., and Sofroniew, M. V. (2016). Astrocyte scar formation aids central nervous system axon regeneration. Nature *532*, 195–200.

Antoine, E., Vlachos, P., and Rylander, M. (2014). Review of Collagen I Hydrogels for Bioengineered Tissue Microenvironments: Characterization of Mechanics, Structure, and Transport. http://dx.doi.org/10.1089/ten.teb.2014.0086.

Arbogast, K.B., and Margulies, S.S. (1997). Regional Differences in Mechanical Properties of the Porcine Central Nervous System.

Arbogast, K.B., and Margulies, S.S. (1998). Material characterization of the brainstem from oscillatory shear tests. J. Biomech. *31*, 801–807.

Avossa, D., Rosato-Siri, M.., Mazzarol, F., and Ballerini, L. (2003). Spinal circuits formation: a study of developmentally regulated markers in organotypic cultures of embryonic mouse spinal cord. Neuroscience *122*, 391–405.

Bailey, J.L., Critser, P.J., Whittington, C., Kuske, J.L., Yoder, M.C., and Voytik-Harbin, S.L. (2011). Collagen oligomers modulate physical and biological properties of three-dimensional self-assembled matrices. Biopolymers *95*, 77–93.

Balentine, J.D. (1978). Pathology of experimental spinal cord trauma. I. The necrotic lesion as a function of vascular injury. Lab. Invest. *39*, 236–253.

Balentine, J.D., Greene, W.B., and Bornstein, M. (1988). In vitro spinal cord trauma. Lab. Invest. *58*, 93–99.

Bankhead, P. (2014). Analyzing fluorescence microscopy images with ImageJ.

Bao, G., and Suresh, S. (2003). Cell and molecular mechanics of biological materials. Nat. Mater. *2*, 715–725.

Bard, J.B., and Hay, E.D. (1975). The behavior of fibroblasts from the developing avian cornea. Morphology and movement in situ and in vitro. J. Cell Biol. *67*, 400–418.

Bareyre, F.M., Kerschensteiner, M., Raineteau, O., Mettenleiter, T.C., Weinmann, O., and Schwab, M.E. (2004). The injured spinal cord spontaneously forms a new intraspinal circuit in adult rats. Nat. Neurosci. *7*, 269–277.

Barocas, V.H., Moon, A.G., and Tranquillo, R.T. (1995). The fibroblast-populated collagen microsphere assay of cell traction force--Part 2: Measurement of the cell traction parameter. J. Biomech. Eng. *117*, 161–170.

Barr, M.L., and Kiernan, J.A. (2004). Barr's the Human Nervous System: An Anatomical Viewpoint (Lippincott Williams and Wilkins).

Barres, B.A. (2008). The mystery and magic of glia: a perspective on their roles in health and disease. Neuron *60*, 430–440.

Basso, D.M., Beattie, M.S., and Bresnahan, J.C. (1996). Graded histological and locomotor outcomes after spinal cord contusion using the NYU weight-drop device versus transection. Exp. Neurol. *139*, 244–256.

Behrmann, D.L., Bresnahan, J.C., and Beattie, M.S. (1994). Modeling of acute spinal cord injury in the rat: neuroprotection and enhanced recovery with methylprednisolone, U-74006F and YM-14673. Exp. Neurol. *126*, 61–75.

Beningo, K.A., Dembo, M., and Wang, Y. (2004). Responses of fibroblasts to anchorage of dorsal extracellular matrix receptors. Proc. Natl. Acad. Sci. U. S. A. *101*, 18024–18029.

Benzel, E.C., Connolly, P.J., DiAngelo, D.J., Fehlings, M.G., Goffin, J., Gokaslan, Z.L., Grob, D., Hart, R.A., Heary, R.F., Heller, J.G., et al. (2012). The Cervical Spine.

Bernick, K.B. (2011). Cell biomechanics of the central nervous system.

Bilgen, M. (2005). A new device for experimental modeling of central nervous system injuries. Neurorehabil. Neural Repair *19*, 219–226.

Bilston, L.E., and Thibault, L.E. (1996). The mechanical properties of the human cervical spinal cord in vitro. Ann. Biomed. Eng. *24*, 67–74.

Bitar, M., Salih, V., Brown, R.A., and Nazhat, S.N. (2007). Effect of multiple unconfined compression on cellular dense collagen scaffolds for bone tissue engineering. J. Mater. Sci. Mater. Med. *18*, 237–244.

Boomkamp, S.D., Riehle, M.O., Wood, J., Olson, M.F., and Barnett, S.C. (2012). The development of a rat in vitro model of spinal cord injury demonstrating the additive effects of Rho and ROCK inhibitors on neurite outgrowth and myelination. Glia *60*, 441–456.

Boyce, V.S., Tumolo, M., Fischer, I., Murray, M., and Lemay, M.A. (2007). Neurotrophic factors promote and enhance locomotor recovery in untrained spinalized cats. J. Neurophysiol. *98*, 1988–1996.

Bradl, M., and Lassmann, H. (2010). Oligodendrocytes: biology and pathology. Acta Neuropathol. *119*, 37–53.

Brakebusch, C., and Fässler, R. (2003). The integrin-actin connection, an eternal love affair. EMBO J. *22*, 2324–2333.

Brandl, F., Sommer, F., and Goepferich, A. (2007). Rational design of hydrogels for tissue engineering: Impact of physical factors on cell behavior. Biomaterials *28*, 134–146.

Braziulis, E., Diezi, M., Biedermann, T., Pontiggia, L., Schmucki, M., Hartmann-Fritsch, F., Luginbühl, J., Schiestl, C., Meuli, M., and Reichmann, E. (2012). Modified plastic compression of collagen hydrogels provides an ideal matrix for clinically applicable skin substitutes. Tissue Eng. Part C. Methods *18*, 464–474.

Bresnahan, J.C., Beattie, M.S., Stokes, B.T., and Conway, K.M. (1991). Three-dimensional computer-assisted analysis of graded contusion lesions in the spinal cord of the rat. J. Neurotrauma *8*, 91–101.

Brown, A.G. (1981). Organization in the Spinal Cord: The Anatomy and Physiology of Identified Neurones (Springer Science & Business Media).

Brown, A.M., and Ransom, B.R. (2007). Astrocyte glycogen and brain energy metabolism. Glia *55*, 1263–1271.

Brown, R.A., Wiseman, M., Chuo, C.-B., Cheema, U., and Nazhat, S.N. (2005). Ultrarapid Engineering of Biomimetic Materials and Tissues: Fabrication of Nano- and Microstructures by Plastic Compression. Adv. Funct. Mater. *15*, 1762–1770.

Bueno, F.R., and Shah, S.B. (2008). Implications of tensile loading for the tissue engineering of nerves. Tissue Eng. Part B. Rev. *14*, 219–233.

Bunge, M.B. (2016). Efficacy of Schwann cell transplantation for spinal cord repair is improved with combinatorial strategies. J. Physiol. *594*, 3533–3538.

Bunge, M.B., and Pearse, D.D. (2003). Transplantation strategies to promote repair of the injured spinal cord. J. Rehabil. Res. Dev. *40*, 55–62.

Bunge, R.P., Puckett, W.R., Becerra, J.L., Marcillo, A., and Quencer, R.M. (1993). Observations on the pathology of human spinal cord injury. A review and classification of 22 new cases with details from a case of chronic cord compression with extensive focal demyelination. Adv. Neurol. *59*, 75–89.

Burgos, M., Calvo, S., Molina, F., Vaquero, C.F., Samarel, A., Llopis, J., and Tranque, P. (2007). PKCepsilon induces astrocyte stellation by modulating multiple cytoskeletal proteins and interacting with Rho A signalling pathways: implications for neuroinflammation. Eur. J. Neurosci. *25*, 1069–1078.

Burney, R.E. (1993). Incidence, Characteristics, and Outcome of Spinal Cord Injury at Trauma Centers in North America. Arch. Surg. *128*, 596.

Busby, G.A., Grant, M.H., MacKay, S.P., and Riches, P.E. (2013). Confined compression of collagen hydrogels.

Bush, T., Puvanachandra, N., Horner, C., Polito, A., Ostenfeld, T., Svendsen, C., Mucke, L., Johnson, M., and Sofroniew, M. (1999). Leukocyte Infiltration, Neuronal Degeneration, and Neurite Outgrowth after Ablation of Scar-Forming, Reactive Astrocytes in Adult Transgenic Mice. Neuron *23*, 297–308.

Bydon, M., Lin, J., Macki, M., Gokaslan, Z.L., and Bydon, A. (2014). The current role of steroids in acute spinal cord injury. World Neurosurg. *82*, 848–854.

Cao, Q., Zhang, Y.P., Iannotti, C., DeVries, W.H., Xu, X.-M., Shields, C.B., and Whittemore, S.R. (2005). Functional and electrophysiological changes after graded traumatic spinal cord injury in adult rat. Exp. Neurol. S3–S16.

Cargill, R.S., and Thibault, L.E. (1996). Acute alterations in [Ca2+]i in NG108-15 cells subjected to high strain rate deformation and chemical hypoxia: an in vitro model for neural trauma. J. Neurotrauma *13*, 395–407.

Carter, J.W., Mirza, S.K., Tencer, A.F., and Ching, R.P. (2000). Canal geometry changes associated with axial compressive cervical spine fracture. Spine (Phila. Pa. 1976). *25*, 46–54.

Carter, M.W., Johnson, K.M., Lee, J.Y., Hulsebosch, C.E., and Gwak, Y.S. (2016). Comparison of Mechanical Allodynia and Recovery of Locomotion and Bladder Function by Different Parameters of Low Thoracic Spinal Contusion Injury in Rats. Korean J. Pain *29*, 86–95.

De Castro, R., Hughes, M.G., Xu, G.-Y., Clifton, C., Calingasan, N.Y., Gelman, B.B., and McAdoo, D.J. (2004). Evidence that infiltrating neutrophils do not release reactive oxygen species in the site of spinal cord injury. Exp. Neurol. *190*, 414–424.

Cavaliere, F., Vicente, E.S., and Matute, C. (2010). An organotypic culture model to study nigro-striatal degeneration. J. Neurosci. Methods *188*, 205–212.

Chandran, P.L., and Barocas, V.H. (2004). Microstructural Mechanics of Collagen Gels in Confined Compression: Poroelasticity, Viscoelasticity, and Collapse. J. Biomech. Eng. *126*, 152.

Chang, G.-L., Hung, T.-K., and Feng, W.W. (1988). An in-vivo measurement and analysis of viscoelastic properties of the spinal cord of cats. J. Biomech. Eng. *110*, 115–122.

Chaplin, M. (2016). Water Structure and Science.

Cheema, U., and Brown, R.A. (2013). Rapid Fabrication of Living Tissue Models by Collagen Plastic Compression: Understanding Three-Dimensional Cell Matrix Repair In Vitro. Adv. Wound Care *2*, 176–184.

Cheng, H., Cao, Y., and Olson, L. (1996). Spinal cord repair in adult paraplegic rats: partial restoration of hind limb function. Science *273*, 510–513.

Cheng, S., Clarke, E.C., and Bilston, L.E. (2008). Rheological properties of the tissues of the central nervous system: a review. Med. Eng. Phys. *30*, 1318–1337.

Cheng, S., Clarke, E.C., and Bilston, L.E. (2009). The effects of preconditioning strain on measured tissue properties. J. Biomech. *42*, 1360–1362.

Chiles, B., and Cooper, P. (1996). Acute spinal injury. N. Engl. J. Med.

Cho, J.-S., Park, H.-W., Park, S.-K., Roh, S., Kang, S.-K., Paik, K.-S., and Chang, M.-S. (2009). Transplantation of mesenchymal stem cells enhances axonal outgrowth and cell survival in an organotypic spinal cord slice culture. Neurosci. Lett. *454*, 43–48.

Choo, A.M., Liu, J., Lam, C.K., Dvorak, M., Tetzlaff, W., and Oxland, T.R. (2007). Contusion, dislocation, and distraction: primary hemorrhage and membrane permeability in distinct mechanisms of spinal cord injury. J. Neurosurg. Spine *6*, 255–266.

Choo, A.M., Liu, J., Dvorak, M., Tetzlaff, W., and Oxland, T.R. (2008). Secondary pathology following contusion, dislocation, and distraction spinal cord injuries. Exp. Neurol. *212*, 490–506.

Choo, A.M.-T., Liu, J., Liu, Z., Dvorak, M., Tetzlaff, W., and Oxland, T.R. (2009). Modeling spinal cord contusion, dislocation, and distraction: characterization of vertebral clamps, injury severities, and node of Ranvier deformations. J. Neurosci. Methods *181*, 6–17.

Christ, A.F., Franze, K., Gautier, H., Moshayedi, P., Fawcett, J., Franklin, R.J.M., Karadottir, R.T., and Guck, J. (2010). Mechanical difference between white and gray matter in the rat cerebellum measured by scanning force microscopy. J. Biomech. *43*, 2986–2992.

Cifra, A., Mazzone, G.L., Nani, F., Nistri, A., and Mladinic, M. (2012). Postnatal developmental profile of neurons and glia in motor nuclei of the brainstem and spinal cord, and its comparison with organotypic slice cultures. Dev. Neurobiol. *72*, 1140–1160.

Clarke, E.C., and Bilston, L.E. (2008). Contrasting biomechanics and neuropathology of spinal cord injury in neonatal and adult rats following vertebral dislocation. J. Neurotrauma *25*, 817–832.

Clarke, E.C., Choo, A.M., Liu, J., Lam, C.K., Bilston, L.E., Tetzlaff, W., and Oxland, T.R. (2008). Anterior fracture-dislocation is more severe than lateral: a biomechanical and neuropathological comparison in rat thoracolumbar spine. J. Neurotrauma *25*, 371–383.

Clarke, E.C., Cheng, S., and Bilston, L.E. (2009). The mechanical properties of neonatal rat spinal cord in vitro, and comparisons with adult. J. Biomech. *42*, 1397–1402.

Condeelis, J., and Pollard, J.W. (2006). Macrophages: obligate partners for tumor cell migration, invasion, and metastasis. Cell *124*, 263–266.

Crapo, P.M., Medberry, C.J., Reing, J.E., Tottey, S., van der Merwe, Y., Jones, K.E., and Badylak, S.F. (2012). Biologic scaffolds composed of central nervous system extracellular matrix. Biomaterials *33*, 3539–3547.

Cullen, D.K., and LaPlaca, M.C. (2006). Neuronal response to high rate shear deformation depends on heterogeneity of the local strain field. J. Neurotrauma *23*, 1304–1319.

Cullen, D.K., Stabenfeldt, S.E., Simon, C.M., Tate, C.C., and LaPlaca, M.C. (2007a). In vitro neural injury model for optimization of tissue-engineered constructs. J. Neurosci. Res. *85*, 3642–3651.

Cullen, D.K., Simon, C.M., and LaPlaca, M.C. (2007b). Strain rate-dependent induction of reactive astrogliosis and cell death in three-dimensional neuronal-astrocytic co-cultures. Brain Res. *1158*, 103–115.

Cullheim, S., and Thams, S. (2007). The microglial networks of the brain and their role in neuronal network plasticity after lesion. Brain Res. Rev. *55*, 89–96.

Czarnecki, A., Tscherter, A., and Streit, J. (2012). Network activity and spike discharge oscillations in cortical slice cultures from neonatal rat. Eur. J. Neurosci. *35*, 375–388.

Darian-Smith, C., and Brown, S. (2000). Functional changes at periphery and cortex following dorsal root lesions in adult monkeys. Nat. Neurosci. *3*, 476–481.

Davalos, D., Grutzendler, J., Yang, G., Kim, J. V, Zuo, Y., Jung, S., Littman, D.R., Dustin, M.L., and Gan, W.-B. (2005). ATP mediates rapid microglial response to local brain injury in vivo. Nat. Neurosci. *8*, 752–758.

Daviaud, N., Garbayo, E., Schiller, P.C., Perez-Pinzon, M., and Montero-Menei, C.N. (2013). Organotypic cultures as tools for optimizing central nervous system cell therapies. Exp. Neurol. *248*, 429–440.

David, S., and Kroner, A. (2011). Repertoire of microglial and macrophage responses after spinal cord injury. Nat. Rev. Neurosci. *12*, 388–399.

Davies, J.E., Huang, C., Proschel, C., Noble, M., Mayer-Proschel, M., and Davies, S.J.A. (2006). Astrocytes derived from glial-restricted precursors promote spinal cord repair. J. Biol. *5*, 7.

Deshmukh, B.S., and Mankar, V.H. (2014). Segmentation of Microscopic Images: A Survey. In 2014 International Conference on Electronic Systems, Signal Processing and Computing Technologies, (IEEE), pp. 362–364.

DeVivo, M.J., and Vogel, L.C. (2004). Epidemiology of spinal cord injury in children and adolescents. J. Spinal Cord Med. *27 Suppl 1*, S4–S10.

Discher, D.E., Janmey, P., and Wang, Y.-L. (2005). Tissue cells feel and respond to the stiffness of their substrate. Science *310*, 1139–1143.

Doyle, L.M., Stafford, P.P., and Roberts, B.L. (2001). Recovery of locomotion correlated with axonal regeneration after a complete spinal transection in the eel. Neuroscience *107*, 169–179.

Drake, R.L., Vogl, A.W., and Mitchell, A.W.M. (2009). Gray's Anatomy for Students: With STUDENT CONSULT Online Access, 2e (Churchill Livingstone).

Drury, J.L., Dennis, R.G., and Mooney, D.J. (2004). The tensile properties of alginate hydrogels. Biomaterials *25*, 3187–3199.

Duval, T., McNab, J.A., Setsompop, K., Witzel, T., Schneider, T., Huang, S.Y., Keil, B., Klawiter, E.C., Wald, L.L., and Cohen-Adad, J. (2015). In vivo mapping of human spinal cord microstructure at 300mT/m. Neuroimage *118*, 494–507.

East, E., and Phillips, J.B. (2008). Tissue engineered cell culture models for nervous system research.

East, E., Golding, J.P., and Phillips, J.B. (2009). A versatile 3D culture model facilitates monitoring of astrocytes undergoing reactive gliosis. J. Tissue Eng. Regen. Med. *3*, 634–646.

East, E., de Oliveira, D.B., Golding, J.P., and Phillips, J.B. (2010). Alignment of astrocytes increases neuronal growth in three-dimensional collagen gels and is maintained following plastic compression to form a spinal cord repair conduit. Tissue Eng. Part A *16*, 3173–3184.

East, E., Golding, J.P., and Phillips, J.B. (2012). Engineering an integrated cellular interface in three-dimensional hydrogel cultures permits monitoring of reciprocal astrocyte and neuronal responses. Tissue Eng. Part C. Methods *18*, 526–536.

Eastwood, M., Mudera, V.C., McGrouther, D.A., and Brown, R.A. (1998). Effect of precise mechanical loading on fibroblast populated collagen lattices: morphological changes. Cell Motil. Cytoskeleton *40*, 13–21.

Edgar, J.M., McLaughlin, M., Yool, D., Zhang, S.-C., Fowler, J.H., Montague, P., Barrie, J.A., McCulloch, M.C., Duncan, I.D., Garbern, J., et al. (2004). Oligodendroglial modulation of fast axonal transport in a mouse model of hereditary spastic paraplegia. J. Cell Biol. *166*, 121–131.

Elias, P.Z., and Spector, M. (2012). Viscoelastic characterization of rat cerebral cortex and type I collagen scaffolds for central nervous system tissue engineering. J. Mech. Behav. Biomed. Mater. *12*, 63–73.

Elkin, B.S., Azeloglu, E.U., Costa, K.D., and Morrison III, B. (2007). Mechanical Heterogeneity of the Rat Hippocampus Measured by Atomic Force Microscope Indentation. J. Neurotrauma *24*, 812–822.

Ellis, E.F., McKinney, J.S., Willoughby, K.A., Liang, S., and Povlishock, J.T. (1995). A new model for rapid stretch-induced injury of cells in culture: characterization of the model using astrocytes. J. Neurotrauma *12*, 325–339.

Emmetsberger, J., and Tsirka, S.E. (2012). Microglial inhibitory factor (MIF/TKP) mitigates secondary damage following spinal cord injury. Neurobiol. Dis. *47*, 295–309.

Engelhardt, E.-M., Stegberg, E., Brown, R. a, Hubbell, J. a, Wurm, F.M., Adam, M., and Frey, P. (2010). Compressed collagen gel: a novel scaffold for human bladder cells. J. Tissue Eng. Regen. Med. *4*, 123–130.

Engesser-Cesar, C., Ichiyama, R.M., Nefas, A.L., Hill, M.A., Edgerton, V.R., Cotman, C.W., and Anderson, A.J. (2007). Wheel running following spinal cord injury improves locomotor recovery and stimulates serotonergic fiber growth. Eur. J. Neurosci. *25*, 1931–1939.

Engler, A.J., Sen, S., Sweeney, H.L., and Discher, D.E. (2006a). Matrix elasticity directs stem cell lineage specification. Cell *126*, 677–689.

Engler, A.J., Sen, S., Sweeney, H.L., and Discher, D.E. (2006b). Matrix elasticity directs stem cell lineage specification. Cell *126*, 677–689.

Evans, M.C., and Barocas, V.H. (2009). The Modulus of Fibroblast-Populated Collagen Gels is not Determined by Final Collagen and Cell Concentration: Experiments and an Inclusion-Based Model. J. Biomech. Eng. *131*, 101014.

Ewoldt, R.H., Johnston, M.T., and Caretta, L.M. (2015). Experimental Challenges of Shear Rheology: How to Avoid Bad Data. (Springer New York), pp. 207–241.

Fallenstein, G.T., Hulce, V.D., and Melvin, J.W. (1969). Dynamic mechanical properties of human brain tissue. J. Biomech. *2*, 217–226.

Farina, C., Aloisi, F., and Meinl, E. (2007). Astrocytes are active players in cerebral innate immunity. Trends Immunol. *28*, 138–145.

Faulkner, J.R., Herrmann, J.E., Woo, M.J., Tansey, K.E., Doan, N.B., and Sofroniew, M. V. (2004). Reactive astrocytes protect tissue and preserve function after spinal cord injury. J. Neurosci. *24*, 2143–2155.

Fawcett, J.W. (2006). Overcoming inhibition in the damaged spinal cord. J. Neurotrauma *23*, 371–383.

Fawcett, J.W., and Asher, R.A. (1999). The glial scar and central nervous system repair. Brain Res. Bull. *49*, 377–391.

Fedorow, C.A., Moon, M.C., Mutch, W.A.C., and Grocott, H.P. (2010). Lumbar cerebrospinal fluid drainage for thoracoabdominal aortic surgery: rationale and practical considerations for management. Anesth. Analg. *111*, 46–58.

Fehlings, M.G., and Baptiste, D.C. (2005). Current status of clinical trials for acute spinal cord injury. Injury *36 Suppl 2*, B113–B122.

Fehlings, M.G., and Nashmi, R. (1997). A new model of acute compressive spinal cord injury in vitro. J. Neurosci. Methods *71*, 215–224.

Fehlings, M.G., Tator, C.H., and Linden, R.D. (1989). The relationships among the severity of spinal cord injury, motor and somatosensory evoked potentials and spinal cord blood flow. Electroencephalogr. Clin. Neurophysiol. Potentials Sect. *74*, 241–259.

Fehlings, M.G., Cadotte, D.W., and Fehlings, L.N. (2011). A series of systematic reviews on the treatment of acute spinal cord injury: a foundation for best medical practice. J. Neurotrauma *28*, 1329–1333.

Feng, C., Cheng, Y., and Chao, P.G. (2013). The influence and interactions of substrate thickness, organization and dimensionality on cell morphology and migration. Acta Biomater. *9*, 5502–5510.

Fiford, R.J., and Bilston, L.E. (2005). The mechanical properties of rat spinal cord in vitro. J. Biomech. *38*, 1509–1515.

Fiford, R.J., Bilston, L.E., Waite, P., and Lu, J. (2004). A vertebral dislocation model of spinal cord injury in rats. J. Neurotrauma *21*, 451–458.

Fitch, M.T., and Silver, J. (1997). Glial cell extracellular matrix: boundaries for axon growth in development and regeneration. Cell Tissue Res. *290*, 379–384.

Fitch, M.T., and Silver, J. (2008). CNS injury, glial scars, and inflammation: Inhibitory extracellular matrices and regeneration failure. Exp. Neurol. *209*, 294–301.

FitzGerald, M.J.T., and Folan-Curran, J. (2001). Clinical Neuroanatomy and Related Neuroscience: Basic and Clinical (W. B. Saunders).

Flanagan, L.A., Ju, Y.-E., Marg, B., Osterfield, M., and Janmey, P.A. (2002). Neurite branching on deformable substrates. Neuroreport *13*, 2411–2415.

Fleming, J.C., Norenberg, M.D., Ramsay, D.A., Dekaban, G.A., Marcillo, A.E., Saenz, A.D., Pasquale-Styles, M., Dietrich, W.D., and Weaver, L.C. (2006). The cellular inflammatory response in human spinal cords after injury. Brain *129*, 3249–3269.

Fortun, J., Hill, C.E., and Bunge, M.B. (2009). Combinatorial strategies with Schwann cell transplantation to improve repair of the injured spinal cord. Neurosci. Lett. *456*, 124–132.

Franze, K., Janmey, P.A., and Guck, J. (2013). Mechanics in neuronal development and repair. Annu. Rev. Biomed. Eng. *15*, 227–251.

Friede, R.L., and Brück, W. (1993). Macrophage functional properties during myelin degradation. Adv. Neurol. *59*, 327–336.

Frigon, A. (2013). Animal Models of Spinal Cord Repair (Totowa, NJ: Humana Press).

Fukuda, S., Nakamura, T., Kishigami, Y., Endo, K., Azuma, T., Fujikawa, T., Tsutsumi, S., and Shimizu, Y. (2005). New canine spinal cord injury model free from laminectomy. Brain Res. Brain Res. Protoc. *14*, 171–180.

Galante, M., Avossa, D., Rosato-Siri, M., and Ballerini, L. (2001). Homeostatic plasticity induced by chronic block of AMPA/kainate receptors modulates the generation of rhythmic bursting in rat spinal cord organotypic cultures. Eur. J. Neurosci. *14*, 903–917.

Gale, K., Kerasidis, H., and Wrathall, J.R. (1985). Spinal cord contusion in the rat: Behavioral analysis of functional neurologic impairment. Exp. Neurol. *88*, 123–134.

Garo, A., Hrapko, M., van Dommelen, J.A.W., and Peters, G.W.M. (2007). Towards a reliable characterisation of the mechanical behaviour of brain tissue: The effects of post-mortem time and sample preparation. Biorheology *44*, 51–58.

Gattlen, C., Clarke, C.B., Piller, N., Kirschmann, G., Pertin, M., Decosterd, I., Gosselin, R.-D., and Suter, M.R. (2016). Spinal Cord T-Cell Infiltration in the Rat Spared Nerve Injury Model: A Time Course Study. Int. J. Mol. Sci. *17*, 352.

Geddes, D.M., Cargill, R.S., and LaPlaca, M.C. (2003). Mechanical stretch to neurons results in a strain rate and magnitude-dependent increase in plasma membrane permeability. J. Neurotrauma *20*, 1039–1049.

Gefen, A., and Margulies, S.S. (2004). Are in vivo and in situ brain tissues mechanically similar? J. Biomech. *37*, 1339–1352.

Geller, H.M., and Fawcett, J.W. (2002). Building a bridge: engineering spinal cord repair. Exp. Neurol. *174*, 125–136.

Georges, P.C., Miller, W.J., Meaney, D.F., Sawyer, E.S., and Janmey, P.A. (2006). Matrices with compliance comparable to that of brain tissue select neuronal over glial growth in mixed cortical cultures. Biophys. J. *90*, 3012–3018.

Georgiou, M., Bunting, S.C.J.J., Davies, H.A., Loughlin, A.J., Golding, J.P., and Phillips, J.B. (2013). Engineered neural tissue for peripheral nerve repair. Biomaterials *34*, 7343–7335.

Ghasemlou, N., Kerr, B.J., and David, S. (2005). Tissue displacement and impact force are important contributors to outcome after spinal cord contusion injury. Exp. Neurol. *196*, 9–17.

Gilad, G.M., Kagan, H.M., and Gilad, V.H. (2001). Lysyl oxidase, the extracellular matrix-forming enzyme, in rat brain injury sites.

Goode, S. (2015). Development of a Computational Spinal Cord Injury Model using the Material Point Method. Computer Methods in Biomechanics and Biomedical Engineering. Montreal, Canada.

Graeber, M.B., and Streit, W.J. (2010). Microglia: biology and pathology. Acta Neuropathol. *119*, 89–105.

Greenburg, G., and Hay, E.D. (1982). Epithelia suspended in collagen gels can lose polarity and express characteristics of migrating mesenchymal cells. J. Cell Biol. *95*, 333–339.

Greenhalgh, A.D., and David, S. (2014). Differences in the phagocytic response of microglia and peripheral macrophages after spinal cord injury and its effects on cell death. J. Neurosci. *34*, 6316–6322.

Griffith, C.K., Miller, C., Sainson, R.C.A., Calvert, J.W., Jeon, N.L., Hughes, C.C.W., and George, S.C. (2005). Diffusion limits of an in vitro thick prevascularized tissue. Tissue Eng. *11*, 257–266.

Gronau, G., Krishnaji, S.T., Kinahan, M.E., Giesa, T., Wong, J.Y., Kaplan, D.L., and Buehler, M.J. (2012). A review of combined experimental and computational procedures for assessing biopolymer structure–process–property relationships. Biomaterials *33*, 8240–8255.

Gruner, J.A. (1992). A Monitored Contusion Model of Spinal Cord Injury in the Rat. J. Neurotrauma *9*, 123–128.

Guerrero, A.R., Uchida, K., Nakajima, H., Watanabe, S., Nakamura, M., Johnson, W.E., and Baba, H. (2012). Blockade of interleukin-6 signaling inhibits the classic pathway and promotes an alternative pathway of macrophage activation after spinal cord injury in mice. J. Neuroinflammation *9*, 40.

Guest, J.D., Hiester, E.D., and Bunge, R.P. (2005). Demyelination and Schwann cell responses adjacent to injury epicenter cavities following chronic human spinal cord injury. Exp. Neurol. *192*, 384–393.

Guth, L., Zhang, Z., and Steward, O. (1999). The unique histopathological responses of the injured spinal cord. Implications for neuroprotective therapy. Ann. N. Y. Acad. Sci. *890*, 366–384.

Hadjipanayi, E., Mudera, V., and Brown, R.A. (2009). Guiding cell migration in 3D: a collagen matrix with graded directional stiffness. Cell Motil. Cytoskeleton *66*, 121–128.

Hamilton, N.B., and Attwell, D. (2010). Do astrocytes really exocytose neurotransmitters? Nat. Rev. Neurosci. *11*, 227–238.

Hanisch, U.-K., and Kettenmann, H. (2007). Microglia: active sensor and versatile effector cells in the normal and pathologic brain. Nat. Neurosci. *10*, 1387–1394.

Harms, J., and Tabasso, G. (1998). Principles of Instrumented Spinal Surgery (Thieme Publishing Group).

Harrison, Cailliet, R., Harrison, D.D., Troyanovich, S.J., and Harrison, S.O. (1999a). A review of biomechanics of the central nervous system-Part I: Spinal canal deformations resulting from changes in posture. J. Manipulative Physiol. Ther. *22*, 227–234.

Harrison, D., Cailliet, R., Harrison, D.D., Troyanovich, S.J., and Harrison, S.O. (1999b). Part II: A review of biomechanics of the central nervous system: spinal cord strains from postural loads. J. Manipulative Physiol. Ther. *22*, 322–332.

Haw, R.T.Y., Tong, C.K., Yew, A., Lee, H.C., Phillips, J.B., and Vidyadaran, S. (2014). A three-dimensional collagen construct to model lipopolysaccharide-induced activation of BV2 microglia. J. Neuroinflammation *11*, 134.

Heck, N., Garwood, J., Schütte, K., Fawcett, J., and Faissner, A. (2003). Astrocytes in culture express fibrillar collagen. Glia *41*, 382–392.

Heidemann, M., Streit, J., and Tscherter, a. (2014). Functional regeneration of intraspinal connections in a new in vitro model. Neuroscience *262*, 40–52.

Herrmann, J.E., Imura, T., Song, B., Qi, J., Ao, Y., Nguyen, T.K., Korsak, R.A., Takeda, K., Akira, S., and Sofroniew, M. V (2008). STAT3 is a critical regulator of astrogliosis and scar formation after spinal cord injury. J. Neurosci. *28*, 7231–7243.

Hines, D.J., Hines, R.M., Mulligan, S.J., and Macvicar, B.A. (2009). Microglia processes block the spread of damage in the brain and require functional chloride channels. Glia *57*, 1610–1618.

Hirakawa, K., Hashizume, K., and Hayashi, T. (1981). Viscoelastic property of human brain -for the analysis of impact injury. Nō to Shinkei = Brain Nerve *33*, 1057–1065.

Hofstetter, C.P., Schwarz, E.J., Hess, D., Widenfalk, J., El Manira, A., Prockop, D.J., and Olson, L. (2002). Marrow stromal cells form guiding strands in the injured spinal cord and promote recovery. Proc. Natl. Acad. Sci. U. S. A. *99*, 2199–2204.

Hooshmand, M.J., Galvan, M.D., Partida, E., and Anderson, A.J. (2014). Characterization of recovery, repair, and inflammatory processes following contusion spinal cord injury in old female rats: is age a limitation? Immun. Ageing *11*, 15.

Hopkins, A.M., DeSimone, E., Chwalek, K., and Kaplan, D.L. (2015). 3D in vitro modeling of the central nervous system. Prog. Neurobiol. *125*, 1–25.

Hovakimyan, M., Guthoff, R.F., and Stachs, O. (2012). Collagen cross-linking: current status and future directions. J. Ophthalmol. *2012*, 406850.

Hsiao, T.W., Tresco, P.A., and Hlady, V. (2015). Astrocytes alignment and reactivity on collagen hydrogels patterned with ECM proteins. Biomaterials *39*, 124–130.

Hu, J.C., and Athanasiou, K.A. (2005). Low-density cultures of bovine chondrocytes: effects of scaffold material and culture system. Biomaterials *26*, 2001–2012.

Hung, T.-K., and Chang, G.-L. (1981). Biomechanical and neurological response of the spinal cord of a puppy to uniaxial tension. J. Biomech. Eng. *103*, 43–47.

Hung, Chang, G.-L., Lin, H.-S., Walter, F.R., and Bunegin, L. (1981a). Stress-strain relationship of the spinal cord of anesthetized cats. J. Biomech. *14*, 269–276.

Hung, T.K., Albin, M.S., Brown, T.D., Bunegin, L., Albin, R., and Jannetta, P.J. (1975). Biomechanical responses to open experimental spinal cord injury. Surg. Neurol. *4*, 271–276.

Hung, T.-K., Chang, G.-L., Chang, J.-L., and Albin, M.S. (1981b). Stress-strain relationship and neurological sequelae of uniaxial elongation of the spinal cord of cats. Surg. Neurol. *15*, 471–476.

Ichihara, K., Taguchi, T., Shimada, Y., Sakuramoto, I., Kawano, S., and Kawai, S. (2001). Gray matter of the bovine cervical spinal cord is mechanically more rigid and fragile than the white matter. J. Neurotrauma *18*, 361–367.

Ichiyama, R., Potuzak, M., Balak, M., Kalderon, N., and Edgerton, V.R. (2009). Enhanced motor function by training in spinal cord contused rats following radiation therapy. PLoS One *4*, e6862.

Iglesias, J., Morales, L., and Barreto, G.E. (2016). Metabolic and Inflammatory Adaptation of Reactive Astrocytes: Role of PPARs. Mol. Neurobiol.

Iwanami, A., Yamane, J., Katoh, H., Nakamura, M., Momoshima, S., Ishii, H., Tanioka, Y., Tamaoki, N., Nomura, T., Toyama, Y., et al. (2005). Establishment of graded spinal cord injury model in a nonhuman primate: the common marmoset. J. Neurosci. Res. *80*, 172–181.

Izzo, R., Guarnieri, G., Guglielmi, G., and Muto, M. (2013). Biomechanics of the spine. Part I: spinal stability. Eur. J. Radiol. *82*, 118–126.

Jaalouk, D.E., and Lammerding, J. (2009). Mechanotransduction gone awry. Nat. Rev. Mol. Cell Biol. *10*, 63–73.

Jäderstad, L.M., Jäderstad, J., and Herlenius, E. (2010). Graft and host interactions following transplantation of neural stem cells to organotypic striatal cultures. Regen. Med. *5*, 901–917.

Jakovcevski, I., Filipovic, R., Mo, Z., Rakic, S., and Zecevic, N. (2009). Oligodendrocyte development and the onset of myelination in the human fetal brain. Front. Neuroanat. *3*, 5.

Jenkins, D.B. (2008). Hollinshead's Functional Anatomy of the Limbs and Back, 9e (Saunders).

Jessell, T.M. (2000). Neuronal specification in the spinal cord: inductive signals and transcriptional codes. Nat. Rev. Genet. *1*, 20–29.

Jones, C.F., Lee, J.H.T., Kwon, B.K., and Cripton, P.A. (2012a). Development of a large-animal model to measure dynamic cerebrospinal fluid pressure during spinal cord injury: Laboratory investigation. J. Neurosurg. Spine *16*, 624–635.

Jones, C.F., Cripton, P.A., and Kwon, B.K. (2012b). Gross Morphological Changes of the Spinal Cord Immediately After Surgical Decompression in a Large Animal Model of Traumatic Spinal Cord Injury. Spine (Phila. Pa. 1976). *37*, E890–E899.

Jones, L.L., Yamaguchi, Y., Stallcup, W.B., and Tuszynski, M.H. (2002). NG2 is a major chondroitin sulfate proteoglycan produced after spinal cord injury and is expressed by macrophages and oligodendrocyte progenitors. J. Neurosci. *22*, 2792–2803.

Jones, L.L., Margolis, R.U., and Tuszynski, M.H. (2003). The chondroitin sulfate proteoglycans neurocan, brevican, phosphacan, and versican are differentially regulated following spinal cord injury. Exp. Neurol. *182*, 399–411.

Joosten, E.A., Dijkstra, S., Brook, G.A., Veldman, H., and Bär, P.R. (2000). Collagen IV deposits do not prevent regrowing axons from penetrating the lesion site in spinal cord injury. J. Neurosci. Res. *62*, 686–691.

Jordan, F.L., and Thomas, W.E. (1988). Brain macrophages: questions of origin and interrelationship. Brain Res. *472*, 165–178.

Jurewicz, A., Matysiak, M., Tybor, K., Kilianek, L., Raine, C.S., and Selmaj, K. (2005). Tumour necrosis factor-induced death of adult human oligodendrocytes is mediated by apoptosis inducing factor. Brain *128*, 2675–2688.

Kagami, S., Kondo, S., Löster, K., Reutter, W., Kuhara, T., Yasutomo, K., and Kuroda, Y. (1999). Alpha1beta1 integrin-mediated collagen matrix remodeling by rat mesangial cells is differentially regulated by transforming growth factor-beta and platelet-derived growth factor-BB. J. Am. Soc. Nephrol. *10*, 779–789.

Kakulas, B.A. (1999). A review of the neuropathology of human spinal cord injury with emphasis on special features. J. Spinal Cord Med. *22*, 119–124.

Kang, K.N., Kim, D.Y., Yoon, S.M., Lee, J.Y., Lee, B.N., Kwon, J.S., Seo, H.W., Lee, I.W., Shin, H.C., Kim, Y.M., et al. (2012). Tissue engineered regeneration of completely transected spinal cord using human mesenchymal stem cells. Biomaterials *33*, 4828–4835.

Kassmann, C.M., and Nave, K.-A. (2008). Oligodendroglial impact on axonal function and survival - a hypothesis. Curr. Opin. Neurol. *21*, 235–241.

Kazakia, G.J., Nauman, E.A., Ebenstein, D.M., Halloran, B.P., and Keaveny, T.M. (2006). Effects of in vitro bone formation on the mechanical properties of a trabeculated hydroxyapatite bone substitute. J. Biomed. Mater. Res. A *77*, 688–699.

Kearney, P.A., Ridella, S.A., Viano, D.C., and Anderson, T.E. (1988). Interaction of contact velocity and cord compression in determining the severity of spinal cord injury. J. Neurotrauma *5*, 187–208.

Kearns, S.M., Scheffler, B., Goetz, A.K., Lin, D.D., Baker, H.D., Roper, S.N., Mandel, R.J., and Steindler, D.A. (2006). A method for a more complete in vitro Parkinson's model: Slice culture bioassay for modeling maintenance and repair of the nigrostriatal circuit. J. Neurosci. Methods *157*, 1–9.

Kerstetter, A.E., and Miller, R.H. (2012). Isolation and culture of spinal cord astrocytes. Methods Mol. Biol. *814*, 93–104.

Khuyagbaatar, B., Kim, K., and Hyuk Kim, Y. (2014). Effect of bone fragment impact velocity on biomechanical parameters related to spinal cord injury: a finite element study. J. Biomech. *47*, 2820–2825.

Kigerl, K.A., Gensel, J.C., Ankeny, D.P., Alexander, J.K., Donnelly, D.J., and Popovich, P.G. (2009). Identification of two distinct macrophage subsets with divergent effects causing either neurotoxicity or regeneration in the injured mouse spinal cord. J. Neurosci. *29*, 13435–13444.

Kim, B.-H., Meeker, H.C., Shin, H.-Y., Kim, J.-I., Jeong, B.-H., Choi, E.-K., Carp, R.I., Kim, Y.-S., Takeda, T., Hosokawa, M., et al. (2008). Physiological properties of astroglial cell lines derived from mice with high (SAMP8) and low (SAMR1, ICR) levels of endogenous retrovirus. Retrovirology *5*, 104.

Kimelberg, H.K., and Norenberg, M.D. (1989). Astrocytes. Sci. Am. *260*, 66–72, 74, 76.

Kirkpatrick, J.C., Fuchs, S., Hermanns, I.M., Peters, K., and Unger, R.E. (2007). Cell culture models of higher complexity in tissue engineering and regenerative medicine. Biomaterials *28*, 5193–5198.

Klapka, N., and Müller, H.W. (2009). Collagen matrix in spinal cord injury. J. Neurotrauma *23*, 422–435.

Kleiman, R., Previtera, M., Parikh, S., Verma, D., Schloss, R., and Langrana, N. (2011). The Effects of Extracellular Matrix Proteins and Stiffness on Neuronal Cell Adhesion. In ASME 2011 Summer Bioengineering Conference, Parts A and B, (ASME), p. 1015.

Kloxin, A.M., Kloxin, C.J., Bowman, C.N., and Anseth, K.S. (2010). Mechanical properties of cellularly responsive hydrogels and their experimental determination. Adv. Mater. *22*, 3484–3494.

Knapp, D.M., Barocas, V.H., Moon, A.G., Yoo, K., Petzold, L.R., and Tranquillo, R.T. (1997). Rheology of reconstituted type I collagen gel in confined compression. J. Rheol. (N. Y. N. Y). *41*, 971.

Kofron, C.M., Fong, V.J., and Hoffman-Kim, D. (2009). Neurite outgrowth at the interface of 2D and 3D growth environments. J. Neural Eng. *6*, 016002.

Kongsui, R., Beynon, S.B., Johnson, S.J., and Walker, F.R. (2014). Quantitative assessment of microglial morphology and density reveals remarkable consistency in the distribution and morphology of cells within the healthy prefrontal cortex of the rat. J. Neuroinflammation *11*, 182.

Krassioukov, A. V, Ackery, A., Schwartz, G., Adamchik, Y., Liu, Y., and Fehlings, M.G. (2002). An in vitro model of neurotrauma in organotypic spinal cord cultures from adult mice. Brain Res. Protoc. *10*, 60–68.

Kreger, S.T., Bell, B.J., Bailey, J., Stites, E., Kuske, J., Waisner, B., and Voytik-Harbin, S.L. (2010). Polymerization and matrix physical properties as important design considerations for soluble collagen formulations. Biopolymers *93*, 690–707.

Kreutzberg, G.W. (1996). Microglia: a sensor for pathological events in the CNS. Trends Neurosci. *19*, 312–318.

Kroeker, S.G., Morley, P.L., Jones, C.F., Bilston, L.E., and Cripton, P.A. (2009). The development of an improved physical surrogate model of the human spinal cord--tension and transverse compression. J. Biomech. *42*, 878–883.

Kumaria, a, and Tolias, C.M. (2008). In vitro models of neurotrauma. Br. J. Neurosurg. *22*, 200–206.

Kwon, B.K., Oxland, T.R., and Tetzlaff, W. (2002a). Animal Models Used in Spinal Cord Regeneration Research. *27*, 1504–1510.

Kwon, B.K., Oxland, T.R., and Tetzlaff, W. (2002b). Animal models used in spinal cord regeneration research. Spine (Phila. Pa. 1976). *27*, 1504–1510.

Kwon, B.K., Tetzlaff, W., Grauer, J.N., Beiner, J., and Vaccaro, A.R. (2004). Pathophysiology and pharmacologic treatment of acute spinal cord injury. Spine J. *4*, 451–464.

Lagord, C., Berry, M., and Logan, A. (2002). Expression of TGFβ2 but Not TGFβ1 Correlates with the Deposition of Scar Tissue in the Lesioned Spinal Cord. Mol. Cell. Neurosci. *20*, 69–92.

Lam, C.J., Assinck, P., Liu, J., Tetzlaff, W., and Oxland, T.R. (2014). Impact depth and the interaction with impact speed affect the severity of contusion spinal cord injury in rats. J. Neurotrauma *31*, 1985–1997.

Lantoine, J., Grevesse, T., Villers, A., Delhaye, G., Mestdagh, C., Versaevel, M., Mohammed, D., Bruyère, C., Alaimo, L., Lacour, S.P., et al. (2016). Matrix stiffness modulates formation and activity of neuronal networks of controlled architectures. Biomaterials *89*, 14–24.

LaPlaca, M.C., Cullen, D.K., McLoughlin, J.J., and Cargill, R.S. (2005a). High rate shear strain of three-dimensional neural cell cultures: a new in vitro traumatic brain injury model. J. Biomech. *38*, 1093–1105.

LaPlaca, M.C., Cullen, D.K., McLoughlin, J.J., and Cargill, R.S. (2005b). High rate shear strain of three-dimensional neural cell cultures: a new in vitro traumatic brain injury model. J. Biomech. *38*, 1093–1105.

LaPlaca, M.C., Simon, C.M., Prado, G.R., and Cullen, D.K. (2007). CNS injury biomechanics and experimental models. Prog. Brain Res. *161*, 13–26.

Larson, R.G. (1999). The Structure and Rheology of Complex Fluids (Topics in Chemical Engineering).

Lee, D.-H., and Lee, J.K. (2013). Animal models of axon regeneration after spinal cord injury. Neurosci. Bull. *29*, 436–444.

Lee, H., McKeon, R.J., and Bellamkonda, R. V (2010). Sustained delivery of thermostabilized chABC enhances axonal sprouting and functional recovery after spinal cord injury. Proc. Natl. Acad. Sci. U. S. A. *107*, 3340–3345.

Lee, J.H.T., Streijger, F., Tigchelaar, S., Maloon, M., Liu, J., Tetzlaff, W., and Kwon, B.K. (2012). A Contusive Model of Unilateral Cervical Spinal Cord Injury Using the Infinite Horizon Impactor. J. Vis. Exp. e3313–e3313.

Lee, J.H.T., Jones, C.F., Okon, E.B., Anderson, L., Tigchelaar, S., Kooner, P., Godbey, T., Chua, B., Gray, G., Hildebrandt, R., et al. (2013). A novel porcine model of traumatic thoracic spinal cord injury. J. Neurotrauma *30*, 142–159.

Lenhossék, M. (1893). Der feinere Bau des Nervensystems im Lichte neuester Forschung (Berlin : Fischer's Medicinische Buchhandlung).

Levis, H.J., Peh, G.S.L., Toh, K.-P., Poh, R., Shortt, A.J., Drake, R. a L., Mehta, J.S., and Daniels, J.T. (2012). Plastic compressed collagen as a novel carrier for expanded human corneal endothelial cells for transplantation. PLoS One *7*, e50993.

Li, G.N., Livi, L.L., Gourd, C.M., Deweerd, E.S., and Hoffman-Kim, D. (2007). Genomic and morphological changes of neuroblastoma cells in response to three-dimensional matrices. Tissue Eng. *13*, 1035–1047.

Li, Y., Field, P.M., and Raisman, G. (1998). Regeneration of adult rat corticospinal axons induced by transplanted olfactory ensheathing cells. J. Neurosci. *18*, 10514–10524.

Liesi, P., and Kauppila, T. (2002). Induction of Type IV Collagen and Other Basement-Membrane-Associated Proteins after Spinal Cord Injury of the Adult Rat May Participate in Formation of the Glial Scar. Exp. Neurol. *173*, 31–45.

Lijnen, P., Petrov, V., Rumilla, K., and Fagard, R. (2003). Transforming growth factor-beta 1 promotes contraction of collagen gel by cardiac fibroblasts through their differentiation into myofibroblasts. Methods Find. Exp. Clin. Pharmacol. *25*, 79–86.

Liu, T., Houle, J.D., Ph, D., Xu, J., Eng, M., Chan, B.P., and Chew, S.Y. (2012). Nanofibrous Collagen Nerve Conduits for Spinal Cord Repair. *18*.

Lo, C.M., Wang, H.B., Dembo, M., and Wang, Y.L. (2000). Cell movement is guided by the rigidity of the substrate. Biophys. J. *79*, 144–152.

Loy, D.N., Sroufe, A.E., Pelt, J.L., Burke, D.A., Cao, Q.-L., Talbott, J.F., and Whittemore, S.R. (2005). Serum biomarkers for experimental acute spinal cord injury:

rapid elevation of neuron-specific enolase and S-100beta. Neurosurgery *56*, 391–397; discussion 391–397.

Lu, Y.-B., Franze, K., Seifert, G., Steinhäuser, C., Kirchhoff, F., Wolburg, H., Guck, J., Janmey, P., Wei, E.-Q., Käs, J., et al. (2006). Viscoelastic properties of individual glial cells and neurons in the CNS. Proc. Natl. Acad. Sci. U. S. A. *103*, 17759–17764.

Luna, C., Detrick, L., Shah, S.B., Cohen, A.H., and Aranda-Espinoza, H. (2013). Mechanical properties of the lamprey spinal cord: Uniaxial loading and physiological strain. J. Biomech.

Lundgaard, I., Li, B., Xie, L., Kang, H., Sanggaard, S., Haswell, J.D.R., Sun, W., Goldman, S., Blekot, S., Nielsen, M., et al. (2015). Direct neuronal glucose uptake heralds activity-dependent increases in cerebral metabolism. Nat. Commun. *6*, 6807.

Lusardi, T.A., Rangan, J., Sun, D., Smith, D.H., and Meaney, D.F. (2004). A device to study the initiation and propagation of calcium transients in cultured neurons after mechanical stretch. Ann. Biomed. Eng. *32*, 1546–1558.

Macaya, D., and Spector, M. (2012). Injectable hydrogel materials for spinal cord regeneration: a review. Biomed. Mater. *7*, 012001.

Macosko, C.W. (1994). Rheology : principles, measurements, and applications (VCH).

Malvern Instruments Ltd. (2016). Rheology and Viscocity.

Marar, B.C. (1974). The pattern of neurological damage as an aid to the diagnosis of the mechanism in cervical-spine injuries. J. Bone Joint Surg. Am. *56*, 1648–1654.

Marsh, B.C., Astill, S.L., Utley, A., and Ichiyama, R.M. (2011). Movement rehabilitation after spinal cord injuries: emerging concepts and future directions. Brain Res. Bull. *84*, 327–336.

Martens, W., Sanen, K., Georgiou, M., Struys, T., Bronckaers, A., Ameloot, M., Phillips, J., and Lambrichts, I. (2014). Human dental pulp stem cells can differentiate into Schwann cells and promote and guide neurite outgrowth in an aligned tissue-engineered collagen construct in vitro. FASEB J. *28*, 1634–1643.

Mazuchowski, E.L., and Thibault, L.E. (2003). Biomechanical Properties of the Human Spinal Cord and Pia Mater. In Summer Bioengineering Conference, (Key Biscayne, Florida), p. 1205.

McDonald, J.W., and Sadowsky, C. (2002). Spinal-cord injury. Lancet *359*, 417–425.

McKeon, R.J., Schreiber, R.C., Rudge, J.S., and Silver, J. (1991). Reduction of neurite outgrowth in a model of glial scarring following CNS injury is correlated with the expression of inhibitory molecules on reactive astrocytes. J. Neurosci. *11*, 3398–3411.

McKillop, W.M., Dragan, M., Schedl, A., and Brown, A. (2013). Conditional Sox9 ablation reduces chondroitin sulfate proteoglycan levels and improves motor function following spinal cord injury. Glia *61*, 164–177.

McLaurin, J.A., and Yong, V.W. (1995). Oligodendrocytes and myelin. Neurol. Clin. *13*, 23–49.

McTigue, D.M., and Tripathi, R.B. (2008). The life, death, and replacement of oligodendrocytes in the adult CNS. J. Neurochem. *107*, 1–19.

McTigue, D.M., Popovich, P.G., Jakeman, L.B., and Stokes, B.T. (2000). Strategies for spinal cord injury repair. Prog. Brain Res. *128*, 3–8.

Metz, G.A., Curt, A., van de Meent, H., Klusman, I., Schwab, M.E., and Dietz, V. (2000). Validation of the weight-drop contusion model in rats: a comparative study of human spinal cord injury. J. Neurotrauma *17*, 1–17.

Meyer, G., and Amer, N.M. (1988). Novel optical approach to atomic force microscopy. Appl. Phys. Lett. *53*, 1045.

Mezger, T.G. (2006). The Rheology Handbook: For Users of Rotational and Oscillatory Rheometers (Vincentz Network GmbH & Co KG).

Mi, S., Chen, B., Wright, B., and Connon, C.J. (2010). Plastic compression of a collagen gel forms a much improved scaffold for ocular surface tissue engineering over conventional collagen gels. J. Biomed. Mater. Res. A *95*, 447–453.

Michael-Titus, A.T., and Priestley, J. V. (2014). Omega-3 fatty acids and traumatic neurological injury: from neuroprotection to neuroplasticity? Trends Neurosci. *37*, 30–38.

Micol, L.A., Ananta, M., Engelhardt, E.-M., Mudera, V.C., Brown, R.A., Hubbell, J.A., and Frey, P. (2011). High-density collagen gel tubes as a matrix for primary human bladder smooth muscle cells. Biomaterials *32*, 1543–1548.

Middleditch, A., and Oliver, J. (2005). Functional Anatomy of the Spine (Elsevier Health Sciences).

Miller, K., Chinzei, K., Orssengo, G., and Bednarz, P. (2000). Mechanical properties of brain tissue in-vivo: experiment and computer simulation. J. Biomech. *33*, 1369–1376.

Milligan, C. (1991). Brain macrophages and microglia respond differently to lesions of the developing and adult visual system. J. Comp. ….

Miron-Mendoza, M., Seemann, J., and Grinnell, F. (2010). The differential regulation of cell motile activity through matrix stiffness and porosity in three dimensional collagen matrices. Biomaterials *31*, 6425–6435.

Morrison, B., Saatman, K.E., Meaney, D.F., and McIntosh, T.K. (1998). In vitro central nervous system models of mechanically induced trauma: a review. J. Neurotrauma *15*, 911–928.

Moshayedi, P., Costa, L. da F., Christ, A., Lacour, S.P., Fawcett, J., Guck, J., and Franze, K. (2010). Mechanosensitivity of astrocytes on optimized polyacrylamide gels analyzed by quantitative morphometry. J. Phys. Condens. Matter *22*, 194114.

Moshayedi, P., Ng, G., Kwok, J.C.F., Yeo, G.S.H., Bryant, C.E., Fawcett, J.W., Franze, K., and Guck, J. (2014). The relationship between glial cell mechanosensitivity and foreign body reactions in the central nervous system. Biomaterials *35*, 3919–3925.

Nicolle, S., Lounis, M., Willinger, R., and Palierne, J.-F. (2005). Shear linear behavior of brain tissue over a large frequency range. Biorheology *42*, 209–223.

Nimmerjahn, A., Kirchhoff, F., and Helmchen, F. (2005). Resting microglial cells are highly dynamic surveillants of brain parenchyma in vivo. Science *308*, 1314–1318.

Nishi, R.A., Liu, H., Chu, Y., Hamamura, M., Su, M.-Y., Nalcioglu, O., and Anderson, A.J. (2007). Behavioral, histological, and ex vivo magnetic resonance imaging assessment of graded contusion spinal cord injury in mice. J. Neurotrauma *24*, 674–689.

Nógrádi, A., and Vrbová, G. (2013). Anatomy and Physiology of the Spinal Cord.

Norenberg, M.D., Smith, J., and Marcillo, A. (2004a). The pathology of human spinal cord injury: defining the problems. J. Neurotrauma *21*, 429–440.

Norenberg, M.D., Smith, J., and Marcillo, A. (2004b). The pathology of human spinal cord injury: defining the problems. J. Neurotrauma *21*, 429–440.

NSCISC (2011). NSCISC.

O'Connor, S.M., Stenger, D.A., Shaffer, K.M., and Ma, W. (2001). Survival and neurite outgrowth of rat cortical neurons in three-dimensional agarose and collagen gel matrices. Neurosci. Lett. *304*, 189–193.

O'Rourke, C. (2015). Development of Novel, Robust 3D CNS Tissue Models for Neurobiological Studies and Drug Discovery. Open University.

O'Rourke, C., Drake, R.A.L., Cameron, G.W.W., Loughlin, A.J., and Phillips, J.B. (2015). Optimising contraction and alignment of cellular collagen hydrogels to achieve reliable and consistent engineered anisotropic tissue. J. Biomater. Appl. *30*, 599–607.

Oakland, R.J., Hall, R.M., Wilcox, R.K., and Barton, D.C. (2006). The biomechanical response of spinal cord tissue to uniaxial loading. Proc. Inst. Mech. Eng. H. *220*, 489–492.

Oberheim, N.A., Takano, T., Han, X., He, W., Lin, J.H.C., Wang, F., Xu, Q., Wyatt, J.D., Pilcher, W., Ojemann, J.G., et al. (2009). Uniquely hominid features of adult human astrocytes. J. Neurosci. *29*, 3276–3287.

Oberheim, N.A., Goldman, S.A., and Nedergaard, M. (2012). Heterogeneity of astrocytic form and function. Methods Mol. Biol. *814*, 23–45.

Okada, M., Miyamoto, O., Shibuya, S., Zhang, X., Yamamoto, T., and Itano, T. (2007). Expression and role of type I collagen in a rat spinal cord contusion injury model. Neurosci. Res. *58*, 371–377.

Onifer, S.M., Rabchevsky, A.G., and Scheff, S.W. (2007). Rat models of traumatic spinal cord injury to assess motor recovery. ILAR J. *48*, 385–395.

Oxland, T.R., Bhatnagar, T., Choo, A.M., Dvorak, M.F., Tetzlaff, W., and Cripton, P.A. (2010). Biomechanical Aspects of Spinal Cord Injury. pp. 159–180.

Oxland, T.R., Bhatnagar, T., Choo, A.M., Dvorak, M.F., Tetzlaff, W., and Cripton, P.A. (2011). Neural Tissue Biomechanics (Berlin, Heidelberg: Springer Berlin Heidelberg).

Parenteau-Bareil, R., Gauvin, R., and Berthod, F. (2010). Collagen-Based Biomaterials for Tissue Engineering Applications. Materials (Basel). *3*, 1863–1887.

Park, J.H., Kim, J.H., Oh, S.-K., Baek, S.R., Min, J., Kim, Y.W., Kim, S.T., Woo, C.-W., and Jeon, S.R. (2016). Analysis of equivalent parameters of two spinal cord injury devices: the New York University impactor versus the Infinite Horizon impactor. Spine J.

Parsley, C.P., Cheng, K.W., Song, L., and Hochman, S. (1998). Thin slice CNS explants maintained on collagen-coated culture dishes. J. Neurosci. Methods *80*, 65–74.

Parsons, J.W., and Coger, R.N. (2002). A new device for measuring the viscoelastic properties of hydrated matrix gels. J. Biomech. Eng. *124*, 145–154.

Pearse, D.D., Lo, T.P., Cho, K.S., Lynch, M.P., Garg, M.S., Marcillo, A.E., Sanchez, A.R., Cruz, Y., and Dietrich, W.D. (2005). Histopathological and behavioral characterization of a novel cervical spinal cord displacement contusion injury in the rat. J. Neurotrauma *22*, 680–702.

Pekny, M. (2001). Astrocytic intermediate filaments: lessons from GFAP and vimentin knock-out mice. Prog. Brain Res. *132*, 23–30.

Pekny, M., and Nilsson, M. (2005). Astrocyte activation and reactive gliosis. Glia *50*, 427–434.

Pekny, M., and Pekna, M. (2004). Astrocyte intermediate filaments in CNS pathologies and regeneration. J. Pathol. *204*, 428–437.

Penning, L., and Wilmink, J.T. (1981). Biomechanics of lumbosacral dural sac. A study of flexion-extension myelography. Spine (Phila. Pa. 1976). *6*, 398–408.

Persson, C., McLure, S.W.D., Summers, J., and Hall, R.M. (2009). The effect of bone fragment size and cerebrospinal fluid on spinal cord deformation during trauma: an ex vivo study. J. Neurosurg. Spine *10*, 315–323.

Persson, C., Summers, J.L., and Hall, R.M. (2010). Modelling of Spinal Cord Biomechanics : In Vitro and Computational Approaches. In Neural Tissue Biomechanics, L.E. Bilston, ed. (Springer New York), pp. 181–201.

Persson, C., Summers, J., and Hall, R.M. (2011). The importance of fluid-structure interaction in spinal trauma models. J. Neurotrauma *28*, 113–125.

Peters, A., Palay, S.L., and Webster, H. deF. (1976). The Fine Structure of the Nervous System: neurons and their supporting cells (Oxford University Press, USA).

Pfister, B.J., Weihs, T.P., Betenbaugh, M., and Bao, G. (2003). An in vitro uniaxial stretch model for axonal injury. Ann. Biomed. Eng. *31*, 589–598.

Phansalkar, N., More, S., Sabale, A., and Joshi, M. (2011). Adaptive local thresholding for detection of nuclei in diversity stained cytology images. In 2011 International Conference on Communications and Signal Processing, (IEEE), pp. 218–220.

Phillips, J.B. (2014). Building stable anisotropic tissues using cellular collagen gels. Organogenesis *10*, 6–8.

Phillips, J.B., and Brown, R. (2011). Micro-structured materials and mechanical cues in 3D collagen gels. Methods Mol. Biol. *695*, 183–196.

Phillips, J.B., Bunting, S.C.J., Hall, S.M., and Brown, R.A. (2005). Neural tissue engineering: a self-organizing collagen guidance conduit. Tissue Eng. *11*, 1611–1617.

Pickett, G.E., Campos-Benitez, M., Keller, J.L., and Duggal, N. (2006). Epidemiology of traumatic spinal cord injury in Canada. Spine (Phila. Pa. 1976). *31*, 799–805.

Picout, D.R., and Ross-Murphy, S.B. (2003). Rheology of biopolymer solutions and gels. ScientificWorldJournal. *3*, 105–121.

Pleasant, J.M., Carlson, S.W., Mao, H., Scheff, S.W., Yang, K.H., and Saatman, K.E. (2011). Rate of neurodegeneration in the mouse controlled cortical impact model is influenced by impactor tip shape: implications for mechanistic and therapeutic studies. J. Neurotrauma *28*, 2245–2262.

Popovich, P.G., Wei, P., and Stokes, B.T. (1997). Cellular inflammatory response after spinal cord injury in Sprague-Dawley and Lewis rats. J. Comp. Neurol. *377*, 443–464.

Preibisch, S., Saalfeld, S., and Tomancak, P. (2009). Globally optimal stitching of tiled 3D microscopic image acquisitions. Bioinformatics *25*, 1463–1465.

Prendergast, V., and Sullivan, C. (2000). Acute spinal cord injury. Nursing considerations for the first 72 hours. Crit. Care Nurs. Clin. North Am. *12*, 499–508.

Probert, L., Eugster, H.P., Akassoglou, K., Bauer, J., Frei, K., Lassmann, H., and Fontana, A. (2000). TNFR1 signalling is critical for the development of demyelination and the limitation of T-cell responses during immune-mediated CNS disease. Brain *123 ( Pt 1*, 2005–2019.

Prüss, H., Kopp, M.A., Brommer, B., Gatzemeier, N., Laginha, I., Dirnagl, U., and Schwab, J.M. (2011). Non-resolving aspects of acute inflammation after spinal cord injury (SCI): indices and resolution plateau. Brain Pathol. *21*, 652–660.

Purves, D., Augustine, George. J Fitzpatrick, D., Hall, W.C., LaMantia, A.-S., McNamara, J.O., and White, L.E. (2008). Neuroscience (Sinauer Associates, Inc.).

Quasar, J. (2009). Neuron Wikipedia.

Quincozes-Santos, A., Bobermin, L.D., Latini, A., Wajner, M., Souza, D.O., Gonçalves, C.-A., and Gottfried, C. (2013). Resveratrol protects C6 astrocyte cell line against hydrogen peroxide-induced oxidative stress through heme oxygenase 1. PLoS One *8*, e64372.

Raineteau, O., and Schwab, M.E. (2001). Plasticity of motor systems after incomplete spinal cord injury. Nat. Rev. Neurosci. *2*, 263–273.

Ransom, B.R., and Ransom, C.B. (2012). Astrocytes: multitalented stars of the central nervous system. Methods Mol. Biol. *814*, 3–7.

Ransom, B., Behar, T., and Nedergaard, M. (2003). New roles for astrocytes (stars at last). Trends Neurosci. *26*, 520–522.

Raub, C.B., Putnam, A.J., Tromberg, B.J., and George, S.C. (2010). Predicting bulk mechanical properties of cellularized collagen gels using multiphoton microscopy. Acta Biomater. *6*, 4657–4665.

Ravikumar, M., Jain, S., Miller, R.H., Capadona, J.R., and Selkirk, S.M. (2012). An organotypic spinal cord slice culture model to quantify neurodegeneration. J. Neurosci. Methods *211*, 280–288.

Reier, P.J. (1979). Penetration of grafted astrocytic scars by regenerating optic nerve axons in Xenopus tadpoles. Brain Res. *164*, 61–68.

Rice, T., Larsen, J., Rivest, S., and Yong, V.W. (2007). Characterization of the early neuroinflammation after spinal cord injury in mice. J. Neuropathol. Exp. Neurol. *66*, 184–195.

Ridet, J.L., Malhotra, S.K., Privat, A., and Gage, F.H. (1997). Reactive astrocytes: cellular and molecular cues to biological function. Trends Neurosci. *20*, 570–577.

Rivlin, A.S., and Tator, C.H. (1978). Effect of duration of acute spinal cord compression in a new acute cord injury model in the rat. Surg. Neurol. *10*, 38–43.

Rodicio, M.C., and Barreiro-Iglesias, A. (2012). [Lampreys as an animal model in regeneration studies after spinal cord injury]. Rev. Neurol. *55*, 157–166.

Rohn, C.L. (1995). Analytical Polymer Rheology: Structure-Processing-Property Relationships. Hanser-Gardner Publ.

Rolls, A., Shechter, R., and Schwartz, M. (2009). The bright side of the glial scar in CNS repair. Nat. Rev. Neurosci. *10*, 235–241.

Ropper, A.E., Neal, M.T., and Theodore, N. (2015). Acute management of traumatic cervical spinal cord injury. Pract. Neurol. *15*, 266–272.

Rosato-Siri, M., Grandolfo, M., and Ballerini, L. (2002). Activity-dependent modulation of GABAergic synapses in developing rat spinal networks in vitro. Eur. J. Neurosci. *16*, 2123–2135.

Rossitti, S. (1993). Biomechanics of the pons-cord tract and its enveloping structures: An overview. Acta Neurochir. (Wien). *124*, 144–152.

Ruch, W.J. (1997). Atlas of Common Subluxations of the Human Spine and Pelvis (CRC Press).

Sandner, B., Prang, P., Rivera, F.J., Aigner, L., Blesch, A., and Weidner, N. (2012). Neural stem cells for spinal cord repair. Cell Tissue Res. *349*, 349–362.

Sayer, F.T., Kronvall, E., and Nilsson, O.G. (2006). Methylprednisolone treatment in acute spinal cord injury: the myth challenged through a structured analysis of published literature. Spine J. *6*, 335–343.

Schechner, J.S., Nath, A.K., Zheng, L., Kluger, M.S., Hughes, C.C., Sierra-Honigmann, M.R., Lorber, M.I., Tellides, G., Kashgarian, M., Bothwell, A.L., et al. (2000). In vivo formation of complex microvessels lined by human endothelial cells in an immunodeficient mouse. Proc. Natl. Acad. Sci. U. S. A. *97*, 9191–9196.

Scheff, S., and Roberts, K.N. (2008). Infinite Horizon Spinal Cord Contusion Model. In Animal Models of Acute Neurological Injuries,.

Scheff, S.W., Rabchevsky, A.G., Fugaccia, I., Main, J.A., and Lumpp, J.E. (2003). Experimental modeling of spinal cord injury: characterization of a force-defined injury device. J. Neurotrauma *20*, 179–193.

Schindelin, J., Arganda-Carreras, I., Frise, E., Kaynig, V., Longair, M., Pietzsch, T., Preibisch, S., Rueden, C., Saalfeld, S., Schmid, B., et al. (2012). Fiji: an open-source platform for biological-image analysis. Nat. Methods *9*, 676–682.

Schmidt, C.E., and Leach, J.B. (2003). Neural tissue engineering: strategies for repair and regeneration. Annu. Rev. Biomed. Eng. *5*, 293–347.

Schwab, M., and Bartholdi, D. (1996a). Degeneration and regeneration of axons in the lesioned spinal cord. Physiol. Rev. *76*, 319–370.

Schwab, M.E., and Bartholdi, D. (1996b). Degeneration and regeneration of axons in the lesioned spinal cord. Physiol. Rev. *76*, 319–370.

Sekhon, L.H., and Fehlings, M.G. (2001). Epidemiology, demographics, and pathophysiology of acute spinal cord injury. Spine (Phila. Pa. 1976). *26*, S2–S12.

Serpooshan, V., Muja, N., Marelli, B., and Nazhat, S.N. (2011). Fibroblast contractility and growth in plastic compressed collagen gel scaffolds with microstructures correlated with hydraulic permeability. J. Biomed. Mater. Res. A *96*, 609–620.

Shacklock, M., Butler, D., and Slater, H. (1994). The dynamic central nervous system: structure and clinical neurobiomechanics. In Grieve's Modern Manual Therapy Vertebral Column., pp. pp. 21–38.

Sharif-Alhoseini, M., and Rahimi-Movaghar, V. (2014). Animal Models in Traumatic Spinal Cord Injury. In Topics in Paraplegia, (InTech),.

Sharpe, W.N., Vaidyanathan, R., Yuan, B., Bao, G., and Edwards, R.L. (1997). Effect of etch holes on the mechanical properties of polysilicon. J. Vac. Sci. Technol. B Microelectron. Nanom. Struct. *15*, 1599.

Shearer, M.C., and Fawcett, J.W. (2001). The astrocyte/meningeal cell interface--a barrier to successful nerve regeneration? Cell Tissue Res. *305*, 267–273.

Sheerin, F. (2004). Spinal cord injury: anatomy and physiology of the spinal cord. Emerg. Nurse *12*, 30–36.

Sheerin, F. (2005a). Spinal cord injury: causation and pathophysiology. Emerg. Nurse *12*, 29–38.

Sheerin, F. (2005b). Spinal cord injury: acute care management. Emerg. Nurse *12*, 26–34.

Sheng, H., Wang, H., Homi, H.M., Spasojevic, I., Batinic-Haberle, I., Pearlstein, R.D., and Warner, D.S. (2004). A no-laminectomy spinal cord compression injury model in mice. J. Neurotrauma *21*, 595–603.

Shetye, S.S., Troyer, K.L., Streijger, F., Lee, J.H.T., Kwon, B.K., Cripton, P.A., and Puttlitz, C.M. (2014). Nonlinear viscoelastic characterization of the porcine spinal cord. Acta Biomater. *10*, 792–797.

Shi, R., and Pryor, J.D. (2002). Pathological changes of isolated spinal cord axons in response to mechanical stretch. Neuroscience *110*, 765–777.

Shi, R., and Whitebone, J. (2006). Conduction deficits and membrane disruption of spinal cord axons as a function of magnitude and rate of strain. J. Neurophysiol. *95*, 3384–3390.

Shi, Y., Iyer, R., Soundararajan, A., Dobkin, D., and Vesely, I. (2005). Collagen-based Tissue Engineering as Applied to Heart Valves. Conf. Proc. ... Annu. Int. Conf. IEEE Eng. Med. Biol. Soc. IEEE Eng. Med. Biol. Soc. Annu. Conf. *5*, 4912–4915.

Short, D.J., El Masry, W.S., and Jones, P.W. (2000). High dose methylprednisolone in the management of acute spinal cord injury - a systematic review from a clinical perspective. Spinal Cord *38*, 273–286.

Silver, J., and Miller, J.H. (2004). Regeneration beyond the glial scar. Nat. Rev. Neurosci. *5*, 146–156.

Siriphorn, A., Dunham, K. a, Chompoopong, S., and Floyd, C.L. (2012). Postinjury administration of 17β-estradiol induces protection in the gray and white matter with associated functional recovery after cervical spinal cord injury in male rats. J. Comp. Neurol. *520*, 2630–2646.

Snell, R.S. (2009). Clinical Neuroanatomy (Lippincott Williams & Wilkins).

Sobel, R.A. (1998). The extracellular matrix in multiple sclerosis lesions. J. Neuropathol. Exp. Neurol. *57*, 205–217.

Sofroniew, M. V (2009a). Molecular dissection of reactive astrogliosis and glial scar formation. Trends Neurosci. *32*, 638–647.

Sofroniew, M. V (2009b). Molecular dissection of reactive astrogliosis and glial scar formation. Trends Neurosci. *32*, 638–647.

Sofroniew, M. V, and Vinters, H. V (2010). Astrocytes: biology and pathology. Acta Neuropathol. *119*, 7–35.

Somerson, S.K., and Stokes, B.T. (1987). Functional analysis of an electromechanical spinal cord injury device. Exp. Neurol. *96*, 82–96.

Soubeyrand, M., Laemmel, E., Court, C., Dubory, A., Vicaut, E., and Duranteau, J. (2013). Rat model of spinal cord injury preserving dura mater integrity and allowing measurements of cerebrospinal fluid pressure and spinal cord blood flow. Eur. Spine J. *22*, 1810–1819.

Spinal Research (2011). Facts and figures | Spinal Research.

Squire, L.R., Berg, D., Bloom, F.E., du Lac, S., Ghosh, A., and Spitzer, N.C. (2013). Fundamental Neuroscience.

Steuer, I., and Guertin, P.A. (2009). Spinal cord injury research in mice: 2008 review. ScientificWorldJournal. *9*, 490–498.

Stichel, C.C., Niermann, H., D'Urso, D., Lausberg, F., Hermanns, S., and Müller, H.W. (1999). Basal membrane-depleted scar in lesioned CNS: characteristics and relationships with regenerating axons. Neuroscience *93*, 321–333.

Stokes, B.T. (1992). Experimental spinal cord injury: a dynamic and verifiable injury device. J. Neurotrauma *9*, 129–131; discussion 131–134.

Stokes, B.T., and Jakeman, L.B. (2002). Experimental modelling of human spinal cord injury: a model that crosses the species barrier and mimics the spectrum of human cytopathology. Spinal Cord *40*, 101–109.

Streit, W.J., Walter, S.A., and Pennell, N.A. (1999). Reactive microgliosis. Prog. Neurobiol. *57*, 563–581.

Stuart, K., and Panitch, A. (2008). Influence of chondroitin sulfate on collagen gel structure and mechanical properties at physiologically relevant levels. Biopolymers *89*, 841–851.

Sundararaghavan, H.G., Monteiro, G.A., Firestein, B.L., and Shreiber, D.I. (2009). Neurite growth in 3D collagen gels with gradients of mechanical properties. Biotechnol. Bioeng. *102*, 632–643.

Sundström, E., and Mo, L.-L. (2002). Mechanisms of glutamate release in the rat spinal cord slices during metabolic inhibition. J. Neurotrauma *19*, 257–266.

Suresh Babu, R., Sunandhini, R.L., Sridevi, D., Periasamy, P., and Namasivayam, A. (2012). Locomotor behavior of bonnet monkeys after spinal contusion injury: footprint study. Synapse *66*, 509–521.

Suzuki, M., and Raisman, G. (1992). The glial framework of central white matter tracts: segmented rows of contiguous interfascicular oligodendrocytes and solitary astrocytes give rise to a continuous meshwork of transverse and longitudinal processes in the adult rat fimbria. Glia *6*, 222–235.

Taheri, H., and Samyn, P. (2016). Effect of homogenization (microfluidization) process parameters in mechanical production of micro- and nanofibrillated cellulose on its rheological and morphological properties. Cellulose *23*, 1221–1238.

Talac, R., Friedman, J.A., Moore, M.J., Lu, L., Jabbari, E., Windebank, A.J., Currier, B.L., and Yaszemski, M.J. (2004). Animal models of spinal cord injury for evaluation of tissue engineering treatment strategies. Biomaterials *25*, 1505–1510.

Taoka, Y., and Okajima, K. (1998). Spinal cord injury in the rat. Prog. Neurobiol. *56*, 341–358.

Tarlov, I.M. (1954). Spinal cord compression studies. III. Time limits for recovery after gradual compression in dogs. AMA. Arch. Neurol. Psychiatry *71*, 588–597.

Tarlov, I.M. (1972). Acute spinal cord compression paralysis. J. Neurosurg. *36*, 10–20.

Tator, C.H. (2006). Review of treatment trials in human spinal cord injury: issues, difficulties, and recommendations. Neurosurgery *59*, 957–982; discussion 982–987.

Tator, C.H., and Fehlings, M.G. (1991). Review of the secondary injury theory of acute spinal cord trauma with emphasis on vascular mechanisms. J. Neurosurg. *75*, 15–26.

Teng, Y.D., Lavik, E.B., Qu, X., Park, K.I., Ourednik, J., Zurakowski, D., Langer, R., and Snyder, E.Y. (2001). Functional recovery following traumatic spinal cord injury mediated by a unique polymer scaffold seeded with neural stem cells.

Teo, L., Rosenfeld, J. V., and Bourne, J.A. (2012). Models of CNS injury in the nonhuman primate: A new era for treatment strategies. Transl. Neurosci. *3*, 181–195.

Tetzlaff, W., Okon, E.B., Karimi-Abdolrezaee, S., Hill, C.E., Sparling, J.S., Plemel, J.R., Plunet, W.T., Tsai, E.C., Baptiste, D., Smithson, L.J., et al. (2011). A systematic review of cellular transplantation therapies for spinal cord injury. J. Neurotrauma *28*, 1611–1682.

Thiele, J., Ma, Y., Bruekers, S.M.C., Ma, S., and Huck, W.T.S. (2014). 25th Anniversary Article: Designer Hydrogels for Cell Cultures: A Materials Selection Guide. Adv. Mater. *26*, 125–148.

Thuret, S., Moon, L.D.F., and Gage, F.H. (2006). Therapeutic interventions after spinal cord injury. Nat. Rev. Neurosci. *7*, 628–643.

Tønnesen, J., Parish, C.L., Sørensen, A.T., Andersson, A., Lundberg, C., Deisseroth, K., Arenas, E., Lindvall, O., and Kokaia, M. (2011). Functional integration of grafted neural stem cell-derived dopaminergic neurons monitored by optogenetics in an in vitro Parkinson model. PLoS One *6*, e17560.

Toth, J.M., Wang, M., Estes, B.T., Scifert, J.L., Seim, H.B., and Turner, A.S. (2006). Polyetheretherketone as a biomaterial for spinal applications. Biomaterials *27*, 324–334.

Tremoleda, J.L., Thau-Zuchman, O., Davies, M., Foster, J., Khan, I., Vadivelu, K.C., Yip, P.K., Sosabowski, J., Trigg, W., and Michael-Titus, A.T. (2016). In vivo PET imaging of the neuroinflammatory response in rat spinal cord injury using the TSPO tracer [18F]GE-180 and effect of docosahexaenoic acid. Eur. J. Nucl. Med. Mol. Imaging *43*, 1710–1722.

Troup, J.D. (1986). Biomechanics of the lumbar spinal canal. Clin. Biomech. (Bristol, Avon) *1*, 31–43.

Tscherter, A., Heuschkel, M.O., Renaud, P., and Streit, J. (2001). Spatiotemporal characterization of rhythmic activity in rat spinal cord slice cultures. Eur. J. Neurosci. *14*, 179–190.

Tukmachev, D., Forostyak, S., Koci, Z., Zaviskova, K., Vackova, I., Vyborny, K., Sandvig, I., Sandvig, A., Medberry, C.J., Badylak, S.F., et al. (2016). Injectable Extracellular Matrix Hydrogels as Scaffolds for Spinal Cord Injury Repair. Tissue Eng. Part A *22*, 306–317.

Tunturi, A.R. (1978). Elasticity of the spinal cord, pia, and denticulate ligament in the dog. J. Neurosurg. *48*, 975–979.

Vahidi, B., Park, J.W., Kim, H.J., and Jeon, N.L. (2008). Microfluidic-based strip assay for testing the effects of various surface-bound inhibitors in spinal cord injury. J. Neurosci. Methods *170*, 188–196.

Velegol, D., and Lanni, F. (2001). Cell traction forces on soft biomaterials. I. Microrheology of type I collagen gels. Biophys. J. *81*, 1786–1792.

Vialle, L.R.G., Grochocki, L.R., and Nohama, P. (2007). NYU device: automation of the Weight-drop rod. In World Congress on Medical Physics and Biomedical Engineering 2006, (Berlin, Heidelberg: Springer Berlin Heidelberg), pp. 728–730.

Visavadiya, N.P., Patel, S.P., VanRooyen, J.L., Sullivan, P.G., and Rabchevsky, A.G. (2016). Cellular and subcellular oxidative stress parameters following severe spinal cord injury. Redox Biol. *8*, 59–67.

Volpato, F.Z., Führmann, T., Migliaresi, C., Hutmacher, D.W., and Dalton, P.D. (2013). Using extracellular matrix for regenerative medicine in the spinal cord. Biomaterials *34*, 4945–4955.

Van Wagoner, N.J., and Benveniste, E.N. (1999). Interleukin-6 expression and regulation in astrocytes. J. Neuroimmunol. *100*, 124–139.

Waibl, H. (1973). Contributions to the Topography of the Spinal Cord of the Albino Rat (Rattus norvegicus) (Berlin, Heidelberg: Springer Berlin Heidelberg).

Wakatsuki, T., and Elson, E.L. (2003). Reciprocal interactions between cells and extracellular matrix during remodeling of tissue constructs. Biophys. Chem. *100*, 593–605.

Wakatsuki, T., Kolodney, M.S., Zahalak, G.I., and Elson, E.L. (2000). Cell mechanics studied by a reconstituted model tissue. Biophys. J. *79*, 2353–2368.

Wanner, I.B., Deik, A., Torres, M., Rosendahl, A., Neary, J.T., Lemmon, V.P., and Bixby, J.L. (2008). A new in vitro model of the glial scar inhibits axon growth. Glia *56*, 1691–1709.

Wanner, I.B., Anderson, M.A., Song, B., Levine, J., Fernandez, A., Gray-Thompson, Z., Ao, Y., and Sofroniew, M. V (2013). Glial scar borders are formed by newly proliferated, elongated astrocytes that interact to corral inflammatory and fibrotic cells via STAT3-dependent mechanisms after spinal cord injury. J. Neurosci. *33*, 12870–12886.

Weidner, N., Ner, A., Salimi, N., and Tuszynski, M.H. (2001). Spontaneous corticospinal axonal plasticity and functional recovery after adult central nervous system injury. Proc. Natl. Acad. Sci. U. S. A. *98*, 3513–3518.

Weightman, A., Jenkins, S., Pickard, M., Chari, D.M., and Yang, Y. (2014a). Alignment of multiple glial cell populations in 3D nanofiber scaffolds: Toward the development of multicellular implantable scaffolds for repair of neural injury. Nanomedicine Nanotechnology, Biol. Med. *10*, 291–295.

Weightman, A.P., Pickard, M.R., Yang, Y., and Chari, D.M. (2014b). An in vitro spinal cord injury model to screen neuroregenerative materials. Biomaterials *35*, 3756–3765.

White, A.A., and Panjabi, M.M. (1990). Clinical Biomechanics of the Spne (Philadelphia: JB Lippincott).

Wilcox, R.K., Boerger, T.O., Hall, R.M., Barton, D.C., Limb, D., and Dickson, R.A. (2002). Measurement of canal occlusion during the thoracolumbar burst fracture process. J. Biomech. *35*, 381–384.

Wilhelmsson, U., Li, L., Pekna, M., Berthold, C.-H., Blom, S., Eliasson, C., Renner, O., Bushong, E., Ellisman, M., Morgan, T.E., et al. (2004). Absence of glial fibrillary acidic protein and vimentin prevents hypertrophy of astrocytic processes and improves post-traumatic regeneration. J. Neurosci. *24*, 5016–5021.

Wilke, H.J., Neef, P., Caimi, M., Hoogland, T., and Claes, L.E. (1999). New in vivo measurements of pressures in the intervertebral disc in daily life. Spine (Phila. Pa. 1976). *24*, 755–762.

Willits, R.K., and Skornia, S.L. (2004). Effect of collagen gel stiffness on neurite extension. J. Biomater. Sci. Polym. Ed. *15*, 1521–1531.

Windle, W.F., and Chambers, W.W. (1950). Regeneration in the spinal cord of the cat and dog. J. Comp. Neurol. *93*, 241–257.

Wrathall, J.R., Pettegrew, R.K., and Harvey, F. (1985). Spinal cord contusion in the rat: production of graded, reproducible, injury groups. Exp. Neurol. *88*, 108–122.

Wu, V.W., and Schwartz, J.P. (1998). Cell culture models for reactive gliosis: new perspectives. J. Neurosci. Res. *51*, 675–681.

Yeung, T., Georges, P.C., Flanagan, L.A., Marg, B., Ortiz, M., Funaki, M., Zahir, N., Ming, W., Weaver, V., and Janmey, P.A. (2005). Effects of substrate stiffness on cell morphology, cytoskeletal structure, and adhesion. Cell Motil. Cytoskeleton *60*, 24–34.

Yiu, G., and He, Z. (2006a). Glial inhibition of CNS axon regeneration. Nat. Rev. Neurosci. *7*, 617–627.

Yiu, G., and He, Z. (2006b). Glial inhibition of CNS axon regeneration. Nat. Rev. Neurosci. *7*, 617–627.

Yu, A.C., Lee, Y.L., and Eng, L.F. (1993). Astrogliosis in culture: I. The model and the effect of antisense oligonucleotides on glial fibrillary acidic protein synthesis. J. Neurosci. Res. *34*, 295–303.

Yu, S., Kaneko, Y., Bae, E., Stahl, C.E., Wang, Y., van Loveren, H., Sanberg, P.R., and Borlongan, C. V. (2009). Severity of controlled cortical impact traumatic brain injury in rats and mice dictates degree of behavioral deficits. Brain Res. *1287*, 157–163.

Zhang, Y.P., Burke, D.A., Shields, L.B.E., Chekmenev, S.Y., Dincman, T., Zhang, Y., Zheng, Y., Smith, R.R., Benton, R.L., DeVries, W.H., et al. (2008). Spinal cord contusion based on precise vertebral stabilization and tissue displacement measured by combined assessment to discriminate small functional differences. J. Neurotrauma *25*, 1227–1240.

Zhang, Z., Zhang, Y.P., Shields, L.B.E., and Shields, C.B. (2014). Technical comments on rodent spinal cord injuries models. Neural Regen. Res. *9*, 453.

Zhou, X., He, X., and Ren, Y. (2014). Function of microglia and macrophages in secondary damage after spinal cord injury. Neural Regen. Res. *9*, 1787–1795.

Zurita, M., Aguayo, C., Bonilla, C., Otero, L., Rico, M., Rodríguez, A., and Vaquero, J. (2012). The pig model of chronic paraplegia: a challenge for experimental studies in spinal cord injury. Prog. Neurobiol. *97*, 288–303.

# Appendix I

## Materials

The equipment used and equipment suppliers are listed within Table I.I.

**Table I.I: Equipment and Suppliers**

| Equipment | Supplier |
|---|---|
| **-20°C Freezer** | Jencons Plc, East Grinstead UK |
| **4°C Refrigerator** | Jencons Plc, East Grinstead UK |
| **-80°C Freezer** | Sanyo Biomedical Europe, BV |
| **Autoclave** | Priorclave, London UK |
| **Automatic Pipette (Pipetteboy®)** | Scientific Laboratory Supplies Ltd, Nottingham UK |
| **Balance AT21 Comparator** | A&D Instruments Ltd, Oxford UK |
| **Balance GR200 (Accuracy 0;01g)** | A&D Instruments Ltd, Oxford UK |
| **Balance GX-2000 EC** | Sartorius, Goettingen, Germany |
| **Centrifuge (Tissue Culture) Harrier 15/80** | Sanyo, Japan. |
| **Class I Laminar Flow Cabinet** | Howorth Airtech Ltd, UK |
| **Class II Laminar Flow Cabinet** | Heraeus, Hanau Germany |
| **Confocal Microscope laser scanning inverted LSM700** | Carl Zeiss Ltd, UK. |
| **Cryopreservation Freezer** | - |
| **Eppendorf Centrifuge 5415R** | Hyland Scientific, Stanwood, Washington USA. |
| **Fiji Is Just Image J (FIJI) Image analysis software version: Madison** | |
| **Fume Cupboard** | Whiteley fume extraction solutions Ltd, Bradford UK |

| | |
|---|---|
| **Gilson Pipettes P2, P20, P200 and P1000** | Fisher Brand, Fisher Scientific Loughborough UK |
| **Glass Universals** | Scientific Laboratory Supplies Ltd, Nottingham UK |
| **Hatteras PCI3000 Precision Cortical Impactor** | Hatteras Instruments Inc., North Carolina, USA |
| **Ice blocks** | Medicool MC28 Laminar Medica UK |
| **ImageJ image analysis software version 1.51g** | |
| **Incubator** | Sanyo Biomedical Europe, BV Amsterdam, Holland |
| **Infinite Horizons Spinal Cord Impactor** | Precision Systems and Instrumentation, Kentucky, USA |
| **Light Microscope** | Olympus Optical Co. Ltd, London UK |
| **Liquid Nitrogen Dewar BIO65** | Jencons Plc, East Grinstead UK |
| **Magnetic Stirrer** | Scientific Laboratory Supplies Ltd, Nottingham UK |
| **Magnetic Stirrer Bar** | Scientific Laboratory Supplies Ltd, Nottingham UK |
| **Microwave** | ProLine, France |
| **Oven** | Genlab Ltd, Cheshire UK |
| **pH meter (Jenway 3510)** | VWR International Poole UK |
| **Plate Shaker** | Bibby Sterilin Stone, Staffordshire UK. |
| **PSI IH Spinal Cord Impactor Software version 5.0** | Precision Systems and Instrumentation, Kentucky, USA |
| **Rheometer (Kinexus pro+)** | Malvern Instruments Ltd., Malvern, UK |
| **rSpace for Kinexus Rheology software** | Malvern Instruments Ltd., Malvern, UK |
| **Real Architecture For 3D Tissue (RAFT) absorbers** | Lonza Biological, Cambridge UK |
| **Scalpel Handle** | Swann-Morton, Sheffield, UK |
| **Scissors, curved blade (HWB003-11)** | Karl Hammacher |
| **Spatula (231-1059)** | VWR, Lutterworth, UK |
| **Test tube holder** | Fisher Scientific, Leicestershire, UK |
| **Tethering bars (10 count, cross stitch plastic mesh)** | Darice, Amazon, UK |

| | |
|---|---|
| **Tweezers, extra-fine point (T147)** | TAAB, Berkshire, UK |
| **Water Bath** | Fisher Scientific, Leicestershire UK. |
| **Water Purifier** | Triple Red Laboratory Technology UK. |

General chemicals and reagents used in this study are shown in Table I.II.

**Table I.II General Chemicals and Reagents**

| Chemicals/reagents | Storage conditions | Supplier |
|---|---|---|
| **Bovine Serum Albumin (BSA)** | 4°C | Sigma-Aldrich Ltd., Dorset UK |
| **Calcein-AM** | -20°C | ThermoFisher Scientific, Northumberland UK |
| **Collagen (type-I rat tail >2mg/ml in 0.6% (v/v) Acetic acid)** | 4°C | First Link Ltd, Wolverhampton UK |
| **DNase type II from bovine pancreas** | -20°C | Sigma-Aldrich Ltd., Dorset UK |
| **DPBS** | Room Temperature | Bio-Whittaker, Lonza, Verviers, Belgium |
| **Dulbecco's modified Eagle's medium (DMEM)** | 4°C | Lonza Biological, Cambridge UK |
| **Earle's balanced salt solution (EBSS)** | Room Temperature | Sigma-Aldrich Ltd., Dorset UK |
| **Ethidium Homodimer** | -20°C | ThermoFisher Scientific, Northumberland UK |
| **Ethylenediaminetetraacetic acid (EDTA)** | Room Temperature | Sigma-Aldrich Ltd., Dorset UK |
| **Ethanol** | Room temperature, Flammables cupboard | VWR international, Poole UK |
| **ELISA kit (rIL-6)** | 4°C | 2B Scientific, Oxfordshire UK. |
| **Fairy liquid** | Room Temperature | Local Store |
| **Foetal Bovine Serum (FBS)** | -20°C | Bio-Whittaker, Lonza, Verviers, Belgium |
| **Goat Serum Blocking Solution (5%)** | 4°C | Sigma-Aldrich Ltd., Dorset UK |
| **Glucose Powder** | Room Temperature | Sigma-Aldrich Ltd., Dorset UK |
| **Ham's F-12** | 4°C | ThermoFisher Scientific, Northumberland UK |

| | | |
|---|---|---|
| **Horse Serum** | -20°C | Sigma-Aldrich Ltd., Dorset UK |
| **Hydrochloric Acid (HCl)** | Room Temperture | Fisher Scientific, Loughborough UK |
| **Hydrogen peroxide** | 4°C | Sigma-Aldrich Ltd., Dorset UK |
| **L-glutamine** | -20°C | Sigma-Aldrich Ltd., Dorset UK |
| **Magnesium Sulphate ($MgSO_4$)** | Room Temperature | Sigma-Aldrich Ltd., Dorset UK |
| **10X Minimum Essential Media** | 4°C | Sigma-Aldrich Ltd., Dorset UK |
| **Neutralising solution (predominantly sodium hydroxide)** | 4°C | Tap Biosystems now part of Sartorium Stedim Biotech, Hertfordshire UK |
| **Paraformaldehyde (PFA) powder** | Room Temperature | Sigma-Aldrich Ltd., Dorset UK |
| **Penicillin/Streptomycin** | -20°C | Bio-Whittaker, Lonza, Verviers, Belgium |
| **PBS tablets** | Room Temperature | Oxoid Thermo Scientific,Northumberland UK |
| **pH Standards** | -20°C | Scientific Laboratory Supplies Ltd, Nottingham UK |
| **Poly-D-lysine powder** | Room Temperature | Sigma-Aldrich Ltd., Dorset UK |
| **Sterile Water** | Room Temperature | Baxter Healthcare, UK |
| **Sodium Hydroxide (NaOH)** | Room Temperature | Fisher Scientific, Loughborough UK |
| **Soy-bean Trypsin Inhibitor (SBTI)** | 4°C | Sigma-Aldrich Ltd., Dorset UK |
| **Transforming growth factor-beta1 (TGF-β1)** | -20°C | Sigma-Aldrich Ltd., Dorset UK |
| **Trigene** | Room Temperature | Scientific Laboratory Supplies Ltd, Nottingham UK |
| **Tris** | Room temperature | Sigma-Aldrich Ltd., Dorset UK |
| **Trypan Blue** | Room Temperature | Sigma-Aldrich Ltd., Dorset UK |
| **Trypsin from bovine pancreas** | -20°C | Sigma-Aldrich Ltd., Dorset UK |
| **Trypsin (passaging cells)** | -20°C | Sigma-Aldrich Ltd., Dorset UK |

| | | |
|---|---|---|
| **Triton X-100** | Room Temperature | BDH laboratory supplies, Poole UK |
| **Virkon** | Room Temperature | Scientific Laboratory Supplies Ltd, Nottingham UK |

The general consumables and plastic ware used in this study are shown in Table I.III

**Table I.III Consumables and Plastic ware**

| Item | Size | Supplier |
|---|---|---|
| **Bijou** | 5ml | Scientific Laboratory Supplies Ltd, Nottingham UK |
| **Blue Roll** | - | - |
| **Cell scraper** | 18mm blade length 260mm handle | Fisher Scientific, Leicestershire UK. |
| **Closed Flask Caps** | For 75cm$^3$ tissue culture flasks | Scientific Laboratory Supplies Ltd, Nottingham UK |
| **Cryovial** | 1.5ml | Nange Nunc International Corporation. New York USA |
| **Disposable Plastic syringe** | 1ml,2ml,5ml,10ml, 20ml 50ml | Scientific Laboratory Supplies Ltd, Nottingham UK |
| **Falcon Tubes** | 15ml, 50ml | Fisher Scientific, Leicestershire UK. |
| **Glass Beaker** | 100ml 250ml 600ml | - |
| **Glass Duran Bottle** | 1L 5L | Fisher Scientific, Leicestershire UK. |
| **Glass cover slips** | 22mmx47mm | Scientific Laboratory Supplies Ltd, Nottingham UK |
| **Haemocytometer neubauer** | 22mmx47mm | VWR International Poole UK |
| **Microplate Adhesive Sealing Film** | 96 well plate | PerkinElmer, Windsor UK |
| **Optiplate™** | 96 well plate | PerkinElmer, Windsor UK |
| **Parafilm** | To seal edges of 96 well plate and Tethering moulds | Bemis, Oshkosh, Wisconsin USA |
| **Pipette tips** | 20µl, 200µl, 1000µl | Starlab, Ahrensburg Germany |
| **Scalpel Blade flat edge** | | Swann-Morton UK |
| **Spatula** | - | - |
| **Sterile Pot** | 60ml, 150ml, 250ml | Scientific Laboratory Supplies Ltd, Nottingham |

| | | |
|---|---|---|
| **Syringe Filter (single use)** | 0.22μm pore size | Millex Merck Millipore, Germanys |
| **Tissue Culture Dishes** | 60mmx10mm | Corning BV |
| **Tissue Culture Flasks** | $25cm^2$, $75cm^2$, $125cm^2$, | ThermoFisher Scientific, Northumberland UK |
| **Universal** | 30ml | Scientific Laboratory Supplies Ltd, Nottingham |
| **Weighing Boat** | - | - |
| **Well Plates nunclon delta surface** | 96well (flat), 24 well, 12 well, 6 well | ThermoScientific, Northumberland UK |
| **Wide Bore optifit pipette tips pre-sterilised** | 1000μl | Biohit UK. |

# Appendix II

## Statistics

The results of the Tukey's multiple comparisons one-way ANOVA comparing the elastic moduli of FH and FS, Cellular and acellular gels are presented in Table II.I.

**Table II.I: Results of Tukey's Multiple Comparisons One-way ANOVA Comparing the Elastic Moduli of FH and FS, Cellular and Acellular gels**

| Frequency | Tukey's Multiple Comparisons Test: | Significant | P-value |
|---|---|---|---|
| **1 Hz** | FH Acellular Day 1 vs. FH Acellular Day 5 | No | > 0.9999 |
| **1 Hz** | FH Acellular Day 1 vs. FH Cellular Day 1 | No | 0.9997 |
| **1 Hz** | FH Acellular Day 1 vs. FH Cellular Day 5 | No | > 0.9999 |
| **1 Hz** | FH Acellular Day 5 vs. FH Cellular Day 1 | No | > 0.9999 |
| **1 Hz** | FH Acellular Day 5 vs. FH Cellular Day 5 | No | > 0.9999 |
| **1 Hz** | FH Cellular Day 1 vs. FH Cellular Day 5 | No | 0.9995 |
| **1 Hz** | FH Acellular Day 1 vs. FS Acellular Day 1 | Yes | < 0.0001 |
| **1 Hz** | FH Acellular Day 1 vs. FS Acellular Day 5 | Yes | 0.0003 |
| **1 Hz** | FH Acellular Day 1 vs. FS Cellular Day 1 | Yes | < 0.0001 |
| **1 Hz** | FH Acellular Day 1 vs. FS Cellular Day 5 | Yes | < 0.0001 |
| **1 Hz** | FH Acellular Day 5 vs. FS Acellular Day 1 | Yes | < 0.0001 |
| **1 Hz** | FH Acellular Day 5 vs. FS Acellular Day 5 | Yes | 0.0004 |
| **1 Hz** | FH Acellular Day 5 vs. FS Cellular Day 1 | Yes | < 0.0001 |
| **1 Hz** | FH Acellular Day 5 vs. FS Cellular Day 5 | Yes | < 0.0001 |
| **1 Hz** | Cellular Day 1 vs. FS Acellular Day 1 | Yes | < 0.0001 |
| **1 Hz** | Cellular Day 1 vs. FS Acellular Day 5 | Yes | 0.001 |
| **1 Hz** | Cellular Day 1 vs. FS Cellular Day 1 | Yes | < 0.0001 |
| **1 Hz** | Cellular Day 1 vs. FS Cellular Day 5 | Yes | < 0.0001 |
| **1 Hz** | Cellular Day 5 vs. FS Acellular Day 1 | Yes | < 0.0001 |
| **1 Hz** | Cellular Day 5 vs. FS Acellular Day 5 | Yes | 0.0003 |

| | | | |
|---|---|---|---|
| **1 Hz** | Cellular Day 5 vs. FS Cellular Day 1 | Yes | < 0.0001 |
| **1 Hz** | Cellular Day 5 vs. FS Cellular Day 5 | Yes | < 0.0001 |
| **1 Hz** | FS Acellular Day 1 vs. FS Acellular Day 5 | Yes | < 0.0001 |
| **1 Hz** | FS Acellular Day 1 vs. FS Cellular Day 1 | Yes | < 0.0001 |
| **1 Hz** | FS Acellular Day 1 vs. FS Cellular Day 5 | Yes | < 0.0001 |
| **1 Hz** | FS Acellular Day 5 vs. FS Cellular Day 1 | Yes | < 0.0001 |
| **1 Hz** | FS Acellular Day 5 vs. FS Cellular Day 5 | Yes | < 0.0001 |
| **1 Hz** | FS Cellular Day 1 vs. FS Cellular Day 5 | Yes | < 0.0001 |
| **5 Hz** | Acellular Day 1 vs. Acellular Day 5 | No | > 0.9999 |
| **5 Hz** | Acellular Day 1 vs. Cellular Day 1 | No | > 0.9999 |
| **5 Hz** | Acellular Day 1 vs. Cellular Day 5 | No | > 0.9999 |
| **5 Hz** | Acellular Day 5 vs. Cellular Day 1 | No | > 0.9999 |
| **5 Hz** | Acellular Day 5 vs. Cellular Day 5 | No | > 0.9999 |
| **5 Hz** | Cellular Day 1 vs. Cellular Day 5 | No | 0.9989 |
| **5 Hz** | Acellular Day 1 vs. FS Acellular Day 1 | Yes | < 0.0001 |
| **5 Hz** | Acellular Day 1 vs. FS Acellular Day 5 | Yes | < 0.0001 |
| **5 Hz** | Acellular Day 1 vs. FS Cellular Day 1 | Yes | < 0.0001 |
| **5 Hz** | Acellular Day 1 vs. FS Cellular Day 5 | Yes | < 0.0001 |
| **5 Hz** | Acellular Day 5 vs. FS Acellular Day 1 | Yes | < 0.0001 |
| **5 Hz** | Acellular Day 5 vs. FS Acellular Day 5 | Yes | < 0.0001 |
| **5 Hz** | Acellular Day 5 vs. FS Cellular Day 1 | Yes | < 0.0001 |
| **5 Hz** | Acellular Day 5 vs. FS Cellular Day 5 | Yes | < 0.0001 |
| **5 Hz** | Cellular Day 1 vs. FS Acellular Day 1 | Yes | < 0.0001 |
| **5 Hz** | Cellular Day 1 vs. FS Acellular Day 5 | Yes | < 0.0001 |
| **5 Hz** | Cellular Day 1 vs. FS Cellular Day 1 | Yes | < 0.0001 |
| **5 Hz** | Cellular Day 1 vs. FS Cellular Day 5 | Yes | < 0.0001 |
| **5 Hz** | Cellular Day 5 vs. FS Acellular Day 1 | Yes | < 0.0001 |
| **5 Hz** | Cellular Day 5 vs. FS Acellular Day 5 | Yes | < 0.0001 |
| **5 Hz** | Cellular Day 5 vs. FS Cellular Day 1 | Yes | < 0.0001 |
| **5 Hz** | Cellular Day 5 vs. FS Cellular Day 5 | Yes | < 0.0001 |
| **5 Hz** | FS Acellular Day 1 vs. FS Acellular Day 5 | Yes | < 0.0001 |
| **5 Hz** | FS Acellular Day 1 vs. FS Cellular Day 1 | Yes | < 0.0001 |
| **5 Hz** | FS Acellular Day 1 vs. FS Cellular Day 5 | Yes | < 0.0001 |
| **5 Hz** | FS Acellular Day 5 vs. FS Cellular Day 1 | Yes | < 0.0001 |

| | | | |
|---|---|---|---|
| **5 Hz** | FS Acellular Day 5 vs. FS Cellular Day 5 | Yes | < 0.0001 |
| **5 Hz** | FS Cellular Day 1 vs. FS Cellular Day 5 | Yes | < 0.0001 |
| **10 Hz** | FS Acellular Day 1 vs. FS Acellular Day 5 | Yes | < 0.0001 |
| **10 Hz** | FS Acellular Day 1 vs. FS Cellular Day 1 | Yes | < 0.0001 |
| **10 Hz** | FS Acellular Day 1 vs. FS Cellular Day 5 | Yes | < 0.0001 |
| **10 Hz** | FS Acellular Day 5 vs. FS Cellular Day 1 | Yes | < 0.0001 |
| **10 Hz** | FS Acellular Day 5 vs. FS Cellular Day 5 | Yes | < 0.0001 |
| **10 Hz** | FS Cellular Day 1 vs. FS Cellular Day 5 | Yes | 0.0002 |
| **20 Hz** | FS Acellular Day 1 vs. FS Acellular Day 5 | Yes | < 0.0001 |
| **20 Hz** | FS Acellular Day 1 vs. FS Cellular Day 1 | Yes | < 0.0001 |
| **20 Hz** | FS Acellular Day 1 vs. FS Cellular Day 5 | Yes | < 0.0001 |
| **20 Hz** | FS Acellular Day 5 vs. FS Cellular Day 1 | Yes | < 0.0001 |
| **20 Hz** | FS Acellular Day 5 vs. FS Cellular Day 5 | Yes | < 0.0001 |
| **20 Hz** | FS Cellular Day 1 vs. FS Cellular Day 5 | Yes | 0.0003 |

The statistically significant results of the statistical analysis of cellular alignment at distances from the impact zone across a ten day period are presented in Table II.II.

**Table II.II: Statistical analysis of cellular alignment at distances from the impact zone across a ten day period.**

| Tukey's multiple comparisons test at distance (μm) / time (days) from impact. | Summary | Adjusted P Value |
|---|---|---|
| Day 1 100 vs. Day 1 500 | * | 0.0174 |
| Day 1 100 vs. Day 1 600 | *** | 0.0003 |
| Day 1 100 vs. Day 1 800 | ** | 0.0035 |
| Day 1 200 vs. Day 10 200 | * | 0.0158 |
| Day 1 300 vs. Day 10 300 | * | 0.0213 |
| Day 5 100 vs. Day 5 300 | * | 0.0282 |
| Day 5 100 vs. Day 5 400 | *** | 0.0002 |
| Day 5 100 vs. Day 5 500 | ** | 0.0013 |
| Day 5 100 vs. Day 5 600 | **** | < 0.0001 |
| Day 5 100 vs. Day 5 700 | *** | 0.0004 |
| Day 5 100 vs. Day 5 800 | **** | < 0.0001 |
| Day 5 100 vs. Day 5 900 | **** | < 0.0001 |
| Day 5 100 vs. Day 5 1000 | **** | < 0.0001 |
| Day 5 200 vs. Day 5 600 | ** | 0.0084 |
| Day 5 200 vs. Day 5 800 | ** | 0.0073 |
| Day 5 200 vs. Day 5 900 | **** | < 0.0001 |
| Day 5 200 vs. Day 5 1000 | ** | 0.0029 |
| Day 5 300 vs. Day 5 900 | * | 0.041 |
| Day 10 100 vs. Day 10 300 | ** | 0.0038 |
| Day 10 100 vs. Day 10 400 | **** | < 0.0001 |
| Day 10 100 vs. Day 10 500 | **** | < 0.0001 |
| Day 10 100 vs. Day 10 600 | **** | < 0.0001 |
| Day 10 100 vs. Day 10 700 | **** | < 0.0001 |
| Day 10 100 vs. Day 10 800 | **** | < 0.0001 |
| Day 10 100 vs. Day 10 900 | **** | < 0.0001 |
| Day 10 100 vs. Day 10 1000 | **** | < 0.0001 |
| Day 10 200 vs. Day 10 500 | * | 0.0201 |
| Day 10 200 vs. Day 10 600 | **** | < 0.0001 |
| Day 10 200 vs. Day 10 700 | **** | < 0.0001 |
| Day 10 200 vs. Day 10 800 | **** | < 0.0001 |
| Day 10 200 vs. Day 10 900 | **** | < 0.0001 |
| Day 10 200 vs. Day 10 1000 | **** | < 0.0001 |
| Day 10 300 vs. Day 10 600 | ** | 0.0043 |

| | | |
|---|---|---|
| Day 10 300 vs. Day 10 700 | *** | 0.0005 |
| Day 10 300 vs. Day 10 800 | **** | < 0.0001 |
| Day 10 300 vs. Day 10 900 | **** | < 0.0001 |
| Day 10 300 vs. Day 10 1000 | **** | < 0.0001 |
| Day 10 400 vs. Day 10 800 | *** | 0.0005 |
| Day 10 400 vs. Day 10 900 | *** | 0.0002 |
| Day 10 400 vs. Day 10 1000 | **** | < 0.0001 |
| Day 10 500 vs. Day 10 800 | ** | 0.0028 |
| Day 10 500 vs. Day 10 900 | ** | 0.0012 |
| Day 10 500 vs. Day 10 1000 | **** | < 0.0001 |
| Day 10 600 vs. Day 10 1000 | ** | 0.0082 |
| Day 10 700 vs. Day 10 1000 | * | 0.0161 |